



**ON THE ALBER EQUATION FOR RANDOM
WATER-WAVES**

Agustinus Ribal

Submitted to fulfilment of the requirements for the degree of
Doctor of Philosophy

Centre for Ocean Engineering, Science and Technology
Faculty of Engineering and Industrial Sciences
Swinburne University of Technology
Melbourne, Australia
2013

Abstract

In this thesis, we investigated the instability of two-dimensional wave-fields and its concurrent evolution in time by means of the Alber equation for narrow-banded random surface-waves in deep water subject to inhomogeneous disturbances. A linear partial differential equation (PDE) is obtained after applying inhomogeneous disturbances to the Alber equation and based on the solution of this PDE, the instability of the ocean wave surface is studied by given a spectrum. The study is started from symmetric spectra with variable spectral width in directions perpendicular and parallel to the carrier wave, namely, a very simple structure of the square spectrum and the rectangular spectrum, and a popular Lorentz spectrum and then continued for realistic asymmetric JONSWAP spectrum of ocean waves with variable directional spreading and steepness. For the symmetric spectra, it is found that the instability is independent of the spectral width which is perpendicular to the carrier waves while for JONSWAP spectrum, it is found that instability depends on the directional spreading and parameters α and γ of the JONSWAP spectrum. α and γ are the energy scale and the peak-enhancement factor, respectively, and both influence the mean steepness of waves with such a spectrum, although in different ways. Specifically, if the instability stops due to the directional spreading, an increased value of steepness by increasing α or γ can reactivate it. A criterion for the instability is suggested as a dimensionless “width parameter”, Π . For the unstable conditions, long-time evolution is simulated by integrating the Alber equation numerically. Recurrent evolution which is a stochastic counterpart of the Fermi–Pasta–Ulam recurrence obtained for the cubic Schrödinger equation is obtained. This recurrence enables us to study the probability of freak waves and the results are compared to the values given by the Rayleigh distribution that was obtained for the linear waves as well as to the Forristall distribution based on the second-order theory. Interestingly, it is found that stability/instability transition, the most unstable mode, recurrence duration and freak wave probability all depend solely on the dimensionless “width parameter”, Π .

Keywords: modulational instability, long-time evolution, probability of freak waves, inhomogeneous disturbances, nonlinear waves.

Acknowledgement

I would like to express my appreciation to my principal supervisor, Professor Alexander Babanin, and my co-supervisors, Professor Michael Stiassnie from Technion, Israel Institute of Technology, Haifa, Israel and Associate Professor Alessandro Toffoli from University of Plymouth, United Kingdom, for their invaluable technical guidance, support, wisdom and encouragement throughout the full period of my postgraduate research studies at Swinburne University of Technology. I am thankful to them for giving me an opportunity to work with them in order to improve my knowledge in both theoretical and experimental ocean waves.

I am greatly indebted to Professor Michael Stiassnie and his wife Hadassa Stiassnie for giving me an opportunity to visit Israel, the Holy land, in general and in particular to study at the Faculty of Civil and Environmental Engineering, Technion – Israel Institute of Technology, Haifa. Their hospitality during my stay in Israel is really appreciated.

I wish to extend my gratitude to Professor Ian Young, Vice-Chancellor and President of The Australian National University, Australia who won the grant and funded this project through the Australian Research Council (ARC) Grants No. LP0882422 and DP1093349. I wish to thank Dr. Ruslan Puscasu for his valuable help with English of the thesis. Moreover, I also wish to thank Associate Professor Jarrod Hurley at Swinburne supercomputer during the simulations which is very much appreciated. I thank Dr. Stefan Zieger for his valuable assistance for my research studies particularly in Matlab.

I would also like to thank my family for their moral support for my studies and my son, Arjuna Ribal, and daughters, Arfelial Ribal and Armelvica Ribal, for their patience and being good children.

Finally, my praise to the Lord, Jesus Christ, because of His blessings everything can be done.

Declaration by Candidate

I, Agustinus Ribal, hereby declare that this submission is entirely my own work and that, to the best of my knowledge and belief, it contains no material previously published or written by another person nor material which to a substantial extent has been accepted for the award of any other degree or diploma of the university or other institute of higher learning, except where due reference is made in the text.

18th April 2013

Agustinus Ribal

Table of Contents

Abstract	i
Acknowledgement	ii
Declaration by Candidate	iii
Table of Contents	iv
List of Figures	vii
List of Tables	xvi
1 Introduction	1
1.1 Background	1
1.2 Objectives.....	4
1.3 Outline of the thesis.....	4
2 Literature review	6
2.1 Introduction	6
2.2 Derivation of the Alber equation.....	9
2.2.1 The Davey – Stewartson equations.....	9
2.2.2 The Alber equation.....	11
2.3 Modulational instability in one spatial dimension	15
2.4 Modulational instability in two spatial dimensions	18
2.5 Long-time evolution of an unstable water-wave train	22
2.6 Ocean wave statistics	30
2.6.1 Wave height distributions	30
2.6.2 Significant wave height.....	37
3 Linear stability analysis in two spatial dimensions	41
3.1 Introduction	41
3.2 The Alber equation in waves of infinite depth.....	42
3.3 Correlation function for homogeneous seas.....	43

3.4	Instability of inhomogeneous disturbances	44
3.4.1	Square spectrum and its growth rate	51
3.4.2	Rectangular spectrum and its growth rate.....	59
3.4.3	Lorentz spectrum and its growth rate.....	67
3.4.4	JONSWAP spectrum and its growth rate.....	77
3.4.4.1	Lorentzian spectrum	78
3.4.4.2	Unidirectional JONSWAP spectrum.....	82
3.4.4.3	JONSWAP spectrum with a directional distribution	94
3.5	Interpretation of the initial disturbances.....	100
3.5.1	Spectral interpretation of the initial conditions.....	100
3.5.2	Connection to the initial surface elevation.....	104
3.6	Concluding remarks	106
4	Long-time evolution in two spatial dimensions.....	109
4.1	Introduction	109
4.2	Numerical solution of the Alber equation	112
4.2.1	Non-dimensional Alber equation	112
4.2.2	Numerical scheme.....	113
4.2.3	Periodicity in \tilde{x}	115
4.2.4	Condition at large \tilde{r}	116
4.3	Stochastic recurrence.....	122
4.3.1	Description of the initial conditions.....	122
4.3.2	Invariants of motion	126
4.3.3	Justification for truncating the \tilde{r} -axis	127
4.3.4	Recurrence for unidirectional JONSWAP spectrum	131
4.3.5	Recurrence for JONSWAP spectrum with directional distribution	137
4.4	Concluding remarks	144
5	Application to the statistics of freak waves in directional sea states.....	145
5.1	Introduction	145
5.2	Theoretical background.....	151
5.2.1	The Rayleigh distribution.....	151

5.2.2	The Forristall distribution on infinitely deep water	152
5.2.3	Probability distribution of the wave height.....	154
5.3	Recurrent solutions.....	156
5.4	The probability of freak waves.....	158
5.4.1	Unidirectional sea states.....	158
5.4.2	Directional sea states.....	166
5.4.3	Comparison to the Forristall distribution.....	171
5.5	Concluding remarks	175
6	Summary and Conclusions	177
6.1	Summary	177
6.2	Further work.....	184
	References	185
	Appendix A: Derivation of the Invariants	191
	Publications.....	194

List of Figures

Figure 2.1: Instability growth rate of a uniform wave train subject to two-dimensional perturbations. The labels indicate the number of unstable harmonics (including the fundamental perturbation, which is denoted by \blacktriangle), (Yuen and Lake, 1982, Fig. 11).....	24
Figure 2.2: Time evolution of unstable uniform wave trains subject to perturbations specified in Figure 2.1. The case numbers correspond to the encircled numbers in Figure 2.1. Note that the maximum number of prominent peaks appearing in time for each case is equal to the case number as predicted by the relationship (Yuen and Lake, 1982, Fig. 12).....	25
Figure 2.3: Region of instability of a uniform solution to infinitesimal disturbance with wave vector (p, q) . The line within the instability region denotes the locus of maximum instability (Martin and Yuen, 1980a, Fig. 1).	25
Figure 2.4: Long-time behaviour of the random version of the Benjamin-Feir instability. Shown are the cases of a uniform wavetrain ($\sigma = 0$), a narrow spectrum $\sigma = O(\Delta)$ and a broad spectrum $\sigma = O(1)$, (Janssen, 1983, Fig. 3).....	26
Figure 2.5: Isolines of the non-dimensional growth-rate, $\tilde{\Omega}_i$, for three spectra: (a) square spectrum; (b) Lorentz spectrum; (c) Gaussian spectrum. Dots refer to the cases where they studied long-time evolution (Stiassnie et al., 2008, Fig. 2).	27
Figure 2.6: The values of $\tilde{\rho}(0,0,\tilde{\tau}) / \tilde{\rho}_h(0)$ as a function of time for three different initial spectra: \blacksquare , square (A_1); $\square\square\square$, Gaussian (A_3); --- , Lorentz (A_2). A_1 , A_2 and A_3 refer to Figure 2.5 (Stiassnie et al., 2008, Fig. 11).	28
Figure 2.7: Three cases near the marginal-stability curve (Stiassnie et al., 2008, Fig. 15).	29
Figure 2.8: The values of $\tilde{\rho}(0,0,\tilde{\tau}) / \tilde{\rho}_h(0)$ as a function of time for three cases near the threshold of instability. \blacksquare , P_1 ; --- , P_2 ; $\square\square\square$, P_3 . P_1 , P_2 and P_3 refer to Figure 2.7 (Stiassnie et al., 2008, Fig. 14).	29
Figure 2.9: The significant wave height in the Rayleigh probability density function (Holthuijsen, 2007, Fig. 4.9).	39
Figure 3.1: Square spectrum.	52

Figure 3.2: Stability diagrams for square spectra, giving the dimensionless growth rate, $\tilde{\Omega}_i$, of the inhomogeneous disturbances. The number on the line represents the dimensionless growth rate and the square in each figure indicates the footprint of a quarter of the initial spectrum while \tilde{P} and \tilde{Q} are the dimensionless wavenumbers of the disturbances and \tilde{W} is the dimensionless spectral width. (a) $\tilde{W} = 0$, (b) $\tilde{W} = 1$, (c) $\tilde{W} = 2$ 58

Figure 3.3: Relation between the dimensionless growth rate, $\tilde{\Omega}_i$, and the dimensionless spectral width, \tilde{W} , in which the wavenumber of the disturbance which is perpendicular to the carrier wave, \tilde{Q} , is zero. The horizontal line represents the dimensionless wavenumber of the disturbance which is parallel to the carrier wave, the vertical line reveals the dimensionless growth rate and the number on the line represents the dimensionless spectral width with 0.25 increments. 59

Figure 3.4: Maximum values of the dimensionless growth rate, $\tilde{\Omega}_i^{(max)}$, as a function of dimensionless spectral width in direction parallel to the carrier wave, \tilde{W}_1 , for one-dimensional spectrum. 62

Figure 3.5: Values of the dimensionless most unstable mode, $\tilde{P}^{(max)}$, for which the dimensionless maximum growth rate, $\tilde{\Omega}_i^{(max)}$, is obtained for one-dimensional spectrum. 63

Figure 3.6: Isolines for the special case of a rectangular spectrum where horizontal line reveals the dimensionless wavenumber of the disturbance and vertical line indicates the dimensionless spectral width which is parallel to the carrier wave. The value on each line represents the dimensionless growth rate. . 64

Figure 3.7: The footprints of the elongated spectrum (a) and the stretched spectrum (b). 64

Figure 3.8: Relation between dimensionless growth rate, $\tilde{\Omega}_i$, and the dimensionless wavenumber of the disturbance which is parallel to the carrier-wave. The number on the line represents the dimensionless geometric average of the spectral widths, $\sqrt{\tilde{W}_1\tilde{W}_2}$, for elongated spectra in which the wavenumber of the disturbance which is perpendicular to the carrier wave, \tilde{Q} , is zero. 66

Figure 3.9: Relation between dimensionless growth rate, $\tilde{\Omega}_i$, and the dimensionless wavenumber of the disturbance which is parallel to the carrier wave. The number on the line represents the dimensionless geometric average of the spectral widths, $\sqrt{\tilde{W}_1\tilde{W}_2}$, for stretched spectra in which the wavenumber of the disturbance which is perpendicular to the carrier wave, \tilde{Q} , is zero. ... 66

Figure 3.10: Stability diagrams for elongated spectra, giving the dimensionless growth rate, $\tilde{\Omega}_i$, of the inhomogeneous disturbances. The number on the line represents the dimensionless growth rate and the rectangular in each figure indicates the footprint of a quarter of the initial spectrum while \tilde{P} and \tilde{Q} are the dimensionless wavenumbers of the disturbances and \tilde{W}_1 and \tilde{W}_2 are the dimensionless spectral widths. (a) $\tilde{W}_1 = 5/\sqrt{20}$, $\tilde{W}_2 = 1/\sqrt{20}$; (b) $\tilde{W}_1 = 10/\sqrt{20}$, $\tilde{W}_2 = 2/\sqrt{20}$; (c) $\tilde{W}_1 = 20/\sqrt{20}$, $\tilde{W}_2 = 4/\sqrt{20}$ 68

Figure 3.11: Stability diagrams for stretched spectra, giving the dimensionless growth rate, $\tilde{\Omega}_i$, of the inhomogeneous disturbances. The number on the line represents the dimensionless growth rate and the rectangular in each figure indicates the footprint of a quarter of the initial spectrum while \tilde{P} and \tilde{Q} are the dimensionless wavenumbers of the disturbances and \tilde{W}_1 and \tilde{W}_2 are the dimensionless spectral widths. (a) $\tilde{W}_1 = 1/\sqrt{20}$, $\tilde{W}_2 = 5/\sqrt{20}$; (b) $\tilde{W}_1 = 2/\sqrt{20}$, $\tilde{W}_2 = 10/\sqrt{20}$; (c) $\tilde{W}_1 = 4/\sqrt{20}$, $\tilde{W}_2 = 20/\sqrt{20}$ 69

Figure 3.12: Stability diagrams for rectangular spectra, giving the dimensionless growth rate, $\tilde{\Omega}_i$, of the inhomogeneous disturbances. The number on the line represents the dimensionless growth rate and the rectangular/square in each figure indicates the footprint of a quarter of the initial spectrum while \tilde{P} and \tilde{Q} are the dimensionless wavenumbers of the disturbances and \tilde{W}_1 and \tilde{W}_2 are the dimensionless spectral widths. (a) $\tilde{W}_1 = 1$, $\tilde{W}_2 = 1$; (b) $\tilde{W}_1 = 1$, $\tilde{W}_2 = 1/5$; (c) $\tilde{W}_1 = 1$, $\tilde{W}_2 = 5$ 70

Figure 3.13: A two-dimensional Lorentz spectrum (a) and its isolines (b). 71

Figure 3.14: Stability diagrams for Lorentz spectra, giving the dimensionless growth rate, $\tilde{\Omega}_i$, of the inhomogeneous disturbances. The number on the line represents the dimensionless growth rate while \tilde{P} and \tilde{Q} are the dimensionless wavenumbers of the disturbances and \tilde{W}_1 and \tilde{W}_2 are the

dimensionless spectral widths. (a) $\tilde{W}_1 = 0.25, \tilde{W}_2 = 0.25$; (b) $\tilde{W}_1 = 0.25, \tilde{W}_2 = 0.05$; (c) $\tilde{W}_1 = 0.25, \tilde{W}_2 = 1.25$	76
Figure 3.15: Comparison between the original JONSWAP spectrum (black line) and the JONSWAP spectrum (red line) as given in equation (3.44).	78
Figure 3.16: A Lorentzian spectrum (blue line) as in the equation (3.46) and the JONSWAP spectrum (red line) as given in equation (3.44).	80
Figure 3.17: Instability diagram in the $\alpha - \gamma$ plane of the Lorentzian spectrum. α is the Philips parameter and γ is the peak enhancement factor. The red line represents the marginal instability.....	81
Figure 3.18: Validation of the “general-method” $\bullet \bullet \bullet \bullet$, against the analytical solution \blacksquare , for a one-dimensional Lorentz spectrum. (a) most unstable mode, (b) its growth rate.	85
Figure 3.19: Validation of the “general-method” $\bullet \bullet \bullet \bullet$, against the analytical solution \blacksquare , for a two-dimensional Lorentz spectrum. (a) most unstable mode, (b) its growth rate.	86
Figure 3.20: Instability diagram in the $\varepsilon - \gamma$ plane of the unidirectional JONSWAP spectrum. Solid line represents the steepness as a function of γ which is the marginal instability line and dashed lines represent the values of different α	89
Figure 3.21: Results of linear stability analysis for unidirectional JONSWAP spectra as a function of the “width-parameter” Π_1 . (a) most unstable mode, (b) its growth rate.....	93
Figure 3.22: Results of linear stability analysis for the JONSWAP spectra with directional distributions as a function of the “width-parameter” Π_2 . (a) most unstable mode, (b) its growth rate.	99
Figure 3.23: Schematic description of the main homogeneous spectrum and the inhomogeneous disturbances (see Fig. 4 of Stiassnie et al. (2008)).....	106
Figure 4.1: Schematic description of the numerical domain for one-dimensional case (see Fig. 5 of Stiassnie et al., 2008).....	115
Figure 4.2: The energy spectrum for the peak enhancement factor $\gamma = 20$ with different values of the energy scale α	123




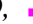
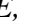


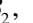
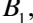



Figure 4.3: The energy spectrum for the peak enhancement factor $\gamma=10$ with different values of the energy scale α .	124
Figure 4.4: Energy directional spreading as a function of angle θ for different values of the parameter n .	125
Figure 4.5: Non-dimensional growth rate, $\tilde{\Omega}_i$, for $\alpha=0.016$, $\gamma=10$ and $\sigma=0.08$ where the horizontal axis represents the dimensionless wavenumber of the disturbance in direction parallel to the carrier wave.	128
Figure 4.6: The influence of the extent of the \tilde{r}_1 domain on the maximum value of $\tilde{\rho}$ at $\tilde{r}_1=0$ as a function of non-dimensional time $\tilde{\tau}$, for $(\tilde{r}_1)_{end}=10\tilde{x}_{end}$, $(\tilde{r}_1)_{end}=15\tilde{x}_{end}$, $(\tilde{r}_1)_{end}=20\tilde{x}_{end}$ and $(\tilde{r}_1)_{end}=30\tilde{x}_{end}$. These calculations are for a homogeneous unidirectional JONSWAP spectrum and an inhomogeneous unidirectional JONSWAP disturbance with $\alpha=0.016$, $\gamma=10$, $\tilde{P}_1^{(max)}=1.52$, $\delta=0.1$.	129
Figure 4.7: The influence of the extent of the \tilde{r}_1 domain on the real part of the second invariant I_2 as a function of non-dimensional time $\tilde{\tau}$. These cases are the same as in Figure 4.6.	130
Figure 4.8: The influence of the extent of the \tilde{r}_1 domain on the imaginary part of the second invariant I_2 as a function of non-dimensional time $\tilde{\tau}$. These cases are the same as in Figure 4.6.	130
Figure 4.9: The influence of the extent of the \tilde{r}_1 domain of the third invariant I_3 as a function of non-dimensional time $\tilde{\tau}$. These cases are the same as in Figure 4.6.	130
Figure 4.10: Recurrence solutions for unidirectional JONSWAP spectra with $\gamma=20$; A,  ; B,  ; C,  ; D,  ; E,  (see Table 4.3).	132
Figure 4.11: Isolines of $\tilde{\rho}(\tilde{x},0,\tilde{\tau})/\tilde{\rho}_h(0)$. Each case refers to Table 4.3 for $\gamma=20$.	133
Figure 4.12: Recurrence solutions for unidirectional JONSWAP spectra with $\gamma=10$; B ₄ ,  ; B ₃ ,  ; B ₂ ,  ; B ₁ ,  (see Table 4.3).	134
Figure 4.13: Isolines of $\tilde{\rho}(\tilde{x},0,\tilde{\tau})/\tilde{\rho}_h(0)$. Each case refers to Table 4.3 for $\gamma=10$.	134
Figure 4.14: Values of $\tilde{\rho}_{max}(\tilde{x},0,\tilde{\tau})/\tilde{\rho}_h(0)$ as a function of non-dimensional time, $\tilde{\tau}$, for three cases near the threshold of instability for $\gamma=10$, $\sigma=0.08$, $\delta=0.1$; P ₁ ,  ; P ₂ ,  ; P ₃ , 	135











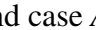
Figure 4.15: α versus γ , three cases near the marginal stability where red line represents the marginal-instability line.	136
Figure 4.16: $\tilde{\Omega}_i$ versus \tilde{P} , four cases of simple and complex recurrence, $A_1(\tilde{P} = 0.795)$, $A_2(\tilde{P} = 0.954)$, $A_3(\tilde{P} = 1.113)$ and $A_4(\tilde{P} = 1.272)$. All other parameters are the same as in Figure 4.5.	136
Figure 4.17: Values of $\tilde{\rho}_{max}(\tilde{r} = 0)$ as a function of non-dimensional time, $\tilde{\tau}$, for three cases in the complex recurrence and one case in the simple recurrence. A_1 ,  , A_2 ,  , A_3 ,  , A_4 ,  . A_1, A_2, A_3 and A_4 as shown in Figure 4.16.	137
Figure 4.18: Comparison between the solution for unidirectional JONSWAP spectrum  , and JONSWAP spectrum with degree of directional distribution $n = 90$,  . Both spectra have the same $\gamma = 20$ and $\varepsilon = 0.13$ ($\alpha = 0.01$).	138
Figure 4.19: Isolines for JONSWAP spectrum with $\gamma = 10$, $\alpha = 0.016$, $\sigma = 0.08$, $n = 2$ and $k_0 = 1$. k_1 and k_2 are the wavenumbers in direction perpendicular and parallel to the carrier wave, respectively.	139
Figure 4.20: Isolines for JONSWAP spectrum with $\gamma = 10$, $\alpha = 0.016$, $\sigma = 0.08$, $n = 10$ and $k_0 = 1$. k_1 and k_2 are the wavenumbers in direction perpendicular and parallel to the carrier wave, respectively.	139
Figure 4.21: Isolines for JONSWAP spectrum with $\gamma = 10$, $\alpha = 0.016$, $\sigma = 0.08$, $n = 50$ and $k_0 = 1$. k_1 and k_2 are the wavenumbers in direction perpendicular and parallel to the carrier wave, respectively.	140
Figure 4.22: The initial homogeneous correlation function with respect to \tilde{r}_1 . The red line represents the imaginary part and the blue line represents the real part.	141
Figure 4.23: The initial homogeneous correlation function with respect to \tilde{r}_2 . The red line represents the imaginary part and the blue line represents the real part.	141
Figure 4.24: Three-dimensional image of the real part of the initial homogeneous correlation function.	142
Figure 4.25: The influence of the directional spreading on the variation of the maximum value of $\tilde{\rho}$ at $\tilde{\mathbf{r}} = \mathbf{0}$, as a function of non-dimensional time, $\tilde{\tau}$	142

Figure 4.26: Isolines of $\tilde{\rho}(\tilde{x}, \mathbf{0}, \tilde{\tau}) / \tilde{\rho}_h(\mathbf{0})$. Each case refers to Figure 4.25.	143
Figure 5.1: Comparison between the probability of wave height for the unidirectional and directional sea states based on the Forristall distribution and the probability of wave height given by the Rayleigh distribution.	154
Figure 5.2: A typical cycle of the long-time recurring evolution of $\tilde{\rho}_m(\tilde{\tau}) / \tilde{\rho}_h(0)$ as a function of the dimensionless time for unidirectional JONSWAP spectra with $\gamma = 20$ and five different values of the energy scale.	157
Figure 5.3: A typical cycle of the long-time recurring evolution of $\tilde{\rho}_m(\tilde{\tau}) / \tilde{\rho}_h(0)$ as a function of the dimensionless time for unidirectional JONSWAP spectra with $\gamma = 10$ and four different values of the energy scale.	157
Figure 5.4: A typical cycle of the long-time recurring evolution of $\tilde{\rho}_m(\tilde{\tau}) / \tilde{\rho}_h(\mathbf{0})$ as a function of the dimensionless time for JONSWAP spectra with two different degrees of the directional distribution $\cos^n(\theta)$ and with $\alpha = 0.016$ and $\gamma = 10$	157
Figure 5.5: Probability density function pdf($\tilde{\rho} / \tilde{\rho}_h$) and probability function $P(\tilde{\rho} / \tilde{\rho}_h)$ (solid line) as functions of $\tilde{\rho} / \tilde{\rho}_h$ for unidirectional JONSWAP spectra with $\gamma = 20$	160
Figure 5.6: The probability of freak waves ($\hat{H} / H_{rms0} \geq 2.84; \hat{H} \geq 2H_s$) for the Rayleigh distribution,  , and the probability obtained from the Alber equation for unidirectional JONSWAP spectra with $\gamma = 20$: case A (○), case B (□), case C (△), case D (+) and case E (◇) (see Table 5.1). The inset shows probability function for the Rayleigh distribution (solid line) and case E (dashed line) starting from zero wave height.	161
Figure 5.7: The probability of freak waves ($\hat{H} / H_{rms0} \geq 2.84; \hat{H} \geq 2H_s$) for the Rayleigh distribution and for unidirectional JONSWAP spectra with $\gamma = 20$ as in Figure 5.6, linear scales.	162
Figure 5.8: The probability of freak waves ($\hat{H} / H_{rms0} \geq 4.26; \hat{H} \geq 3H_s$) for the Rayleigh distribution and the probability obtained from the Alber equation for unidirectional JONSWAP spectra with $\gamma = 20$ as in Figure 5.6, linear scales.	162

- Figure 5.9: Probability density function pdf($\tilde{\rho} / \tilde{\rho}_h$) and probability function $P(\tilde{\rho} / \tilde{\rho}_h)$ (solid line) as functions of $\tilde{\rho} / \tilde{\rho}_h$ for unidirectional JONSWAP spectra with $\gamma=10$ 163
- Figure 5.10: The probability of freak waves ($\hat{H} / H_{rms0} \geq 2.84; \hat{H} \geq 2H_s$) for the Rayleigh distribution, , and the probability obtained from the Alber equation for unidirectional JONSWAP spectra with $\gamma=10$: case B_1 (\circ), case B_2 (\square), case B_3 (\diamond) and case B_4 (\triangle). The inset shows probability function for the Rayleigh distribution (solid line) and case B_4 (dashed line) starting from zero wave height. 164
- Figure 5.11: The probability of freak waves ($\hat{H} / H_{rms0} \geq 2.84; \hat{H} \geq 2H_s$) for the Rayleigh distribution and for unidirectional JONSWAP spectra with $\gamma=10$ as in Figure 5.10, linear scales. 164
- Figure 5.12: The probability of freak waves ($\hat{H} / H_{rms0} \geq 4.26; \hat{H} \geq 3H_s$) for the Rayleigh distribution and the probability obtained from the Alber equation for unidirectional JONSWAP spectra with $\gamma=10$ as in Figure 5.10, linear scales. 165
- Figure 5.13: Probability density function pdf($\tilde{\rho} / \tilde{\rho}_h$) and probability function $P(\tilde{\rho} / \tilde{\rho}_h)$ (solid line) as functions of $\tilde{\rho} / \tilde{\rho}_h$ cases A_1 (left) and A_2 (right) of Table 5.2. 166
- Figure 5.14: The probability of freak waves ($\hat{H} / H_{rms0} \geq 2.84; \hat{H} \geq 2H_s$) for the Rayleigh distribution, , and the probability obtained from the Alber equation for JONSWAP spectra with different degrees of the directional distributions: case A_1 () and case A_2 () (see Table 5.2). The inset shows probability function for the Rayleigh distribution (solid line) and case A_1 (dashed line) starting from zero wave height. 167
- Figure 5.15: The probability of freak waves ($\hat{H} / H_{rms0} \geq 2.84; \hat{H} \geq 2H_s$) for the Rayleigh distribution and for JONSWAP spectra with different directional distributions with value of parameters $\gamma=10$, $\alpha=0.016$ and the linear vertical axis (see Table 5.2). 168
- Figure 5.16: The probability of freak waves ($\hat{H} / H_{rms0} \geq 4.26; \hat{H} \geq 3H_s$) for the Rayleigh distribution and for JONSWAP spectra with different directional

distributions and value parameters $\gamma=10$, $\alpha=0.016$ and the linear vertical axis (see Table 5.2).....	169
Figure 5.17: Simple relations between the probability of freak waves and the dimensionless “width parameter”, Π	170
Figure 5.18: The comparison between the probability of wave height obtained from the Forristall distribution for the unidirectional sea states and the probability obtained from the Alber equation, i.e. case B_1	172
Figure 5.19: The comparison between the probability of wave height obtained from the Forristall distribution for the unidirectional sea states and the probability obtained from the Alber equation, i.e. case A	172
Figure 5.20: The comparison between the probability of wave height obtained from the Forristall distribution for the unidirectional sea states and the probability obtained from the Alber equation, i.e. cases A and B_1	173
Figure 5.21: The comparison between the probability of wave height obtained from the Forristall distribution for directional sea states and the probability obtained from the Alber equation, i.e. case B_1	174
Figure 5.22: The comparison between the probability of wave height obtained from the Forristall distribution for directional sea states and the probability obtained from the Alber equation, i.e. case A_1	174

List of Tables

Table 2.1: Various models for random ocean wave fields.....	7
Table 3.1: Results for unidirectional JONSWAP spectra where ε is the steepness, $p_1^{(max)}$ is the wavenumber of the most unstable mode and $\Omega_1^{(max)}$ is the maximum growth rate. α and γ are the Philips parameter and peak enhancement factor, respectively.	89
Table 3.2: Results for unidirectional JONSWAP spectra where ε is the steepness, $\tilde{P}_1^{(max)}$ is the dimensionless wavenumber of the most unstable mode and $\tilde{\Omega}_1^{(max)}$ is the dimensionless maximum growth rate. α and γ are the Philips parameter and peak enhancement factor, respectively.....	90
Table 3.3: The results for the JONSWAP spectra with directional distributions where γ is the peak enhancement factor, α is the energy scale, n is the degree of directional energy distribution, A_d is the normalization factor of the directional spreading, ε is the wave steepness, $\tilde{P}_2^{(max)}$ is the dimensionless wavenumber of the most unstable mode and $\tilde{\Omega}_2^{(max)}$ is the dimensionless maximum growth rate.	96
Table 4.1: Values of parameters of initial conditions for unidirectional JONSWAP spectrum.	123
Table 4.2: Comparison for the maximum deviation of I_3 (in percents) from its value at $\tilde{\tau}=0$ for all four cases throughout the calculated evolutions.....	131
Table 4.3: Spectral parameters and evolution features for unidirectional JONSWAP spectra.....	133
Table 4.4: Spectral parameters for JONSWAP spectra with directional distribution, with $\gamma=10$, $\alpha=0.016$. n is the degree of the directional distribution and A_d is the normalization factor (equation (3.57)), $\tilde{P}_2^{(max)}$, \tilde{W} , \tilde{W}_l and \tilde{W}_r are dimensionless wavenumber of the disturbance which is the point of maximum growth rate and dimensionless spectral widths of the rectangular spectra, respectively.	139

Table 4.5: Spectral parameters and evolution features for JONSWAP spectra with three different degrees of the directional distributions, n , and $\gamma=10$, $\alpha=0.016$.
 A_d is the normalization factor of the directional spreading. 143

Table 5.1: The probability of wave height for unidirectional JONSWAP spectra where H_f stands for freak wave height and H_s is the significant wave height.
..... 165

Table 5.2: The probability of wave height for JONSWAP spectra with different degrees of the directional distributions where H_f stands for freak wave height and H_s is the significant wave height..... 169

Chapter 1

Introduction

1.1 Background

Air travel is the fastest growing mode of transportation in the world today (Ruffles, 2001). However, it is inevitable that in terms of shipping cost, e.g. per tonne mile, ships are two orders of magnitude more efficient than the air freight (Faulkner, 2002, Toffoli et al., 2003). It is therefore necessary to provide safe navigation and to prevent accidents leading to increased risk of life, property and environment (Toffoli et al., 2003). In order to guarantee maritime safety, accurate information of wave height for the safety of shipping or operational transportation is necessary. In addition, wave height information is important for the design of marine and coastal structures, oceanographic applications and naval architectures. One of the most important issues in this regard is related to extreme wave events during storms. These extreme events are dangerous for the vessels around the oceans (see e.g. Toffoli et al., 2003, 2005).

Although the forecasts are accurate, the abnormal waves often known as freak or rogue waves cannot be predicted even with the modern wave forecasting. This is because the modern forecasting systems only determine the evolution of the spectrum, but they do not provide any information on the instantaneous position of the water surface (e.g. Janssen and Bidlot, 2009). There is no standard definition for these very exceptional waves. Most commonly, freak waves are defined as waves with a very unusual height appearing on the sea surface for a short period of time (see e.g. Lawton, 2001). Kharif and Pelinovsky (2003) argued that the freak waves are waves which are too high, too asymmetric and too steep. The most popular definition, however, is the comparison to the significant wave height. According to such definition, freak waves are those whose heights exceed the significant wave height more than two times, or sometimes more specifically 2.2 times (see e.g. Kharif and Pelinovsky, 2003, Janssen, 2003). It is believed that more than 200 ship accidents over the past two decades, including the loss

of super tankers and container ships exceeding 200 meters in length, have been caused mostly by rogue waves (ABC Science online, 2004).

There have been numerous observations of freak waves not only in the deep water but also on the shallow water or even at the coastline; see for example, Kharif and Pelinovsky (2003), Didenkulova et al. (2006), Dysthe et al. (2008) and Nikolkina and Didenkulova (2011). Recently, Nikolkina and Didenkulova (2012) provided a catalogue of the freak waves reported in media from 2006 to 2010 where 106 data were collected. They concluded that 78 out of 106 events are true freak waves while the rest are possible freak waves. As a special event, the accident of the cruise ship “*Louis Majesty*” was analysed by Cavaleri et al. (2012).

Therefore, based on the above facts, it is important to study the freak waves to save vessels as well as lives. However, since the main cause of these very exceptional waves is still unknown, it will be studied based on the some mechanisms that are responsible for their generation.

Generally, there are three mechanisms responsible for the formation of these very exceptionally waves (see, for example, Onorato et al., 2002, Kharif and Pelinovsky, 2003). Firstly, White and Fornberg (1998) argued that the presence of strong currents can be one of such mechanisms. This argument is supported by the work of Onorato et al. (2011) through numerical simulations based on the modified nonlinear Schrödinger equation derived by Hjelmervik and Trulsen (2009) that accounts for the current, and by the experiments in wave flume done by Toffoli et al. (2011). Another mechanism that is responsible for the formation of freak waves is suggested by Pelinovsky et al. (2000). Using analytical and numerical solution of Korteweg–de Vries equation for the shallow water with an initial condition corresponding to the expected freak wave, they found that freak waves are almost linear waves. Thus, it can be concluded that the second mechanism responsible for the generation of freak waves is the simple linear superposition of the waves. A third mechanism of the freak wave generation is modulational instability (Trulsen and Dysthe, 1997, Onorato et al., 2002). This last mechanism has been shown experimentally (see e.g. Onorato et al., 2009a, 2009b, Babanin et al., 2010, 2011a, 2011b), theoretically (see e.g. Tracy and Chen, 1988) and numerically (see e.g. Onorato et al., 2003, Toffoli et al., 2010b). Babanin et al. (2011b)

argued that in deep water modulational instability is the more likely cause of extreme waves, including rogue events, than the linear superposition.

In practical sense, a major issue is the dynamics of modulational instability in directional wave fields. While such instability in one-dimensional cases is well established and described (most often by means of nonlinear Schrödinger Equation, e.g. Janssen, 1981, Tracy and Chen, 1988, Onorato et al., 2003, Kharif and Pelinovsky, 2003, Kharif et al., 2010), it has been argued that is impaired or may be even suppressed in real directional seas (Babanin et al., 2010, 2011a, 2011b). Onorato et al. (2009a, 2009b) conducted studies of such two-dimensional cases. Their analyses were based on varying the degree of the directional distributions while keeping the steepness of the spectrum constant. Babanin et al. (2010, 2011b), however, argued that modulational instability does not only depend on the directional spreading but it also depends on steepness. They showed that if wave fields stabilize due to the broader directional spreading, an increase of the steepness could reactivate the instability.

Modulational instability in inhomogeneous wave fields will be addressed in this thesis by means of the two-dimensional Alber equation (Alber, 1978), which is a stochastic version of the cubic Schrödinger equation. Recently, Stiassnie et al. (2008) studied the instability of narrow spectra homogeneous seas and its subsequent evolution in time, subject to inhomogeneous disturbances by means of the one-dimensional Alber equation. They discovered the recurrent solution, which is the stochastic counterpart of the Fermi–Pasta–Ulam recurrence obtained for the cubic Schrödinger equation, in the area of instability. Moreover, Regev et al. (2008) used the work of Stiassnie et al. (2008) to study the probability of freak waves occurrence initialised by Gaussian spectra. Therefore, extending the work of Stiassnie et al. (2008) and Regev et al. (2008) from one spatial dimension to two spatial dimensions will be the main contributions of the present work. This will include a study of waves with realistic sea states characterized by the JONSWAP (Joint North Sea Wave Project) spectrum (Hasselmann et al., 1973), with and without directional distributions.

1.2 Objectives

Three main objectives have been set in this thesis which will be addressed by means of the two-spatial-dimensions of the Alber equation subject to inhomogeneous disturbances. The specific objectives are to:

- a. Determine the unstable condition based first on simple square spectra and rectangular spectra, then continued on the basis of more general Lorentz spectra and finally of realistic ocean wave JONSWAP spectra;
- b. Simulate the long-time evolution of wave fields for the unstable conditions obtained in Part (a), including JONSWAP spectrum with and without a directional distribution;
- c. Determine probability of occurrence of freak waves for both unidirectional and directional sea states.

1.3 Outline of the thesis

In this thesis, Chapter 2 is the literature survey. It includes previous findings based on the cubic Schrödinger equation, on the Alber equation and on the Kinetic equation, modulational instability in one and two spatial dimensions, and long-time evolution. Because of the particular topic, this thesis gives derivation of the Alber equation and describes wave height distributions including statistics of linear waves and nonlinear waves. The latter is based on the second- and third-order theories.

In Chapter 3, the linear instability of two-dimensional wave fields is investigated by means of the Alber equation for narrow-banded random surface waves in deep water subject to inhomogeneous disturbances. In this Chapter, instability of the ocean surface waves will be studied for a given spectrum and the most unstable mode and its growth rate will be determined. We start from a simple structure of the spectrum, that is square spectrum and rectangular spectrum, then continue with Lorentz spectrum. Finally, instability of realistic ocean wave JONSWAP spectrum is investigated for three different cases, the so called “Lorentzian” spectrum, i.e. the symmetric version of the JONSWAP, unidirectional JONSWAP spectrum and JONSWAP spectra with directional distributions.

Based on the instability conditions obtained in Chapter 3, the long-time evolution in two spatial dimensions will be shown in Chapter 4. In this regard, the Alber equation will be integrated numerically. To this end, a finite difference scheme is established and the boundary conditions as well as the initial conditions are determined. Derivation of the invariants of motion for the two-dimensional Alber equation as a quality control of the numerical solution is also given in this Chapter. Details of the derivation of invariants of motion are deferred to Appendix A.

Applications of the new results to the statistics of freak waves in both unidirectional and directional sea states are given in Chapter 5. These include comparisons to the Rayleigh distribution which was obtained for linear waves as well as to the Forristall distribution based on the second-order theory. Probability of freak waves is determined for both unidirectional JONSWAP spectra with variables energy scale and the peak enhancement factor and for JONSWAP spectra with various degrees of directional distribution. Finally, conclusions and discussions of the results are summarised in Chapter 6.

Chapter 2

Literature review

2.1 Introduction

The nonlinear evolution in time t and space $\mathbf{x} = (x_1, x_2)$ of ocean-wave fields is usually described by equations for the free-surface elevation $\eta(\mathbf{x}, t)$ or related quantities, such as an amplitude spectrum given by its \mathbf{x} to \mathbf{k} Fourier transform. For deep water, two frequently mentioned deterministic equations are: Zakharov equation for broad-amplitude spectra and the cubic Schrödinger equation for narrow spectra (see Zakharov 1968). The cubic Schrödinger equation is given by:

$$i \left(\frac{\partial A}{\partial t} + \frac{1}{2} \sqrt{\frac{g}{k_0}} \frac{\partial A}{\partial x_1} \right) - \frac{1}{4} \sqrt{\frac{g}{k_0^3}} \left(\frac{\partial^2 A}{\partial x_1^2} - 2 \frac{\partial^2 A}{\partial x_2^2} \right) = \frac{1}{2} \sqrt{gk_0^5} |A|^2 A \quad (2.1)$$

where $A(\mathbf{x}, t)$ is the complex amplitude envelope, centered around the carrier wave-number $\mathbf{k}_0 = (k_0, 0)$, and related to the free-surface elevation $\eta(\mathbf{x}, t)$ by

$$2\eta(\mathbf{x}, t) = A(\mathbf{x}, t) \exp[i(k_0 x_1 - \sqrt{gk_0} t)] + \text{c.c.} \quad (2.2)$$

In the above and elsewhere in this thesis, g is the acceleration due to gravity and $*$ stands for the complex conjugate. It is generally assumed that (2.1) and (2.2) also describe the evolution when $A(\mathbf{x}, t)$ and $\eta(\mathbf{x}, t)$ are random functions.

Longuet-Higgins (1976) and Alber (1978) have used (2.1) as their starting point for the formulation of two rather different stochastic evolution equations. Longuet-Higgins assumed that the wave-field is a homogeneous and nearly Gaussian random process; whereas Alber enabled the random process to be inhomogeneous, but required Gaussianity (see next section for details derivation of Alber's work). To somewhat clarify the above terminology we define the two-point space correlation function

$$\rho(\mathbf{x}, \mathbf{r}, t) = \left\langle A\left(\mathbf{x} + \frac{1}{2}\mathbf{r}, t\right) A^*\left(\mathbf{x} - \frac{1}{2}\mathbf{r}, t\right) \right\rangle \quad (2.3)$$

where $\langle \rangle$ denotes the ensemble average and \mathbf{r} is the spacing. We further mention a fourth order average which appears during the derivations:

$$f(\mathbf{x}, \mathbf{r}, t) = \left\langle A^2\left(\mathbf{x} + \frac{1}{2}\mathbf{r}, t\right) A^*\left(\mathbf{x} + \frac{1}{2}\mathbf{r}, t\right) A^*\left(\mathbf{x} - \frac{1}{2}\mathbf{r}, t\right) - A^2\left(\mathbf{x} - \frac{1}{2}\mathbf{r}, t\right) A^*\left(\mathbf{x} - \frac{1}{2}\mathbf{r}, t\right) A^*\left(\mathbf{x} + \frac{1}{2}\mathbf{r}, t\right) \right\rangle. \quad (2.4)$$

One should note that: (i) for a homogeneous process

$$\rho_h = \rho_h(\mathbf{r}, t) \quad (2.5)$$

is independent of \mathbf{x} ; and (ii) that for a nearly Gaussian process (2.4) reduces to

$$f(\mathbf{x}, \mathbf{r}, t) = 2\rho(\mathbf{x}, \mathbf{r}, t) \left[\rho\left(\mathbf{x} + \frac{1}{2}\mathbf{r}, \mathbf{0}, t\right) - \rho\left(\mathbf{x} - \frac{1}{2}\mathbf{r}, \mathbf{0}, t\right) \right] + c(\mathbf{x}, \mathbf{r}, t) \quad (2.6)$$

where $c(\mathbf{x}, \mathbf{r}, t)$ is the fourth order cumulant assumed to be small under the assumption of weak non-Gaussianity or zero under the assumption of strict Gaussianity. It is also important to mention that for a homogeneous process (2.6) becomes

$$f_h(\mathbf{r}, t) = c_h(\mathbf{r}, t) \quad (2.7)$$

which has to be estimated by using sixth order averages and a closure given by the assumption of vanishing sixth order cumulants. We summarise the four possibilities in the following Table 2.1.

Table 2.1: Various models for random ocean wave fields.

Homogeneous Gaussian	Yes	No
	Yes	Pierson (1955)
No	Longuet-Higgins (1976)	Crawford et al. (1980)

From Table 2.1, it is clear that Crawford et al. (1980) provide the more general option, but their result is so cumbersome that it has never been used so far. Pierson's (1955) model turns out to be stationary as well and disregards the contribution of nonlinear interactions altogether.

Longuet-Higgins (1976) result is actually the narrow-band limit of the Hasselmann (1962) kinetic equation. The kinetic equation has been the most frequently used stochastic model so far but its time scale is proportional to ε^{-4} , where ε is a typical small wave steepness (see also Janssen (2003) the non-resonant kinetic equation and Annenkov & Shrira (2006) for the extended kinetic equation). These equations were derived for homogeneous wave fields where the key step in the derivation is the assumption that the phases of the components are close to each other in wavenumber space and remain uncorrelated to the lowest order (Stiassnie et al. 2008).

Alber (1978) has used his equation to study the instability of a homogeneous wave-field to inhomogeneous disturbances. Alber's findings are actually the stochastic counterpart of the well-known deterministic Benjamin-Feir instability, which is obtained for the cubic Schrödinger equation. The growth rates of the inhomogeneous instabilities are proportional to ε^2 , reflecting the fact that the time scale of Alber equation is proportional to ε^{-2} . Although Alber does not state it explicitly, the choice of his initial small inhomogeneous disturbances discloses a certain correlation between their phases and those of the homogeneous base state.

From the cubic Schrödinger equation, it is known that the Benjamin-Feir instability does not lead to a permanent end state, but to an unsteady series of modulation and demodulation cycles, called the Fermi-Pasta-Ulam recurrence phenomenon (see Yuen & Ferguson Jr 1978a,b, Janssen 1981 or Stiassnie & Kroszynski 1982). Stiassnie et al. (2008) solved the Alber equation in one spatial dimension numerically and showed that a stochastic parallel to the Fermi-Pasta-Ulam recurrence exists. Their initial homogeneous wave fields have simple one-dimensional spectra of three different types: Square, Lorentz and Gaussian. This stochastic recurrence enabled them to study the probability of waves that are twice or three times higher than the significant wave height and which are usually called freak waves (see Kharif and Pelinovsky 2003; Onorato et al. 2004; Mori et al. 2007). This classification is related to the work of Longuet-Higgins (1952) who showed that the wave heights in a wave field with a narrow spectrum,

within the theory of linear waves, are Rayleigh distributed. From the Rayleigh distribution one can calculate that the probabilities for waves that are twice or three times higher than the significant wave height are 3×10^{-4} and 10^{-8} , respectively. The latter is such an extremely rare event that it would require an unrealistic long period of approximately 30 years to encounter such an exceptional freak wave (Regev et al. , 2008). Moreover, Regev et al. (2008) used the one-dimensional Alber equation to study the probability of freak waves initialized by a Gaussian spectrum.

The aforementioned findings are limited to unidirectional wave fields. Real sea states, however, are characterized by wave components propagating along different directions. Numerical (e.g. Onorato et al. 2002; Socquet-Juglard et al. 2005; Gramstad and Trulsen 2007; Eliasson and Shukla 2010) and experimental (Onorato et al. 2009b; Waseda et al. 2009) studies have revealed that wave directional spreading reduces the effect of instability and concurrently reduces the probability of freak waves occurrence. Although for one-dimensional wave trains qualitative features of this instability are well-established (Babanin et al., 2010, 2011a), for the directional wave fields quantitative guidance exists, but is much less certain (Babanin 2011, 2011b).

Based on the Alber equation, the present work shows that more realistic JONSWAP spectra of ocean waves with directional distributions can actually reproduce a stochastic recurrence which is parallel to Fermi-Pasta-Ulam recurrence and the conditions for its occurrence are also specified. The periodicity of the stochastic properties in space, and their recurring structure in time, render the calculation of extreme conditions such as the occurrence of freak wave straightforward, by taking one recurrence cycle to establish the probability density function (pdf) and then calculating the probability of the freak waves.

2.2 Derivation of the Alber equation

2.2.1 The Davey – Stewartson equations

Davey and Stewartson (1974) used the multiple scales method to derive the two coupled nonlinear partial differential equation which describe the evolution of a three-dimensional wave-packet of the wavenumber k on finite depth water. These results are known as the Davey-Stewartson equations.

Alber (1978) used these equations as a starting point to derive a new equation based on the two-point correlation function. He normalized the wave height so that his equation for the wave height was different from the Davey – Stewartson equations. His wave height $\zeta(x, y, t)$ of a weakly nonlinear progressive wave, above its undisturbed water level is written in the form

$$2\zeta(x, y, t) = \varepsilon A(X, Y, \tau) e^{i(k_0 x - \omega_0 t)} + c. c., \quad (2.8)$$

where $\omega_0 = \sqrt{gk_0}$ which is the carrier frequency, $X = \varepsilon(x - c_{g_0} t)$, $Y = \varepsilon y$, $c. c.$ stands for complex conjugate, x and y are physical variables and $\tau = \varepsilon^2 t$ where t is time. $A(X, Y, \tau)$ is the complex envelope of the narrow-banded sea, with carrier wavenumber $\mathbf{k}_0 = (k_0, 0)$, carrier wavelength $2\pi/k_0$ and carrier period $2\pi/\omega_0$. X is the direction of the carrier group velocity c_{g_0} and the carrier dispersion relation for wave of depth h is given by the linear relation as follows:

$$\omega_0^2 = gk_0\sigma; \text{ where } \sigma = \tanh(k_0 h). \quad (2.9)$$

The group velocity is obtained by taking the first derivative of the dispersion relation with respect to the carrier wavenumber and it can be written as

$$c_{g_0} = \omega'(k_0) = \frac{g}{2\omega_0} \{\sigma + k_0 h(1 - \sigma^2)\}.$$

Following Davey and Stewartson (1974), one will obtain the following pair of evolutionary equations for the complex amplitude $A(X, Y, \tau)$.

$$i \frac{\partial A}{\partial \tau} + \lambda \frac{\partial^2 A}{\partial X^2} + \mu \frac{\partial^2 A}{\partial Y^2} = \nu |A|^2 A + \nu_1 A Q, \quad (2.10)$$

$$\lambda_1 \frac{\partial^2 Q}{\partial X^2} + \mu_1 \frac{\partial^2 Q}{\partial Y^2} = \kappa_1 \frac{\partial^2 |Q|^2}{\partial Y^2}, \quad (2.11)$$

where

$$\lambda = \frac{1}{2} \omega''(k_0) = -\frac{g}{8k_0\sigma\omega_0} [\{\sigma - k_0 h(1 - \sigma^2)\}^2 + 4k_0^2 h^2 \sigma^2 (1 - \sigma^2)] \leq 0,$$

$$v = \frac{\omega_0 k_0^2}{16\sigma^4} \left[9 - 10\sigma^2 + 9\sigma^4 - \frac{2\sigma^2}{gh - c_{g_0}^2} \{4c_p^2 + 4c_p c_{g_0}(1 - \sigma^2) + gh(1 - \sigma^2)^2\} \right],$$

$$\mu = \frac{\omega'(k_0)}{2k_0} = \frac{c_{g_0}}{2k_0} > 0,$$

$$c_p = \frac{\omega_0}{k_0},$$

$$v_1 = \frac{k_0^4 \{2c_p + c_{g_0}(1 - \sigma^2)\}}{c_{g_0}},$$

$$\lambda_1 = gh - c_{g_0}^2 \geq 0; \mu_1 = gh,$$

$$\kappa_1 = \frac{g^2 h c_{g_0}}{4k_0 \sigma} \left\{ \frac{2c_p + c_{g_0}(1 - \sigma^2)}{gh - c_{g_0}^2} \right\}.$$

For deep water waves, $k_0 h$ approaches infinity and as a consequence σ approaches 1 as $\sigma = \tanh(k_0 h)$ and then the above coefficients can be written as

$$\lambda = -\frac{1}{8} \sqrt{\frac{g}{k_0^3}},$$

$$\mu = \frac{1}{4} \sqrt{g/k_0^3}, \tag{2.12}$$

$$\tilde{v} \rightarrow v = \frac{1}{2} \sqrt{gk_0^5}.$$

2.2.2 The Alber equation

When A is a random function of X and Y and assuming that the Davey – Stewartson equations which are equations (2.10) and (2.11) describe the evolution of the wave train for the complex amplitude $A(\mathbf{X}, \tau)$, the equation for slow variation of the two-point space correlation function will be derived as follows.

The two-point space correlation function is defined as

$$\rho(\mathbf{X}_1, \mathbf{X}_2, \tau) = \langle A(\mathbf{X}_1, \tau) A^*(\mathbf{X}_2, \tau) \rangle, \tag{2.13}$$

where the superscript * denotes the complex conjugates and the angle brackets denote an ensemble average.

In order to obtain the equation for the two-point correlation function, ρ , from the envelope amplitude equation (2.10), Alber adopted Wigner's method (Weigner, 1932) as follows where equation (2.10) at point $\mathbf{X}_1 = (X_1, Y_1)$ is written as:

$$i \frac{\partial A(\mathbf{X}_1)}{\partial \tau} + \lambda \frac{\partial^2 A(\mathbf{X}_1)}{\partial X_1^2} + \mu \frac{\partial^2 A(\mathbf{X}_1)}{\partial Y_1^2} = v |A(\mathbf{X}_1)|^2 A(\mathbf{X}_1) + v_1 A(\mathbf{X}_1) Q(\mathbf{X}_1).$$

Multiplying this equation by $A^*(\mathbf{X}_2)$, gives

$$\begin{aligned} i \frac{\partial A(\mathbf{X}_1)}{\partial \tau} A^*(\mathbf{X}_2) + \lambda \frac{\partial^2 A(\mathbf{X}_1)}{\partial X_1^2} A^*(\mathbf{X}_2) + \mu \frac{\partial^2 A(\mathbf{X}_1)}{\partial Y_1^2} A^*(\mathbf{X}_2) \\ = v |A(\mathbf{X}_1)|^2 A(\mathbf{X}_1) A^*(\mathbf{X}_2) + v_1 A(\mathbf{X}_1) A^*(\mathbf{X}_2) Q(\mathbf{X}_1). \end{aligned} \quad (2.14)$$

Furthermore, equation (2.10) for $A^*(\mathbf{X}_2)$ can be written as

$$i \frac{\partial A^*(\mathbf{X}_2)}{\partial \tau} + \lambda \frac{\partial^2 A^*(\mathbf{X}_2)}{\partial X_2^2} + \mu \frac{\partial^2 A^*(\mathbf{X}_2)}{\partial Y_2^2} = v |A^*(\mathbf{X}_2)|^2 A^*(\mathbf{X}_2) + v_1 A^*(\mathbf{X}_2) Q(\mathbf{X}_2).$$

Multiplying this equation by $A(\mathbf{X}_1)$ yields,

$$\begin{aligned} i \frac{\partial A^*(\mathbf{X}_2)}{\partial \tau} A(\mathbf{X}_1) + \lambda \frac{\partial^2 A^*(\mathbf{X}_2)}{\partial X_2^2} A(\mathbf{X}_1) + \mu \frac{\partial^2 A^*(\mathbf{X}_2)}{\partial Y_2^2} A(\mathbf{X}_1) \\ = v |A^*(\mathbf{X}_2)|^2 A^*(\mathbf{X}_2) A(\mathbf{X}_1) + v_1 A^*(\mathbf{X}_2) A(\mathbf{X}_1) Q(\mathbf{X}_2). \end{aligned} \quad (2.15)$$

Taking the ensemble averages of equation (2.14) and equation (2.15), one can get the following:

$$\begin{aligned} i \frac{\partial}{\partial \tau} \langle A(\mathbf{X}_1) A^*(\mathbf{X}_2) \rangle + \lambda \left[\frac{\partial^2}{\partial X_1^2} - \frac{\partial^2}{\partial X_2^2} \right] \langle A(\mathbf{X}_1) A^*(\mathbf{X}_2) \rangle \\ + \mu \left[\frac{\partial^2}{\partial Y_1^2} - \frac{\partial^2}{\partial Y_2^2} \right] \langle A(\mathbf{X}_1) A^*(\mathbf{X}_2) \rangle \\ - v_1 \langle A(\mathbf{X}_1) A^*(\mathbf{X}_2) \rangle [Q(\mathbf{X}_1) - Q(\mathbf{X}_2)] \\ - v [\langle A(\mathbf{X}_1) A^*(\mathbf{X}_1) A(\mathbf{X}_1) A^*(\mathbf{X}_2) \rangle - \langle A(\mathbf{X}_2) A^*(\mathbf{X}_2) A(\mathbf{X}_1) A^*(\mathbf{X}_2) \rangle] \\ = 0. \end{aligned} \quad (2.16)$$

Making use of equation (2.13), equation (2.16) can be rewritten as:

$$\begin{aligned}
i \frac{\partial \rho}{\partial \tau} + \lambda \left[\frac{\partial^2 \rho}{\partial X_1^2} - \frac{\partial^2 \rho}{\partial X_2^2} \right] + \mu \left[\frac{\partial^2 \rho}{\partial Y_1^2} - \frac{\partial^2 \rho}{\partial Y_2^2} \right] - v_1 \rho [Q(\mathbf{X}_1) - Q(\mathbf{X}_2)] \\
- v [\langle A(\mathbf{X}_1) A^*(\mathbf{X}_1) A(\mathbf{X}_1) A^*(\mathbf{X}_2) \rangle \\
- \langle A(\mathbf{X}_2) A^*(\mathbf{X}_2) A(\mathbf{X}_1) A^*(\mathbf{X}_2) \rangle] = 0.
\end{aligned} \tag{2.17}$$

Replacing the derivatives with respect to X_1 , X_2 , Y_1 and Y_2 by the derivatives with respect to the average coordinates

$$X = \frac{1}{2}(X_1 + X_2); Y = \frac{1}{2}(Y_1 + Y_2) \tag{2.18}$$

and with respect to the spatial separation coordinates

$$r_1 = (X_1 - X_2); r_2 = (Y_1 - Y_2). \tag{2.19}$$

From equation (2.18) and equation (2.19), one can easily obtain the following identities

$$X_1 = X + \frac{1}{2}r_1; X_2 = X - \frac{1}{2}r_1; Y_1 = Y + \frac{1}{2}r_2; Y_2 = Y - \frac{1}{2}r_2$$

which gives

$$\mathbf{X}_1 = \left[X + \frac{1}{2}r_1, Y + \frac{1}{2}r_2 \right] = \left[\mathbf{X} + \frac{1}{2}\mathbf{r} \right]; \quad \mathbf{X}_2 = \left[X - \frac{1}{2}r_1, Y - \frac{1}{2}r_2 \right] = \left[\mathbf{X} - \frac{1}{2}\mathbf{r} \right].$$

Moreover, based on equation (2.18) and equation (2.19), we can get the following first partial derivative with respect to X_1 , that is

$$\frac{\partial \rho}{\partial X_1} = \rho_{X_1} = \rho_X X_{X_1} + \rho_X (r_1)_{X_1}$$

and its second partial derivative is

$$\frac{\partial^2 \rho}{\partial X_1^2} = (\rho_X X_{X_1} + \rho_X (r_1)_{X_1})_{X_1}$$

which yields

$$\frac{\partial^2 \rho}{\partial X_1^2} = \rho_{XX} X_{X_1}^2 + 2\rho_{Xr_1} (r_x)_{X_1} X_{X_1} + \rho_X X_{X_1 X_1} + \rho_{r_1 r_1} (r_1)_{X_1}^2 + \rho_{r_1} (r_1)_{X_1 X_1}.$$

Making use of equation (2.18) and equation (2.19), one can easily simplify the second partial derivative with respect to X_1 as follows:

$$\frac{\partial^2 \rho}{\partial X_1^2} = \frac{1}{4} \rho_{XX} + \rho_{Xr_1} + \rho_{r_1 r_1}.$$

Similarly, the second partial derivative with respect to X_2 is

$$\frac{\partial^2 \rho}{\partial X_2^2} = \frac{1}{4} \rho_{XX} - \rho_{Xr_1} + \rho_{r_1 r_1}.$$

From these second order partial derivative with respect to X_1 and X_2 , it can be shown that

$$\frac{\partial^2 \rho}{\partial X_1^2} - \frac{\partial^2 \rho}{\partial X_2^2} = 2 \frac{\partial^2 \rho}{\partial X \partial r_1}.$$

Similar calculations can be applied for Y_1 and Y_2 so that we obtain

$$\frac{\partial^2 \rho}{\partial Y_1^2} - \frac{\partial^2 \rho}{\partial Y_2^2} = 2 \frac{\partial^2 \rho}{\partial Y \partial r_2}.$$

Substituting these identities into equation (2.16) yields

$$\begin{aligned} i \frac{\partial \rho}{\partial \tau} + 2\lambda \frac{\partial^2 \rho}{\partial X \partial r_1} + 2\mu \frac{\partial^2 \rho}{\partial Y \partial r_2} - v_1 \rho \left[Q \left(\mathbf{X} + \frac{1}{2} \mathbf{r} \right) - Q \left(\mathbf{X} - \frac{1}{2} \mathbf{r} \right) \right] \\ - v [\langle A(\mathbf{X}_1) A^*(\mathbf{X}_1) A(\mathbf{X}_1) A^*(\mathbf{X}_2) \rangle \\ - \langle A(\mathbf{X}_2) A^*(\mathbf{X}_2) A(\mathbf{X}_1) A^*(\mathbf{X}_2) \rangle] = 0. \end{aligned} \quad (2.20)$$

Since this second order correlation of the evolutionary equation involves fourth order correlation terms, there are two assumptions that have to be made namely $A(\mathbf{X}, \tau)$ corresponds initially to a Gaussian random process and the evolving random statistical amplitude field retains the same Gaussian statistical properties. The advantage of these assumptions is that the fourth-order cumulant vanishes and then one can write the fourth order correlation in terms of the products of pairs of second order correlation, i.e:

$$\langle A(\mathbf{X}_1) A^*(\mathbf{X}_1) A(\mathbf{X}_1) A^*(\mathbf{X}_2) \rangle = 2 \langle A(\mathbf{X}_1) A^*(\mathbf{X}_2) \rangle \langle A(\mathbf{X}_1) A^*(\mathbf{X}_1) \rangle = 2 \rho \overline{a^2}(\mathbf{X}_1)$$

where $\overline{a^2}$ is the ensemble averaged mean square amplitude equivalent to

$$\langle A(\mathbf{X}_1)A^*(\mathbf{X}_1) \rangle = 2\overline{\zeta^2}.$$

Similarly, it can be shown that

$$\langle A(\mathbf{X}_2)A^*(\mathbf{X}_2)A(\mathbf{X}_1)A^*(\mathbf{X}_2) \rangle = 2\langle A(\mathbf{X}_1)A^*(\mathbf{X}_2) \rangle \langle A(\mathbf{X}_2)A^*(\mathbf{X}_2) \rangle = 2\rho\overline{a^2}(\mathbf{X}_2).$$

Moreover, the terms involving ensemble averages of the form $\langle A(\mathbf{X}_1)A(\mathbf{X}_1) \rangle$ in the cumulant expansion vanish because of the required invariance of such a correlation to the addition of a random constant to the phases.

Therefore, under Gaussian closure approximation, (2.20) can be written as

$$\begin{aligned} i\frac{\partial\rho}{\partial\tau} + 2\lambda\frac{\partial^2\rho}{\partial X\partial r_1} + 2\mu\frac{\partial^2\rho}{\partial Y\partial r_2} - v_1\rho\left[Q\left(\mathbf{X} + \frac{1}{2}\mathbf{r}\right) - Q\left(\mathbf{X} - \frac{1}{2}\mathbf{r}\right)\right] \\ - 2v\rho\left[\overline{a^2}\left(\mathbf{X} + \frac{1}{2}\mathbf{r}\right) - \overline{a^2}\left(\mathbf{X} - \frac{1}{2}\mathbf{r}\right)\right] = 0, \end{aligned} \quad (2.21)$$

where $\overline{a^2}(\mathbf{X}) = \rho\left(\mathbf{X} + \frac{1}{2}\mathbf{r}, \mathbf{X} - \frac{1}{2}\mathbf{r}, \tau\right)\big|_{\mathbf{r}=\mathbf{0}}$.

Equation (2.21) is nowadays known as the Alber equation with stretched/slow variables.

2.3 Modulational instability in one spatial dimension

The stability/instability of finite amplitude gravity waves on deep water has been a matter of interest for many researchers. As Dysthe (1979) pointed out that a lot of attention has been drawn to the instability of the wave train upon the modulational perturbation. The first indication of modulational instability for weakly nonlinear waves on deep water was observed by Lighthill (1965) who used the theory of Whitham (1965) and studied the evolution of weakly nonlinear waves on deep water (Yuen and Lake, 1980). He examined two sets of the initial condition namely a wave packet with a Gaussian envelope and a slightly modulated Stokes wavetrain.

Furthermore, Benjamin and Feir (1967) used the Euler equation to investigate theoretically the stability of period wavetrains under small disturbance in the form of a pair of side-band modes. They found that a uniform wavetrain is unstable under perturbations in the interval

$$0 < p < 2\sqrt{2}k_0^2 a_0,$$

where a_0 is the wave amplitude, k_0 is the peak wavenumber and p is the wavenumber of the disturbance. The maximum instability occurs when $p = p^{(max)}$, where

$$p^{(max)} = 2k_0^2 a_0,$$

and the maximum growth rate ($\text{Im}(\Omega^{(max)})$) is

$$\text{Im}(\Omega^{(max)}) = \frac{1}{2} \omega_0 k_0^2 a_0^2,$$

where ω_0 is the angular frequency of the uniform wavetrains. For details of derivation, one can refer to Mei et al. (2005, page, 761 - 763) (see also: Yuen and Lake, 1980). Another derivation which is based on the Zakharov equation, one can refer to the work of Mei et al. (2005, page 866 - 868). One should note that the instability of nonlinear waves in the general form was studied by Zakharov (1966) but it was written in Russian version and then it was translated into English by R.T. Beyer one year later which was in 1967. In addition, Benjamin and Feir (1967) conducted experimental observations based on their prediction and found that both theoretical investigations and experimental observations are in fairly good agreement. This result is now known as the Benjamin-Feir instability.

Recently, Janssen (2003) introduced the so-called Benjamin Feir Index (BFI) which is the ratio of steepness, ε , to the bandwidth of the spectrum and it can be written as

$$BFI = \frac{\varepsilon}{\Delta\omega/\omega_0}$$

where $\Delta\omega$ and ω_0 are the bandwidth and the peak in the frequency spectrum, respectively. Since BFI is usually normalized, however, a random wave train is unstable if $BFI > 1$. Moreover, one should note that the ratio in Janssen's BFI used to be called an "Ursell number" by Onorato et al. (2001). As reported by Onorato et al. (2001), if the Ursell number is really small compared to one, then the waves are essentially linear. However, when the Ursell number is greater or equal to one, then the dynamics becomes nonlinear (see also Osborne and Petti, 1994 for full review of the Ursell number).

Mei et al. (2005) reported that the instability of gravity waves in infinitely deep water has been studied in several ways during the last few decades. Longuet-Higgins (1978a, 1978b) studied the instability numerically where the disturbance collinear with the fundamental wave and for both the perturbation which is less or equal to the primary wave (superharmonics) and the perturbation which greater than the primary wave (subharmonics).

The application of nonlinear Schrödinger equation is the most successful and elegant approach to study the modulational perturbation for small amplitudes (Dysthe, 1979). This nonlinear Schrödinger equation was derived by Zakharov (1968) by allowing the finite amplitude wavetrain to be subjected to modulational perturbation in two spatial dimensions both parallel and perpendicular to the direction of the wavetrain. Later, the extension to waves on the finite depth was done by Davey and Stewartson (1974) which is now known as the Davey and Stewartson equation. Based on the Davey and Stewartson equation, Alber (1978) and Alber and Saffman (1978) derived the equation describing the evolution of the random wavetrain albeit for the narrow spectra and studied the effect of randomness on the stability properties of a two-dimensional nonlinear wavetrain. This equation is actually the stochastic counterpart of the well-known cubic Schrödinger equation. Recently, based on the one spatial dimension of Alber equation, Stiassnie et al. (2008) studied the linear instability of narrow spectra homogeneous seas, namely square spectra, Lorentz spectra and Gaussian spectra, and its subsequent evolution in time, subject to inhomogeneous disturbances where according to the kinetic equation no spectral evolution is expected. In the region of instability, recurrent evolution which is the stochastic counterpart of the Fermi–Pasta–Ulam recurrence obtained for the cubic Schrödinger equation was discovered. Regev et al. (2008), then, used the results of Stiassnie et al. (2008) to study the probability of occurrence of freak waves. Moreover, they found the simple relation between the Janssen’s Benjamin Feir Index (Janssen, 2003) as given by

$$BFI = \frac{1}{\tilde{W}\sqrt{2}} \quad (2.22)$$

where \tilde{W} is the dimensionless spectral width with $\tilde{W} = W/\varepsilon k_0$. ε and k_0 are the steepness and the carrier wave, respectively.

Here, the marginal instability line is determined by a new parameter, Π_1 , for unidirectional JONSWAP spectra and details are presented in Chapter 3.

2.4 Modulational instability in two spatial dimensions

All aforementioned facts are limited to the unidirectional wave fields which sometimes correspond to the long crested wave fields. The real sea states, however, are characterized by wave components propagating along different directions (directional distributions) which sometimes correspond to the short crested wave fields.

Directional wave fields can be conveniently represented by one-dimensional spectrum, e.g. $S(f)$ which is a frequency spectrum, multiplied by a directional spreading, $D(f, \theta)$, which can be written as follows (Babanin and Soloviev, 1987, 1998b):

$$X(f, \theta) = S(f)D(f, \theta) \quad (2.23)$$

where f and θ are the frequency and the angle of the directional distribution with respect to the main propagation of the waves, respectively. Moreover, the directional spreading must satisfy the following condition

$$\int_{-\pi}^{\pi} D(f, \theta) d\theta = 1. \quad (2.24)$$

Following Babanin and Soloviev (1998b), the directional spreading can be written as

$$D(f, \theta) = A_d(f)K(f, \theta). \quad (2.25)$$

Substituting (2.25) into (2.24) gives

$$A_d(f)^{-1} = \int_{-\pi}^{\pi} K(f, \theta) d\theta \quad (2.26)$$

where A_d is the inverse normalized directional spectral width and $K(f, \theta)$ is the normalized directional spectrum:

$$K(f, \theta_{max}) = 1,$$

where θ_{max} is the maximum value in the dominant direction in which the waves were travelling.

The higher values of A_d correspond to narrower directional distributions. A_d is a convenient property to use as a proxy of the directional spread because there is an extensive parameterisation available for its dependences (Babanin and Soloviev, 1987, 1998b) and it is unambiguously analytically connected with other existing directional-spread characteristics used in literature, even for bi-modal directional spectra. For example, for the normalised spectrum $K(f, \theta) = \cos^{n(f)}(\theta - \theta_{max})$ where $|\theta| \leq \pi/2$, this analytical connection is:

$$A_d = \frac{\Gamma(1 + 0.5n)}{\sqrt{\pi}\Gamma(0.5 + 0.5n)}, \quad (2.27)$$

where n is the degree of directional spreading. For other options of A_d and $K(f, \theta)$ one can refer to the work of Babanin and Soloviev (1998b).

There have been numerous attempts to investigate the role of modulational instability in two spatial dimensions numerically and experimentally. Onorato et al. (2009a, 2009b), for example, observed the modulational instability in the two dimensional wave basin in Marintek, Norway, which is one of the largest tank in the world. They found that modulational instability leads to a significantly large number of extreme waves when the spreading coefficient n of the directional spreading is greater than 24 ($A_d = 1.975$). A completely different experiment conducted by Waseda et al. (2009) at Tokyo University, Japan, found a similar result where the modulational instability is still active when the degree of the directional spreading is greater than 10 ($A_d = 1.294$). Note that in both experiments carried out by Onorato et al. (2009a, 2009b) and Waseda et al. (2009), the wave makers were prescribed by JONSWAP spectra with different peak enhancement factors and energy scales. Onorato et al. (2009a, 2009b) used the peak enhancement, $\gamma = 6$, and the energy scale, $\alpha = 0.016$, of the JONSWAP spectrum while the peak enhancement and the energy scale of the JONSWAP spectrum used by Waseda et al. (2009) were $\gamma = 3$ and $\alpha = 0.004$, respectively. From numerical investigations, for instance, Eliasson and Shukla (2010) derived a nonlinear wave-kinetic equation for gravity waves in 2+2 dimensions (two spatial dimensions and two velocity dimensions) and carried out numerical simulations to study the stability and

nonlinear spatiotemporal evolution of narrow-banded waves. Their modelling results agreed well with the experiments conducted by Onorato et al. (2009a, 2009b). Thus, both experimental and theoretical results concluded that the modulational instability process, which is one of the main mechanisms of extreme waves formation in deep water, random, long-crested (or unidirectional) waves, seem to be quenched when short-crested waves are considered.

Babanin et al. (2010, 2011b), however, argued that, for a given bandwidth, directional spreading is not the only property of surface wave fields to influence the modulational instability. They have shown experimentally that if the directional spreading becomes too broad and wave field stabilizes, the increase of steepness can re-activate the instability. They suggested a Direction Modulation Index (M_{Id}), analogous to the Benjamin-Feir Index in the wavenumber domain, which identifies the limits in directional wave fields:

$$M_{Id} = A_d \cdot \varepsilon \quad (2.28)$$

where ε is the wave steepness and A_d is the normalization factor of the directional spreading as defined by Babanin and Soloviev (1998b). Babanin et al. (2011b), investigated the modulational instability in a two-dimensional wave basin for quasi-monochromatic wave trains with different steepness/directional-width combinations and found that the limit of the direction modulation index is $M_{Id} \approx 0.18$. Note that the steepness calculated in Babanin et al. (2011b) is higher by the factor of $\sqrt{2}$ compared to the steepness calculated in this research. It was concluded that such a limit corresponds to realistic directional conditions in Babanin and Soloviev (1998b) for oceanic waves and therefore supports the existence of modulational instability in the field.

For more realistic ocean wave spectra (i.e. JONSWAP spectra) as a special case where they assumed that the energy scale of the JONSWAP spectrum is constant, Babanin et al. (2010) defined the direction modulation index as

$$M_{Id} = A_d \sqrt{\gamma} \quad (2.29)$$

where γ is the peak enhancement factor of the JONSWAP spectrum. Furthermore, in relation to the wave development U_{10}/c_p where U_{10} is the wind speed measured at a

height of 10 meters and c_p is the phase speed, they used the equation (19) of Babanin and Soloviev (1998b), that is

$$A_d = 1.12 \left(\frac{U_{10}}{c_p} \right)^{-0.5} + (2\pi)^{-1} \quad (2.30)$$

and equation (44) of Babanin and Soloviev (1998a), which is

$$\sqrt{\gamma} = 1.10 \sqrt{\frac{U_{10}}{c_p}} \quad (2.31)$$

to define the following direction modulational index

$$M_{Id} = 1.23 + \frac{1.1}{2\pi} \sqrt{\frac{U_{10}}{c_p}} \quad (2.32)$$

which is a weak function of the wind forcing, and its value at the spectral peak varies from 1.40 to 1.79 for U_{10}/c_p in the range from 0.89 to 10 where $U_{10}/c_p = 0.89$ signifies full development (Babanin et al., 2010).

One should also note that another version of the Benjamin Feir Index which includes the directional effect has been introduced by Mori et al. (2011) which is given in the following:

$$BFI_{2D} = \frac{\varepsilon}{\sqrt{\delta_\omega^2 + \frac{\alpha_2 \delta_\theta^2}{2}}} \quad (2.33)$$

where ε , δ_ω and δ_θ are the steepness, frequency bandwidth and directional bandwidth, respectively, while α_2 is a constant.

In this research, however, we will introduce a new parameter, Π_2 , to determine the marginal instability criteria based on JONSWAP spectra with directional distributions. This parameter is a further development of “directional BFI” introduced earlier by Babanin et al. (2010). It has already been extensively used for investigations of modulational instability in directional wave fields, tested and even quantified experimentally as one can find in Babanin (2011) and Babanin et al. (2011b).

Another advantage of using Π_2 is due to the fact that the directional property A_d employed by Π_2 formulation is a robust characteristic of wave directional spectrum well established experimentally and in the field observations. Comprehensive parameterisations for this property are available through the wave spectrum and at all stages of wave development (Babanin and Soloviev, 1987, 1998b) in the same terms as parameterisations for JONSWAP. Therefore, at any stage, Π_2 can be expressed through both observations-based one-dimensional wave spectra and directional wave spectra. The details of this result are presented and discussed in Chapter 3.

2.5 Long-time evolution of an unstable water-wave train

It is well-known that the existence of steady, continuous, progressive wave trains of finite amplitude, the permanent form of which results from the balance between dispersion and nonlinear effect (see Hasimoto and Ono, 1972, Stiassnie and Kroszynski, 1982, for review) is one of the remarkable properties of weakly nonlinear dispersive system. In relation to the gravity water waves at uniform depth, the search for precise forms of such wave trains has been the subject of many researchers since the classical work of Stokes (1847). The discovery of the modulational instability of such wave trains in fluid mechanics has been predicted by Lighthill (1965), Whitham (1965) and Benjamin and Feir (1967). Now the question is what will happen for unstable condition at very long time?

In the presence of dissipation, Janssen (1981) argued that limited cycle behaviour seems likely to occur because the tendency toward a new equilibrium is accompanied by an increase in the entropy of the system. Moreover, recent results show that if the dissipation is taken into account, the modulational instability can be stabilized and in the wavenumber space, the area of instability shrinks as time increases (Segur et al., 2005). This conclusion is also confirmed by Wu et al. (2006) by conducting fully nonlinear simulations. Besides that, Kharif et al. (2010) revisited analytically the work of Segur et al. (2005) by taking into account both dissipation and wind input. They found that in the presence of dissipation, carrier waves of given wavenumber may suffer modulational instability when the friction velocity is larger than a threshold value. On the other hand, for a given friction velocity, they found that only carrier waves whose numbers are less than a threshold value are unstable, otherwise dissipation prevents

instability developing over time. Recently, Onorato and Proment (2012) studied the effect of wind and dissipation on the nonlinear stage of the modulational instability and found that an initial stable wave packet could become unstable because of wind and the initial unstable wave packet could be stabilized by dissipation.

In the absence of dissipation, however, it is not obvious that limit cycle behaviour occurs (Janssen, 1981). This indicates that there is no permanent end state, but an unsteady series of modulation and demodulation cycles known as Fermi-Pasta-Ulam recurrence phenomenon (Stiassnie and Kroszynski, 1982, Stiassnie et al., 2008).

Yuen and Ferguson (1978b) showed from the numerical solution the influence of initial condition on the long-time evolution based on one spatial dimensional nonlinear Schrödinger equation (see also Yuen and Lake, 1980). From their numerical experiments, they demonstrated that long-time evolution of an unstable wave train is governed by unstable mode and their harmonics contained in the initial condition. They also found that the stable harmonics receive energy but they never become the dominant mode at any stage of the evolution. As shown in the previous section, the uniform wave train is unstable under the perturbation in the interval

$$0 < p < 2\sqrt{2}k_0^2 a_0,$$

where p is the wavenumber of the disturbance, k_0 is the carrier wave and a_0 is the wave amplitude.

For long-time evolution, Yuen and Ferguson Jr (1978b) found that the initial conditions through the instability results seem to determine simple recurrence and complex recurrence. In particular, they found that if the initial perturbation wavenumber lies within the range

$$\sqrt{2}k_0^2 a_0 < p < 2\sqrt{2}k_0^2 a_0,$$

then the evolution will yield a simple recurrence whereas when the values of initial perturbation wavenumber are in the range

$$0 < p < \sqrt{2}k_0^2 a_0,$$

then complex recurrence will be yielded from the evolution. As illustrations, they have simulated several cases where different numbers of harmonics fall within the unstable

region as shown in the following Figure 2.1. The vertical axis represents the normalized growth rate, while the horizontal axis reveals the wavenumber of the disturbances divided by $2k_0^2 a_0$. The results from their numerical simulations are shown in Figure 2.2.

It is clearly seen from Figure 2.2 that Case 1a and Case 1 give a simple recurrence solution. This is because the double value of the wavenumber, i.e. $2p$ where p is the wavenumber of the disturbance is outside the instability region. On the other hand, Cases 2, 3, 4 and 5 give complex recurrence solution since n times the wavenumber of the disturbance falls into the instability region for any integer $n \geq 2$.

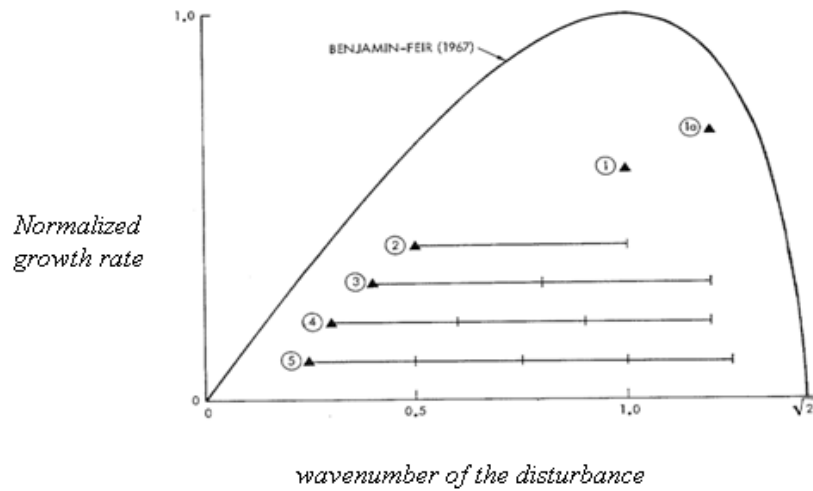


Figure 2.1: Instability growth rate of a uniform wave train subject to two-dimensional perturbations. The labels indicate the number of unstable harmonics (including the fundamental perturbation, which is denoted by \blacktriangle), (Yuen and Lake, 1982, Fig. 11).

For two spatial dimensions of the nonlinear Schrödinger equation, Yuen and Ferguson Jr (1978a) also found that the long-time evolution exhibits the Fermi-Pasta-Ulan recurrence phenomenon. They had simulated a wide range of initial conditions and found that the initial condition is reconstructed or almost reconstructed. Moreover, Martin and Yuen (1980a) observed that for the two-dimensional nonlinear Schrödinger equation where the instability region is infinity in extent, they found that the energy initially contained in low modes can leak to unstable higher harmonic in a quasi-recurring fashion. The instability area is shown in the following Figure 2.3 where p and q are the wavenumber of the disturbance.

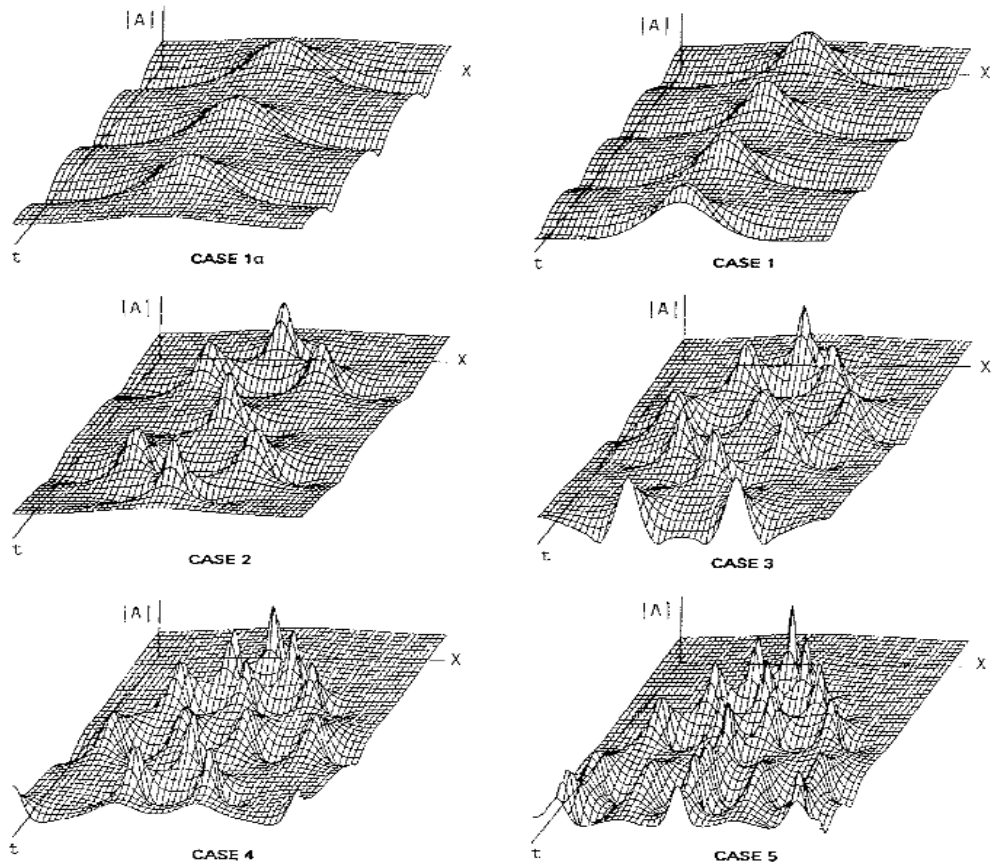


Figure 2.2: Time evolution of unstable uniform wave trains subject to perturbations specified in Figure 2.1. The case numbers correspond to the encircled numbers in Figure 2.1. Note that the maximum number of prominent peaks appearing in time for each case is equal to the case number as predicted by the relationship (Yuen and Lake, 1982, Fig. 12).

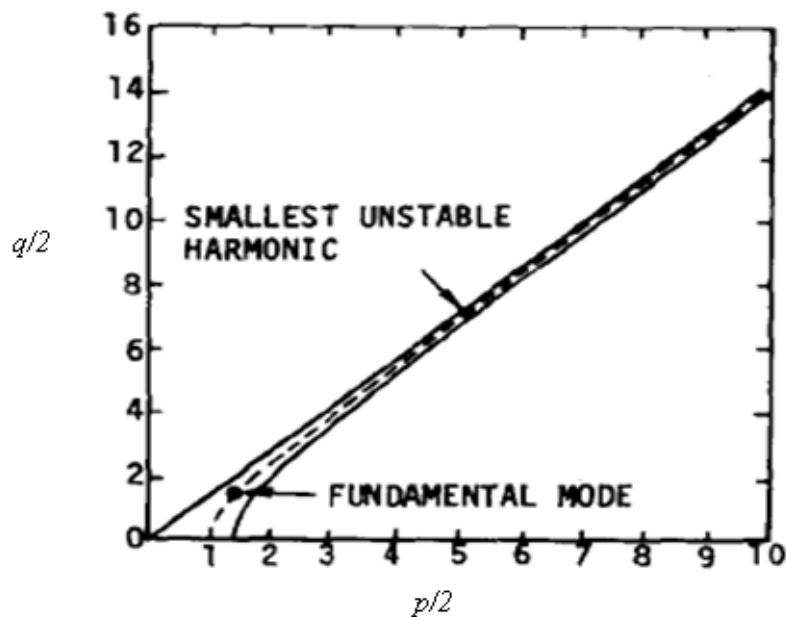


Figure 2.3: Region of instability of a uniform solution to infinitesimal disturbance with wave vector (p, q) . The line within the instability region denotes the locus of maximum instability (Martin and Yuen, 1980a, Fig. 1).

All of the aforementioned findings are based on the well-known nonlinear Schrödinger equation. The stochastic version of the nonlinear Schrödinger equation has been derived by Alber (1978) and Alber and Saffman (1978) which is normally known as the Alber equation. Janssen (1983) was the first one who studied the long-time behaviour of a random inhomogeneous field on weakly nonlinear surface gravity waves based on the one spatial dimension of the Alber equation. He particularly studied the long-time evolution near the threshold of instability by means of a multiple-time scale technique and found two interesting cases. His first finding is for small but finite bandwidth where the amplitude of the unstable modulation shows overshoot followed by oscillation around its time-asymptotic value. This oscillation is damped owing the phase mixing except in the limit of vanishing bandwidth because there is a perfect recurrence. Another finding is that for large bandwidth the damping due to phase mixing becomes overwhelming so that no overshoot is found. Janssen's findings are summarized in the following Figure 2.4, where ρ is the two-point correlation function, σ is the spectral width and τ_1 is the timescale.

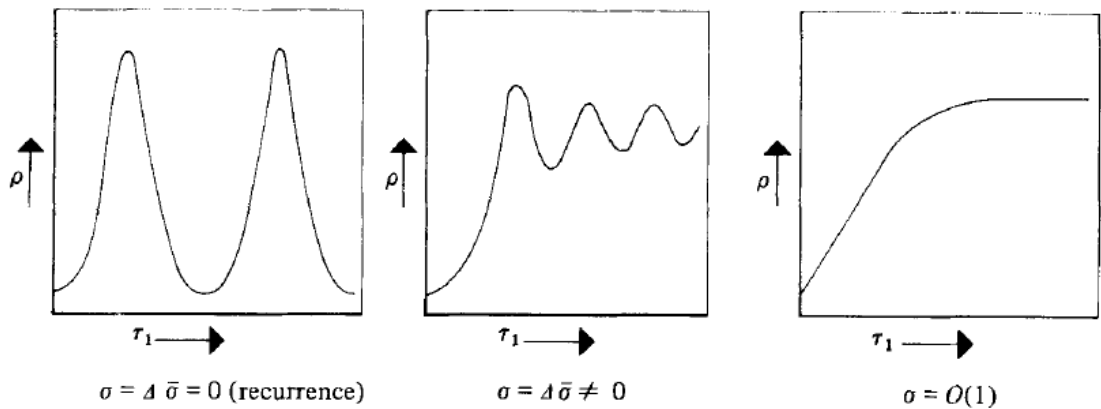


Figure 2.4: Long-time behaviour of the random version of the Benjamin-Feir instability. Shown are the cases of a uniform wavetrain ($\sigma=0$), a narrow spectrum $\sigma=O(\Delta)$ and a broad spectrum $\sigma=O(1)$, (Janssen, 1983, Fig. 3).

Recently, Stiassnie et al. (2008) studied the linear stability of narrow spectra homogeneous seas and its subsequent evolution in time subject to inhomogeneous disturbance by means of one spatial dimension of the Alber equation. In order to study the long-time evolution, they solved the Alber equation numerically. To this end, a finite different scheme has been established and boundary conditions as well as initial conditions have been determined. They discovered the recurrence solution in the area of

the instability by choosing the most unstable mode. The isolines of the dimensionless growth rate $\tilde{\Omega}_i$ of three different spectra namely square spectrum, Lorentz spectrum and Gaussian spectrum as shown in the following Figure 2.5. The vertical axis represents dimensionless spectral width, \tilde{W} and the horizontal axis represents the dimensionless wavenumber of the disturbance, \tilde{K} .

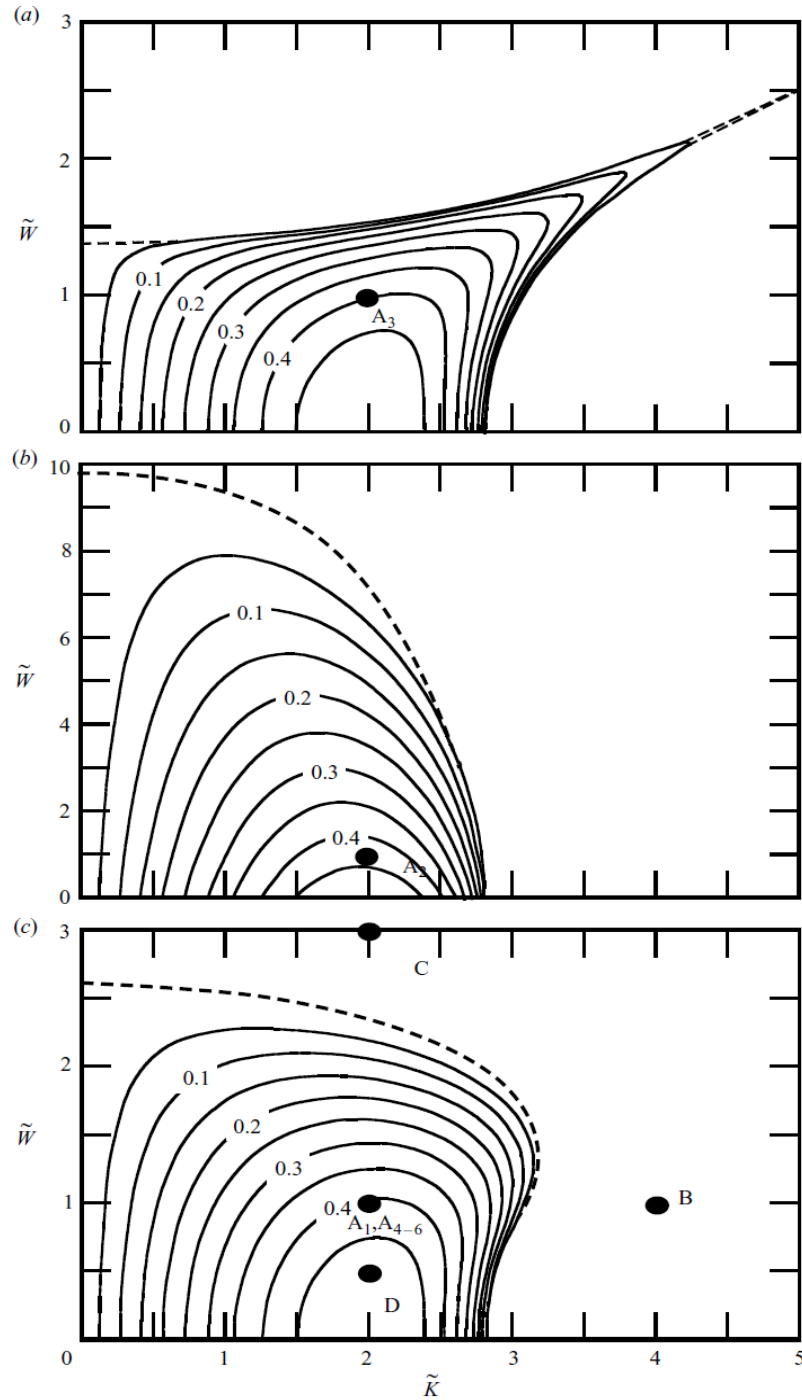


Figure 2.5: Isolines of the non-dimensional growth-rate, $\tilde{\Omega}_i$, for three spectra: (a) square spectrum; (b) Lorentz spectrum; (c) Gaussian spectrum. Dots refer to the cases where they studied long-time evolution (Stiassnie et al., 2008, Fig. 2).

Furthermore, the influence of the shape of the initial spectra and the inhomogeneous disturbances were investigated. As an example, Figure 2.6 shows the long-time evolution of $\tilde{\rho}(0,0,\tilde{\tau})/\tilde{\rho}_h(0)$ for three different initial homogeneous spectra.

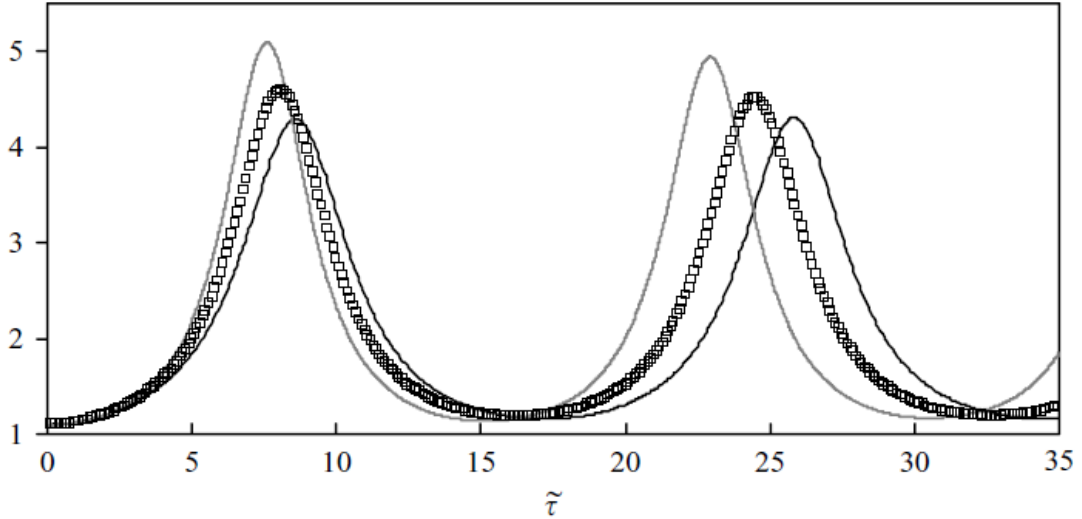


Figure 2.6: The values of $\tilde{\rho}(0,0,\tilde{\tau})/\tilde{\rho}_h(0)$ as a function of time for three different initial spectra: \blacksquare , square (A_1); $\square\square\square$, Gaussian (A_3); — , Lorentz (A_2). A_1 , A_2 and A_3 refer to Figure 2.5 (Stiassnie et al., 2008, Fig. 11).

Using a Lorentz spectrum, Stiassnie et al. (2008) also recovered Janssen's results, who studied the long-time evolution based on the one-dimensional Alber equation near the threshold of the instability, as shown in the following Figure 2.7 and Figure 2.8. As seen from Figure 2.7, P_1 is on the marginal instability line, P_2 lies on the stable area and P_3 is in the area of instability where the vertical axis represents the dimensionless spectral width, \tilde{W} , and the horizontal axis represents the dimensionless wavenumber of the disturbance, \tilde{K} . The results from their numerical simulation are shown in Figure 2.8 where the points on the stable area and on the marginal instability line give an initial small overshoot followed by an oscillation around its time-asymptotic value. On the other hand, the point in the unstable area but very close to the marginal instability line gives recurring solution with a rather long recurrence-period (the period is approaching infinity as they approach the marginal stability line from below).

One should note, however, that Stiassnie et al. (2008) results are very different from the results for homogeneous seas (Alber, 1978). This is because, in Stiassnie et al. (2008), the initial disturbance spectra are profoundly inhomogeneous through their phase

relation to the homogeneous spectrum. This is in contrast with the Alber's work where all initial phases are independently and randomly chosen.

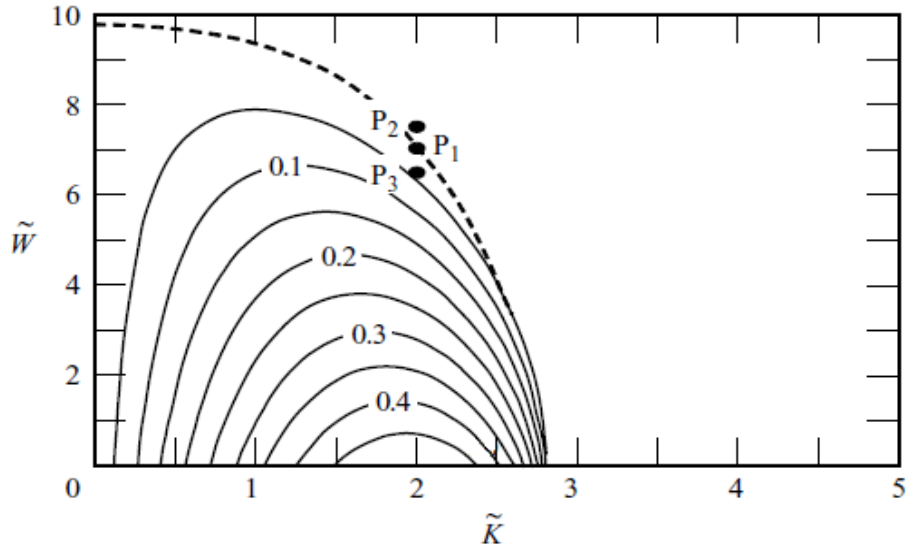


Figure 2.7: Three cases near the marginal-stability curve (Stiassnie et al., 2008, Fig. 15).

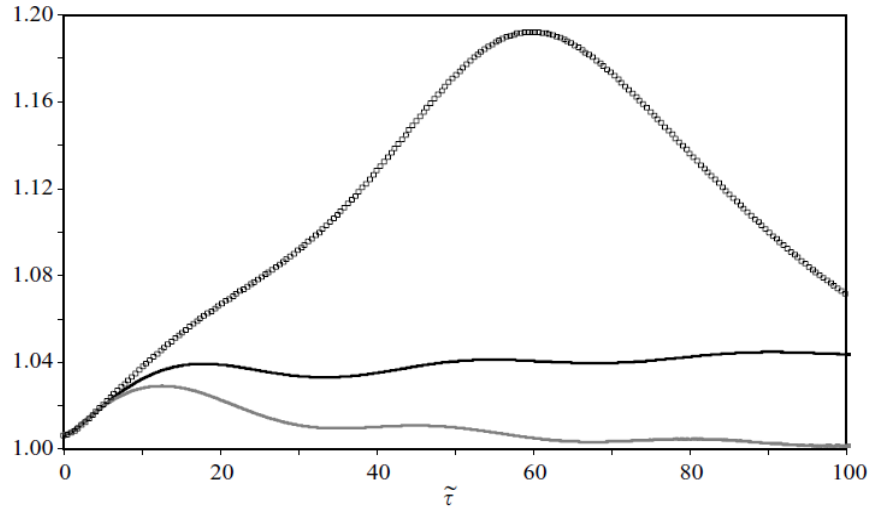


Figure 2.8: The values of $\tilde{\rho}(0,0,\tilde{\tau}) / \tilde{\rho}_h(0)$ as a function of time for three cases near the threshold of instability. \blacksquare , P_1 ; \blacksquare , P_2 ; $\square\square$, P_3 . P_1 , P_2 and P_3 refer to Figure 2.7 (Stiassnie et al., 2008, Fig. 14).

Here, we extend the method used by Stiassnie et al. (2008) to study the two spatial dimensions of the Alber equation and obtain the stochastic recurrence parallel to the well-known Fermi-Pasta-Ulam recurrence obtained from the nonlinear Schrödinger equation. In particular, we used the most realistic ocean wave JONSWAP spectra with and without directional spreading which can be found in Chapter 4.

2.6 Ocean wave statistics

2.6.1 Wave height distributions

Longuet-Higgins (1952) showed that if the wave spectrum is narrow banded and the phases of the Fourier components are uniformly distributed, the probability distributions of linear wave crests and troughs are Rayleigh distributed:

$$P(H \geq \hat{H}) = e^{-\left(\frac{H}{H_{rms}}\right)^2} \quad (2.34)$$

where H is the wave height, $H_{rms} = 2\sqrt{2m_0}$ is the root mean square wave height and m_0 is the variance of the wave spectrum.

In the ocean, however, waves tend to behave differently than predicted by linear theory (Toffoli et al., 2009). Forristall (2000), for example, analysed about 116 hours of hurricane wave data from the Gulf of Mexico and concluded that the Rayleigh distribution substantially over predicted the heights of the highest waves in a record. Moreover, real wave crests are actually higher and sharper while the wave troughs are shallower and flatter compared to the Gaussian process (Ochi, 2005, and the references therein). As a result, the statistical distribution of crests and troughs deviates from the Rayleigh distribution (Toffoli et al., 2008).

In order to improve the linear model, Longuet-Higgins (1963) derived the second order theory for deep water using the Gram-Charlier series. The extension of this model to arbitrary water depths was done by Sharma and Dean (1981). Thus the latter model is able to capture the effect of wave steepness, water depths and directional spreading with no approximation other than the truncation of the small amplitude expansion to the second order (Toffoli et al., 2006). The extended second order theory done by Sharma and Dean (1981) are reproduced here as also reported by Forristall (2000). Let the first-order water surface be given by

$$\eta^{(1)} = \sum_{n=1}^N a_n \cos(\mathbf{k}_n \cdot \mathbf{x} - \omega_n t + \epsilon_n), \quad (2.35)$$

where t is time; \mathbf{x} is the position vector in the plane; ω_n , ϵ_n and \mathbf{k}_n are, respectively, the radian frequency, phase and vector wavenumber of Fourier wave component n ; and

a_n is its amplitude. The frequencies and wavenumbers are related by the linear dispersion equation

$$\omega_n^2 = g|\mathbf{k}_n| \tanh(|\mathbf{k}_n|d), \quad (2.36)$$

where g is the acceleration due to gravity and d is the water depth. The second-order correction to the wave surface given by Sharma and Dean (1981) is then

$$\eta^{(2)} = \frac{1}{4} \sum_{i=1}^N \sum_{j=1}^N a_i a_j \{K^- \cos(\psi_i - \psi_j) + K^+ \cos(\psi_i + \psi_j)\}, \quad (2.37)$$

where

$$K^- = [D_{ij}^- - (\mathbf{k}_i \cdot \mathbf{k}_j + R_i R_j)](R_i R_j)^{-1/2} + (R_i + R_j),$$

$$K^+ = [D_{ij}^+ - (\mathbf{k}_i \cdot \mathbf{k}_j - R_i R_j)](R_i R_j)^{-1/2} + (R_i + R_j),$$

$$D_{ij}^- = \frac{(\sqrt{R_i} - \sqrt{R_j})\{\sqrt{R_j}(k_i^2 - R_i^2) - \sqrt{R_i}(k_j^2 - R_j^2)\}}{(\sqrt{R_i} - \sqrt{R_j})^2 - k_{ij}^- \tanh k_{ij}^- d} + \frac{2(\sqrt{R_i} - \sqrt{R_j})^2 (\mathbf{k}_i \cdot \mathbf{k}_j + R_i R_j)}{(\sqrt{R_i} - \sqrt{R_j})^2 - k_{ij}^- \tanh k_{ij}^- d},$$

$$D_{ij}^+ = \frac{(\sqrt{R_i} + \sqrt{R_j})\{\sqrt{R_i}(k_j^2 - R_j^2) + \sqrt{R_j}(k_i^2 - R_i^2)\}}{(\sqrt{R_i} + \sqrt{R_j})^2 - k_{ij}^+ \tanh k_{ij}^+ d} + \frac{2(\sqrt{R_i} + \sqrt{R_j})^2 (\mathbf{k}_i \cdot \mathbf{k}_j - R_i R_j)}{(\sqrt{R_i} + \sqrt{R_j})^2 - k_{ij}^+ \tanh k_{ij}^+ d},$$

$$k_{ij}^- = |\mathbf{k}_i - \mathbf{k}_j|,$$

$$k_{ij}^+ = |\mathbf{k}_i + \mathbf{k}_j|,$$

$$R_i = \omega_i^2/g,$$

$$\psi_i = \mathbf{k}_i \cdot \mathbf{x} - \omega_i t + \epsilon_i.$$

Note that when the water depth approaches infinity, then the term $\tanh(|\mathbf{k}_n|d)$ approaches 1 which is related to the deep water. As a result, equation (2.37) falls into

the results of Longuet-Higgins (1963). Detailed derivations can also be found in some other literatures such as Toffoli et al. (2007).

Based on the Longuet-Higgins (1963) approach, a number of second order probability distributions have been proposed by some researchers. Tayfun (1980), for example, used the second order theory of Longuet-Higgins (1963) to produce the crest and height distributions from the stokes model. Similarly, Prevosto et al. (2000) derived nonlinear short term probability distribution from a narrow band second order model.

Forristall (2000) used the same technique used by Prevosto (1998) who calculated the skewness of the surface elevation and the most probable crest heights for many combinations of spectral shapes and water depths and extended the work by comparing the results to several sets of field measurements. Also, he fits the Weibull distribution, which is a general form of the Rayleigh distribution, to second-order simulations with a wide variety of wave steepness and Ursell number and applied it to arbitrary water depths. In order to carry out the parameterization of the simulations, he involved two steps of fittings. In the first step, he fits the simulations to the Weibull distribution which is in the form

$$P(\eta_c > \eta) = \exp \left[- \left(\frac{\eta}{\alpha H_s} \right)^\beta \right], \quad (2.38)$$

where η is the water surface, η_c is the crest height and H_s is the significant wave height. Then, he found simple expressions for the Weibull parameters α and β as functions of the water depth and wave spectrum. These expressions are based on parameters that characterize the degree of nonlinearity of the waves, that is, the wave steepness and Ursell number. He found that basing the wave steepness on the mean wave period, rather than the peak period, produced good fits for spectra with the same peak period but different peak enhancement factors. The steepness parameter used in the fits is

$$S_1 = \frac{2\pi H_s}{g T_1^2}, \quad (2.39)$$

where g is the acceleration due to gravity and T_1 is the mean wave period calculated from the ratio of the first two moments of the wave spectrum, i.e. $T_1 = m_0/m_1$. Let

$S(f)$ be the frequency spectrum, then its variance is evaluated as $m_0 = \int S(f) df$ and the first moment is $m_1 = \int fS(f) df$ (Holthuijsen, 2007).

The standard parameter for characterizing the effect of water depth on nonlinearity of waves is the Ursell number. The Ursell number based on the significant wave height and mean period is

$$U_r = \frac{H_s}{k_1^2 d^3}, \quad (2.40)$$

where k_1 is the wavenumber for a frequency of $1/T_1$ and d is the water depth.

As a special case, i.e. the Rayleigh distribution, he found $\alpha = 1/\sqrt{8}$ and $\beta = 2$ which are calculated at zero steepness and Ursell number. The fits for the unidirectional wave simulations are

$$\alpha_1 = 0.3536 + 0.2892S_1 + 0.1060U_r, \quad (2.41)$$

$$\beta_1 = 2 - 2.1597S_1 + 0.0968U_r^2, \quad (2.42)$$

and the fits for the directional waves simulations are

$$\alpha_2 = 0.3536 + 0.2568S_1 + 0.0800U_r, \quad (2.43)$$

$$\beta_2 = 2 - 1.7912S_1 - 0.5302U_r + 0.248U_r^2. \quad (2.44)$$

Now, since the wave height, H , is approximately twice the water surface, i.e. $H \approx 2\eta$, equation (2.38) can be rewritten as

$$P(H > \hat{H}) = \exp \left[- \left(\frac{\hat{H}}{2\alpha H_s} \right)^\beta \right]. \quad (2.45)$$

Moreover, as one can show from the Rayleigh distribution that $H_s = \sqrt{2}H_{rms}$, the parameterization of Weibull distribution as given in equation (2.45) can be rewritten as

$$P(H > \hat{H}) = \exp \left[- \left(\frac{\hat{H}}{2\sqrt{2}\alpha H_{rms}} \right)^\beta \right]. \quad (2.46)$$

Using $\alpha = 1/\sqrt{8}$ and $\beta = 2$, equation (2.46) falls to equation (2.34). Also, it is clearly seen from equation (2.40) that for deep water (i.e. d approaches infinity), the Ursell number is zero, i.e. $U_r = 0$. As a result, equations (2.41) to (2.44) can be reduced to the following. For the unidirectional sea simulations, the values of parameters are

$$\alpha_1 = 0.3536 + 0.2892S_1, \quad (2.47)$$

$$\beta_1 = 2 - 2.1597S_1, \quad (2.48)$$

and for the directional sea simulations, the values of parameters are

$$\alpha_2 = 0.3536 + 0.2568S_1, \quad (2.49)$$

$$\beta_2 = 2 - 1.7912S_1. \quad (2.50)$$

As can be seen from equations (2.47) to (2.50), the Forristall distribution entirely depends on the steepness S_1 . Nevertheless, Forristall has shown a good agreement between his second-order theory and the results from the measurements.

In addition, Toffoli et al. (2007) used the second order finite depth wave theory to investigate the statistical properties of the surface elevation and wave crests in directional sea states. They also compared the experimental data with the results from the numerical simulations and concluded that the second order theory describes the statistical properties of the field data very accurately as long as the nonlinearity is small. Their conclusion is supported by field data measurements obtained from the Lake George, Australia with finite depth water.

Although both aforementioned facts showed good agreement between the second order theory and the measurements of crest amplitude, some other researchers such as Bitner-Gregersen and Magnusson (2004) and Petrova et al. (2006) showed a large deviation from the second-order theory, particularly, in the extreme tail of the distributions. Bitner-Gregersen and Magnusson (2004) analysed the data for unidirectional waves obtained from North seas and the data obtained from the second-order time domain simulations. They showed that the freak waves observed at Draupner could not adequately be accounted for by the second order theory. Moreover, based on their simulations, they concluded that the spectral shapes do influence their results. In

addition, Petrova et al. (2006) analysed a set of data collected during the storm in the north sea and they particularly refer to the Forristall model (Forristall, 2000). They found that although the model is found to be generally adequate for sea states with less severe conditions, the largest crest in the highest sea states especially those with abnormal waves are permanently underestimated. They also pointed out the drawback of the Forristall distribution which does not consider the variation in the directional spreading on the crest height statistics even though they admit that the Forristall model is simple.

In addition, Janssen (2009) reported that second-order approximation can provide an accurate estimate of skewness but it is not in principle adequate to describe the whole probability density function. Besides that, the second order theory only includes effects related to bound waves, while the nonlinear dynamics of free waves is neglected (Toffoli et al., 2010b).

At cubic order, Zakharov (1968) derived the well-known nonlinear Schrödinger equation and studied the instability of quasi-periodic deep-water wavetrains due to modulational perturbation. As reported by Toffoli et al. (2010b), this nonlinear Schrödinger equation can be derived from the Euler equation by assuming that potential flow of free-surface waves is weakly nonlinear, which means the wave steepness $\varepsilon = ka \ll 1$ for wavenumber k and wave amplitude a , and have narrow bandwidth. A modification of the nonlinear Schrödinger equation was derived by Dysthe (1979) on the basis of a systematic asymptotic procedure by taking into account the fourth order in wave steepness and bandwidth. This equation is normally known as Dysthe equation. Due to the narrow bandwidth constraint, the application of the nonlinear Schrödinger equation for ocean wave field is limited. To overcome this problem, Trulsen and Dysthe (1996) extended the Dysthe equation which allows slightly broader bandwidths by adding higher order dispersive terms.

The nonlinear Schrödinger equation and its extensions have received considerable attention by wave communities primarily due to their simplicity and inexpensive computation (Toffoli et al., 2010b). Zakharov and Shabat (1972), for example, solved the nonlinear Schrödinger equation analytically using the inverse scattering transform. Recently, there have been numerous numerical models based on the nonlinear Schrödinger equation to investigate ocean wave statistics which requires the calculation

of many realization of a random sea surface (see, for example, Onorato et al., 2001, Onorato et al., 2002, Socquet-Juglard et al., 2005, Gramstad and Trulsen, 2007, Toffoli et al., 2010b).

The stochastic version of the nonlinear Schrödinger equation was derived by Alber (Alber, 1978, Alber and Saffman, 1978) as shown in the previous section which is now known as the Alber equation. Recently, Stiassnie et al. (2008) solved the one spatial dimension of the Alber equation and discovered the long-time recurrent evolution in the area of instability. This behaviour is a stochastic counterpart of the well-known Fermi-Pasta-Ulam recurrent phenomenon (Fermi et al., 1965) obtained from the cubic Schrödinger equation (revisit the previous section for details of this recurrent phenomenon).

Based on the recurrent solution of the Alber equation, Regev et al. (2008) studied the probability of freak waves in an inhomogeneous ocean by integrating the Alber equation subjected to inhomogeneous disturbances. They showed that bound waves due to quadratic interaction between short waves and swell may act as an inhomogeneous disturbance in the form that is required for instability in the Alber equation. Practically, they used one typical cycle of the recurrence obtained from the Alber equation initialized by Gaussian spectra to establish the probability density function. Furthermore, they calculated the probability of wave height in a straightforward manner. They concluded that there is a strong effect of the spectral width W , which together with the sea wave number and the sea amplitude sets the growth rate, and can also be related to the Benjamin Feir Index (BFI). They also found that there is a weaker effect of the swell amplitude, which affects the size of the small inhomogeneous disturbance.

In this research, we follow a similar method used by Stiassnie et al. (2008) and Regev et al. (2008) but we extended the work to two spatial dimensions in order to study the probability of wave height and in particular to study the probability occurrence of freak waves in the ocean. Moreover, the more realistic ocean wave JONSWAP spectra with and without directional spreading are used. The details of the application to the statistics of freak waves in unidirectional and directional sea states can be found in Chapter 5.

2.6.2 Significant wave height

The concept of the significant (characteristics) wave height was developed during the World War II as part of a project to forecast ocean wave heights and periods (Stewart, 2008). Moreover, as reported by Wiegel (1964) that work at the Scripps Institution of Oceanography (1944) concluded that

. . . wave height estimated by observers corresponds to the average of the highest 20 to 40 per cent of waves. . . Originally, the term significant wave height was attached to the average of these observations, the highest 30 per cent of the waves, but has evolved to become the average of the highest one-third of the waves but has evolved to become the average of the highest $33\frac{1}{3}$ per cent (designated by H_S or $H_{1/3}$).

In practice, significant wave height is defined as the average of the one-third highest observed or measured wave heights. For example, if one is measuring the wave height in several minutes, then pick out say 150 wave crests and record their heights. In order to calculate the significant wave height, sorting the values from the highest to the lowest. Pick the 50 (one-third of 150) largest waves and calculate the average of the 50 waves. This will give the significant wave height (H_S or $H_{1/3}$) of the wave records.

This definition, however, is rarely used. Instead, the significant wave height is commonly evaluated by using a variance which is computed from a spectrum or by applying the statistical inference theory (see Ochi, 2005, for review). The principle evaluation of the significant wave height based on the Rayleigh distribution by assuming that wave spectrum is narrow banded. Therefore, one can write the Rayleigh distribution as follows:

$$p(H) = \frac{H}{4m_0} e^{-\frac{H^2}{8m_0}} \quad ; \quad 0 \leq H < \infty$$

where H is the wave height, m_0 is the variance of the spectrum or zero moment. The variance of the spectrum is equal to the area under the curve of the spectrum and therefore it is calculated using the following formula:

$$m_0 = \int S(k) dk$$

where $S(k)$ is the wave number spectrum.

Following a method used by Ochi (2005), let H^* be the lower limit of the highest one-third of the probability density function. Moreover, since the significant wave height is related to the highest one-third wave heights, one can write the probability of exceeding H^* is 1/3 as

$$P(\hat{H} \geq H^*) = \int_{H^*}^{\infty} \frac{H}{4m_0} e^{-\frac{H^2}{8m_0}} dH = \frac{1}{3}.$$

Solving this integral for H^* yields

$$H^* = \sqrt{8 m_0 \ln 3} \approx \sqrt{8.7889 m_0}. \quad (2.51)$$

Evaluating the expected value of H which is the moment about the origin gives

$$\begin{aligned} \int_{H^*}^{\infty} H p(H) dH &= \int_{H^*}^{\infty} \frac{H^2}{4m_0} e^{-\frac{H^2}{8m_0}} dH \\ &= H^* e^{-\frac{H^{*2}}{8m_0}} + \sqrt{2\pi m_0} - \sqrt{2\pi m_0} \operatorname{erf}\left(\frac{H^* \sqrt{2}}{4\sqrt{m_0}}\right). \end{aligned}$$

Hence, the expected value of H can be written as

$$\int_{H^*}^{\infty} H p(H) dH = H^* e^{-\frac{H^{*2}}{8m_0}} + \sqrt{2\pi m_0} \left\{ 1 - \operatorname{erf}\left(\frac{H^* \sqrt{2}}{4\sqrt{m_0}}\right) \right\}. \quad (2.52)$$

Note that $\operatorname{erf}(x)$ is an error function and is defined as

$$\operatorname{erf}(x) = \frac{2}{\sqrt{\pi}} \int_0^x e^{-t^2} dt.$$

For a special case, when $H^* = 0$, then $\operatorname{erf}(0) = 0$. As a consequence, equation (2.52) gives the mean value of the wave height based on the Rayleigh distribution that is

$$\bar{H} = \sqrt{2\pi m_0},$$

as also obtained by Young (1999) and Holthuijsen (2007) directly from the Rayleigh distribution.

Moreover, equation (2.52) is equal to one-third of the significant wave height which can be written as

$$H^* e^{-\frac{H^{*2}}{8m_0}} + \sqrt{2\pi m_0} \left\{ 1 - \operatorname{erf} \left(\frac{H^* \sqrt{2}}{4\sqrt{m_0}} \right) \right\} = \frac{H_s}{3} \quad (2.53)$$

where H_s is the significant wave height. From equations (2.51) and (2.52), the significant wave height can be rewritten as

$$H_s = 3 \left[\sqrt{8 m_0 \ln 3} e^{-\frac{(\sqrt{8 m_0 \ln 3})^2}{8m_0}} + \sqrt{2\pi m_0} \left\{ 1 - \operatorname{erf} \left(\frac{(\sqrt{8 m_0 \ln 3}) \sqrt{2}}{4\sqrt{m_0}} \right) \right\} \right].$$

After some simplifications of the simple algebra, this equation can be rewritten as

$$H_s = \sqrt{8 m_0 \ln 3} + 3\sqrt{2\pi m_0} \{ 1 - \operatorname{erf}(\sqrt{\ln 3}) \}. \quad (2.54)$$

Furthermore, one can rewrite this equation as follows

$$H_s = 4.0043\sqrt{m_0} \approx 4\sqrt{m_0}. \quad (2.55)$$

Thus, the significant wave height is equal to four times the square root of the area under the spectral function with the narrow-band random process assumption (see also Holthuijsen, 2007, for another review). This significant wave height can be illustrated in the following

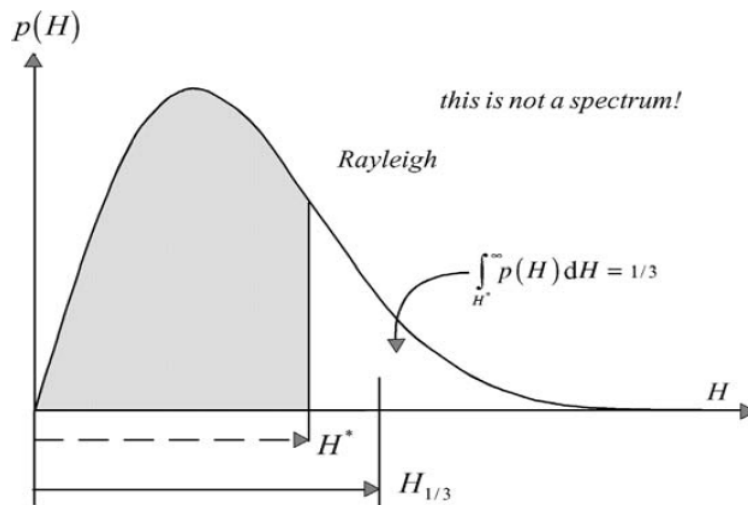


Figure 2.9: The significant wave height in the Rayleigh probability density function (Holthuijsen, 2007, Fig. 4.9).

One interesting point with regards to the above method of calculating significant wave height is the fact that the formula shown in equation (2.54) can be generalized to evaluate the average of the highest $1/n$ observation, denoted by $H_{1/n}$, for Rayleigh distribution, that is

$$H_{1/n} = \sqrt{8 m_0 \ln n} + n\sqrt{2\pi m_0}\{1 - \text{erf}(\sqrt{\ln n})\}. \quad (2.56)$$

As a special case, choosing $n = 1$, will give the mean value of wave heights, $\bar{H} = \sqrt{2\pi m_0}$, as shown before. This is because $\ln 1 = 0$ and $\text{erf}(0) = 0$. Moreover, for $n = 3$ then equation (2.56) falls into equation (2.54). Similarly, for large value of n , $\text{erf}(n)$ approaches 1. As a result, the second term of equation (2.56) vanishes automatically and therefore, equation (2.56) can be rewritten as

$$H_{1/n} = \sqrt{8 m_0 \ln n} \quad (2.57)$$

which falls into the result of Ochi (2005) (his equation (3.81)).

Chapter 3

Linear stability analysis in two spatial dimensions

3.1 Introduction

Linear stability of narrow spectra homogeneous seas for two spatial dimensions is studied in this Chapter. This analysis subjects to inhomogeneous disturbances. A spectrum is called to be narrow if most of the wave energy is concentrated in the vicinity of the carrier waves. Moreover, a wave field is called homogeneous if two-point correlation only depends on the spacing and is independent of the position/location. A two-point correlation function $c(\mathbf{x}, \mathbf{r}, t)$ is defined as (Stiassnie et al., 2008)

$$c(\mathbf{x}, \mathbf{r}, t) \equiv \left\langle \eta(\mathbf{x} + \frac{1}{2}\mathbf{r}, t) \eta(\mathbf{x} - \frac{1}{2}\mathbf{r}, t) \right\rangle,$$

where \mathbf{r} is the spacing and angle brackets $\langle \rangle$ denote ensemble average which is defined as an average taken over randomly chosen initial phases allocated to the various modes of a continuous spectrum. Note that $\langle \eta \rangle = 0$, which is the free surface elevation.

In this Chapter, we start from the Alber equation on the waves in infinity depth to show the correlation function for a homogeneous sea. It is found that the correlation function for a homogeneous sea is a function of on the spacing \mathbf{r} only and is independent of the position. The advantage of this situation enables us to treat the inhomogeneous sea where the correlation function does not only depend on the spacing \mathbf{r} but also depends on the position/location. Furthermore, the correlation function is assumed to be a summation of the correlation function for homogeneous sea and small inhomogeneous disturbance. This small inhomogeneous disturbance is indicated by a small dimensionless inhomogeneity parameter with assumption that $\delta = o(1)$. This leads to a linear first-order partial differential equation which has a straightforward solution. When the spacing is set to be zero, this solution produces the dispersion relation for the disturbance. In order to determine the condition for instability and the actual growth

rate, the spectrum must be specified. Therefore, a number of spectra have been chosen. We start from spectra with very simple structure, namely a square spectrum and a rectangular spectrum which is a general case of the square spectrum. Then, we continue with a popular Lorentz spectrum that has been used by some other researchers such as Crawford et al. (1980) to study the instability of homogeneous wave-fields to inhomogeneous disturbances. We will use two-dimensional versions of these spectra while for one spatial dimension one can refer to the paper of Stiassnie et al. (2008). Furthermore, a more realistic ocean-wave JONSWAP spectrum (Hasselmann et al. 1973) with and without directional distributions are also studied. Finally, the spectral interpretation of the inhomogeneous disturbances is derived. Interrelation between a homogeneous spectrum and the homogeneous correlation function, as well as the interrelation between the spectrum and the decay rate, are shown. Finally, the calculation of the free surface elevation is also included.

3.2 The Alber equation in waves of infinite depth

The Alber equation (Alber, 1978) is designed to study the inhomogeneous random wave fields with arbitrary water depth albeit with narrow spectrum. Therefore, one can simplify it to study the evolution of the wave train on the infinitely deep water by neglecting the mean flow field, i.e. $Q = 0$, in equation (2.21). Moreover, changing the stretched/ slow variable used by Alber to the physical variables and following the definition of the two-point space correlation function in Stiassnie et al. (2008), the two spatial dimensions of the Alber equation for narrow-banded random surface waves, in waves of infinite depth, and in two spatial dimensions can be expressed as

$$\begin{aligned} i \left(\frac{\partial \rho}{\partial t} + \frac{1}{2} \sqrt{\frac{g}{k_0}} \frac{\partial \rho}{\partial x} \right) - \frac{1}{4} \sqrt{\frac{g}{k_0^3}} \left(\frac{\partial^2 \rho}{\partial x \partial r_1} - 2 \frac{\partial^2 \rho}{\partial y \partial r_2} \right) \\ = \sqrt{gk_0^5} \rho(\mathbf{x}, \mathbf{r}, t) \left[\rho \left(\mathbf{x} + \frac{\mathbf{r}}{2}, \mathbf{0}, t \right) - \rho \left(\mathbf{x} - \frac{\mathbf{r}}{2}, \mathbf{0}, t \right) \right] \end{aligned} \quad (3.1)$$

where $\rho(\mathbf{x}, \mathbf{r}, t)$ is the two-point space correlation function and it is defined as:

$$\rho(\mathbf{x}, \mathbf{r}, t) = \langle A \left(\mathbf{x} + \frac{1}{2} \mathbf{r}, t \right) A^* \left(\mathbf{x} - \frac{1}{2} \mathbf{r}, t \right) \rangle. \quad (3.2)$$

The angle brackets $\langle \rangle$ denote the ensemble average, the asterisk stands for the complex conjugate, $\mathbf{x} = (x, y)$ are the horizontal coordinates, $\mathbf{r} = (r_1, r_2)$ are spacing

and t is time. $A(\mathbf{x}, t)$ in (3.2) is the complex envelope of the narrow-banded sea, with carrier wave number $\mathbf{k}_0 = (k_0, 0)$ related to the free surface elevation $\eta(\mathbf{x}, t)$ through

$$2\eta(\mathbf{x}, t) = A(\mathbf{x}, t)e^{i(k_0x - \omega_0t)} + c. c., \quad (3.3)$$

where $\omega_0 = \sqrt{gk_0}$ is the frequency of the carrier waves and g is the acceleration due to gravity.

3.3 Correlation function for homogeneous seas

Following Landsberg (1955, p.126) [see also Kinsman 1965] a homogeneous random ocean surface in two spatial dimensions is given by:

$$2\eta(\mathbf{x}, t) = e^{i(k_0x - \omega_0t)} \int_{-\infty}^{\infty} e^{i[(\mathbf{k}-\mathbf{k}_0)\cdot\mathbf{x} - (\omega_k - \omega_0)t + \theta(\mathbf{k})]} \sqrt{S(\mathbf{k})} d\mathbf{k} + c. c., \quad (3.4)$$

where $\omega_k = \sqrt{g|\mathbf{k}|}$, $\mathbf{k} = (k_1, k_2)$ and $\mathbf{k}_0 = (k_0, 0)$, $\theta(\mathbf{k})$ is a random phase with uniform distribution in $[-\pi, \pi] \times [-\pi, \pi]$ and $S(\mathbf{k})$ is the energy spectrum. The amplitude can be obtained by comparing (3.3) and (3.4), that is

$$A(\mathbf{x}, t) = \int_{-\infty}^{\infty} e^{i[(\mathbf{k}-\mathbf{k}_0)\cdot\mathbf{x} - (\omega_k - \omega_0)t + \theta(\mathbf{k})]} \sqrt{S(\mathbf{k})} d\mathbf{k}. \quad (3.5)$$

Substituting equation (3.5) into equation (3.2) yields,

$$\begin{aligned} & \rho(\mathbf{x}, \mathbf{r}, \tau) \\ &= \int_{-\infty}^{\infty} \int_{-\infty}^{\infty} \langle e^{i[(\mathbf{k}_1 - \mathbf{k}_0)\cdot(\mathbf{x} + \frac{\mathbf{r}}{2}) - (\omega_{k_1} - \omega_0)t + \theta_1(\mathbf{k}_1)]} e^{-i[(\mathbf{k}_2 - \mathbf{k}_0)\cdot(\mathbf{x} - \frac{\mathbf{r}}{2}) - (\omega_{k_2} - \omega_0)t + \theta_2(\mathbf{k}_2)]} \rangle \\ & \times \sqrt{S(\mathbf{k}_1)S(\mathbf{k}_2)} d\mathbf{k}_1 d\mathbf{k}_2 \end{aligned} \quad (3.6)$$

where $\omega_{k_1} = \sqrt{g|\mathbf{k}_1|}$ and $\omega_{k_2} = \sqrt{g|\mathbf{k}_2|}$. From this equation, we have the sum $\theta = \theta_1(\mathbf{k}_1) - \theta_2(\mathbf{k}_2)$, which by itself is a random phase. Note that $\langle e^{i\theta} \rangle = 0$ unless for $\theta = 0$. For the latter to happen we need $\theta_1(\mathbf{k}_1) = \theta_2(\mathbf{k}_2)$. Therefore, the only terms remaining after the averaging are those for which $\mathbf{k}_1 = \mathbf{k}_2$,

$$\rho(\mathbf{x}, \mathbf{r}, \tau) = \int_{-\infty}^{\infty} \int_{-\infty}^{\infty} \left(e^{i[(\mathbf{k}_1 - \mathbf{k}_0)\cdot(\mathbf{x} + \frac{\mathbf{r}}{2}) - (\mathbf{k}_1 - \mathbf{k}_0)\cdot(\mathbf{x} - \frac{\mathbf{r}}{2}) - (\omega_{k_1} - \omega_0)t + (\omega_{k_1} - \omega_0)t]} \right) S(\mathbf{k}_1) d\mathbf{k}_1.$$

As a result, this equation can be simplified as

$$\rho_h(\mathbf{r}) = \int_{-\infty}^{\infty} S(\mathbf{k}) e^{i(\mathbf{k}-\mathbf{k}_0)\cdot\mathbf{r}} d\mathbf{k}. \quad (3.7)$$

As seen from equation (3.7), the correlation function of a homogeneous sea, ρ_h , does not depend on the position \mathbf{x} but only depends on spacing \mathbf{r} which is very consistent with the result one-dimensional case as shown in Stiassnie et al. (2008). Note that equation (3.7) is the trivial solution of the equation (3.1). This situation enables us to study the inhomogeneous seas which are the main consideration of this research.

3.4 Instability of inhomogeneous disturbances

In order to study the inhomogeneous sea, let us consider a solution to the equation (3.1) in the form

$$\rho(\mathbf{x}, \mathbf{r}, \tau) = \rho_h(\mathbf{r}) + \delta\rho_1(\mathbf{x}, \mathbf{r}, t) \quad (3.8)$$

where $\rho_h(\mathbf{r})$ is a homogeneous part which depends only on spacing \mathbf{r} , $\rho_1(\mathbf{x}, \mathbf{r}, t)$ is an inhomogeneous disturbance and δ is the dimensionless inhomogeneity parameter with assumption that $\delta = o(1)$. Substituting equation (3.8) into equation (3.1) and neglecting terms of order δ^2 gives

$$\begin{aligned} i \left(\frac{\partial \rho_1}{\partial t} + \frac{1}{2} \sqrt{\frac{g}{k_0}} \frac{\partial \rho_1}{\partial x} \right) - \frac{1}{4} \sqrt{\frac{g}{k_0^3}} \frac{\partial^2 \rho_1}{\partial x \partial r_1} + \frac{1}{2} \sqrt{\frac{g}{k_0^3}} \frac{\partial^2 \rho_1}{\partial y \partial r_2} \\ = \sqrt{gk_0^5} \rho_h(\mathbf{r}) \left(\rho_1 \left(\mathbf{x} + \frac{1}{2}\mathbf{r}, \mathbf{0}, t \right) - \rho_1 \left(\mathbf{x} - \frac{1}{2}\mathbf{r}, \mathbf{0}, t \right) \right). \end{aligned} \quad (3.9)$$

Also, assuming a disturbance as

$$\rho_1(\mathbf{x}, \mathbf{r}, t) = R(\mathbf{r}) \left\{ e^{i \left(px + qy - \frac{p}{2} \sqrt{\frac{g}{k_0}} t - \Omega t \right)} + * \right\} \quad (3.10)$$

where $R(\mathbf{0})$ is real but it should not be equal to zero and $R(\infty)$ is zero, p and q are wavenumbers of the disturbance which are parallel and perpendicular to the carrier wave, respectively, Ω is its frequency and the asterisk, again, stands for complex conjugate. Ω in general is a complex number where a positive imaginary part Ω_i corresponds to unstable growth and the real part Ω_R corresponds to the oscillation.

Now, substituting equation (3.10) into equation (3.9) by using the following identities

$$\frac{\partial \rho_1}{\partial t} = -i\Omega R(\mathbf{r})e^{i\left(px+qy-\frac{p}{2}\sqrt{\frac{g}{k_0}}t-\Omega t\right)} - \frac{ipR(\mathbf{r})}{2}\sqrt{\frac{g}{k_0}}e^{i\left(px+qy-\frac{p}{2}\sqrt{\frac{g}{k_0}}t-\Omega t\right)},$$

$$\frac{\partial \rho_1}{\partial x} = ipR(\mathbf{r})e^{i\left(px+qy-\frac{p}{2}\sqrt{\frac{g}{k_0}}t-\Omega t\right)},$$

$$\frac{\partial^2 \rho_1}{\partial x \partial r_1} = pi\frac{\partial R(\mathbf{r})}{\partial r_1}e^{i\left(px+qy-\frac{p}{2}\sqrt{\frac{g}{k_0}}t-\Omega t\right)},$$

$$\frac{\partial^2 \rho_1}{\partial y \partial r_2} = qi\frac{\partial R(\mathbf{r})}{\partial r_2}e^{i\left(px+qy-\frac{p}{2}\sqrt{\frac{g}{k_0}}t-\Omega t\right)},$$

$$\rho_1\left(\mathbf{x} + \frac{1}{2}\mathbf{r}, \mathbf{0}, t\right) = R(\mathbf{0})e^{i\left(px+qy-\frac{p}{2}\sqrt{\frac{g}{k_0}}t-\Omega t\right)}e^{i\left(\frac{p}{2}r_1+\frac{q}{2}r_2\right)},$$

and

$$\rho_1\left(\mathbf{x} - \frac{1}{2}\mathbf{r}, \mathbf{0}, t\right) = R(\mathbf{0})e^{i\left(px+qy-\frac{p}{2}\sqrt{\frac{g}{k_0}}t-\Omega t\right)}e^{-i\left(\frac{p}{2}r_1+\frac{q}{2}r_2\right)},$$

yields

$$\begin{aligned} \Omega R(\mathbf{r}) - ip\frac{1}{4}\sqrt{\frac{g}{k_0^3}}\frac{\partial R(\mathbf{r})}{\partial r_1} + i\frac{q}{2}\sqrt{\frac{g}{k_0^3}}\frac{\partial R(\mathbf{r})}{\partial r_2} \\ = \sqrt{gk_0^5}\rho_h(\mathbf{r})R(\mathbf{0})\left(e^{i\left(\frac{p}{2}r_1+\frac{q}{2}r_2\right)} - e^{-i\left(\frac{p}{2}r_1+\frac{q}{2}r_2\right)}\right). \end{aligned} \quad (3.11)$$

Multiplying equation (3.11) by $\frac{4i}{p}\sqrt{\frac{k_0^3}{g}}$ gives

$$\begin{aligned} \frac{\partial R(\mathbf{r})}{\partial r_1} - \frac{2q}{p}\frac{\partial R(\mathbf{r})}{\partial r_2} + \frac{4i\Omega}{p}\sqrt{\frac{k_0^3}{g}}R(\mathbf{r}) \\ = \frac{4ik_0^4}{p}\rho_h(\mathbf{r})R(\mathbf{0})\left(e^{i\left(\frac{p}{2}r_1+\frac{q}{2}r_2\right)} - e^{-i\left(\frac{p}{2}r_1+\frac{q}{2}r_2\right)}\right). \end{aligned} \quad (3.12)$$

Letting

$$\psi = \frac{4i\Omega}{p}\sqrt{\frac{k_0^3}{g}} \text{ and } G(\mathbf{r}) = \frac{4ik_0^4}{p}\rho_h(\mathbf{r})R(\mathbf{0})\left(e^{i\left(\frac{p}{2}r_1+\frac{q}{2}r_2\right)} - e^{-i\left(\frac{p}{2}r_1+\frac{q}{2}r_2\right)}\right)$$

then equation (3.12) becomes a linear first order partial differential equation for $R(\mathbf{r})$

$$\frac{\partial R(\mathbf{r})}{\partial r_1} - \frac{2q}{p}\frac{\partial R(\mathbf{r})}{\partial r_2} + \psi R(\mathbf{r}) = G(\mathbf{r}). \quad (3.13)$$

In order to solve this partial differential equation, the method used in Strikwerda (1989) will be followed by changing the variables from (r_1, r_2) to (α, β) where α and β are defined as

$$\alpha = r_1, \quad \beta = r_2 + \frac{2q}{p} r_1.$$

We define

$$\tilde{R}(\alpha, \beta) = R(r_1, r_2),$$

where (α, β) and (r_1, r_2) are related by the preceding relation. Taking the first order partial derivative with respect to α gives

$$\frac{\partial \tilde{R}}{\partial \alpha} = \frac{\partial R}{\partial r_1} \frac{\partial r_1}{\partial \alpha} + \frac{\partial R}{\partial r_2} \frac{\partial r_2}{\partial \alpha},$$

and then equation (3.13) can then be rewritten as

$$\frac{\partial \tilde{R}}{\partial \alpha} = \frac{\partial R}{\partial r_1} - \frac{2q}{p} \frac{\partial R}{\partial r_2} = -\psi R + G\left(\alpha, \beta - \frac{2q}{p} \alpha\right).$$

Therefore, the first order partial differential equation becomes a first order ordinary differential equation that can be written as

$$\frac{\partial \tilde{R}}{\partial \alpha} + \psi \tilde{R} = G\left(\alpha, \beta - \frac{2q}{p} \alpha\right).$$

Using the method of integrating factor, one can easily get the solution of this ordinary differential equation, which is given by

$$\tilde{R}(\alpha, \beta) = e^{-\int_{\infty}^{\alpha} \psi d\alpha'} \left\{ \int_{\infty}^{\alpha} G\left(\alpha', \beta - \frac{2q}{p} \alpha'\right) e^{\int_{\infty}^{\alpha'} \psi dt} d\alpha' \right\}.$$

Now, assuming that $\tilde{R}(\infty) = 0$, above equation can be written as

$$\tilde{R}(\alpha, \beta) = e^{-\alpha\psi} \left\{ \int_{\infty}^{\alpha} G\left(\alpha', \beta - \frac{2q}{p} \alpha'\right) e^{\psi\alpha'} d\alpha' \right\}.$$

Returning to the original variables, the solution of equation (3.13) is given by

$$R(r_1, r_2) = e^{-\psi r_1} \left\{ \int_{\infty}^{r_1} G \left(r'_1, r_2 + \frac{2q}{p} (r_1 - r'_1) \right) e^{\psi r'_1} dr'_1 \right\}. \quad (3.14)$$

Moreover, as we have

$$\begin{aligned} G \left(r'_1, r_2 + \frac{2q}{p} (r_1 - r'_1) \right) \\ = \frac{4ik_0^4}{p} \rho_h \left(r'_1, r_2 + \frac{2q}{p} (r_1 - r'_1) \right) R(\mathbf{0}) \left(e^{i \left(\frac{p}{2} r'_1 + \frac{q}{2} \left(r_2 + \frac{2q}{p} (r_1 - r'_1) \right) \right)} \right. \\ \left. - e^{-i \left(\frac{p}{2} r'_1 + \frac{q}{2} \left(r_2 + \frac{2q}{p} (r_1 - r'_1) \right) \right)} \right), \end{aligned}$$

equation (3.14) can then be rewritten as

$$\begin{aligned} R(r_1, r_2) = \frac{e^{-\psi r_1}}{p} 4ik_0^4 R(\mathbf{0}) \left\{ \int_{\infty}^{r_1} \rho_h \left(r'_1, r_2 + \frac{2q}{p} (r_1 - r'_1) \right) \left(e^{i \left(\frac{p}{2} r'_1 + \frac{q}{2} \left(r_2 + \frac{2q}{p} (r_1 - r'_1) \right) \right)} \right. \right. \\ \left. \left. - e^{-i \left(\frac{p}{2} r'_1 + \frac{q}{2} \left(r_2 + \frac{2q}{p} (r_1 - r'_1) \right) \right)} \right) e^{\psi r'_1} dr'_1 \right\}. \end{aligned}$$

Taking $\mathbf{r} = \mathbf{0}$, gives

$$R(\mathbf{0}) = \frac{4ik_0^4}{p} R(\mathbf{0}) \left\{ \int_{\infty}^0 \rho_h \left(r'_1, -\frac{2q}{p} r'_1 \right) \left(e^{i \left(\frac{p}{2} r'_1 - \frac{q}{2} \left(\frac{2q}{p} r'_1 \right) \right)} - e^{-i \left(\frac{p}{2} r'_1 - \frac{q}{2} \left(\frac{2q}{p} r'_1 \right) \right)} \right) e^{\psi r'_1} dr'_1 \right\}.$$

Dividing both sides of this equation by $R(\mathbf{0})$ yields

$$1 = \frac{4ik_0^4}{p} \left\{ \int_{\infty}^0 \rho_h \left(r'_1, -\frac{2q}{p} r'_1 \right) \left(e^{i \left(\frac{p}{2} r'_1 - \frac{q}{2} \left(\frac{2q}{p} r'_1 \right) \right)} - e^{-i \left(\frac{p}{2} r'_1 - \frac{q}{2} \left(\frac{2q}{p} r'_1 \right) \right)} \right) e^{\psi r'_1} dr'_1 \right\}.$$

Furthermore, substituting $\rho_h \left(r'_1, -\frac{2q}{p} r'_1 \right)$ into this equation where

$$\rho_h \left(r'_1, -\frac{2q}{p} r'_1 \right) = \int_{-\infty}^{\infty} S(\mathbf{k}) e^{i \left((k_1 - k_0) r'_1 - k_2 \left(\frac{2q}{p} r'_1 \right) \right)} d\mathbf{k}$$

yields,

$$1 = \frac{4ik_0^4}{p} \left\{ \iint_{-\infty}^{\infty} \int_0^{\infty} S(\mathbf{k}) e^{i\left((k_1-k_0)r'_1 - k_2\left(\frac{2q}{p}r'_1\right)\right)} \left(e^{i\left(\frac{p}{2}r'_1 - \frac{q}{2}\left(\frac{2q}{p}r'_1\right)\right)} - e^{-i\left(\frac{p}{2}r'_1 - \frac{q}{2}\left(\frac{2q}{p}r'_1\right)\right)} \right) e^{\psi r'_1} dr'_1 dk_1 dk_2 \right\}.$$

Simplifying this equation gives,

$$1 = \frac{4ik_0^4}{p} \left\{ \iint_{-\infty}^{\infty} \int_0^{\infty} S(\mathbf{k}) \left[e^{\left\{i\left((k_1-k_0) - \frac{2q}{p}k_2 + \frac{p}{2} - \frac{q^2}{p}\right) + \psi\right\}r'_1} - e^{\left\{i\left((k_1-k_0) - \frac{2q}{p}k_2 - \frac{p}{2} + \frac{q^2}{p}\right) + \psi\right\}r'_1} \right] dr'_1 dk_1 dk_2 \right\}.$$

Integrating this result with respect to r'_1 by noting that $Re\{\psi\} < 0$, further gives

$$1 = \frac{4ik_0^4}{p} \left\{ \iint_{-\infty}^{\infty} \left[\frac{1}{i\left((k_1-k_0) - \frac{2q}{p}k_2 + \frac{p}{2} - \frac{q^2}{p}\right) + \psi} - \frac{1}{i\left((k_1-k_0) - \frac{2q}{p}k_2 - \frac{p}{2} + \frac{q^2}{p}\right) + \psi} \right] S(\mathbf{k}) dk_1 dk_2 \right\} \quad (3.15)$$

and after simplification, this equation can be rewritten as

$$1 = \frac{4k_0^4}{p} \left\{ \iint_{-\infty}^{\infty} \frac{\left(p - \frac{2q^2}{p}\right) S(\mathbf{k}) dk_1 dk_2}{\left\{i\left((k_1-k_0) - \frac{2q}{p}k_2\right) + \psi\right\}^2 + \left\{\frac{p}{2} - \frac{q^2}{p}\right\}^2} \right\}. \quad (3.16)$$

Multiplying both numerator and denominator of the equation (3.16) by p , leads to

$$1 = 4k_0^4(p^2 - 2q^2) \left\{ \iint_{-\infty}^{\infty} \frac{S(\mathbf{k}) dk_1 dk_2}{\{i(p(k_1-k_0) - 2qk_2) + p\psi\}^2 + \left\{\frac{p^2 - 2q^2}{2}\right\}^2} \right\}, \quad (3.17)$$

which is the main result of this section. This solution is the dispersion relation for the disturbance and hence, for given p , q and $S(\mathbf{k})$, Ω can be calculated to determine the

condition for instability and the actual growth rate. This solution also agrees with Alber's result, which was obtained with a different approach. This agreement will be shown in the following. As we know, the correlation function ρ can be defined as follows

$$\rho_0(\mathbf{r}) = \int_{-\infty}^{\infty} F_0(\mathbf{k}) e^{i\mathbf{k}\cdot\mathbf{r}} d\mathbf{k}$$

and making use of equation (3.7) gives

$$S(\mathbf{k} + \mathbf{k}_0) = F_0(\mathbf{k}).$$

Letting

$$\boldsymbol{\kappa} = p\mathbf{i} + q\mathbf{j}$$

where p and q are the wavenumber of the disturbance as given in equation (3.17), one will have the following equalities:

$$\begin{aligned} F_0\left(\mathbf{k} + \frac{\boldsymbol{\kappa}}{2}\right) &= S\left(\mathbf{k} + \mathbf{k}_0 + \frac{\boldsymbol{\kappa}}{2}\right) = S\left(k_1 + k_0 + \frac{p}{2}, k_2 + \frac{q}{2}\right), \\ F_0\left(\mathbf{k} - \frac{\boldsymbol{\kappa}}{2}\right) &= S\left(\mathbf{k} + \mathbf{k}_0 - \frac{\boldsymbol{\kappa}}{2}\right) = S\left(k_1 + k_0 - \frac{p}{2}, k_2 - \frac{q}{2}\right). \end{aligned} \quad (3.18)$$

As a result, equation (3.15) can be written as

$$1 = \frac{4ik_0^4}{p} \left\{ \iint_{-\infty}^{\infty} \left[\frac{S\left(k_1 + k_0 - \frac{p}{2}, k_2 - \frac{q}{2}\right)}{i\left(\left(k_1 - \frac{p}{2}\right) - \frac{2q}{p}\left(k_2 - \frac{q}{2}\right) + \frac{p}{2} - \frac{q^2}{p}\right) + \psi} - \frac{S\left(k_1 + k_0 + \frac{p}{2}, k_2 + \frac{q}{2}\right)}{i\left(\left(k_1 + \frac{p}{2}\right) - \frac{2q}{p}\left(k_2 + \frac{q}{2}\right) - \frac{p}{2} + \frac{q^2}{p}\right) + \psi} \right] dk_1 dk_2 \right\}. \quad (3.19)$$

Simplifying equation (3.19) gives

$$1 = \frac{4ik_0^4}{p} \left\{ \iint_{-\infty}^{\infty} \left[\frac{S\left(k_1 + k_0 - \frac{p}{2}, k_2 - \frac{q}{2}\right)}{i\left(k_1 - \frac{p}{2} - \frac{2q}{p}k_2 + \frac{q^2}{p} + \frac{p}{2} - \frac{q^2}{p}\right) + \psi} - \frac{S\left(k_1 + k_0 + \frac{p}{2}, k_2 + \frac{q}{2}\right)}{i\left(k_1 + \frac{p}{2} - \frac{2q}{p}k_2 - \frac{q^2}{p} - \frac{p}{2} + \frac{q^2}{p}\right) + \psi} \right] dk_1 dk_2 \right\}$$

and then it becomes

$$1 = \frac{4ik_0^4}{p} \left\{ \iint_{-\infty}^{\infty} \left[\frac{S\left(k_1 + k_0 - \frac{p}{2}, k_2 - \frac{q}{2}\right)}{i\left(k_1 - \frac{2q}{p}k_2\right) + \psi} - \frac{S\left(k_1 + k_0 + \frac{p}{2}, k_2 + \frac{q}{2}\right)}{i\left(k_1 - \frac{2q}{p}k_2\right) + \psi} \right] dk_1 dk_2 \right\}.$$

Making use of the above equalities as given in the equation (3.18) yields,

$$1 = \frac{4ik_0^4}{p} \left\{ \iint_{-\infty}^{\infty} \left[\frac{F_0\left(\mathbf{k} - \frac{\boldsymbol{\kappa}}{2}\right) - F_0\left(\mathbf{k} + \frac{\boldsymbol{\kappa}}{2}\right)}{i\left(k_1 - \frac{2q}{p}k_2\right) + \psi} \right] dk_1 dk_2 \right\}. \quad (3.20)$$

Substituting the value of $\psi = \frac{4i\Omega}{p} \sqrt{\frac{k_0^3}{g}}$, equation (3.20) becomes

$$1 = -\frac{4ik_0^4}{p} \left\{ \iint_{-\infty}^{\infty} \left[\frac{F_0\left(\mathbf{k} + \frac{\boldsymbol{\kappa}}{2}\right) - F_0\left(\mathbf{k} - \frac{\boldsymbol{\kappa}}{2}\right)}{i\left(k_1 - \frac{2q}{p}k_2\right) + \frac{4i\Omega}{p} \sqrt{\frac{k_0^3}{g}}} \right] dk_1 dk_2 \right\} \quad (3.21)$$

and after simplification, equation (3.21) can be rewritten as

$$1 = -4k_0^4 \sqrt{g} \left\{ \iint_{-\infty}^{\infty} \left[\frac{F_0\left(\mathbf{k} + \frac{\boldsymbol{\kappa}}{2}\right) - F_0\left(\mathbf{k} - \frac{\boldsymbol{\kappa}}{2}\right)}{k_1 p \sqrt{g} - 2q k_2 \sqrt{g} + 4\Omega \sqrt{k_0^3}} \right] dk_1 dk_2 \right\}.$$

Moreover, changing the coefficient of Ω to be 1 gives

$$1 = -\frac{4k_0^4 \sqrt{g}}{4\sqrt{k_0^3}} \left\{ \iint_{-\infty}^{\infty} \left[\frac{F_0\left(\mathbf{k} + \frac{\boldsymbol{\kappa}}{2}\right) - F_0\left(\mathbf{k} - \frac{\boldsymbol{\kappa}}{2}\right)}{\frac{k_1 p}{4} \sqrt{\frac{g}{k_0^3}} - \frac{q k_2}{2} \sqrt{\frac{g}{k_0^3}} + \Omega} \right] dk_1 dk_2 \right\}. \quad (3.22)$$

Also, since we have $\lambda = -\frac{1}{8}\sqrt{g/k_0^3}$ and $\mu = \frac{1}{4}\sqrt{g/k_0^3}$, equation (3.22) now becomes

$$1 = -\sqrt{gk_0^5} \iint_{-\infty}^{\infty} \left[\frac{F_0\left(\mathbf{k} + \frac{\boldsymbol{\kappa}}{2}\right) - F_0\left(\mathbf{k} - \frac{\boldsymbol{\kappa}}{2}\right)}{\Omega - 2\lambda k_1 p - 2\mu q k_2} \right] dk_1 dk_2. \quad (3.23)$$

Therefore, since we have $v = \frac{1}{2}\sqrt{gk_0^5}$, equation (3.23) can be simplified as

$$1 + 2v \iint_{-\infty}^{\infty} \left[\frac{F_0\left(\mathbf{k} + \frac{\boldsymbol{\kappa}}{2}\right) - F_0\left(\mathbf{k} - \frac{\boldsymbol{\kappa}}{2}\right)}{\Omega - 2\lambda k_1 p - 2\mu q k_2} \right] dk_1 dk_2 = 0 \quad (3.24)$$

which is Alber's result for infinitely deep water in his paper (Alber, 1978, eqs (4.10), p. 534). For any further progress with the equation (3.17), $S(\mathbf{k})$ needs to be specified. Note that $S(\mathbf{k})$ is a homogeneous spectrum. Moreover, the spectrum has to be a narrow spectrum that is most of the wave energy is concentrated in the vicinity of the carrier wave and it can be written as $2W \ll k_0$ where W and k_0 are the spectral width and the peak of wavenumber spectrum, respectively. This is because, as has been mentioned in Chapter 2, the Alber equation was derived from the cubic Schrödinger equation.

3.4.1 Square spectrum and its growth rate

In the following, a special spectral shape that will be considered is a square spectrum. Following Stiassnie et al. (2008), a square spectrum for two spatial dimensions can be defined as

$$S(\mathbf{k}) = s_0; \quad k_0 - W < k_1 < k_0 + W; \quad -W < k_2 < W \quad (3.25)$$

where W is the spectral width in directions parallel and perpendicular to the carrier-wave where in this case are chosen to be the same, k_0 is the carrier wave, s_0 is the energy spectrum, k_1 is the wavenumber in direction parallel to the carrier wave and k_2 is the wavenumber in direction perpendicular to carrier-wave. This spectrum is plotted in Figure 3.1.

In order to determine the actual growth rate, the point of maximum growth rate and the condition for instability of this square spectrum, equation (3.25) is substituted into equation (3.17) and then integrating with respect to \mathbf{k} yields the growth rate of unstable disturbance which can only be given in the implicit form:

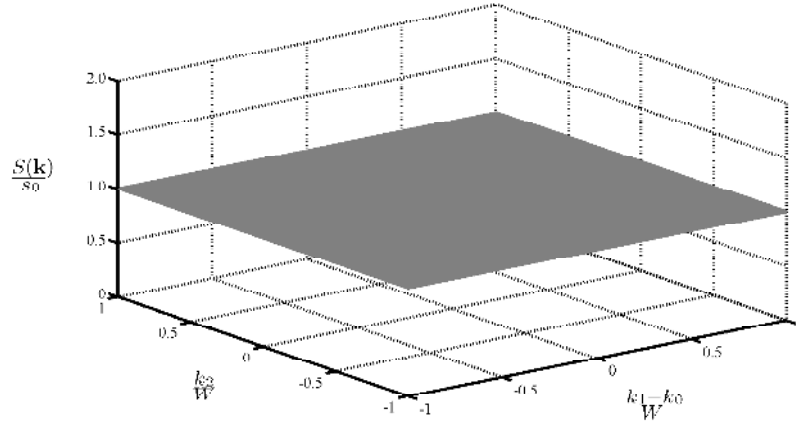


Figure 3.1: Square spectrum.

$$1 = \frac{8k_0^4 s_0}{p} \left[\frac{pW}{2q} \{\operatorname{arctanh}(T_1)\} + W \{\operatorname{arctanh}(T_2)\} - \frac{p\psi}{2q} \{\operatorname{arctan}(T_3)\} - \frac{p^2 - 2q^2}{8q} \{\ln(T_4)\} \right] \quad (3.26)$$

where

$$T_1 = \frac{16qW(4q^4 - 4q^2p^2 + 4p^2\psi^2 + p^4 + 16W^2q^2 - 4p^2W^2)(p^2 - 2q^2)}{T_{11}T_{12} + T_{13}},$$

$$T_{11} = (p^2 - 2q^2)^2 + p^2(-2iW + 2\psi)^2 + 16q^2W^2,$$

$$T_{12} = p^2(2iW + 2\psi)^2 + 16q^2W^2 + (p^2 - 2q^2)^2,$$

$$T_{13} = 64q^2W^2(p^2 - 2q^2)^2,$$

$$T_2 = \frac{8pW(p^2 - 2q^2)(p^4 - 4q^2p^2 + 4p^2\psi^2 - 16q^2W^2 + 4W^2p^2 + 4q^4)}{T_{21}T_{22} + T_{23}},$$

$$T_{21} = (p^2 - 2q^2)^2 - p^2(2iW + 2\psi)^2 - 16q^2W^2,$$

$$T_{22} = (p^2 - 2q^2)^2 - p^2(-2iW + 2\psi)^2 - 16q^2W^2,$$

$$T_{23} = (4ipW + 4p\psi)(p^2 - 2q^2)(-4ipW + 4p\psi)(p^2 - 2q^2),$$

$$T_3 = \frac{128qW^2p^2(p^2 - 2q^2)\psi}{T_{31}T_{32} + T_{33}},$$

$$T_{31} = p^2(2iW + 2\psi)^2 + 16q^2W^2 + (p^2 - 2q^2)^2,$$

$$T_{32} = (p^2 - 2q^2)^2 + p^2(-2iW + 2\psi)^2 + 16q^2W^2,$$

$$T_{33} = -64q^2W^2(p^2 - 2q^2)^2,$$

and

$$T_4 = T_{41}T_{42},$$

$$T_{41} = \frac{(p^2 - 2q^2)^2 + 4\{i(pW - 2qW) + p\psi\}^2}{(p^2 - 2q^2)^2 + 4\{i(pW + 2qW) + p\psi\}^2},$$

$$T_{42} = \frac{(p^2 - 2q^2)^2 + 4\{i(-pW + 2qW) + p\psi\}^2}{(p^2 - 2q^2)^2 + 4\{i(-pW - 2qW) + p\psi\}^2}.$$

Since $\psi = \psi_R + i\psi_I$, where ψ_R and ψ_I are real part and imaginary part of ψ , respectively, and this spectrum is a symmetric spectrum, one can show that the real part of the growth rate, Ω_r , vanishes and therefore the following real part of ψ is obtained

$$\psi_R = -\frac{4\Omega_i}{p} \sqrt{\frac{k_0^3}{g}},$$

where Ω_i is the imaginary part of the growth rate. Furthermore, substituting this result to equation (3.26), defining the small steepness parameter

$$\varepsilon = \sqrt{8s_0}Wk_0$$

and the non-dimensional variables

$$\tilde{\Omega}_i = \frac{\Omega_i}{\varepsilon^2 \sqrt{gk_0}}; \quad \tilde{p} = \frac{p}{\varepsilon k_0}; \quad \tilde{q} = \frac{q}{\varepsilon k_0}; \quad \tilde{W} = \frac{W}{\varepsilon k_0};$$

equation (3.26) becomes

$$1 = \frac{1}{\tilde{p}\tilde{W}^2} \left[\frac{\tilde{p}\tilde{W}}{2\tilde{q}} \{\operatorname{arctanh}(\tilde{T}_1)\} + \tilde{W} \{\operatorname{arctanh}(\tilde{T}_2)\} + \frac{2\tilde{\Omega}_i}{\tilde{q}} \{\operatorname{arctan}(\tilde{T}_3)\} - \frac{\tilde{p}^2 - 2\tilde{q}^2}{8\tilde{q}} \{\ln(\tilde{T}_4)\} \right]$$

and therefore it can be written in dimensionless form as

$$\begin{aligned} & \frac{\tilde{p}\tilde{W}}{2\tilde{q}} \{\operatorname{arctanh}(\tilde{T}_1)\} + \tilde{W} \{\operatorname{arctanh}(\tilde{T}_2)\} + \frac{2\tilde{\Omega}_i}{\tilde{q}} \{\operatorname{arctan}(\tilde{T}_3)\} \\ & - \frac{\tilde{p}^2 - 2\tilde{q}^2}{8\tilde{q}} \{\ln(\tilde{T}_4)\} = \tilde{p}\tilde{W}^2 \end{aligned} \quad (3.27)$$

where

$$\tilde{T}_1 = \frac{16\tilde{q}\tilde{W}(\tilde{p}^4 - 4\tilde{p}^2\tilde{q}^2 + 4\tilde{q}^4 - 4\tilde{W}^2\tilde{p}^2 + 64\tilde{\Omega}_i^2 + 16\tilde{q}^2\tilde{W}^2)(\tilde{p}^2 - 2\tilde{q}^2)}{\tilde{T}_{11} + \tilde{T}_{12}},$$

$$\begin{aligned}
\tilde{T}_{11} &= (512\tilde{Q}^4 - 512\tilde{P}^2\tilde{Q}^2 + 512\tilde{W}^2\tilde{P}^2 + 2048\tilde{Q}^2\tilde{W}^2 + 128\tilde{P}^4 + 4096\tilde{\Omega}_i^2)\tilde{\Omega}_i^2 \\
&\quad - 416\tilde{P}^2\tilde{Q}^4\tilde{W}^2 - 128\tilde{W}^4\tilde{P}^2\tilde{Q}^2, \\
\tilde{T}_{12} &= \tilde{P}^8 + 16\tilde{Q}^8 + 24\tilde{P}^4\tilde{Q}^4 - 8\tilde{P}^6\tilde{Q}^2 - 8\tilde{P}^6\tilde{W}^2 - 32\tilde{P}^2\tilde{Q}^6 + 384\tilde{Q}^6\tilde{W}^2 \\
&\quad + 256\tilde{Q}^4\tilde{W}^4 + 128\tilde{P}^4\tilde{Q}^2\tilde{W}^2 + 16\tilde{W}^4\tilde{P}^4, \\
\tilde{T}_2 &= \frac{8\tilde{P}\tilde{W}(\tilde{P}^2 - 2\tilde{Q}^2)(\tilde{P}^4 - 4\tilde{P}^2\tilde{Q}^2 + 4\tilde{Q}^4 + 4\tilde{P}^2\tilde{W}^2 + 64\tilde{\Omega}_i^2 - 16\tilde{Q}^2\tilde{W}^2)}{\tilde{T}_{21} + \tilde{T}_{22}}, \\
\tilde{T}_{21} &= (512\tilde{P}^2\tilde{W}^2 + 2048\tilde{Q}^2\tilde{W}^2 - 512\tilde{P}^2\tilde{Q}^2 + 4096\tilde{\Omega}_i^2 + 128\tilde{P}^4 + 512\tilde{Q}^4)\tilde{\Omega}_i^2, \\
\tilde{T}_{22} &= \tilde{P}^8 - 128\tilde{P}^4\tilde{Q}^2\tilde{W}^2 + 224\tilde{P}^2\tilde{Q}^4\tilde{W}^2 + 24\tilde{P}^6\tilde{W}^2 - 128\tilde{P}^2\tilde{W}^4\tilde{Q}^2 \\
&\quad + 16\tilde{P}^4\tilde{W}^4 - 128\tilde{Q}^6\tilde{W}^2 + 256\tilde{Q}^4\tilde{W}^4 - 8\tilde{P}^6\tilde{Q}^2 + 24\tilde{P}^4\tilde{Q}^4 \\
&\quad - 32\tilde{P}^2\tilde{Q}^6 + 16\tilde{Q}^8, \\
\tilde{T}_3 &= \frac{-512\tilde{Q}\tilde{W}^2\tilde{P}(\tilde{P}^2 - 2\tilde{Q}^2)\tilde{\Omega}_i}{\tilde{T}_{31} + \tilde{T}_{32}}, \\
\tilde{T}_{31} &= (2048\tilde{Q}^2\tilde{W}^2 + 128\tilde{P}^4 - 512\tilde{P}^2\tilde{Q}^2 + 512\tilde{Q}^4 + 512\tilde{W}^2\tilde{P}^2 + 4096\tilde{\Omega}_i^2)\tilde{\Omega}_i^2 \\
&\quad - 32\tilde{P}^2\tilde{Q}^6 - 128\tilde{Q}^6\tilde{W}^2, \\
\tilde{T}_{32} &= \tilde{P}^8 + 16\tilde{Q}^8 - 8\tilde{P}^6\tilde{Q}^2 + 256\tilde{Q}^4\tilde{W}^4 + 96\tilde{P}^2\tilde{Q}^4\tilde{W}^2 - 128\tilde{W}^4\tilde{P}^2\tilde{Q}^2 \\
&\quad - 8\tilde{P}^6\tilde{W}^2 + 16\tilde{W}^4\tilde{P}^4 + 24\tilde{P}^4\tilde{Q}^4, \\
\tilde{T}_4 &= \frac{\tilde{T}_{41} + \tilde{T}_{42} + \tilde{T}_{43}}{\tilde{T}_{44} + \tilde{T}_{45} + \tilde{T}_{46}}, \\
\tilde{T}_{41} &= \tilde{P}^8 - 128\tilde{P}^3\tilde{W}^4\tilde{Q} - 512\tilde{P}\tilde{W}^4\tilde{Q}^3 + 32\tilde{P}^5\tilde{W}^2\tilde{Q} - 128\tilde{P}^3\tilde{W}^2\tilde{Q}^3 \\
&\quad + 128\tilde{P}\tilde{W}^2\tilde{Q}^5 - 2048\tilde{\Omega}_i^2\tilde{P}\tilde{W}^2\tilde{Q}, \\
\tilde{T}_{42} &= 512\tilde{Q}^4\tilde{\Omega}_i^2 + 128\tilde{P}^4\tilde{\Omega}_i^2 + 16\tilde{Q}^8 + 16\tilde{W}^4\tilde{P}^4 + 96\tilde{P}^2\tilde{Q}^4\tilde{W}^2 \\
&\quad + 2048\tilde{\Omega}_i^2\tilde{Q}^2\tilde{W}^2 + 512\tilde{W}^2\tilde{P}^2\tilde{\Omega}_i^2, \\
\tilde{T}_{43} &= 384\tilde{W}^4\tilde{P}^2\tilde{Q}^2 + 256\tilde{Q}^4\tilde{W}^4 - 32\tilde{P}^2\tilde{Q}^6 - 512\tilde{P}^2\tilde{Q}^2\tilde{\Omega}_i^2 - 8\tilde{P}^6\tilde{W}^2 \\
&\quad - 128\tilde{Q}^6\tilde{W}^2 - 8\tilde{P}^6\tilde{Q}^2 + 24\tilde{P}^4\tilde{Q}^4 + 4096\tilde{\Omega}_i^4, \\
\tilde{T}_{44} &= \tilde{P}^8 + 128\tilde{P}^3\tilde{W}^4\tilde{Q} + 512\tilde{P}\tilde{W}^4\tilde{Q}^3 - 32\tilde{P}^5\tilde{W}^2\tilde{Q} + 128\tilde{P}^3\tilde{W}^2\tilde{Q}^3 \\
&\quad - 128\tilde{P}\tilde{W}^2\tilde{Q}^5 + 2048\tilde{\Omega}_i^2\tilde{P}\tilde{W}^2\tilde{Q}, \\
\tilde{T}_{45} &= 512\tilde{Q}^4\tilde{\Omega}_i^2 + 128\tilde{P}^4\tilde{\Omega}_i^2 + 16\tilde{Q}^8 + 16\tilde{W}^4\tilde{P}^4 + 96\tilde{P}^2\tilde{Q}^4\tilde{W}^2 \\
&\quad + 2048\tilde{\Omega}_i^2\tilde{Q}^2\tilde{W}^2 + 512\tilde{W}^2\tilde{P}^2\tilde{\Omega}_i^2,
\end{aligned}$$

and

$$\begin{aligned}\tilde{T}_{46} = & 384\tilde{W}^4\tilde{P}^2\tilde{Q}^2 + 256\tilde{Q}^4\tilde{W}^4 - 32\tilde{P}^2\tilde{Q}^6 - 512\tilde{P}^2\tilde{Q}^2\tilde{\Omega}_i^2 - 8\tilde{P}^6\tilde{W}^2 \\ & - 128\tilde{Q}^6\tilde{W}^2 - 8\tilde{P}^6\tilde{Q}^2 + 24\tilde{P}^4\tilde{Q}^4 + 4096\tilde{\Omega}_i^4.\end{aligned}$$

Since the growth rate of the disturbance is in the implicit form, a graphical method will be used to determine the maximum growth rate and point of maximum growth rate of the disturbance by plotting a stability diagram based on the equation (3.27). However, plotting the stability diagram based on the equation directly in the $\tilde{P} - \tilde{Q}$ plane, one may get an overlap figure which can lead to very messy results. This is because the power of polynomial \tilde{P} and \tilde{Q} are of the order of five which may have five different roots. Therefore, in order to avoid this situation, the term $\arctan(\tilde{T}_3)$ in the equation (3.27) has to be expanded in the following form where the power of polynomial \tilde{P} and \tilde{Q} are of the order of two:

$$\begin{aligned}\arctan\left(-\frac{512\tilde{Q}\tilde{W}^2\tilde{P}(\tilde{P}^2 - 2\tilde{Q}^2)\tilde{\Omega}_i}{\tilde{T}_{31} + \tilde{T}_{32}}\right) \\ = \arctan\left(\frac{-2\tilde{Q}^2 + \tilde{P}^2 + 2\tilde{P}\tilde{W} + 4\tilde{Q}\tilde{W}}{8\tilde{\Omega}_i}\right) \\ - \arctan\left(\frac{2\tilde{Q}^2 - \tilde{P}^2 + 2\tilde{P}\tilde{W} + 4\tilde{Q}\tilde{W}}{8\tilde{\Omega}_i}\right) \\ + \arctan\left(\frac{2\tilde{Q}^2 - \tilde{P}^2 - 2\tilde{P}\tilde{W} + 4\tilde{Q}\tilde{W}}{8\tilde{\Omega}_i}\right) \\ - \arctan\left(\frac{-2\tilde{Q}^2 + \tilde{P}^2 - 2\tilde{P}\tilde{W} + 4\tilde{Q}\tilde{W}}{8\tilde{\Omega}_i}\right)\end{aligned}$$

where $\tilde{T}_{31} + \tilde{T}_{32}$ as given before. As seen from the expanded term $\arctan(\tilde{T}_3)$, the power of \tilde{P} and \tilde{Q} are quadratic which indicates that they have maximum number of real roots are two.

Moreover, due to the singularity at $\tilde{W} = 0$, equation (3.27) cannot be used to determine the condition for instability and its actual growth rate for this case. Therefore, in order to deal with this problem of vanishing spectral width which corresponds to the deterministic problem for which the well-known Benjamin-Feir instability is discovered (Benjamin and Feir, 1967), the spectrum is defined as follows:

$$S(\mathbf{k}) = 4W^2s_0\delta(k_1 - k_0)\delta(k_2)$$

where $\delta(k_1 - k_0)$ and $\delta(k_2)$ are delta functions in directions parallel and perpendicular to the carrier wave respectively.

Substituting this spectrum into equation (3.17) gives,

$$1 = 4k_0^4(p^2 - 2q^2) \left\{ \iint_{-\infty}^{\infty} \frac{4W^2 s_0 \delta(k_1 - k_0) \delta(k_2) dk_1 dk_2}{[i(p(k_1 - k_0) - 2qk_2) + p\psi]^2 + \left[\frac{p^2 - 2q^2}{2}\right]^2} \right\}.$$

Solving the double integral in the curly brackets by using the properties of the delta function, which are as follows

$$\int_{-\infty}^{\infty} \delta(k_2) f(k_2) dk_2 = f(0)$$

$$\int_{-\infty}^{\infty} \delta(k_1 - k_0) f(k_1) dk_1 = f(k_0),$$

yields

$$1 = 16k_0^4(p^2 - 2q^2)W^2 s_0 \left\{ \frac{1}{(p\psi)^2 + \left(\frac{p^2 - 2q^2}{2}\right)^2} \right\}.$$

Moreover, substituting $\psi_R = -\frac{4\Omega_i}{p} \sqrt{\frac{k_0^3}{g}}$ into this equation leads to the following relation between Ω_i and (p, q)

$$1 = 16k_0^4(p^2 - 2q^2)W^2 s_0 \left\{ \frac{1}{\left(4\Omega_i \sqrt{\frac{k_0^3}{g}}\right)^2 + \left(\frac{p^2 - 2q^2}{2}\right)^2} \right\}. \quad (3.28)$$

Furthermore, switching to non-dimensional form, equation (3.28) can be rewritten as

$$\tilde{\Omega}_i^2 = \frac{(\tilde{p}^2 - 2\tilde{q}^2)(8 - (\tilde{p}^2 - 2\tilde{q}^2))}{64}. \quad (3.29)$$

The dimensionless maximum growth rate is achieved when the dimensionless wavenumbers of the disturbance satisfy the relation

$$\tilde{P}^2 - 2\tilde{Q}^2 = 4.$$

Thus, values of the dimensionless growth rate $\tilde{\Omega}_i$ at $\tilde{Q} = 0$ reach a maximum $\tilde{\Omega}_i = 0.5$ at $\tilde{P} = 2$, and have $\tilde{\Omega}_i = 0$ at $\tilde{P} = 2\sqrt{2}$ and $\tilde{P} = 0$. Figure 3.2 gives five solid isolines for square spectrum, for which $\tilde{\Omega}_i = 0, 0.05, 0.2, 0.35$ and $\tilde{\Omega}_i = 0.45$ with different values of spectral width, i.e. $\tilde{W} = 0.0, 1.0$ and 2.0 . The isoline in which $\tilde{\Omega}_i = 0$ represents the marginal stability line of the spectrum. Moreover, Figure 3.2a was plotted based on the equation (3.29) while Figure 3.2b and Figure 3.2c were plotted based on the equation (3.27). As can be seen from Figure 3.2, the area of instability shrinks or even disappears and the maximum growth rate decreases by increasing spectral width. Similarly, the point of maximum growth rate with respect to \tilde{P} moves away from the point of maximum of the vanishing spectral width, i.e. $\tilde{P} = 2$ when the value of the spectral width is increased. This point of maximum growth rate is normally called the most unstable mode of the disturbance. For example, the dimensionless spectral width $\tilde{W} = 1$ reaches the point of maximum growth rate at $\tilde{P} = 2.223$. Similarly, the dimensionless spectral width $\tilde{W} = 2.0$ reaches the point maximum growth rate at $\tilde{P} = 3.985$. In addition, the dimensionless spectral widths $\tilde{W} = 1.0$ and $\tilde{W} = 2.0$ reach the dimensionless maximum growth rate $\tilde{\Omega}_i = 0.4036$ and $\tilde{\Omega}_i = 0.0735$, respectively. The square in each figure indicates the footprint of a quarter of the initial spectrum as in equation (3.25). The relationship between the dimensionless spectral width and the dimensionless growth rate are shown in Figure 3.3 for the case where the dimensionless wavenumber of the disturbance perpendicular to the carrier wave is zero, i.e. $\tilde{Q} = 0$. The number on the line represents the value of the dimensionless spectral width with 0.25 increments. It shows that by increasing the spectral width, the maximum growth rate decreases. In addition, it is clearly shown that when the dimensionless spectral width is greater than 2.75, the dimensionless maximum growth rate becomes zero which means that the wave field is stable. Particularly, when the dimensionless spectral width for this spectrum is greater than 2.75, then the spectrum is stable to inhomogeneous disturbance. This result appears to be similar to the criterion for Benjamin-Feir instability (Benjamin and Feir, 1967).

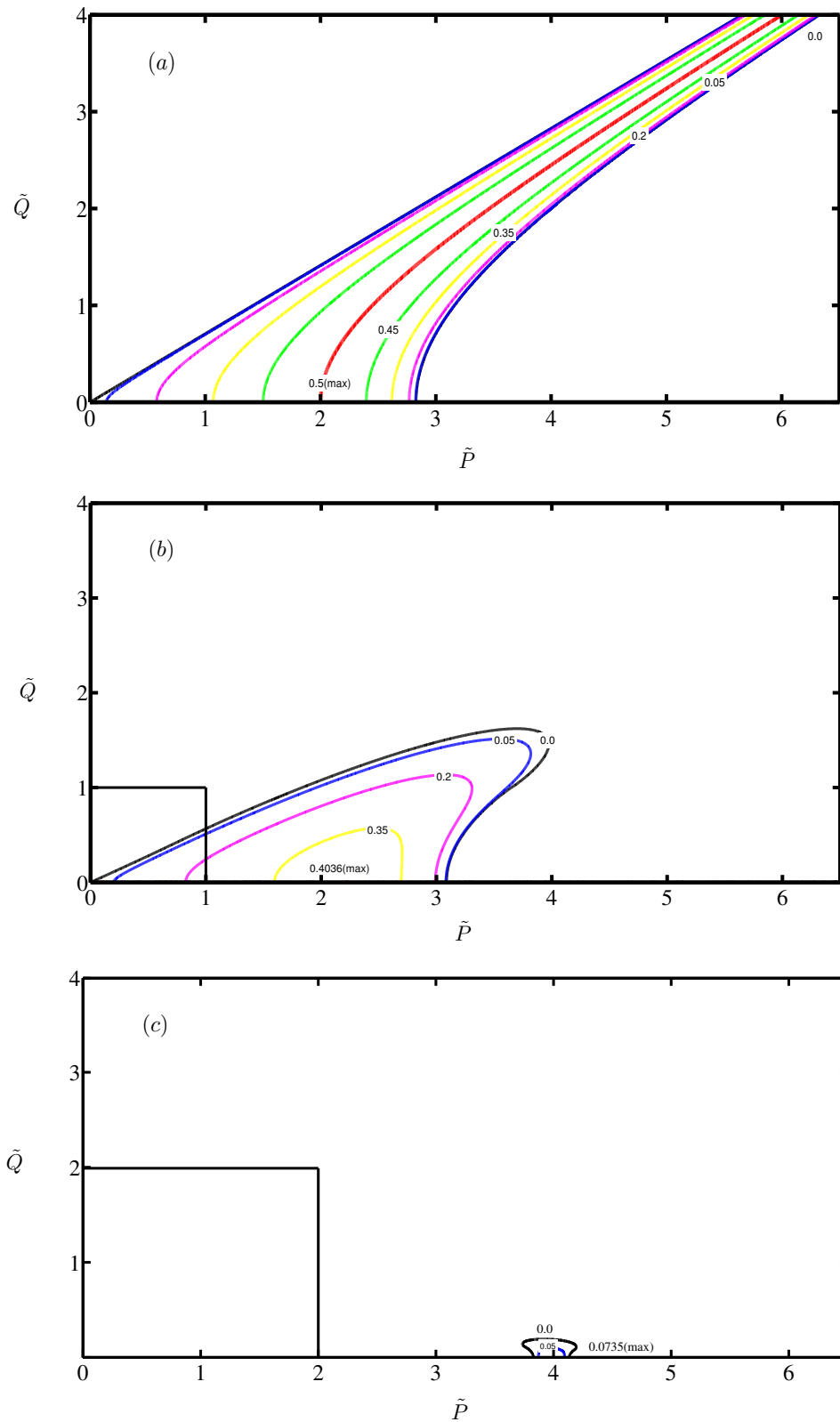


Figure 3.2: Stability diagrams for square spectra, giving the dimensionless growth rate, $\tilde{\Omega}_i$, of the inhomogeneous disturbances. The number on the line represents the dimensionless growth rate and the square in each figure indicates the footprint of a quarter of the initial spectrum while \tilde{P} and \tilde{Q} are the dimensionless wavenumbers of the disturbances and \tilde{W} is the dimensionless spectral width. (a) $\tilde{W} = 0$, (b) $\tilde{W} = 1$, (c) $\tilde{W} = 2$.

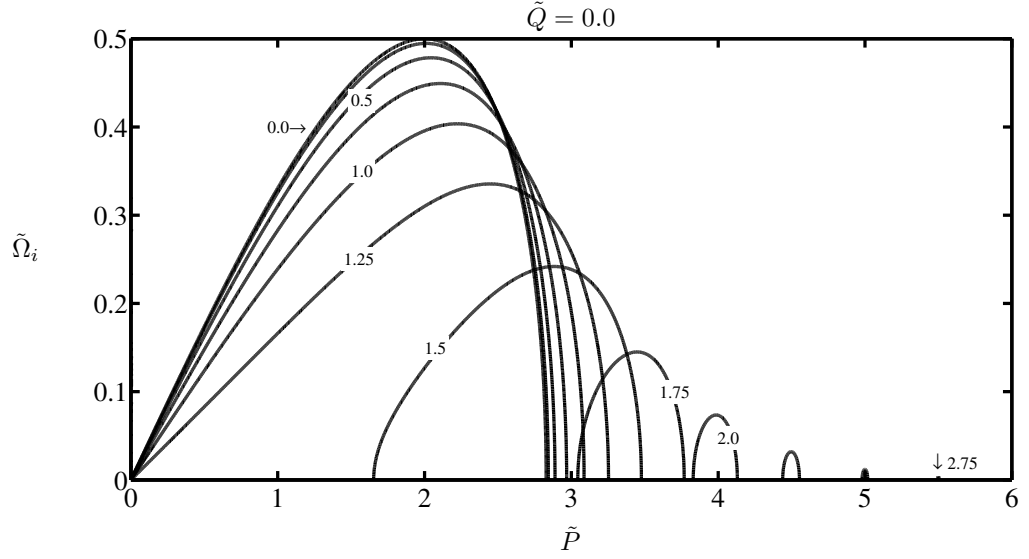


Figure 3.3: Relation between the dimensionless growth rate, $\tilde{\Omega}_i$, and the dimensionless spectral width, \tilde{W} , in which the wavenumber of the disturbance which is perpendicular to the carrier wave, \tilde{Q} , is zero. The horizontal line represents the dimensionless wavenumber of the disturbance which is parallel to the carrier wave, the vertical line reveals the dimensionless growth rate and the number on the line represents the dimensionless spectral width with 0.25 increments.

Since, for this case, the spectral width in directions parallel and perpendicular to the carrier wave were chosen to be the same as shown in Figure 3.2, it is difficult to determine which spectral width has a significant effect on shrinking the region of instability. Therefore, in the next section, we will consider a more general case, i.e. a rectangular spectrum.

3.4.2 Rectangular spectrum and its growth rate

In this section, a more general case of the square spectrum where the spectral width in directions parallel and perpendicular to carrier wave are chosen to be different is considered. Hence, this spectrum is called a rectangular spectrum. The instability and the actual growth rate including the maximum growth rate and the most unstable mode of the disturbance for this spectrum will be determined. In particular, using this spectrum, one can see the influence of the different spectral widths on the instability and the maximum growth rate. Extending the definition of the square spectrum, a rectangular spectrum is defined as

$$S(\mathbf{k}) = s_0; \quad k_0 - W_1 < k_1 < k_0 + W_1; \quad -W_2 < k_2 < W_2 \quad (3.30)$$

where W_1 and W_2 are spectral width in directions parallel and perpendicular to the carrier wave, respectively and other variables are the same as defined in the previous section.

Furthermore, following a similar procedure to that used to determine the growth rate of the unstable disturbance of a square spectrum, using the small steepness, ε , given by relation

$$4W_1W_2s_0 = \left(\frac{\varepsilon}{k_0}\right)^2 / 2,$$

and defining non-dimensional variables

$$\tilde{\Omega}_i = \frac{\Omega_i}{(\varepsilon^2 \sqrt{gk_0})}; \quad \tilde{P} = \frac{p}{\varepsilon k_0}; \quad \tilde{Q} = \frac{q}{\varepsilon k_0}; \quad \tilde{W}_1 = \frac{W_1}{\varepsilon k_0}; \quad \tilde{W}_2 = \frac{W_2}{\varepsilon k_0};$$

one ends up with the following dimensionless equation to determine the actual growth rate of a rectangular spectrum which is, again, can only be given in the implicit form, that is

$$\begin{aligned} 8\tilde{W}_1\tilde{W}_2\tilde{P}\tilde{Q} &= 2\tilde{Q}^2(A_1 + A_2) + 2\tilde{P}\tilde{W}_1(B_1 + B_2) + 16\tilde{\Omega}_i C_1 \\ &+ 4\tilde{Q}\tilde{W}_2(D_1 + D_2) + \tilde{P}^2(E_1 + E_2), \end{aligned} \quad (3.31)$$

where

$$\begin{aligned} A_1 &= \ln \left((-16\tilde{P}\tilde{Q}\tilde{W}_1\tilde{W}_2 + 64\tilde{\Omega}_i^2 - 4\tilde{P}^2\tilde{Q}^2 + 4\tilde{P}^2\tilde{W}_1^2 + \tilde{P}^4 + 4\tilde{Q}^4 + 4\tilde{P}^3\tilde{W}_1 \right. \\ &\quad \left. - 8\tilde{P}^2\tilde{Q}\tilde{W}_2 - 8\tilde{P}\tilde{Q}^2\tilde{W}_1 + 16\tilde{Q}^3\tilde{W}_2 + 16\tilde{Q}^2\tilde{W}_2^2) \right. \\ &\quad \left. / (16\tilde{P}\tilde{Q}\tilde{W}_1\tilde{W}_2 + 64\tilde{\Omega}_i^2 - 4\tilde{P}^2\tilde{Q}^2 + 4\tilde{P}^2\tilde{W}_1^2 + \tilde{P}^4 + 4\tilde{Q}^4 - 4\tilde{P}^3\tilde{W}_1 \right. \\ &\quad \left. - 8\tilde{P}^2\tilde{Q}\tilde{W}_2 + 8\tilde{P}\tilde{Q}^2\tilde{W}_1 + 16\tilde{Q}^3\tilde{W}_2 + 16\tilde{Q}^2\tilde{W}_2^2) \right), \end{aligned}$$

$$\begin{aligned} A_2 &= \ln \left((-16\tilde{P}\tilde{Q}\tilde{W}_1\tilde{W}_2 + 64\tilde{\Omega}_i^2 - 4\tilde{P}^2\tilde{Q}^2 + 4\tilde{P}^2\tilde{W}_1^2 + \tilde{P}^4 + 4\tilde{Q}^4 - 4\tilde{P}^3\tilde{W}_1 \right. \\ &\quad \left. + 8\tilde{P}^2\tilde{Q}\tilde{W}_2 + 8\tilde{P}\tilde{Q}^2\tilde{W}_1 - 16\tilde{Q}^3\tilde{W}_2 + 16\tilde{Q}^2\tilde{W}_2^2) \right. \\ &\quad \left. / (16\tilde{P}\tilde{Q}\tilde{W}_1\tilde{W}_2 + 64\tilde{\Omega}_i^2 - 4\tilde{P}^2\tilde{Q}^2 + 4\tilde{P}^2\tilde{W}_1^2 + \tilde{P}^4 + 4\tilde{Q}^4 + 4\tilde{P}^3\tilde{W}_1 \right. \\ &\quad \left. + 8\tilde{P}^2\tilde{Q}\tilde{W}_2 - 8\tilde{P}\tilde{Q}^2\tilde{W}_1 - 16\tilde{Q}^3\tilde{W}_2 + 16\tilde{Q}^2\tilde{W}_2^2) \right), \end{aligned}$$

$$\begin{aligned}
E_2 = \ln & \left((16\tilde{P}\tilde{Q}\tilde{W}_1\tilde{W}_2 + 64\tilde{\Omega}_i^2 - 4\tilde{P}^2\tilde{Q}^2 + 4\tilde{P}^2\tilde{W}_1^2 + \tilde{P}^4 + 4\tilde{Q}^4 + 4\tilde{P}^3\tilde{W}_1 + 8\tilde{P}^2\tilde{Q}\tilde{W}_2 \right. \\
& - 8\tilde{P}\tilde{Q}^2\tilde{W}_1 - 16\tilde{Q}^3\tilde{W}_2 + 16\tilde{Q}^2\tilde{W}_2^2) \\
& / (-16\tilde{P}\tilde{Q}\tilde{W}_1\tilde{W}_2 + 64\tilde{\Omega}_i^2 - 4\tilde{P}^2\tilde{Q}^2 + 4\tilde{P}^2\tilde{W}_1^2 + \tilde{P}^4 + 4\tilde{Q}^4 + 4\tilde{P}^3\tilde{W}_1 \\
& \left. - 8\tilde{P}^2\tilde{Q}\tilde{W}_2 - 8\tilde{P}\tilde{Q}^2\tilde{W}_1 + 16\tilde{Q}^3\tilde{W}_2 + 16\tilde{Q}^2\tilde{W}_2^2) \right).
\end{aligned}$$

In order to confirm the special case of this problem which is for one-dimensional case, it is not possible to substitute $\tilde{W}_2 = 0$ into equation (3.31) directly due to the singularity reason. Therefore, the spectral width and the wavenumber of the disturbance in direction perpendicular to the carrier wave are set to be equal squared root of the steepness, i.e. $\tilde{W}_2 = \tilde{Q} = \sqrt{\varepsilon}$, and are substituted into equation (3.31). The result is developed into Taylor series in ε while keeping the leading order terms of order ε yields

$$\tilde{W}_1\tilde{P} = \ln(64\tilde{\Omega}_i^2 + 4\tilde{P}^2\tilde{W}_1^2 + \tilde{P}^4 + 4\tilde{P}^3\tilde{W}_1) - \ln(64\tilde{\Omega}_i^2 + 4\tilde{P}^2\tilde{W}_1^2 + \tilde{P}^4 - 4\tilde{P}^3\tilde{W}_1).$$

Simplifying this equation gives

$$\tilde{\Omega}_i = \frac{\tilde{P}}{4} \sqrt{\tilde{P}\tilde{W}_1 \coth\left(\frac{\tilde{W}_1\tilde{P}}{2}\right) - \frac{\tilde{P}^2}{4} - \tilde{W}_1^2}. \quad (3.32)$$

This result is the same as the result obtained by Stiassnie et al. (2008, eq. 2.27). Based on the equation (3.32) we obtain Figure 3.4 and Figure 3.5 which show the relation between dimensionless maximum growth rate, $\tilde{\Omega}_i^{(max)}$, and the dimensionless spectral width which is parallel to the carrier wave, \tilde{W}_1 , (Figure 3.4) and the values of the most unstable mode $\tilde{P}^{(max)}$ for which the maximum growth rate is obtained (Figure 3.5).

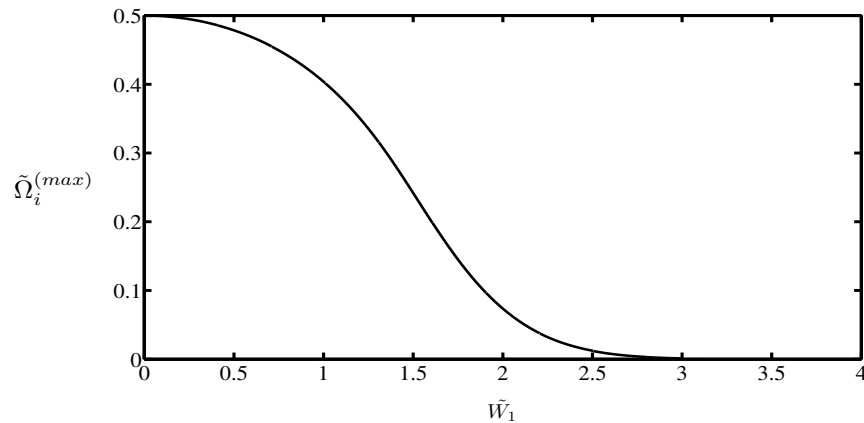


Figure 3.4: Maximum values of the dimensionless growth rate, $\tilde{\Omega}_i^{(max)}$, as a function of dimensionless spectral width in direction parallel to the carrier wave, \tilde{W}_1 , for one-dimensional spectrum.

As seen from Figure 3.4, the dimensionless growth rate of the disturbance reaches the highest maximum value when the dimensionless spectral width in direction parallel to the carrier wave is zero, $\tilde{W}_1 = 0$. Moreover, increasing the spectral width will decrease the maximum growth rate and finally the growth rate becomes zero when the dimensionless spectral width is greater than 2.75, i.e. $\tilde{W}_1 > 2.75$. It is also important to show the values of most unstable mode $\tilde{P}^{(max)}$ in which the maximum growth rate obtained. This information is concluded in Figure 3.5 where the maximum growth rate reaches the highest value at $\tilde{P}^{(max)} = 2$ and the value of $\tilde{P}^{(max)}$ will increase as the maximum growth rate decreases.

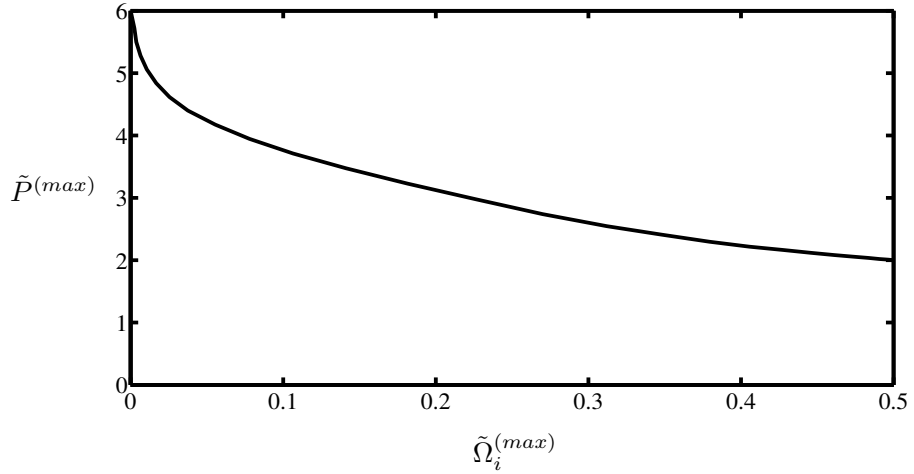


Figure 3.5: Values of the dimensionless most unstable mode, $\tilde{P}^{(max)}$, for which the dimensionless maximum growth rate, $\tilde{\Omega}_i^{(max)}$, is obtained for one-dimensional spectrum.

Another way to confirm our results as shown in the equation (3.31) is to reproduce the one-dimensional case as in the paper of Stiassnie et al. (2008) which is shown in their Figure 2a. To this end, the spectral width which is perpendicular to the carrier wave is set to approach zero, i.e. $\tilde{W}_2 \approx 0$ and the results are shown in Figure 3.6 which is exactly the same as the results obtained by Stiassnie et al. (2008). Note that the red line represents the marginal instability line, where the dimensionless growth rate is equal to zero and the number on each line represents the dimensionless growth rate of the instability with increment 0.05. The horizontal line reveals the dimensionless wavenumber of the disturbance and the vertical line indicates the dimensionless spectral width which is parallel to the carrier wave.

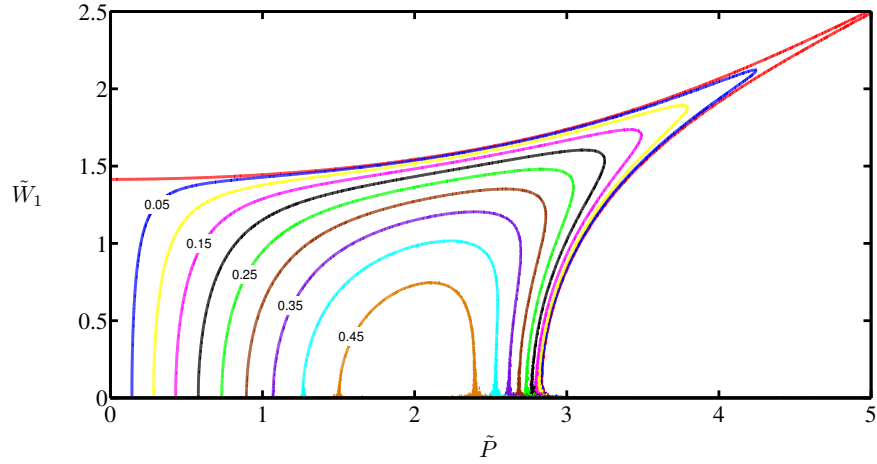


Figure 3.6: Isolines for the special case of a rectangular spectrum where horizontal line reveals the dimensionless wavenumber of the disturbance and vertical line indicates the dimensionless spectral width which is parallel to the carrier wave. The value on each line represents the dimensionless growth rate.

Now, for this rectangular spectrum, two types of spectra have been chosen, namely elongated spectrum and stretched spectrum. The relation between the spectral widths in direction parallel and perpendicular to the carrier wave is given by

$$\tilde{W}_2 = \tilde{W}_1/5 \text{ and } \tilde{W}_2 = 5\tilde{W}_1$$

respectively. The footprints of these spectra are shown in Figure 3.7. However, in order to present the instability area, only a quarter of the footprint of the spectrum will be shown.

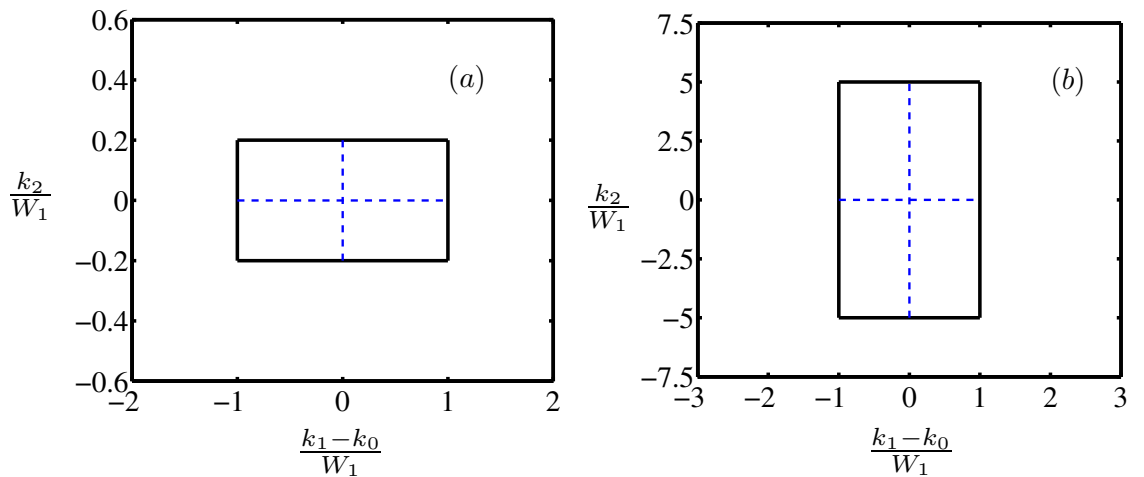


Figure 3.7: The footprints of the elongated spectrum (a) and the stretched spectrum (b).

In order to compare this result to the square spectrum, we keep the original area of spectrum to be the same. For elongated spectra, the relation between dimensionless

growth rate, $\tilde{\Omega}_i$, and the geometric average of the dimensionless spectral widths where the wavenumber of the disturbance in direction perpendicular to the carrier wave, \tilde{Q} , is zero is shown in Figure 3.8. Note that the geometric averages is calculated by taking the square root of the product of \tilde{W}_1 and \tilde{W}_2 . As seen from the figure, the dimensionless growth rate is zero, which means the wave field is stable, when the geometric average of \tilde{W}_1 and \tilde{W}_2 is greater than 1.25. Unlike elongated spectra, the growth rate of the stretched spectrum decreases slowly by increasing the spectral width as shown in Figure 3.9. Moreover, the point of maximum growth rate with respect to \tilde{P} axis increases slowly starting from $\tilde{P}^{(max)} = 2$ which is the most unstable mode for the vanishing spectral width. For example, when choosing $\tilde{W}_1 = 5/\sqrt{20}$ and $\tilde{W}_2 = 1/\sqrt{20}$ which gives the geometric average of \tilde{W}_1 and \tilde{W}_2 , equal 0.5, i.e. $\sqrt{\tilde{W}_1\tilde{W}_2} = 0.5$, this spectrum reaches the point of maximum at $\tilde{P}^{(max)} = 2.014$. Similarly, the spectrum whose spectral width $\tilde{W}_1 = 4/\sqrt{20}$ and $\tilde{W}_2 = 20/\sqrt{20}$, where $\sqrt{\tilde{W}_1\tilde{W}_2} = 2$, reaches the maximum at $\tilde{P}^{(max)} = 2.172$. Furthermore, when the geometric average of \tilde{W}_1 and \tilde{W}_2 is greater than 6.5, the maximum growth rate of this spectrum becomes zero which means the spectrum is stable to inhomogeneous disturbance. Note that for the special case where $\tilde{W}_1 = \tilde{W}_2 = 0$, the result of a rectangular spectrum is the same as the results obtained from the square spectrum as shown in Figure 3.2a. Moreover, this special case is also similar to the result of Martin and Yuen (1980a). Furthermore, the stability diagrams for $\tilde{W}_1 > 0$ and $\tilde{W}_2 > 0$ are shown in Figure 3.10 and Figure 3.11. As can be seen from both figures, all spectra have a similar behaviour to the square spectra where an increase value of the spectral width, the area of instability shrinks. In terms of stability, the elongated spectra reach the stable condition quickly while the stretched spectra reach the stable condition slowly. In addition, as shown in Figure 3.10 the maximum growth rate decreases rapidly when the spectral width increases. When choosing $\tilde{W}_1 = 20/\sqrt{20}$ and $\tilde{W}_2 = 4/\sqrt{20}$, for example, the area of instability disappeared. The dimensionless maximum growth rate of the disturbance of Figure 3.10a and Figure 3.10b are $\tilde{\Omega}_i = 0.3743$ and $\tilde{\Omega}_i = 0.033$, respectively while Figure 3.10c shows that the spectrum is stable to inhomogeneous disturbance. These maximum growth rates occur at the dimensionless wavenumber of the disturbance, which is parallel to the carrier wave, at $\tilde{P}^{(max)} = 2.329$ and $\tilde{P}^{(max)} = 4.458$, respectively.

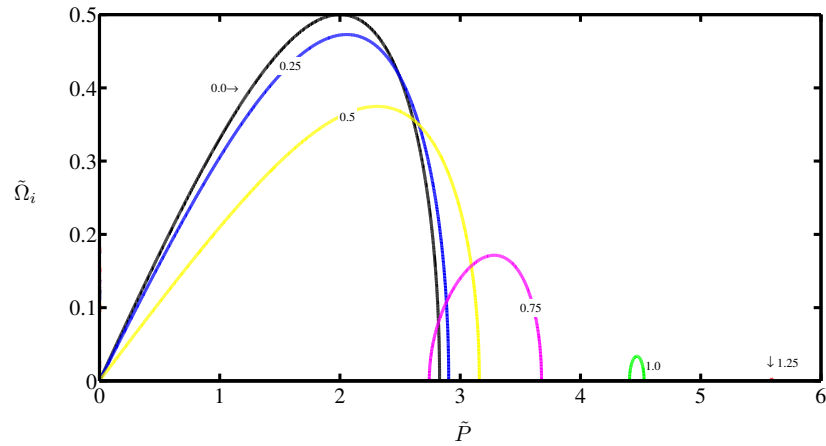


Figure 3.8: Relation between dimensionless growth rate, $\tilde{\Omega}_i$, and the dimensionless wavenumber of the disturbance which is parallel to the carrier-wave. The number on the line represents the dimensionless geometric average of the spectral widths, $\sqrt{\tilde{W}_1 \tilde{W}_2}$, for elongated spectra in which the wavenumber of the disturbance which is perpendicular to the carrier wave, \tilde{Q} , is zero.

Moreover, similar to the instability diagrams of the square spectrum, the rectangular shape in each figure on both Figure 3.10 and Figure 3.11 represents a footprint of a quarter of the initial spectrum. Also, from all three cases of spectra, we can conclude that by increasing spectral width, the area of instability shrinks and the maximum growth rate decreases. In addition, when the spectral width reaches a certain value, then the spectrum becomes stable to inhomogeneous disturbances.

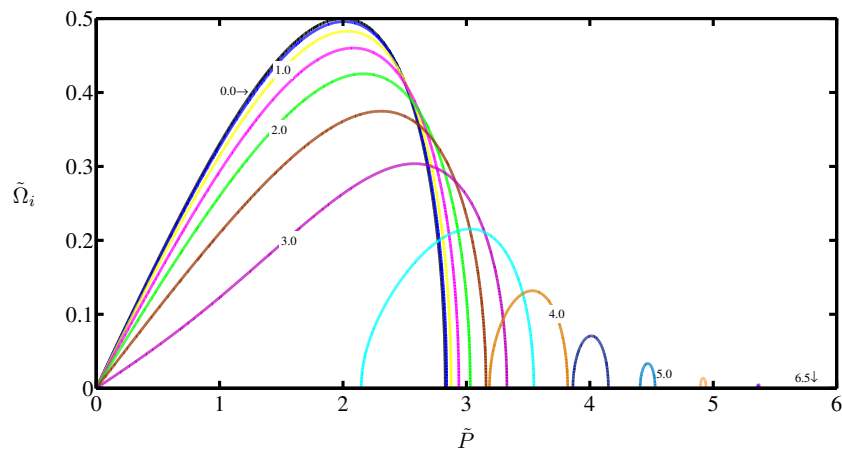


Figure 3.9: Relation between dimensionless growth rate, $\tilde{\Omega}_i$, and the dimensionless wavenumber of the disturbance which is parallel to the carrier wave. The number on the line represents the dimensionless geometric average of the spectral widths, $\sqrt{\tilde{W}_1 \tilde{W}_2}$, for stretched spectra in which the wavenumber of the disturbance which is perpendicular to the carrier wave, \tilde{Q} , is zero.

In all of the previous cases that have been simulated, both spectral widths, in directions parallel and perpendicular to the carrier wave were changed simultaneously for the rectangular spectrum. In Figure 3.12, however, we keep the spectral width in the direction parallel to the carrier wave constant and we change the spectral width which is perpendicular to the carrier wave. Interestingly, all three cases give the same maximum growth rate and the point of maximum growth rate. This indicates that the maximum growth rate occurs at $\tilde{Q} = 0$. Moreover, the point of maximum growth rate and the maximum growth rate depend only on the spectral width in direction parallel to the carrier wave. In other words, this means the maximum growth rate is independent of the spectral width in direction perpendicular to the carrier wave as shown in Figure 3.12 and is a function of \tilde{W}_1 only. In addition, all of the cases in Figure 3.12 reach the maximum growth rate at $\tilde{\Omega}_i^{(max)} = 0.4036$. This conclusion is interesting as well as challenging. This is because based on some experiments in the wave flumes and numerical simulations, the instability does depend on the spectral width in direction perpendicular to carry wave albeit with different spectra (see: e.g. Onorato et al. (2009a,b), Toffoli (2010) and Babanin et al. (2011)). However, since the equation for the growth rate of the disturbance is rather cumbersome, it is difficult to show the independence of the spectral width in direction perpendicular to the carrier wave and will be left to the next section.

3.4.3 Lorentz spectrum and its growth rate

Another spectrum for which will be going to study its instability and determine its growth rate, including the maximum growth rate and the most unstable mode, is called a Lorentz spectrum. The similarity of this spectrum with the previous cases is that all of them are symmetric spectra. Therefore, with the Alber equation, one can show that the imaginary part of the dispersion relation will vanish. The advantage of this property is that one can only solve the real part of the dispersion relation to determine its growth rate and the area of instability. This is particularly useful when the dispersion relation cannot be solved analytically.

A two-dimensional Lorentz spectrum is defined as (see: Crawford et al. (1980))

$$S(\mathbf{k}) = \frac{W_1 W_2 a_0^2}{2\pi^2 [(k_1 - k_0)^2 + W_1^2] [k_2^2 + W_2^2]} \quad (3.33)$$

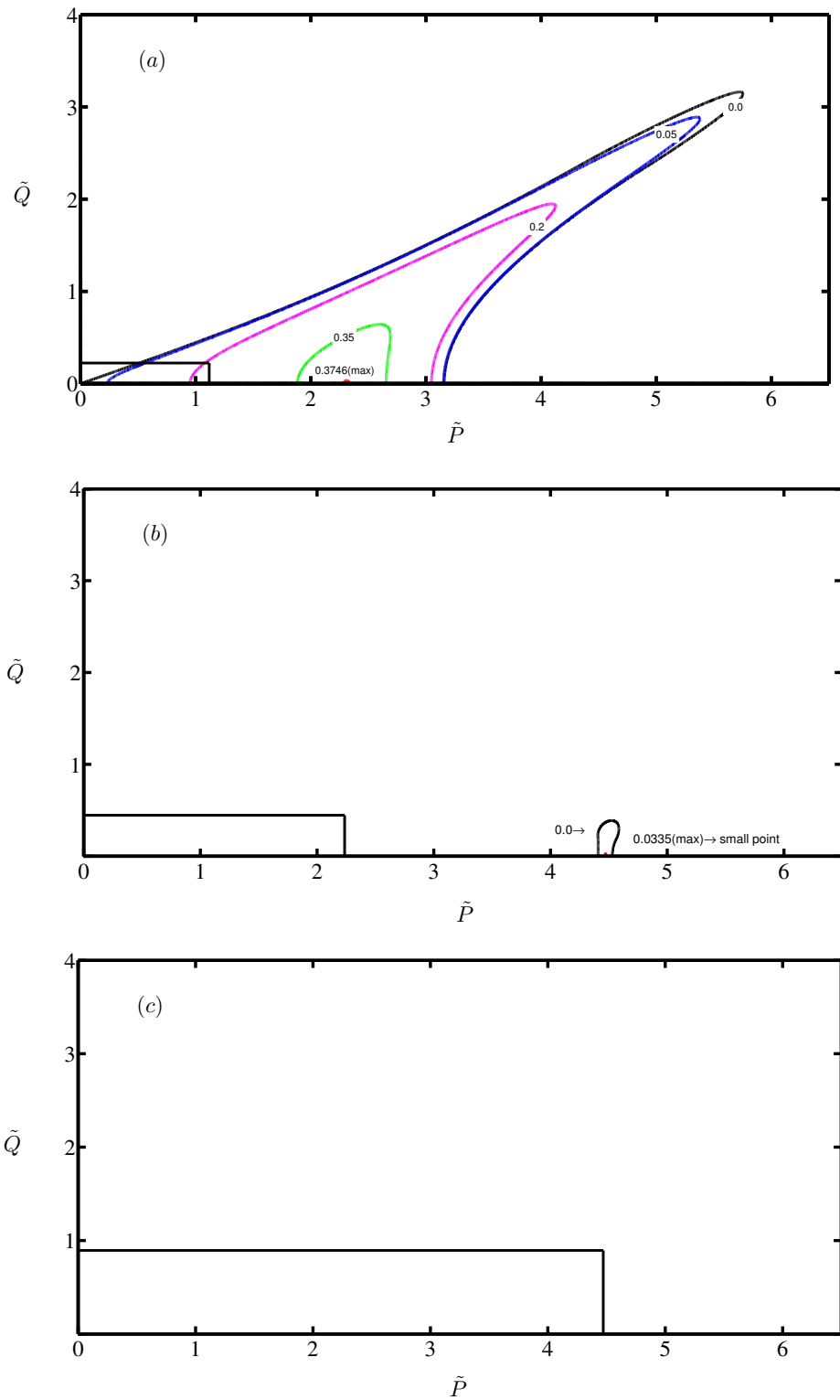


Figure 3.10: Stability diagrams for elongated spectra, giving the dimensionless growth rate, \tilde{Q}_1 , of the inhomogeneous disturbances. The number on the line represents the dimensionless growth rate and the rectangular in each figure indicates the footprint of a quarter of the initial spectrum while \tilde{P} and \tilde{Q} are the dimensionless wavenumbers of the disturbances and \tilde{W}_1 and \tilde{W}_2 are the dimensionless spectral widths. (a) $\tilde{W}_1 = 5/\sqrt{20}$, $\tilde{W}_2 = 1/\sqrt{20}$; (b) $\tilde{W}_1 = 10/\sqrt{20}$, $\tilde{W}_2 = 2/\sqrt{20}$; (c) $\tilde{W}_1 = 20/\sqrt{20}$, $\tilde{W}_2 = 4/\sqrt{20}$.

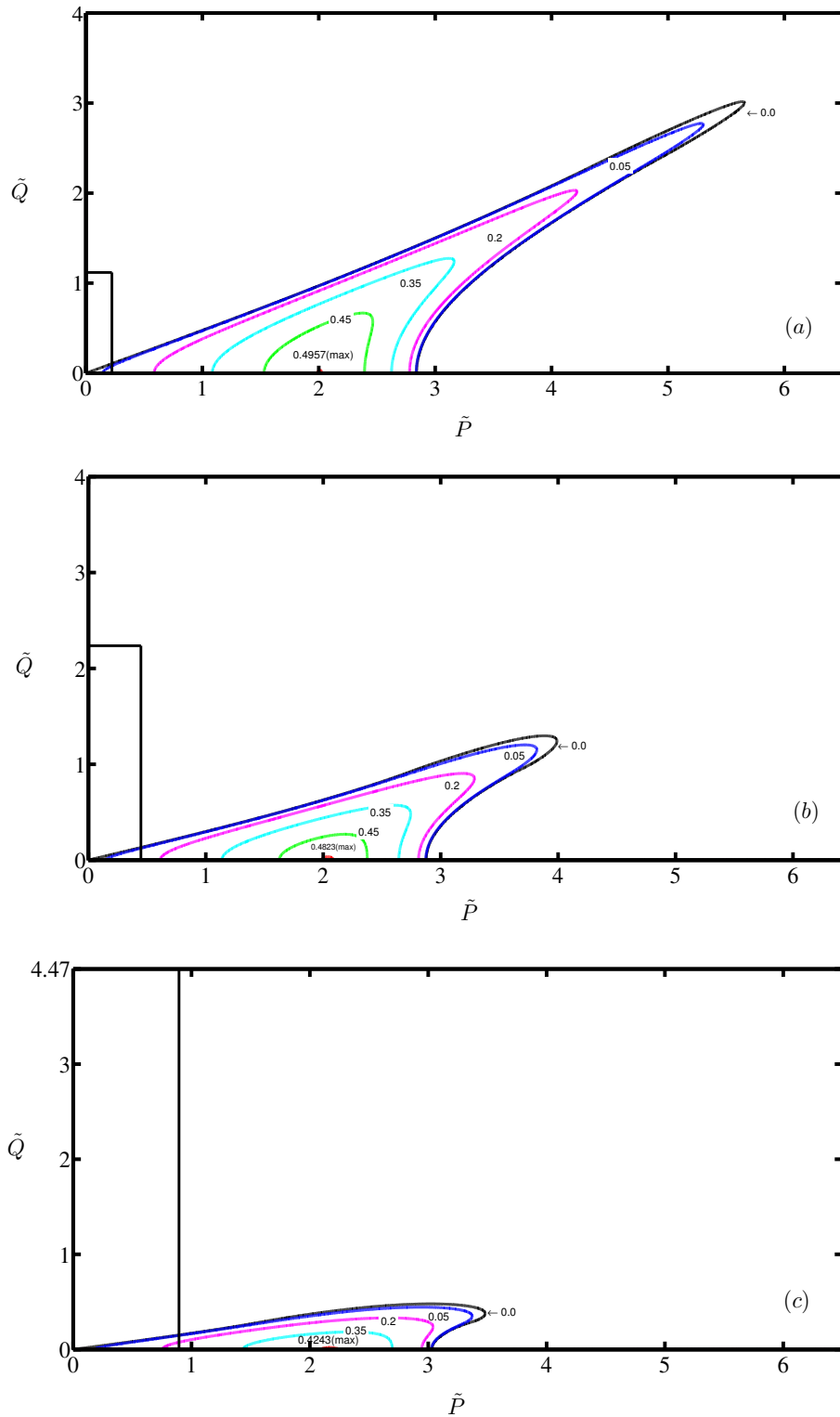


Figure 3.11: Stability diagrams for stretched spectra, giving the dimensionless growth rate, $\tilde{\Omega}_i$, of the inhomogeneous disturbances. The number on the line represents the dimensionless growth rate and the rectangular in each figure indicates the footprint of a quarter of the initial spectrum while \tilde{P} and \tilde{Q} are the dimensionless wavenumbers of the disturbances and \tilde{W}_1 and \tilde{W}_2 are the dimensionless spectral widths. (a) $\tilde{W}_1 = 1/\sqrt{20}$, $\tilde{W}_2 = 5/\sqrt{20}$; (b) $\tilde{W}_1 = 2/\sqrt{20}$, $\tilde{W}_2 = 10/\sqrt{20}$; (c) $\tilde{W}_1 = 4/\sqrt{20}$, $\tilde{W}_2 = 20/\sqrt{20}$.

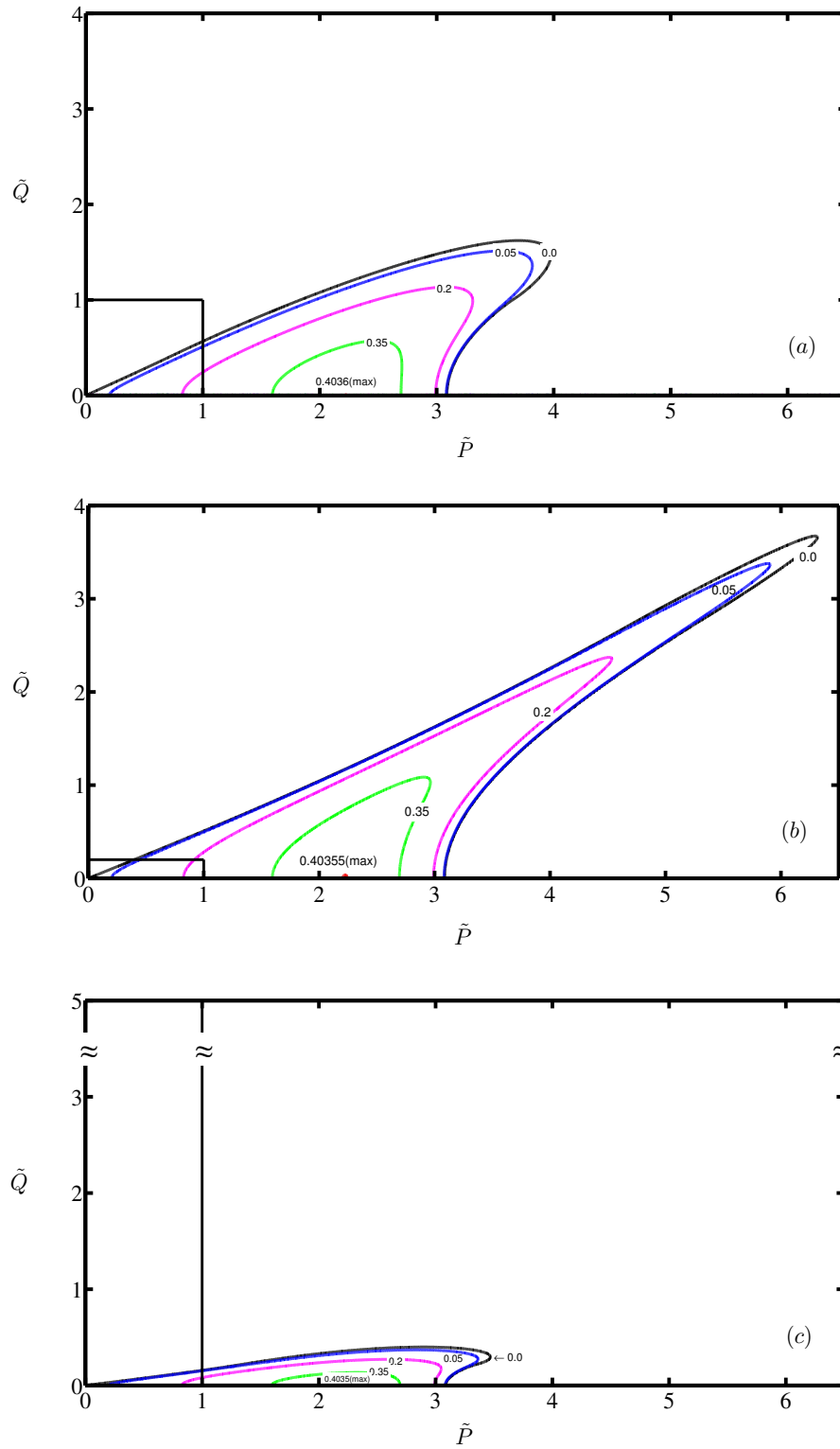


Figure 3.12: Stability diagrams for rectangular spectra, giving the dimensionless growth rate, \tilde{Q}_i , of the inhomogeneous disturbances. The number on the line represents the dimensionless growth rate and the rectangular/square in each figure indicates the footprint of a quarter of the initial spectrum while \tilde{P} and \tilde{Q} are the dimensionless wavenumbers of the disturbances and \tilde{W}_1 and \tilde{W}_2 are the dimensionless spectral widths. (a) $\tilde{W}_1 = 1, \tilde{W}_2 = 1$; (b) $\tilde{W}_1 = 1, \tilde{W}_2 = 1/5$; (c) $\tilde{W}_1 = 1, \tilde{W}_2 = 5$.

where a_0 is wave amplitude and $a_0^2/2$ is the energy density; W_1 and W_2 are measures of the spectral width in directions parallel and perpendicular to the carrier wave, respectively and other variables are the same as mentioned in the previous section. This spectrum is plotted in the following Figure 3.13 where part (a) shows the spectrum in three-dimensional space while part (b) shows its isolines. It is clearly seen from the figure that the spectrum is symmetric.

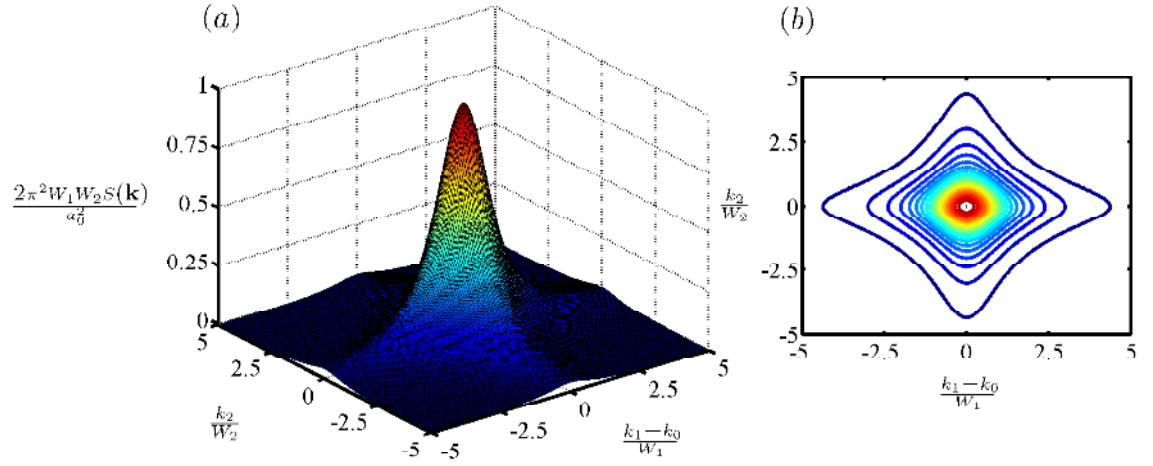


Figure 3.13: A two-dimensional Lorentz spectrum (a) and its isolines (b).

In order to determine the actual growth rate including the maximum growth rate and the most unstable mode, the spectrum in equation (3.33) is substituted to the dispersion relation of the disturbance in equation (3.17). However, for simplicity, a Lorentz spectrum as in (3.33) is substituted into (3.15) instead of substituting it into (3.17), where $\psi = \frac{4i\Omega}{p} \sqrt{\frac{k_0^3}{g}}$, gives

$$1 = \frac{4k_0^4 W_1 W_2 a_0^2}{2\pi^2} \left\{ \iint_{-\infty}^{\infty} \left[\frac{1}{p(k_1 - k_0) - 2qk_2 + \frac{p^2}{2} - q^2 + \frac{4\Omega k_0^2}{\omega_0}} \right. \right. \\ \left. \left. - \frac{1}{p(k_1 - k_0) - 2qk_2 - \frac{p^2}{2} + q^2 + \frac{4\Omega k_0^2}{\omega_0}} \right] \left[\frac{dk_1 dk_2}{\{(k_1 - k_0)^2 + W_1^2\} \{k_2^2 + W_2^2\}} \right] \right\}. \quad (3.34)$$

In order to solve this integral, the method used by Crawford et al. (1980) which is actually the application of the residue theorem that can be found in any complex

analysis books will be followed. Firstly, we integrate the terms in curly brackets of (3.34) with respect to k_1 that is

$$\int_{-\infty}^{\infty} \left[\frac{1}{p(k_1 - k_0) - 2qk_2 + \frac{p^2}{2} - q^2 + \frac{4\Omega k_0^2}{\omega_0}} - \frac{1}{p(k_1 - k_0) - 2qk_2 - \frac{p^2}{2} + q^2 + \frac{4\Omega k_0^2}{\omega_0}} \right] \left[\frac{1}{\{(k_1 - k_0)^2 + W_1^2\}\{k_2^2 + W_2^2\}} \right] dk_1. \quad (3.35)$$

This integral has one pole in the upper half plane at $k_1 = k_0 + iW_1$ and three poles in the lower half plane, namely at $k_1 = k_0 - iW_1$, $k_1 = \frac{1}{p} \left(2qk_2 + \frac{p^2}{2} - q^2 - \frac{4\Omega k_0^2}{\omega_0} \right) + k_0$ and $k_1 = \frac{1}{p} \left(2qk_2 - \frac{p^2}{2} + q^2 - \frac{4\Omega k_0^2}{\omega_0} \right) + k_0$. Integrating over the standard contour in the upper half plane, equation (3.35) can be deduced to be [see Zuevsky (2008)]

$$\frac{2\pi i}{2iW_1[k_2^2 + W_2^2]} \left\{ \left[\frac{1}{ipW_1 - 2qk_2 + \frac{p^2}{2} - q^2 + \frac{4\Omega k_0^2}{\omega_0}} - \frac{1}{ipW_1 - 2qk_2 - \frac{p^2}{2} + q^2 + \frac{4\Omega k_0^2}{\omega_0}} \right] \right\}.$$

Substituting this result into (3.34) leads to

$$1 = \frac{2k_0^4 W_2 a_0^2}{\pi} \left\{ \int_{-\infty}^{\infty} \left[\frac{1}{ipW_1 - 2qk_2 + \frac{p^2}{2} - q^2 + \frac{4\Omega k_0^2}{\omega_0}} - \frac{1}{ipW_1 - 2qk_2 - \frac{p^2}{2} + q^2 + \frac{4\Omega k_0^2}{\omega_0}} \right] \frac{dk_2}{[k_2^2 + W_2^2]} \right\}. \quad (3.36)$$

Following a procedure similar to the integration of (3.35) over k_1 , the integral equation in (3.36) has one pole in the lower half plane, i.e. at $k_2 = -iW_2$ and three poles in the upper half plane, namely at $k_2 = iW_2$, $k_2 = \frac{1}{2q} \left(ipW_1 + \frac{p^2}{2} - q^2 + \frac{4\Omega k_0^2}{\omega_0} \right)$ and

$k_2 = \frac{1}{2q} \left(ipW_1 - \frac{p^2}{2} + q^2 + \frac{4\Omega k_0^2}{\omega_0} \right)$. Integrating over the standard contour in the lower half plane, equation (3.36) can be written as

$$1 = 2k_0^4 a_0^2 \left[\frac{1}{ipW_1 - 2iqW_2 + \frac{p^2}{2} - q^2 + \frac{4\Omega k_0^2}{\omega_0}} - \frac{1}{ipW_1 - 2iqW_2 - \frac{p^2}{2} + q^2 + \frac{4\Omega k_0^2}{\omega_0}} \right].$$

Simplifying this equation yields,

$$2k_0^4 a_0^2 (p^2 - 2q^2) = \left(\frac{p^2}{2} - q^2 \right)^2 - \left(ipW_1 + 2iqW_2 + \frac{4\Omega k_0^2}{\omega_0} \right)^2.$$

Rearranging this result and making $4\Omega k_0^2/\omega_0$ the subject leads to

$$\frac{4\Omega k_0^2}{\omega_0} = \pm \sqrt{\left(\frac{p^2}{2} - q^2 \right)^2 - 4k_0^4 a_0^2 \left(\frac{p^2}{2} - q^2 \right) - ipW_1 - 2iqW_2}.$$

In order to get the imaginary parts of Ω to be positive, the values under the square root of the above equation must be negative and then it can be rewritten as

$$\frac{4\Omega k_0^2}{\omega_0} = \pm i \sqrt{\left(\frac{p^2}{2} - q^2 \right) \left(4k_0^4 a_0^2 - \left(\frac{p^2}{2} - q^2 \right) \right) - ipW_1 - 2iqW_2}.$$

It is clearly that the sign of the square root must be positive. Hence,

$$\frac{4\Omega k_0^2}{\omega_0} = i \sqrt{\left(\frac{p^2}{2} - q^2 \right) \left(4k_0^4 a_0^2 - \left(\frac{p^2}{2} - q^2 \right) \right) - ipW_1 - 2iqW_2}.$$

Thus, the real part is zero, that is $\Omega_R = 0$ and the imaginary part is given by:

$$\Omega_i = \frac{\omega_0}{4k_0^2} \sqrt{\left(\frac{p^2}{2} - q^2 \right) \left(4k_0^4 a_0^2 - \left(\frac{p^2}{2} - q^2 \right) \right) - pW_1 - 2qW_2}.$$

Therefore, the growth rate of unstable disturbances, where $\omega_0 = \sqrt{gk_0}$ can be rewritten as

$$\Omega_i = \frac{\sqrt{gk_0}}{2} \left\{ \sqrt{\left[\frac{1}{4} \left(\frac{p}{k_0} \right)^2 - \frac{1}{2} \left(\frac{q}{k_0} \right)^2 \right] \left[2a_0^2 k_0^2 - \frac{1}{4} \left(\frac{p}{k_0} \right)^2 + \frac{1}{2} \left(\frac{q}{k_0} \right)^2 \right]} - \frac{W_1 p}{2k_0^2} - \frac{W_2 q}{k_0^2} \right\}. \quad (3.37)$$

Defining non-dimensional variables

$$\tilde{\Omega}_i = \Omega_i / (\varepsilon^2 \sqrt{gk_0}); \quad \tilde{P} = p / \varepsilon k_0; \quad \tilde{Q} = q / \varepsilon k_0; \quad \tilde{W}_1 = W_1 / \varepsilon k_0; \quad \tilde{W}_2 = W_2 / \varepsilon k_0;$$

and the steepness

$$\varepsilon = a_0 k_0,$$

the dimensionless growth-rate of unstable disturbances is given by

$$\tilde{\Omega}_i = \frac{1}{2} \left\{ \sqrt{\left[\frac{\tilde{P}^2}{4} - \frac{\tilde{Q}^2}{2} \right] \left[2 - \frac{\tilde{P}^2}{4} + \frac{\tilde{Q}^2}{2} \right]} - \frac{\tilde{W}_1 \tilde{P}^2}{2} - \tilde{W}_2 \tilde{Q}^2 \right\}. \quad (3.38)$$

The one-dimensional counterpart of (3.33) is

$$S_1(k) = \frac{W_1 a_0^2}{2\pi [(k_1 - k_0)^2 + W_1^2]} \quad (3.39)$$

and the growth rate of unstable disturbances is given by

$$\Omega_i^{(1)} = \frac{p}{4} \sqrt{\frac{g}{k_0}} \left\{ \sqrt{2a_0^2 k_0^2 - \frac{1}{4} \left(\frac{p}{k_0} \right)^2} - \frac{W_1}{k_0} \right\}. \quad (3.40)$$

Turning to the dimensionless form, equation (3.40) can be rewritten as

$$\tilde{\Omega}_i^{(1)} = \frac{\tilde{P}}{4} \left\{ \sqrt{\left[2 - \frac{\tilde{P}^2}{4} \right]} - \tilde{W}_1 \right\}. \quad (3.41)$$

From equation (3.41) and the condition of instability $\tilde{\Omega}_i^{(1)} > 0$, one can see that equation (3.39) is stable for any \tilde{P} if

$$\tilde{W}_1 > \sqrt{2}. \quad (3.42)$$

In order to determine the point of maximum growth rate, one can take the first order derivative with respect to \tilde{P} of equation (3.41), and then solve it for \tilde{P} yields,

$$\tilde{P}_1^{(max)} = \sqrt{4 - \frac{\tilde{W}_1^2}{2} - \frac{\tilde{W}_1}{2} \sqrt{16 + \tilde{W}_1^2}} \quad (3.43)$$

and the maximum growth rate itself is

$$\tilde{\Omega}_i^{(1)(max)} = \frac{\tilde{P}_1^{(max)}}{4} \left\{ \sqrt{\left[2 - \frac{(\tilde{P}_1^{(max)})^2}{4} \right]} - \tilde{W}_1 \right\}.$$

For the two-dimensional Lorentz spectrum in (3.33), taking the first partial derivative of equation (3.38) with respect to \tilde{P} and \tilde{Q} respectively leads to the following relation,

$$\tilde{P}\tilde{W}_2 + \tilde{Q}\tilde{W}_1 = 0.$$

Since $\tilde{P}, \tilde{Q}, \tilde{W}_1$ and \tilde{W}_2 are all taken to be positive, there is no maximum within the domain of instability. Thus, the largest value of $\tilde{\Omega}_i$ is located on the boundaries from which the only possible choice is $\tilde{Q} = 0$, since $\tilde{\Omega}_i = 0$ otherwise. Substituting $\tilde{Q} = 0$ into equation (3.38) yields equation (3.41) and the accompanying condition (3.42) which is independent of \tilde{W}_2 .

Therefore, the most unstable mode is

$$\left(\tilde{P}_2^{(max)}, \tilde{Q}_2^{(max)} \right) = \left(\tilde{P}_1^{(max)}, 0 \right)$$

and its maximum growth rate is

$$\tilde{\Omega}_i^{(max)} = \tilde{\Omega}_i^{(1)(max)}.$$

As an illustration, Figure 3.14 shows three different spectra where spectral width in the direction parallel to the carrier wave is kept constant, e.g. $\tilde{W}_1 = 0.25$, while the spectral width which is perpendicular to the carrier wave is varied, namely, $\tilde{W}_2 = 0.05, 0.25$, and 1.25. As can be seen from the figure, the maximum growth rate of the three different spectra is $\tilde{\Omega}_i^{(max)} = 0.37915$ and the point of maximum growth rate is at $\tilde{P}^{(max)} = 1.8622$ which are all the same. Moreover, based on Figure 3.14, one can see that the role of spectral width which is perpendicular to the carrier wave is only to shrink the area of the instability. Moreover, the independence of the spectral width in direction perpendicular to the carrier wave is proven here analytically. Therefore, based on these three spectra, namely, a square spectrum, a rectangular spectrum and a Lorentz spectrum, it can be concluded that the maximum growth rate and the most unstable mode are independent of spectral width which is perpendicular to the carrier wave. However, the reconciliation with the experiments is still unanswered yet and it will be

considered in the next section by using a more realistic ocean wave JONSWAP (JOint North Sea Wave Project) spectrum (Hasselmann, 1973).

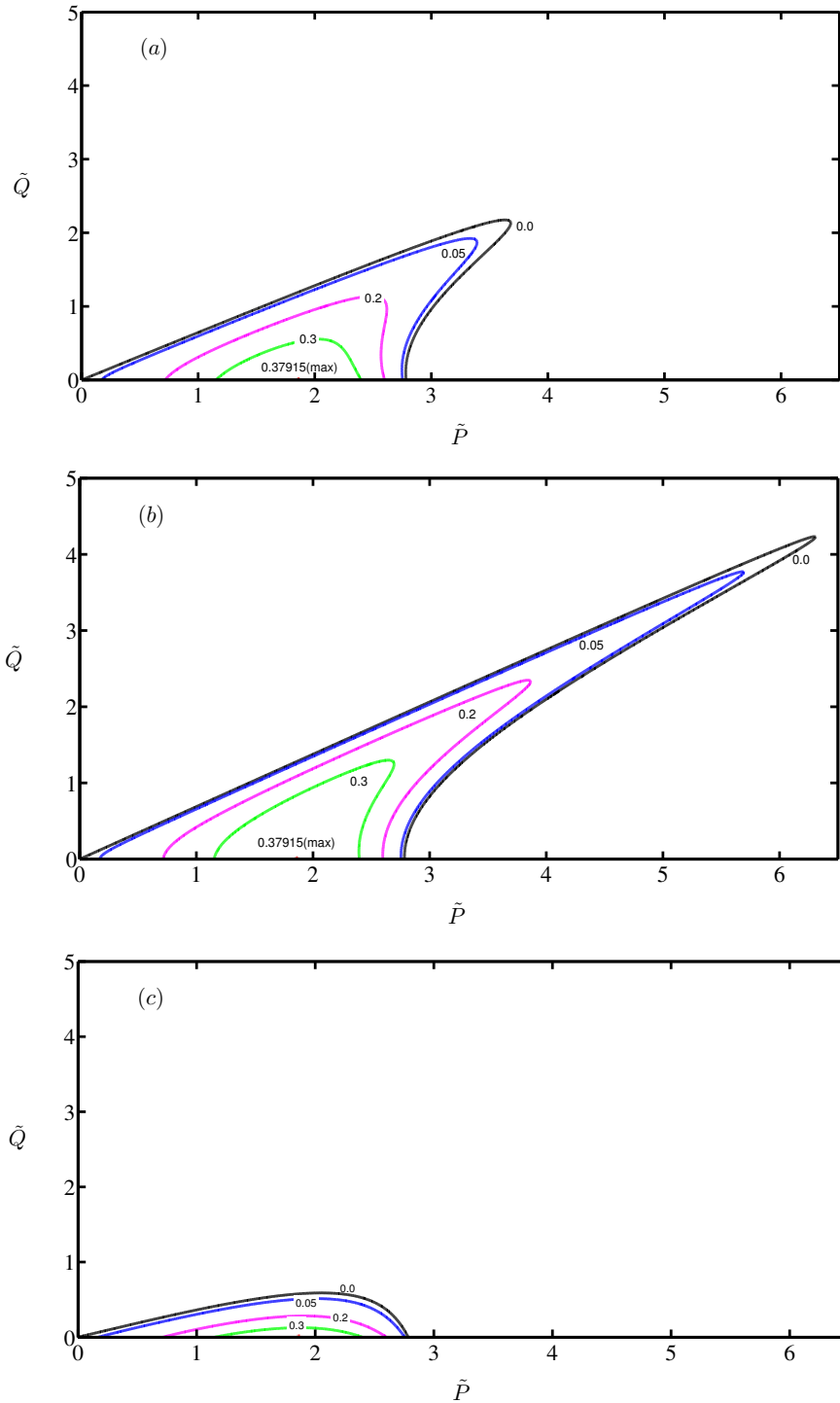


Figure 3.14: Stability diagrams for Lorentz spectra, giving the dimensionless growth rate, $\tilde{\Omega}_i$, of the inhomogeneous disturbances. The number on the line represents the dimensionless growth rate while \tilde{P} and \tilde{Q} are the dimensionless wavenumbers of the disturbances and \tilde{W}_1 and \tilde{W}_2 are the dimensionless spectral widths. (a) $\tilde{W}_1 = 0.25, \tilde{W}_2 = 0.25$; (b) $\tilde{W}_1 = 0.25, \tilde{W}_2 = 0.05$; (c) $\tilde{W}_1 = 0.25, \tilde{W}_2 = 1.25$.

3.4.4 JONSWAP spectrum and its growth rate

All of the spectra that have been studied so far are not the realistic ocean wave spectra. As a result, it is difficult to compare the conclusion from the previous sections to the experimental results which used a more realistic ocean wave spectrum. Therefore, in this section, instability of a more realistic ocean spectrum will be studied. This type of parametric spectra were first introduced by Pierson-Moskowitz (1964) with assumption that if the wind blew steadily for a long time over a large area, the waves would come into equilibrium with the wind. This was the concept of a fully developed sea. However, Hasselmann et al. (1973) found that the wave spectrum is hardly ever fully developed. It continues to develop through non-linear wave-wave interactions even for very long times and distances (Stewart, 2008). This conclusion was originally made after analysing data collected during the Joint North Sea Wave Observation Project which produced a parameterization now known as JONSWAP spectrum.

In order to study conditions of the instability including the actual maximum growth rate and the point of maximum growth rate of the instability, there are three different cases to be considered. Firstly, a similar method used by Janssen (1985), Onorato et al. (2003) and Fedele (2004) will be followed where a JONSWAP spectrum will be only expanded around its peak. The result of this approximation falls to the Lorentzian spectrum which is a symmetric spectrum and then it will be called a Lorentzian spectrum. The advantage of using this approximation enables us to solve equation (3.17) analytically. Secondly, the instability condition based on the unidirectional JONSWAP spectrum will be determined. However, since using this type of spectrum equation (3.17) cannot be integrated analytically it will be solved numerically. A general method will be designed to deal with this problem including its verification. Finally, the instability based on a JONSWAP spectrum with directional distribution will be studied. Solving this case numerically is very high computational cost for the dispersion relation of the disturbance as given in equation (3.17). To overcome this issue, it is assumed that the maximum growth rate occurs at $q = 0$ which is the wavenumber of the disturbance perpendicular to carrier wave. This assumption will reduce the required computational resources significantly for the numerical simulations.

3.4.4.1 Lorentzian spectrum

In this section, a unidirectional JONSWAP spectrum (Hasselmann et al., 1973) as a function of the wavenumber will be written as

$$F(k) = \frac{\alpha}{2k^3} e^{-\left(\frac{3k_0^2}{2k^2}\right)} \gamma e^{-\left[\frac{1}{2\sigma^2 k_0}(\sqrt{k}-\sqrt{k_0})^2\right]} \quad (3.44)$$

where γ is a peak-enhancement factor, σ is a peak-width parameter, α is the energy scale or Philips parameter and k_0 is the peak wavenumber. Note that this spectrum is slightly different from the original JONSWAP spectrum. The different is the term $\exp\left(\frac{-3k_0^2}{2k^2}\right)$ where in the original JONSWAP spectrum this term is $\exp\left(\frac{-5k_0^2}{4k^2}\right)$. The comparison of these two spectra is shown in Figure 3.15 where black line represents the original JONSWAP spectrum while the red line represents the JONSWAP spectrum as shown in equation (3.44). Both cases are for $\alpha = 0.016$, $\gamma = 10$, $k_0 = 1$ and $\sigma = 0.08$.

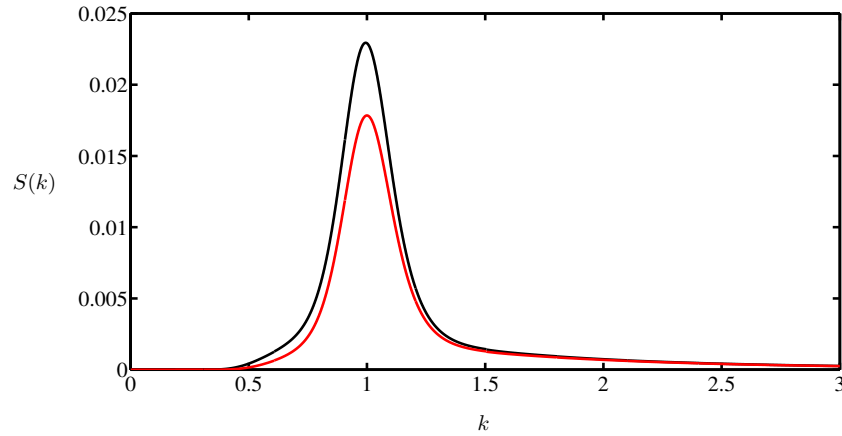


Figure 3.15: Comparison between the original JONSWAP spectrum (black line) and the JONSWAP spectrum (red line) as given in equation (3.44).

The reason to choose this kind of spectrum is because it enables us to approximate the spectrum around its peak to obtain the symmetric spectrum. Then, previously method applied for Lorentz spectrum which is also a symmetric spectrum can be employed here. Following Janssen (1985) and Onorato et al. (2003), the spectrum $F(k)$, which is presented in equation (3.44), is expanded around its peak by second order Taylor expansion and it leads to,

$$F(k) = \frac{\alpha e^{-\frac{3}{2}\gamma}}{2k_0^3} - \left(\frac{3\alpha e^{-\frac{3}{2}\gamma}}{2k_0^5} + \frac{\alpha e^{-\frac{3}{2}\gamma} \ln \gamma}{16k_0^5 \sigma^2} \right) (k - k_0)^2.$$

After simplification, this equation can be rewritten as

$$F(k) = \frac{\alpha e^{-\frac{3}{2}\gamma}}{2k_0^3} \left\{ 1 - \left(\frac{24\sigma^2 + \ln \gamma}{8k_0^2 \sigma^2} \right) (k - k_0)^2 \right\}.$$

The terms in the curly brackets of the right hand side of above equation can be approximated as follows

$$1 - \left(\frac{24\sigma^2 + \ln \gamma}{8k_0^2 \sigma^2} \right) (k - k_0)^2 \approx \frac{1}{1 + \left(\frac{24\sigma^2 + \ln \gamma}{8k_0^2 \sigma^2} \right) (k - k_0)^2}.$$

Hence, the unidirectional JONSWAP spectrum can be rewritten as

$$F(k) = \frac{\alpha e^{-\frac{3}{2}\gamma}}{2k_0^3} \left\{ \frac{\frac{8k_0^2 \sigma^2}{24\sigma^2 + \ln \gamma}}{\frac{8k_0^2 \sigma^2}{24\sigma^2 + \ln \gamma} + (k - k_0)^2} \right\}. \quad (3.45)$$

Let $a = \frac{8k_0^2 \sigma^2}{24\sigma^2 + \ln \gamma}$ and $b = \frac{\alpha e^{-\frac{3}{2}\gamma}}{2k_0^3}$, then equation (3.45) can be simplified as

$$F(k) = \frac{a b}{a + (k - k_0)^2}. \quad (3.46)$$

Thus, this spectrum becomes a Lorentzian spectrum which is a symmetric spectrum and is similar to one obtained by Onorato et al. (2003). The comparison of this spectrum with the JONSWAP spectrum as presented in equation (3.44) is shown in Figure 3.16 by taking $\alpha = 0.016$, $\gamma = 10$, $k_0 = 1$ and $\sigma = 0.08$. The blue line represents the Lorentzian spectrum and the red line represents the JONSWAP spectrum.

Moreover, one-dimensional case of the equation (3.17) falls to the equation (2.17) of Stiassnie et al. (2008), that is,

$$1 = 4k_0^4 \left\{ \int_{-\infty}^{\infty} \frac{F(k) dk}{\{i(k - k_0) + \psi\}^2 + \frac{p^2}{4}} \right\}. \quad (3.47)$$

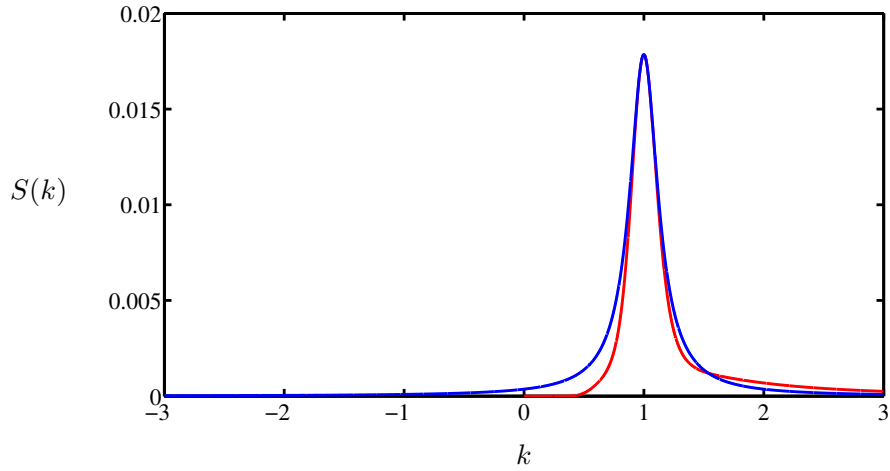


Figure 3.16: A Lorentzian spectrum (blue line) as in the equation (3.46) and the JONSWAP spectrum (red line) as given in equation (3.44).

Substituting equation (3.46) into equation (3.47) and using $\psi = \frac{4i\Omega}{p} \sqrt{\frac{k_0^3}{g}}$, where, as has been mentioned before, Ω is the frequency of the disturbance and its positive values of the imaginary part, $\Omega_i > 0$, are related to the instability yields the growth rate of the disturbance

$$\Omega_i = \frac{p}{4} \sqrt{\frac{g}{k_0^3}} \left\{ \sqrt{4\pi b k_0^4 \sqrt{a} - \frac{p^2}{4} - \sqrt{a}} \right\}. \quad (3.48)$$

The point of maximum growth rate is obtained by taking the first partial derivative of equation (3.48) with respect to p and after standard algebra the following equation is obtained

$$p^{(max)} = \frac{1}{2} \sqrt{32\pi b k_0^4 \sqrt{a} - 2a - 2\sqrt{a^2 + 32\pi b a^{\frac{3}{2}} k_0^4}}.$$

Therefore, the maximum growth rate is

$$\Omega_i^{(max)} = \frac{p^{(max)}}{4} \sqrt{\frac{g}{k_0^3}} \left\{ \sqrt{4\pi b k_0^4 \sqrt{a} - \frac{(p^{(max)})^2}{4} - \sqrt{a}} \right\}.$$

In Figure 3.17, the marginal instability in which maximum growth rate approaches zero, $\Omega_i \rightarrow 0$, is shown. In order to obtain such marginal instability, one will consider equation (3.48) in which Ω_i approaches zero and find that there are three possible values

of p namely $p = 0$ and $p = \pm 2\sqrt{4\pi b k_0^4 \sqrt{a} - a}$. Taking $p > 0$ will give the same result for $p < 0$ while for $p = 0$, the solution is trivial. Therefore, an explicit equation for α which leads to a marginal stability condition as a function of γ is given by

$$\alpha = \frac{\sqrt{2} \sigma e^{\frac{3}{2}}}{\pi \gamma \sqrt{24\sigma^2 + \ln(\gamma)}}$$

In Figure 3.17, solution is shown for $\sigma = 0.08$.

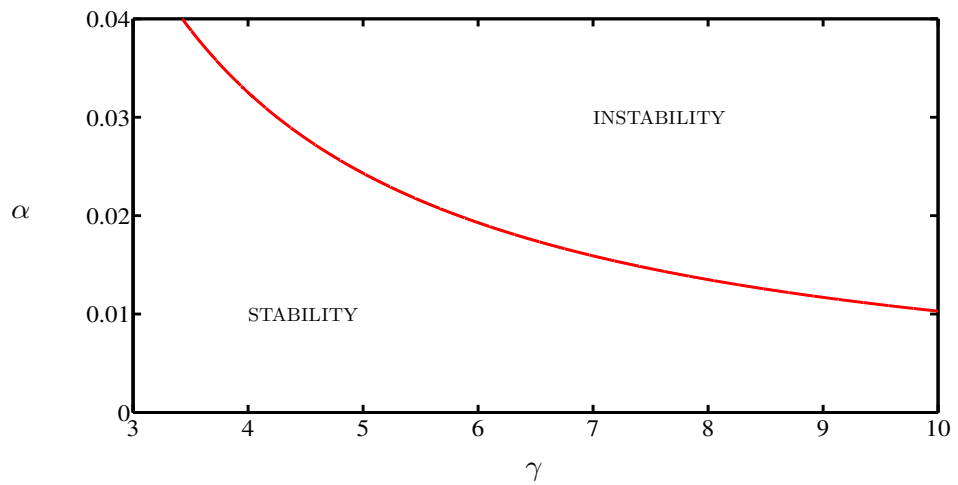


Figure 3.17: Instability diagram in the $\alpha - \gamma$ plane of the Lorentzian spectrum. α is the Philips parameter and γ is the peak enhancement factor. The red line represents the marginal instability.

Figure 3.17 is similar to the Figure 1 of Onorato et al. (2003) which was obtained from the nonlinear Schrödinger equation where the spectra with higher values of α and γ are more likely to show the modulational instability. Moreover, as has been shown in Babanin et al. (2010, 2011b), steepness plays an important role in the instability. Hence, since the steepness of a JONSWAP spectrum depends on the parameters, α and γ , in the following, the relations of these three parameters will be investigated. To be consistent with the previous cases, namely a square spectrum, a rectangular spectrum and the Lorentz spectrum, the steepness of any spectrum, $F(k)$, is calculated using the following formula

$$\varepsilon = k_0 \sqrt{2m_0}, \text{ where } m_0 = \int_{-\infty}^{\infty} F(k) dk.$$

Thus, the steepness of this Lorentzian spectrum is given by

$$\varepsilon = \sqrt{2} \sqrt{\frac{\pi\sqrt{2} \alpha \gamma \sigma}{e^{\frac{3}{2}} \sqrt{24\sigma^2 + \ln(\gamma)}}}$$

Dividing both sides of this equation by $\alpha \times \gamma$ and then substituting the equation for α as a marginal instability condition on the right hand side gives

$$\frac{\varepsilon}{\alpha \times \gamma} = \frac{\pi\sqrt{2}}{e^{\frac{3}{2}}} \approx 1.$$

Therefore, the instability/stability areas based on the Lorentzian spectrum are clearly seen in Figure 3.17. Choosing any combinations of α and γ in the instability regime, one can easily calculate the actual growth rate including the maximum growth rate as well as the point of maximum growth rate using equation (3.48). The advantage of this Lorentzian spectrum enables us to study the instability for the dispersion relation as given in equation (3.17) analytically and helps to study the JONSWAP spectrum which is asymmetric spectrum. Therefore, in the next section, the instability and stability conditions of the original asymmetric JONSWAP spectrum will be studied.

3.4.4.2 Unidirectional JONSWAP spectrum

Following Holthuijsen (2007, p.160), a unidirectional JONSWAP spectrum as a function of frequency is defined as

$$s(f) = \frac{\alpha g^2}{(2\pi)^4 f^5} e^{-\frac{5}{4} \left(\frac{f_0}{f}\right)^4} \gamma e^{\frac{-1}{2\sigma^2 f_0^2} (f-f_0)^2} \quad (3.49)$$

where f_0 is the peak frequency. Using the dispersion relation on the deep water that is $\omega^2 = gk$ and $s(k) = s(f) \frac{df}{dk}$, the unidirectional JONSWAP spectrum as a function of frequency can be transformed into the wave number, k , yielding

$$s(k) = \frac{\alpha}{2k^3} e^{-\left(\frac{5k_0^2}{4k^2}\right)} \gamma e^{-\left[\frac{1}{2\sigma^2 k_0} (\sqrt{k} - \sqrt{k_0})^2\right]} \quad (3.50)$$

where k_0 is the peak wavenumber. For the total energy density of any spectrum, the following relations are chosen (Dysthe et al., 2003, Stiassnie et al., 2008)

$$\frac{a_0^2}{2} \equiv \frac{(\varepsilon/k_0)^2}{2} \equiv \int s(k) dk.$$

Moreover, the one-dimensional counterpart of the equation (3.17) where $\psi = \frac{4i\Omega}{p} \sqrt{\frac{k_0^3}{g}}$ can be written in the form of integral equation as follows:

$$1 = 4k_0^4 p^2 \int_{-\infty}^{\infty} \frac{s(k_1) dk_1}{\frac{p^4}{4} - \left[p(k_1 - k_0) + \frac{4k_0^2 \Omega}{\sqrt{gk_0}} \right]^2}. \quad (3.51)$$

In order to determine the maximum growth rate and the point of maximum growth of the spectrum, equation (3.50) is substituted into equation (3.51). However, since the integral in equation (3.51) cannot be solved analytically for asymmetric spectrum such as a JONSWAP spectrum, it is necessary to seek an approximate solution. To this end, the original spectrum $s(k)$ will be replaced by a sum of weighted Dirac-delta functions as follows:

$$s(k) = \sum_{l_{min}}^{l_{max}} s_l \delta(k - k_l)$$

where $k_l = l\Delta k$, $s_l = s(k_l)\Delta k$ and $l = 1, 2, \dots, L$.

Substituting this equation into equation (3.51) gives

$$1 = 4k_0^4 p^2 \sum_{l_{min}}^{l_{max}} \frac{s_l}{\frac{p^4}{4} - \left[p(k_l - k_0) + \frac{4k_0^2 \Omega}{\sqrt{gk_0}} \right]^2}.$$

Note that all of the quantities in this equation have numerical values, and that only Ω is unknown. Besides that, using Matlab, this equation can be reduced into a polynomial equation of order $L = 2(l_{max} - l_{min} + 1)$, that is

$$\sum_{\mu=0}^L a_{\mu} \Omega^{\mu} = 0$$

where a_{μ} is a constant. However, the highest order algebraic equation that can be used is up to $L = 70$, due to the limitation of the Matlab to solve the polynomial for these cases. Note that the convergence of this numerical solution has been checked by taking $L = 30, 40, 50, 60$ and 70 . Furthermore, seeking the root for Ω with the largest imaginary contribution will give the maximum growth rate of the given spectrum. From

this, it is also straightforward to get the point of maximum growth. The validity of this rather “general-method” is firstly demonstrated by using one-dimensional Lorentz spectrum as given by Stiassnie et al. (2008) and then using a two-dimensional Lorentz spectrum as in Section 3.4.3. The reason to choose these spectra is because both spectra have analytical solutions to compare with. Stiassnie et al. (2008) defined a one-dimensional Lorentz spectrum as

$$s(k) = \frac{0.09W a_0^2}{4[(k - k_0)^2 + 0.02W^2]}$$

where W is the spectral width and $a_0^2/2$ is the energy density. The growth rate of this spectrum in the non-dimensional form is given by (see equation (2.28) of Stiassnie et al. (2008))

$$\tilde{\Omega}_i = \frac{\tilde{P}}{4} \left(\sqrt{2 - \frac{\tilde{P}^2}{4}} - \sqrt{0.02\tilde{W}} \right)$$

where $\tilde{\Omega}_i = \Omega_i/(\varepsilon^2 \sqrt{gk_0})$; $\tilde{P} = p/\varepsilon k_0$; $\tilde{W} = w/\varepsilon k_0$.

In order to apply the “general method” to the Lorentz spectrum, the following procedures will be carried out. As known, the limit of k is along real number, but for the numerical reasons, it has to be truncated. Therefore, let k_{min} and k_{max} be the lower limit and the upper limit of k , respectively, then Δk is defined as

$$\Delta k = \frac{k_{max} - k_{min}}{L}$$

and thus,

$$s_l = s(k_l)(\Delta k) = \left(\frac{0.09W a_0^2}{4[(k_l - k_0)^2 + 0.02W^2]} \right) \left(\frac{k_{max} - k_{min}}{L} \right)$$

where

$$k_l = k_{min} + \left(\frac{k_{max} - k_{min}}{L} \right) \left(l - \frac{1}{2} \right), l = 1, 2, 3, \dots, L.$$

The point of maximum growth rate as well as the maximum growth rate obtained from the “general-method” are shown in Figure 3.18 and marked by dots, while the analytical

solutions are given by the solid line. As seen from the figure, the results obtained from the “general method” and from the analytical solution are hardly distinguished. Moreover, the results are given in the dimensionless variables.

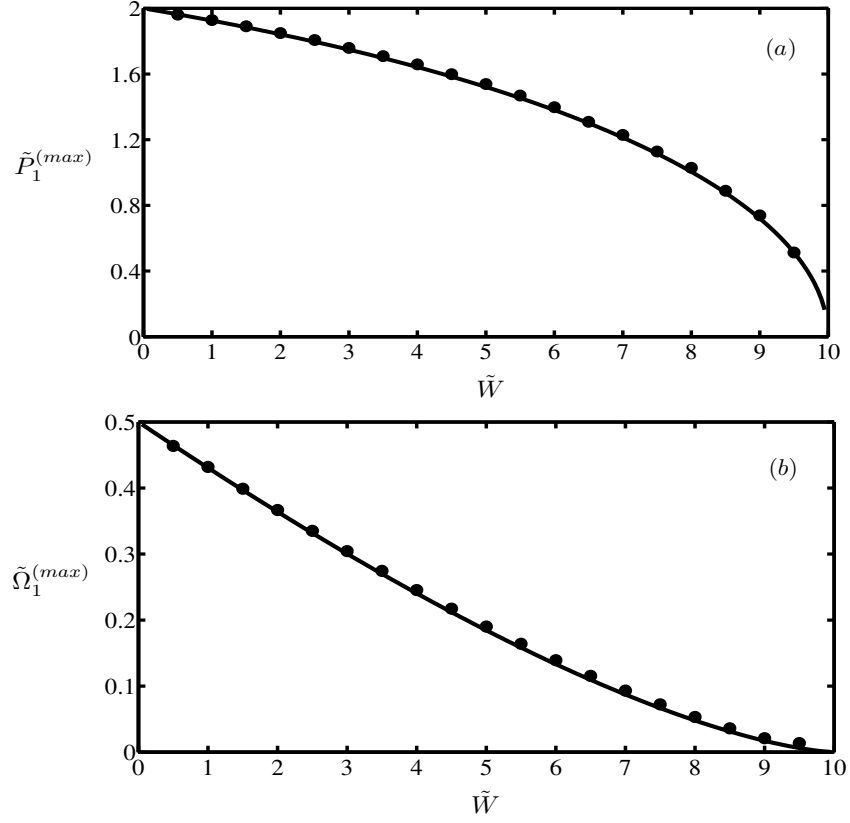


Figure 3.18: Validation of the “general-method” $\bullet\bullet\bullet\bullet$, against the analytical solution — , for a one-dimensional Lorentz spectrum. (a) most unstable mode, (b) its growth rate.

For a two-dimensional Lorentz spectrum, the following procedure will be carried out. As has been shown analytically, the maximum growth rate occurs at the wavenumber of the disturbance which is perpendicular to the carrier wave, i.e. $q = 0$ and therefore only one spatial dimension of the disturbance will be considered. However, the spectrum will be kept two-dimensional. Therefore, the dispersion relation of the disturbance for this particular case is defined as

$$1 = 4k_0^4 p^2 \int_{-\infty}^{\infty} \frac{s(k_1) dk_1}{\frac{p^4}{4} - \left[p(k_1 - k_0) + \frac{4k_0^2 \Omega}{\sqrt{gk_0}} \right]^2}$$

where

$$s(k_1) = \int_{-\infty}^{\infty} S(k_1, k_2) dk_2.$$

Now, as given in the equation (3.33), two-dimensional Lorentz spectrum can be rewritten as

$$S(k_1, k_2) = \frac{W_1 W_2 a_0^2}{2\pi^2 [(k_1 - k_0)^2 + W_1^2] [k_2^2 + W_2^2]}.$$

Hence, one can easily obtain the following spectrum

$$s(k_1) = \frac{W_1 a_0^2}{2\pi [(k_1 - k_0)^2 + W_1^2]}.$$

Following a similar method in applying the “general method” to the one-dimensional Lorentz spectrum, the maximum growth rate and the point of maximum growth rate for a two-dimensional Lorentz spectrum are shown in the following figures where the results from the general method are marked by dots while the results from the analytical solution are shown by a solid line.

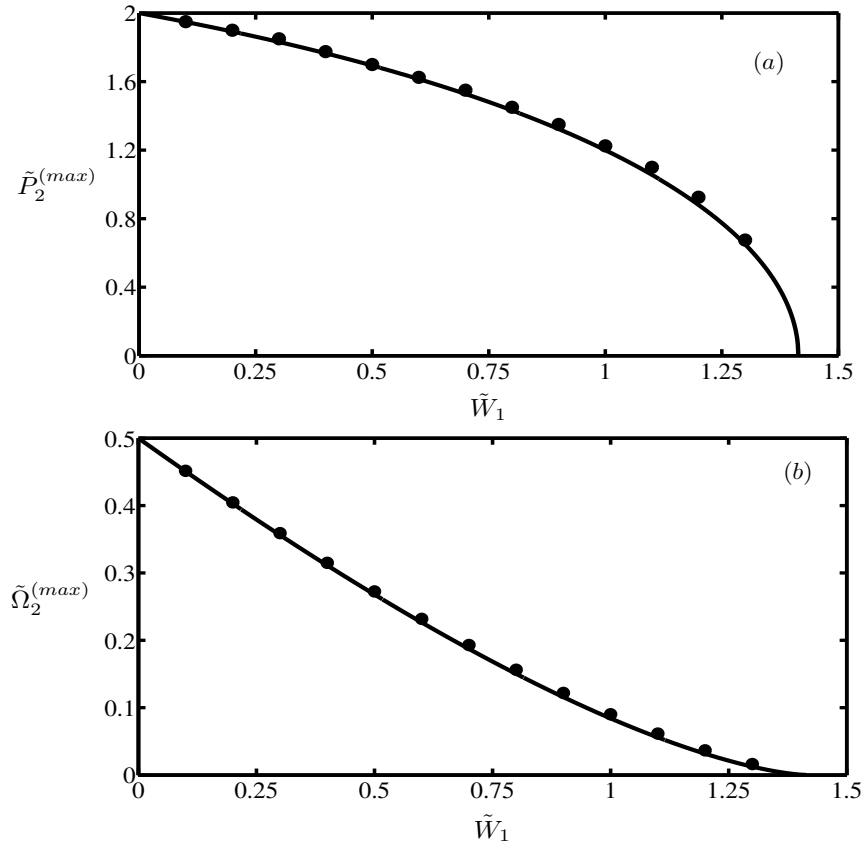


Figure 3.19: Validation of the “general-method” ••••, against the analytical solution ———, for a two-dimensional Lorentz spectrum. (a) most unstable mode, (b) its growth rate.

As we can see from these simulations, the results based on the “general method” (marked by dots) are not significantly different from the results obtained from the analytical solution which is represented by the solid line. Therefore, it is reasonable to apply this method for any spectrum including an asymmetric spectrum. In order to apply the “general method” to determine the maximum growth rate and the point of maximum growth rate for a unidirectional JONSWAP spectrum as in the equation (3.50) the following procedures will be carried out.

Let us consider the JONSWAP spectrum as two parts, namely for $0 < k < k_0$ as the first part and $k_0 < k < \infty$ as the second part. Hence, the first part, Δk and k_l are given by

$$\Delta k = \frac{2k_0}{L},$$

and

$$k_l = \frac{2k_0}{L} \left(l - \frac{1}{2} \right), l = 1, 2, \dots, L,$$

and therefore, s_l can be written as

$$s_l = \left(\frac{2k_0}{L} \right) \left(\frac{\alpha}{2k_l^3} e^{-\left(\frac{5k_0^2}{4k_l^2} \right)} \gamma e^{-\left[\frac{1}{2\sigma^2 k_0} (\sqrt{k_l} - \sqrt{k_0})^2 \right]} \right).$$

For the second part, the value of k is up to infinity. However, again, for the numerical purposes it will be truncated at $k = k_{max}$. Thus, following a similar procedure to that used for the first part of the spectrum, Δk is defined as

$$\Delta k = \frac{2(k_{max} - k_0)}{L}$$

while k_l is given by

$$k_l = k_0 + \frac{2(k_{max} - k_0)}{L} \left(\left(l - \frac{L}{2} \right) - \frac{1}{2} \right).$$

Thus, s_l can also be written as

$$s_l = \left(\frac{2(k_{max} - k_0)}{L} \right) \left(\frac{\alpha}{2k_l^3} e^{-\left(\frac{5k_0^2}{4k_l^2} \right)} \gamma e^{-\left[\frac{1}{2\sigma^2 k_0} (\sqrt{k_l} - \sqrt{k_0})^2 \right]} \right).$$

Now, the question that needs to be answered is how to choose the values of the energy scale, α , and the peak enhancement factor, γ , of a JONSWAP spectrum so that the modulational instability occurs. In order to answer this question, the result obtained

based on the Lorentzian spectrum will be used. As has been shown in Subsection 3.4.4.1, the marginal instability line of the Lorentzian spectrum satisfies the condition

$$\frac{\varepsilon}{\alpha \times \gamma} = 1.$$

This condition enables us to find the relation between α, γ and ε . Moreover, calculating steepness from the equation (3.50) gives

$$\varepsilon^2 = 2k_0^2 m_0 = k_0^2 \alpha \int_0^\infty \frac{1}{k^3} \exp\left(-\frac{5k_0^2}{4k^2}\right) \gamma^{\exp\left[-\frac{(\sqrt{k}-\sqrt{k_0})^2}{2\sigma^2 k_0}\right]} dk.$$

For $k_0 = 1$, $\sigma = 0.08$, and taking the values of k from 0.1 to 4, the above equation can be rewritten as

$$\varepsilon^2 = \alpha \int_{0.1}^4 \frac{1}{k^3} \exp\left(-\frac{5}{4k^2}\right) \gamma^{\exp\left[\frac{(\sqrt{k}-1)^2}{2(0.08)^2}\right]} dk.$$

Let

$$f(\gamma) = \int_{0.1}^4 \frac{1}{k^3} \exp\left(-\frac{5}{4k^2}\right) \gamma^{\exp\left[\frac{(\sqrt{k}-1)^2}{2(0.08)^2}\right]} dk,$$

one will then get the following equation

$$\alpha = \frac{\varepsilon^2}{f(\gamma)}. \quad (3.52)$$

Moreover, using the marginal instability condition obtained from the Lorentzian spectrum, that is $\alpha = \varepsilon / \gamma$, gives the final equation as

$$\varepsilon = \frac{f(\gamma)}{\gamma}.$$

Furthermore, plotting this equation as well as the isolines of the equation (3.52) yields the results as shown in Figure 3.20.

Therefore, Figure 3.20 enables us to localize the instability/stability area in order to determine the values of α and γ of a JONSWAP spectrum. Choosing the values of α and γ in the instability area, taking $k_0 = 1$ which is a peak wavenumber and applying the “general method”, one will get the maximum growth rate and the most unstable mode as summarized in Table 3.1 where ε is the wave steepness, $p_1^{(max)}$ is the

wavenumber of the most unstable mode and $\Omega_1^{(max)}$ is the maximum growth rate. Note that, in applying the “general method”, the acceleration due to the gravity is taken to be 1 for simplicity, i.e, $g = 1$. The range of α which is the energy scale were taken from some authors such as Babanin and Soloviev (1998a) and Onorato et al. (2009a, 2009b).

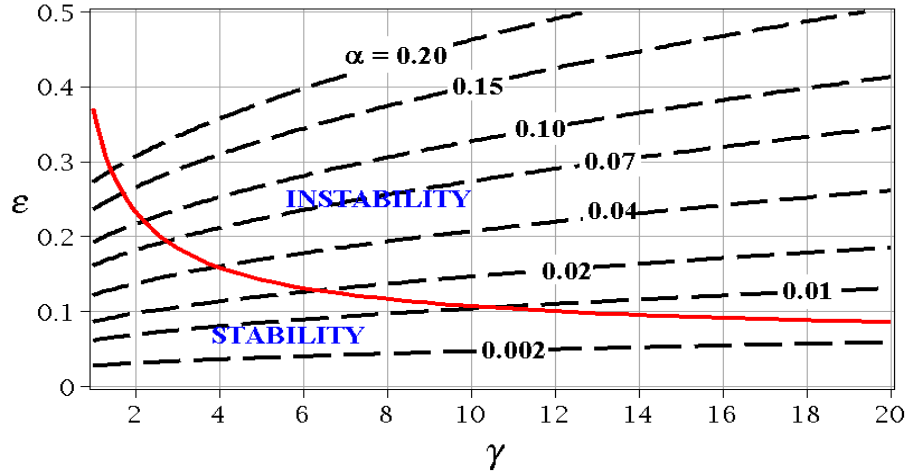


Figure 3.20: Instability diagram in the $\varepsilon - \gamma$ plane of the unidirectional JONSWAP spectrum. Solid line represents the steepness as a function of γ which is the marginal instability line and dashed lines represent the values of different α .

Table 3.1: Results for unidirectional JONSWAP spectra where ε is the steepness, $p_1^{(max)}$ is the wavenumber of the most unstable mode and $\Omega_1^{(max)}$ is the maximum growth rate. α and γ are the Philips parameter and peak enhancement factor, respectively.

α	γ	$p_1^{(max)}$	$\Omega_1^{(max)}$	ε
0.016	10	0.1886	0.0021379098	0.125779445
0.02	10	0.2241	0.0035098887	0.140625695
0.025	10	0.2641	0.0053465805	0.157224306
0.03	10	0.2971	0.0072657537	0.172230598
0.016	13	0.2311	0.0038441075	0.13779321
0.02	13	0.2721	0.0057026371	0.154057492
0.025	13	0.3061	0.0081193006	0.172241513
0.03	13	0.3501	0.0106057991	0.188681124
0.0081	17	0.1621	0.0015892432	0.108026501
0.016	17	0.2721	0.0060827217	0.151826573
0.02	17	0.3151	0.0085229135	0.169747269
0.025	17	0.3601	0.0116491023	0.189783217
0.03	17	0.3901	0.0148376920	0.207897098
0.0081	20	0.1921	0.0023880541	0.114756297
0.016	20	0.2961	0.0077131614	0.16128501
0.02	20	0.3421	0.0105633553	0.180322124
0.025	20	0.3801	0.0141926891	0.201606263
0.03	20	0.4291	0.0178793148	0.220848596

Note that $p_1^{(max)}$ and $\Omega_1^{(max)}$ in Table 3.1 are in dimensional form which can be transformed into the dimensionless form using the following relations

$$\tilde{P}_1^{(max)} = \frac{p_1^{(max)}}{\varepsilon k_0} \quad \text{and} \quad \tilde{\Omega}_1^{(max)} = \frac{\Omega_1^{(max)}}{\varepsilon^2 \sqrt{g k_0}}.$$

However, since $k_0 = 1$ and $g = 1$ have been using in this simulation, the previous relations then becomes

$$\tilde{P}_1^{(max)} = \frac{p_1^{(max)}}{\varepsilon} \quad \text{and} \quad \tilde{\Omega}_1^{(max)} = \frac{\Omega_1^{(max)}}{\varepsilon^2}.$$

Therefore, the results for $p_1^{(max)}$ and $\Omega_1^{(max)}$ in Table 3.1 can be transformed into the dimensionless form as shown in Table 3.2.

Table 3.2: Results for unidirectional JONSWAP spectra where ε is the steepness, $\tilde{P}_1^{(max)}$ is the dimensionless wavenumber of the most unstable mode and $\tilde{\Omega}_1^{(max)}$ is the dimensionless maximum growth rate. α and γ are the Philips parameter and peak enhancement factor, respectively.

α	γ	ε	$\tilde{P}_1^{(max)}$	$\tilde{\Omega}_1^{(max)}$
0.016	10	0.125779445	1.49945	0.135135678
0.02	10	0.140625695	1.59359	0.177485954
0.025	10	0.157224306	1.67977	0.216290147
0.03	10	0.172230598	1.72501	0.244940190
0.016	13	0.13779321	1.67715	0.202460308
0.02	13	0.154057492	1.76622	0.240275829
0.025	13	0.172241513	1.77716	0.273679935
0.03	13	0.188681124	1.85551	0.297910965
0.0081	17	0.108026501	1.50056	0.136185148
0.016	17	0.151826573	1.79218	0.263877504
0.02	17	0.169747269	1.85629	0.295789320
0.025	17	0.189783217	1.89743	0.323427432
0.03	17	0.207897098	1.87641	0.343296599
0.0081	20	0.114756297	1.67398	0.181338958
0.016	20	0.16128501	1.83588	0.296513456
0.02	20	0.180322124	1.89716	0.324865701
0.025	20	0.201606263	1.88536	0.349185862
0.03	20	0.220848596	1.94296	0.366573938

As we know, the steepness of wave fields described by the JONSWAP spectrum depends on the peak enhancement coefficient, γ , and Philips parameter, α . This means,

when the value of γ or α increases, then the steepness will increase as well. As can be seen from Table 3.2, an increase in the value of steepness is accompanied by an increase in the value of the maximum growth rate. These results are in qualitative agreement with the experimental data (Babanin et al., 2011b) as well as with the numerical simulation (Eliasson and Shukla, 2010). In addition, the narrower the spectrum, the point of maximum growth rate converges to the dimensionless wavenumber of the perturbation which is parallel to the carrier wave, $\tilde{P}_1^{(max)} = 2$. This is also consistent with the results in Stiassnie et al. (2008) in which the maximum growth rate occurs at $\tilde{P}_1^{(max)} = 2$ for vanishing spectral width.

In order to present these results in another way, dimensional analysis approach is performed. Let $\Omega_1^{(max)}$ be the growth-rate of the most unstable disturbance which depends on the physical quantities namely; the acceleration due to the gravity, g , the total energy, $a_0^2/2$, the peak wavenumber, k_0 , and the spectral width, W , which is defined as the quotient of the total energy to the spectral peak s_0 . In particular, for a unidirectional JONSWAP spectrum, $s_0 = \alpha\gamma e^{-1.25}/2k_0^3$ and $W = a_0^2 k_0^3 / (\alpha\gamma e^{-1.25})$. Thus, there must exist a function

$$f\left(\Omega_1^{(max)}, g, \frac{a_0^2}{2}, k_0, a_0^2 k_0^3 / (\alpha\gamma e^{-1.25})\right) = 0.$$

Using k_0 and g as fundamental quantities and applying Buckingham Pi theorem (Buckingham, 1914) assures the existence of the function

$$f_1\left(\Omega_1^{(max)} / \sqrt{gk_0}, \varepsilon^2, \varepsilon^2 / \alpha\gamma\right) = 0$$

where $\varepsilon = a_0 k_0 = o(1)$ is typical wave-steepness. Without loss of generality, f_1 can be replaced by

$$f_2\left(\frac{\Omega_1^{(max)}}{\varepsilon^2 \sqrt{gk_0}}, \frac{\varepsilon}{\alpha\gamma}, \varepsilon\right) = 0.$$

In this equation, $\Omega_1^{(max)} / (\varepsilon^2 \sqrt{gk_0})$ and $\varepsilon / (\alpha\gamma)$ are both usually of $O(1)$, whereas ε is $o(1)$, so that approximately

$$\frac{\Omega_1^{(max)}}{\varepsilon^2 \sqrt{gk_0}} = f_3 \left(\frac{\varepsilon}{\alpha\gamma} \right). \quad (3.53)$$

As seen from (3.53), $\Omega_1^{(max)}/(\varepsilon^2 \sqrt{gk_0})$ which is the dimensionless maximum growth rate is a function of $\varepsilon/(\alpha\gamma)$ which is called the dimensionless “width parameter”,

$$\Pi_1 = \frac{\varepsilon}{\alpha\gamma}, \quad (3.54)$$

for unidirectional JONSWAP spectrum. Note that Π_1 is the dimensionless scaled width in the peak direction. Moreover, this dimensionless analysis was inspired by the Benjamin Feir Index (BFI) as introduced by Onorato et al. (2001) and Janssen (2003). Therefore, it has to be mentioned that this dimensionless width parameter shows the detailed meaning of the ratio of wave steepness to wave bandwidth in the spectral context. Note that Π_1 is related to BFI, but it is not another form of BFI. The latter had been introduced for quasi-monochromatic wave trains, being ratio of steepness to bandwidth, which are unambiguous properties in such trains. They are not unambiguous for wave fields with continuous spectrum. In a JONSWAP spectrum, both α and γ are connected with both steepness and bandwidth. Moreover, neither of them is constant in evolving wave spectra and, even on average, any change to α is accompanied by a change to γ (e.g. Babanin and Soloviev 1998a; Onorato et al. 2003).

For spectrum of ocean waves, e.g. JONSWAP spectrum as the most popular parameterization, same steepness can be achieved either by varying α and keeping γ constant, or vice versa. This same steepness, therefore, has different implications for the spectral bandwidth and for modulational instability. If we increase α , then to keep the steepness constant we should decrease γ . This means that spectra become broader and this leads to corresponding implications for the instability of nonlinear groups – i.e. the growth rates of most unstable modes are expected to decrease or even be suppressed. If we increase γ , then to keep the steepness constant we should decrease α . Such combination will instigate rapid narrowing of the spectral bandwidth of dominant waves, which we expect to be associated with their instability, and which is the most important outcome in practical sense, e.g. for wave breaking or freak wave probability.

Thus, separation of the relative contributions of α and γ into the total steepness and the characteristic bandwidth of waves with continuous spectrum identify important physical

differences between wave fields with full spectrum and quasi-monochromatic wave trains. It does not deny the previous analogies in terms of BFI, but expands them and is an important new contribution of this research.

The results in Table 3.2, $\tilde{P}_1^{(max)}$ and $\tilde{\Omega}_1^{(max)}$ are plotted as a function of dimensionless “width-parameter”, Π_1 , obtained from the unidirectional JONSWAP spectrum using a “general method” (marked by dots), as well as the best linear fit for $\tilde{P}_1^{(max)}$ and $\tilde{\Omega}_1^{(max)}$.

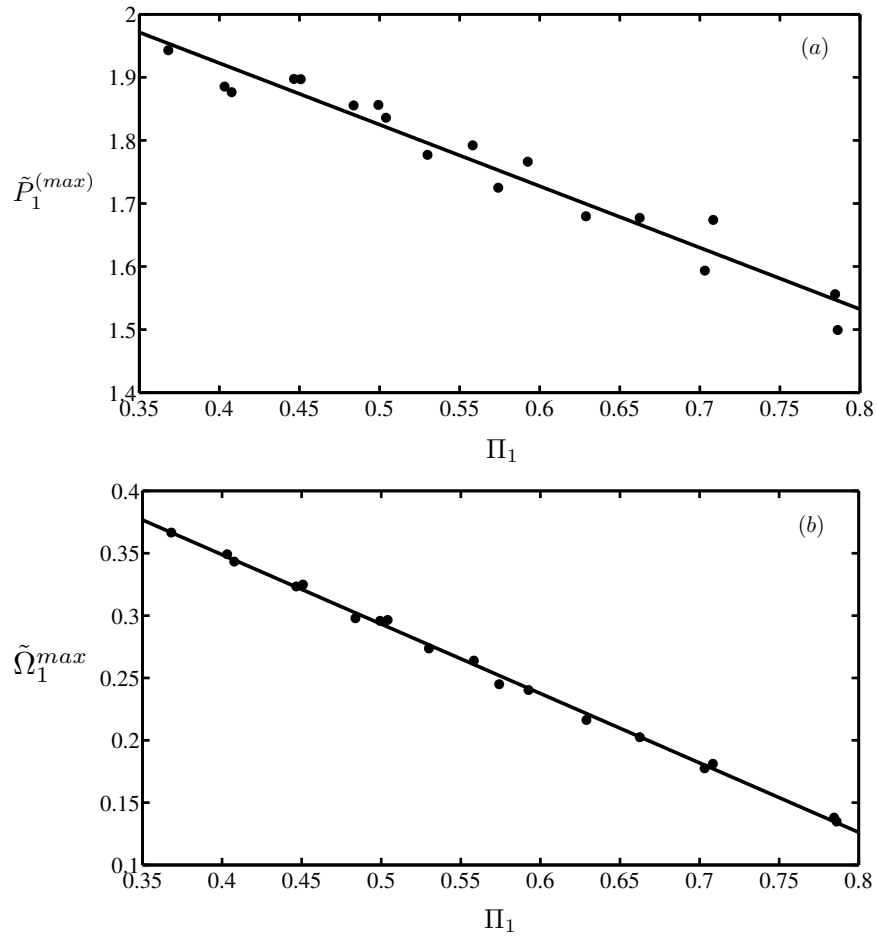


Figure 3.21: Results of linear stability analysis for unidirectional JONSWAP spectra as a function of the “width-parameter” Π_1 . (a) most unstable mode, (b) its growth rate.

The equations for the straight lines in Figure 3.21 are

$$\tilde{P}_1^{(max)} = 2.313 - 0.976\Pi_1, \quad (3.55)$$

$$\tilde{\Omega}_1^{(max)} = 0.572 - 0.557\Pi_1. \quad (3.56)$$

From the second equation, it is clearly seen that unidirectional JONSWAP spectra are stable to inhomogeneous disturbance when $\Pi_1 \geq 1$ as for this condition the maximum growth rate $\tilde{\Omega}_1^{(\max)}$ is negative.

3.4.4.3 JONSWAP spectrum with a directional distribution

Directional wave fields can be conveniently represented by a unidirectional JONSWAP spectrum as in the equation (3.50) multiplied by the directional spreading (see Komen et al., 1994, Babanin and Soloviev, 1998b, Young, 1999, Holthuijsen, 2007) that is

$$S(k, \theta) = s(k)D(\theta)$$

where $s(k)$ as in equation (3.50) and the directional spreading must satisfy the following condition

$$\int D(\theta) d\theta = 1.$$

In this thesis, the directional spreading used is as

$$D(\theta) = A_d \cos^n \theta; \quad -\frac{\pi}{2} \leq \theta \leq \frac{\pi}{2},$$

where n is the degree of the directional distribution and

$$A_d = \frac{1}{\sqrt{\pi}} \frac{\Gamma\left(1 + \frac{n}{2}\right)}{\Gamma\left(\frac{1+n}{2}\right)} \quad (3.57)$$

which is a normalization factor. Let us transform the polar coordinate into the Cartesian coordinate, that is into k_1 and k_2 plane, by using the following relations:

$$k_1 = k \cos \theta,$$

$$k_2 = k \sin \theta,$$

gives

$$k = \sqrt{k_1^2 + k_2^2}, \quad \theta = \arctan\left(\frac{k_2}{k_1}\right) \text{ and its Jacobian } J = \frac{1}{\sqrt{k_1^2 + k_2^2}}$$

Substituting k and θ into $S(k, \theta)$ and multiplying it by its Jacobian gives a JONSWAP spectrum with directional distribution as a function of wave numbers k_1 and k_2 as follows:

$$S(\mathbf{k}) = \frac{\alpha \Gamma\left(1 + \frac{n}{2}\right) k_1^n}{2\sqrt{\pi} (\sqrt{k_1^2 + k_2^2})^{4+n} \Gamma\left(\frac{1+n}{2}\right)} e^{-\left(\frac{5k_0^2}{4(k_1^2+k_2^2)}\right)} \gamma e^{\left[\frac{1}{2\sigma^2} \left(\sqrt{\frac{k_1^2+k_2^2}{k_0}} - 1\right)\right]^2} \quad (3.58)$$

where

$$0 < k_1 < k, \quad -k < k_2 < k.$$

Substituting equation (3.58) into equation (3.17) will give a very complex integral which cannot be solved even numerically due to the very expensive numerical computations. Therefore, a simplified problem is considered. To this end, as has been mentioned before, it is assumed that the maximum growth rate occurs at $q = 0$. This assumption will reduce the required computational resources significantly. As a result, only one-dimensional case of the disturbance is considered but the spectrum will be kept two-dimensional. Moreover, JONSWAP spectrum with the directional distribution is integrated with respect to k_2 to obtain a spectrum $s(k_1)$ which is identical to a unidirectional JONSWAP spectrum. Thus, the dispersion relation for the disturbance of the simplified two-dimensional Alber equation is given by

$$1 = 4k_0^4 p^2 \int_{-\infty}^{\infty} \frac{s(k_1) dk_1}{\frac{p^4}{4} - \left[p(k_1 - k_0) + \frac{4k_0^2 \Omega}{\sqrt{gk_0}} \right]^2}$$

where

$$s(k_1) = \int_{-\infty}^{\infty} S(k_1, k_2) dk_2.$$

Now, following a similar procedure to that used for the unidirectional JONSWAP spectrum in choosing the values of the energy scale, α , and the peak enhancement, γ , for JONSWAP spectrum with directional distribution, we have to choose the values of the degrees of the directional spreading. Applying a “general method” by taking $L = 68$, gives the results as summarized in Table 3.3 where α and γ are the energy scale

and the peak enhancement factor of JONSWAP spectrum, respectively, while n , A_d and ε are degree of the directional distribution, normalization factor of the directional distributions and wave steepness. $\tilde{P}_2^{(max)}$ and $\tilde{\Omega}_2^{(max)}$ are dimensionless wavenumber of the most unstable mode and the maximum growth rate, respectively. As can be seen from Table 3.3, the directional spreading influences the maximum growth rate.

Table 3.3: The results for the JONSWAP spectra with directional distributions where γ is the peak enhancement factor, α is the energy scale, n is the degree of directional energy distribution, A_d is the normalization factor of the directional spreading, ε is the wave steepness, $\tilde{P}_2^{(max)}$ is the dimensionless wavenumber of the most unstable mode and $\tilde{\Omega}_2^{(max)}$ is the dimensionless maximum growth rate.

γ	α	n	A_d	ε	$\tilde{P}_2^{(max)}$	$\tilde{\Omega}_2^{(max)}$
10	0.016	10	1.293449	0.125779445	1.49945009	0.103061156
10	0.016	24	1.9748	0.125779445	1.44777233	0.129749152
10	0.016	50	2.83508	0.125779445	1.49945009	0.135296362
10	0.016	90	3.79522	0.125779445	1.49945009	0.136053185
10	0.02	5	0.9375	0.140625695	1.394482002	0.104022026
10	0.02	10	1.293449	0.140625695	1.543814598	0.149014376
10	0.02	24	1.9748	0.140625695	1.593592129	0.17364694
10	0.02	50	2.83508	0.140625695	1.593592129	0.17820623
10	0.02	90	3.79522	0.140625695	1.593592129	0.178574921
10	0.025	3	0.75	0.157224306	1.374469414	0.105382144
10	0.025	5	0.9375	0.157224306	1.527117568	0.149706074
10	0.025	10	1.293449	0.157224306	1.628883003	0.192063491
10	0.025	24	1.9748	0.157224306	1.679765721	0.213532238
10	0.025	50	2.83508	0.157224306	1.679765721	0.217140195
10	0.025	90	3.79522	0.157224306	1.679765721	0.217334517
10	0.03	3	0.75	0.172230598	1.515990787	0.141451084
10	0.03	5	0.9375	0.172230598	1.620501833	0.185175889
10	0.03	10	1.293449	0.172230598	1.725012879	0.224421404
10	0.03	24	1.9748	0.172230598	1.725012879	0.242974363
10	0.03	50	2.83508	0.172230598	1.725012879	0.245857355
10	0.03	90	3.79522	0.172230598	1.725012879	0.245932363
13	0.016	5	0.9375	0.13779321	1.473947809	0.122675204
13	0.016	10	1.293449	0.13779321	1.626350093	0.171097024
13	0.016	24	1.9748	0.13779321	1.677150855	0.19784429
13	0.016	50	2.83508	0.13779321	1.677150855	0.202964984
13	0.016	90	3.79522	0.13779321	1.677150855	0.203471936
13	0.02	3	0.75	0.154057492	1.454651746	0.121223442
13	0.02	5	0.9375	0.154057492	1.610437742	0.168516896
13	0.02	10	1.293449	0.154057492	1.714295074	0.213779789

13	0.02	24	1.9748	0.154057492	1.766223739	0.236854369
13	0.02	50	2.83508	0.154057492	1.766223739	0.24093222
13	0.02	90	3.79522	0.154057492	1.766223739	0.241244783
13	0.025	3	0.75	0.172241513	1.568146935	0.165307239
13	0.025	5	0.9375	0.172241513	1.724903571	0.211060497
13	0.025	10	1.293449	0.172241513	1.777155783	0.251982095
13	0.025	24	1.9748	0.172241513	1.777155783	0.271277643
13	0.025	50	2.83508	0.172241513	1.777155783	0.274395901
13	0.025	90	3.79522	0.172241513	1.777155783	0.274562236
13	0.03	3	0.75	0.188681124	1.643513639	0.199740427
13	0.03	5	0.9375	0.188681124	1.749512584	0.243120036
13	0.03	10	1.293449	0.188681124	1.802512057	0.279810707
13	0.03	24	1.9748	0.188681124	1.855511529	0.296272944
13	0.03	50	2.83508	0.188681124	1.855511529	0.298712484
13	0.03	90	3.79522	0.188681124	1.855511529	0.298761072
17	0.0081	24	1.9748	0.108026501	1.528328687	0.131260356
17	0.0081	50	2.83508	0.108026501	1.528328687	0.13835607
17	0.0081	90	3.79522	0.108026501	1.528328687	0.138430626
17	0.016	3	0.75	0.151826573	1.4760262	0.137748952
17	0.016	5	0.9375	0.151826573	1.634101295	0.187548983
17	0.016	10	1.293449	0.151826573	1.739484692	0.235219736
17	0.016	24	1.9748	0.151826573	1.79217639	0.259840652
17	0.016	50	2.83508	0.151826573	1.79217639	0.264297149
17	0.016	90	3.79522	0.151826573	1.79217639	0.264732563
17	0.02	3	0.75	0.169747269	1.644209071	0.181488893
17	0.02	5	0.9375	0.169747269	1.750249068	0.229418607
17	0.02	10	1.293449	0.169747269	1.803269067	0.272246699
17	0.02	24	1.9748	0.169747269	1.856289066	0.292879086
17	0.02	50	2.83508	0.169747269	1.856289066	0.296333676
17	0.02	90	3.79522	0.169747269	1.856289066	0.296593436
17	0.025	3	0.75	0.189783217	1.739352962	0.22263848
17	0.025	5	0.9375	0.189783217	1.792044661	0.26706741
17	0.025	10	1.293449	0.189783217	1.844736359	0.304563255
17	0.025	24	1.9748	0.189783217	1.897428057	0.3214471
17	0.025	50	2.83508	0.189783217	1.897428057	0.324042943
17	0.025	90	3.79522	0.189783217	1.897428057	0.324168136
17	0.03	3	0.75	0.207897098	1.780207633	0.253931571
17	0.03	5	0.9375	0.207897098	1.876409073	0.294738049
17	0.03	10	1.293449	0.207897098	1.876409073	0.327792124
17	0.03	24	1.9748	0.207897098	1.876409073	0.341862087
17	0.03	50	2.83508	0.207897098	1.876409073	0.343906513
17	0.03	90	3.79522	0.207897098	1.876409073	0.343965016
20	0.0081	10	1.293449	0.114756297	1.621697505	0.13852836
20	0.0081	24	1.9748	0.114756297	1.621697505	0.173147318
20	0.0081	50	2.83508	0.114756297	1.673982217	0.180909058

20	0.0081	90	3.79522	0.114756297	1.673982217	0.182136873
20	0.016	3	0.75	0.16128501	1.587872297	0.173962811
20	0.016	5	0.9375	0.16128501	1.736677198	0.224068648
20	0.016	10	1.293449	0.16128501	1.835880466	0.27009808
20	0.016	24	1.9748	0.16128501	1.835880466	0.292855631
20	0.016	50	2.83508	0.16128501	1.835880466	0.296878536
20	0.016	90	3.79522	0.16128501	1.835880466	0.297270163
20	0.02	3	0.75	0.180322124	1.69751772	0.215784496
20	0.02	5	0.9375	0.180322124	1.797339082	0.262747368
20	0.02	10	1.293449	0.180322124	1.897160445	0.303315854
20	0.02	24	1.9748	0.180322124	1.897160445	0.322256043
20	0.02	50	2.83508	0.180322124	1.897160445	0.325341374
20	0.02	90	3.79522	0.180322124	1.897160445	0.325572844
20	0.025	3	0.75	0.201606263	1.786154828	0.254450447
20	0.025	5	0.9375	0.201606263	1.885358095	0.2970917
20	0.025	10	1.293449	0.201606263	1.885358095	0.332130697
20	0.025	24	1.9748	0.201606263	1.934959729	0.347385797
20	0.025	50	2.83508	0.201606263	1.885358095	0.34968603
20	0.025	90	3.79522	0.201606263	1.885358095	0.349814646
20	0.03	3	0.75	0.220848596	1.843344298	0.283419003
20	0.03	5	0.9375	0.220848596	1.893152176	0.322165487
20	0.03	10	1.293449	0.220848596	1.942960054	0.352626277
20	0.03	24	1.9748	0.220848596	1.942960054	0.365338154
20	0.03	50	2.83508	0.220848596	1.942960054	0.36712232
20	0.03	90	3.79522	0.220848596	1.942960054	0.367165831

Moreover, following a similar procedure to that outlined in the one-dimensional case, it is concluded that $\tilde{P}_2^{(\max)} = p_2^{(\max)} / \varepsilon k_0$ and $\tilde{\Omega}_2^{(\max)} = \Omega_2^{(\max)} / \varepsilon^2 \sqrt{gk_0}$ are functions of a slightly corrected dimensionless “width-parameter”,

$$\Pi_2 = \frac{\varepsilon}{\alpha\gamma} + \frac{\beta}{\varepsilon A_d}, \quad \text{with } \beta \ll 1. \quad (3.59)$$

Note that $\varepsilon / \alpha\gamma$ and $1 / \varepsilon A_d$ are the dimensionless scaled widths in the peak direction and the transverse direction, respectively. The transverse scaled width $1 / (\varepsilon A_d)$ arises naturally when the energy $a_0^2 / 2$ is divided by the spectral peak $s_0 = \alpha\gamma A_d e^{-1.25} / (2k_0^3)$ as well as by the spectral width $W = a_0^2 k_0^3 / (\alpha\gamma e^{-1.25})$ and finally scaled by ε . Figure 3.22 gives $\tilde{P}_2^{(\max)}$ and $\tilde{\Omega}_2^{(\max)}$ as a function of Π_2 for all different combinations of ε , α , γ and n (marked by dots) obtained from Table 3.2 and

Table 3.3, as well as the best linear fit for $\tilde{P}_2^{(max)}$ and $\tilde{\Omega}_2^{(max)}$ which gave $\beta = 0.0256$. Π_2 is a convenient measure to use due to the fact that the directional property A_d employed by Π_2 formulation, as well as the parameters of JONSWAP spectrum, are characteristics of wave directional spectrum well established experimentally and in the field observations. Comprehensive parameterizations for this property are available for the wave spectrum and at all stages of wave development (Babanin and Soloviev, 1987; 1998b), and therefore at any stage Π_2 can be expressed through both observations-based one-dimensional wave spectra and directional wave spectra.

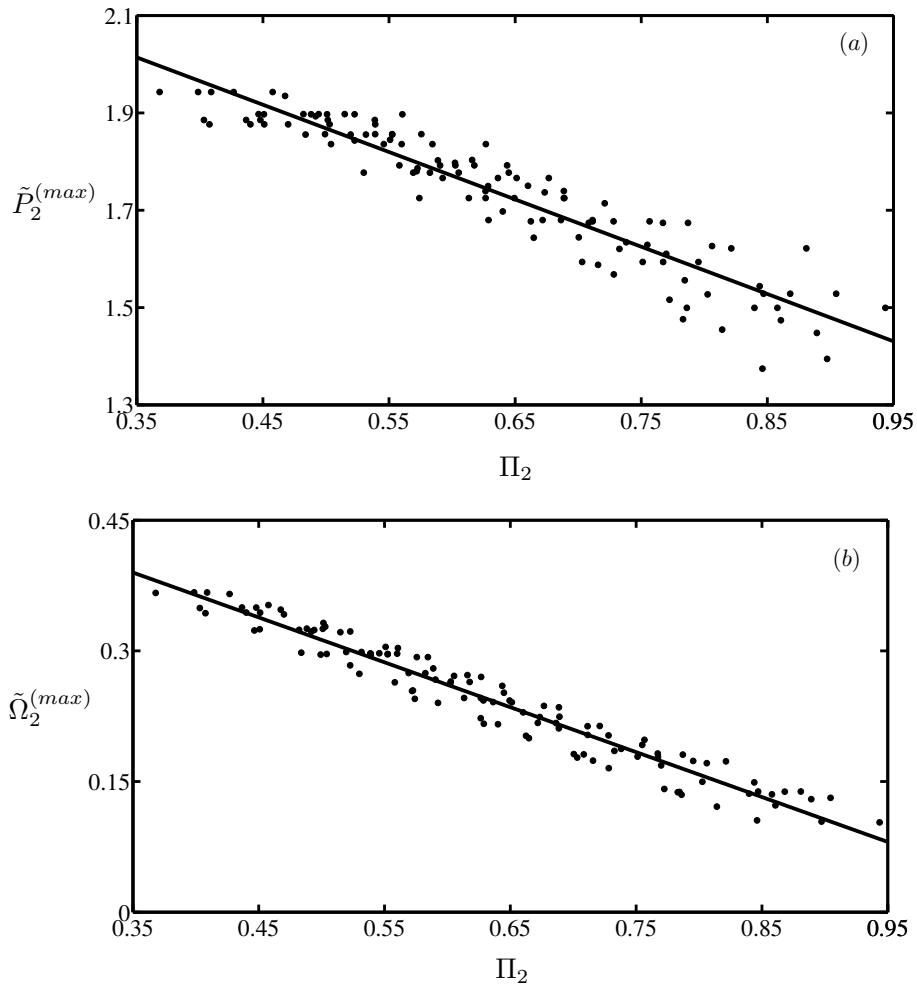


Figure 3.22: Results of linear stability analysis for the JONSWAP spectra with directional distributions as a function of the “width-parameter” Π_2 . (a) most unstable mode, (b) its growth rate.

The equations for the straight lines in Figure 3.22 are

$$\tilde{P}_2^{(max)} = 2.355 - 0.974\Pi_2, \quad (3.60)$$

$$\tilde{\Omega}_2^{(\max)} = 0.571 - 0.516\Pi_2. \quad (3.61)$$

It becomes clear from the last equation that JONSWAP spectra with directional distributions are stable to inhomogeneous disturbance when $\Pi_2 \geq 1.1$ as for this condition $\tilde{\Omega}_2^{(\max)}$ is negative.

3.5 Interpretation of the initial disturbances

In this section, spectral interpretation of the inhomogeneous disturbance will be derived. In the first part, it will be shown that the correlation function of a homogeneous sea and the homogeneous spectrum are a Fourier transform pair. Moreover, the connection between the initial disturbance and the surface elevation will be derived in the second part. Note that for one-dimensional problem, one can refer to the work of Stiassnie et al. (2008) in which the following derivations were based on.

3.5.1 Spectral interpretation of the initial conditions

As given in the equation (3.10), there are no limitations for decay rate $R(\mathbf{r})$ except that $R(\mathbf{0}) \neq 0$ are real and $R(\infty) = 0$ for each axis. Following a similar way to equation (3.8), the influence of the small initial disturbance on the homogeneous spectrum can be written as

$$S(\mathbf{x}, \mathbf{k}) = S_h(\mathbf{k}) + \delta S_1(\mathbf{x}, \mathbf{k}). \quad (3.62)$$

Starting from equation (3.6); an interpretation for $S_1(\mathbf{x}, \mathbf{k})$ can be obtained by replacing $S(\mathbf{k})$ with $S(\mathbf{x}, \mathbf{k})$ which is

$$\rho(\mathbf{x}, \mathbf{r}, t) = \int_{-\infty}^{\infty} e^{i(\mathbf{k}-\mathbf{k}_0)\cdot\mathbf{r}} \sqrt{S\left(\mathbf{k}, \mathbf{x} + \frac{1}{2}\mathbf{r}, t\right) S\left(\mathbf{k}, \mathbf{x} - \frac{1}{2}\mathbf{r}, t\right)} d\mathbf{k}. \quad (3.63)$$

Using equation (3.62), the spectrum can be written as

$$\begin{aligned} S\left(\mathbf{k}, \mathbf{x} + \frac{1}{2}\mathbf{r}, t\right) &= S_h(\mathbf{k}, t) + \delta S_1\left(\mathbf{k}, \mathbf{x} + \frac{1}{2}\mathbf{r}, t\right), \\ S\left(\mathbf{k}, \mathbf{x} - \frac{1}{2}\mathbf{r}, t\right) &= S_h(\mathbf{k}, t) + \delta S_1\left(\mathbf{k}, \mathbf{x} - \frac{1}{2}\mathbf{r}, t\right). \end{aligned}$$

Substituting these results into the equation (3.63) and omitting terms of order δ^2 yields,

$$\begin{aligned} & \sqrt{S\left(\mathbf{k}, \mathbf{x} + \frac{1}{2}\mathbf{r}, t\right) S\left(\mathbf{k}, \mathbf{x} - \frac{1}{2}\mathbf{r}, t\right)} \\ &= \sqrt{S_h^2(\mathbf{k}, t) + \delta S_h(\mathbf{k}, t) \left(S_1\left(\mathbf{k}, \mathbf{x} + \frac{1}{2}\mathbf{r}, t\right) + S_1\left(\mathbf{k}, \mathbf{x} - \frac{1}{2}\mathbf{r}, t\right)\right)}. \end{aligned}$$

Approximating the values under the square root on the right hand side, above equation can be rewritten as

$$\begin{aligned} & \sqrt{S\left(\mathbf{k}, \mathbf{x} + \frac{1}{2}\mathbf{r}, t\right) S\left(\mathbf{k}, \mathbf{x} - \frac{1}{2}\mathbf{r}, t\right)} \\ &= S_h(\mathbf{k}, t) + \frac{\delta}{2} \left(S_1\left(\mathbf{k}, \mathbf{x} + \frac{1}{2}\mathbf{r}, t\right) + S_1\left(\mathbf{k}, \mathbf{x} - \frac{1}{2}\mathbf{r}, t\right)\right) + O(\delta^2). \end{aligned}$$

Moreover, substituting this result into equation (3.63) yields,

$$\begin{aligned} \rho(\mathbf{x}, \mathbf{r}, t) &= \int_{-\infty}^{\infty} e^{i(\mathbf{k}-\mathbf{k}_0)\cdot\mathbf{r}} \left(S_h(\mathbf{k}, t) \right. \\ &\quad \left. + \frac{\delta}{2} \left(S_1\left(\mathbf{k}, \mathbf{x} + \frac{1}{2}\mathbf{r}, t\right) + S_1\left(\mathbf{k}, \mathbf{x} - \frac{1}{2}\mathbf{r}, t\right) \right) \right) d\mathbf{k}. \end{aligned} \quad (3.64)$$

Also, from equation (3.10), the disturbance at $t = 0$ becomes

$$\rho_1(\mathbf{x}, \mathbf{r}) = R(\mathbf{r}) \left(e^{i(p\mathbf{x}+q\mathbf{y})} + e^{-i(p\mathbf{x}+q\mathbf{y})} \right).$$

For simplicity, let $\mathbf{c} = (p, q)$ be the wavenumber vector of the disturbance, then the disturbance becomes

$$\rho_1(\mathbf{x}, \mathbf{r}) = R(\mathbf{r}) \left(e^{i(\mathbf{c}\cdot\mathbf{x})} + e^{-i(\mathbf{c}\cdot\mathbf{x})} \right).$$

As $e^{i(\mathbf{c}\cdot\mathbf{x})} = \cos(\mathbf{c}\cdot\mathbf{x}) + i \sin(\mathbf{c}\cdot\mathbf{x})$, above inhomogeneous disturbances can be rewritten as

$$\rho_1(\mathbf{x}, \mathbf{r}) = 2R(\mathbf{r}) \cos(\mathbf{c}\cdot\mathbf{x}). \quad (3.65)$$

Similarly, assuming the spectral disturbance at $t = 0$ as

$$S_1(\mathbf{x}, \mathbf{k}) = 2S(\mathbf{k}) \cos(\mathbf{c}\cdot\mathbf{x}). \quad (3.66)$$

Equation (3.64) at $t = 0$ will give

$$\rho(\mathbf{x}, \mathbf{r}) = \int_{-\infty}^{\infty} e^{i(\mathbf{k}-\mathbf{k}_0)\cdot\mathbf{r}} \left(S_h(\mathbf{k}) + \frac{\delta}{2} \left(S_1\left(\mathbf{k}, \mathbf{x} + \frac{1}{2}\mathbf{r}\right) + S_1\left(\mathbf{k}, \mathbf{x} - \frac{1}{2}\mathbf{r}\right) \right) \right) d\mathbf{k}.$$

Making use of equation (3.8) at $t = 0$ gives

$$\rho(\mathbf{x}, \mathbf{r}) = \rho_h(\mathbf{r}) + \delta \rho_1(\mathbf{x}, \mathbf{r}).$$

Hence, from these previous consecutive two equations, one obtains

$$\rho_h(\mathbf{r}) = \int_{-\infty}^{\infty} S_h(\mathbf{k}) e^{i(\mathbf{k}-\mathbf{k}_0)\cdot\mathbf{r}} d\mathbf{k}$$

and

$$\rho_1(\mathbf{x}, \mathbf{r}) = \frac{1}{2} \int_{-\infty}^{\infty} \left(S_1\left(\mathbf{k}, \mathbf{x} + \frac{1}{2}\mathbf{r}\right) + S_1\left(\mathbf{k}, \mathbf{x} - \frac{1}{2}\mathbf{r}\right) \right) e^{i(\mathbf{k}-\mathbf{k}_0)\cdot\mathbf{r}} d\mathbf{k}. \quad (3.67)$$

Making use of equation (3.66), one will obtain,

$$S_1\left(\mathbf{k}, \mathbf{x} + \frac{1}{2}\mathbf{r}\right) = 2S(\mathbf{k}) \left(\cos(\mathbf{c} \cdot \mathbf{x}) \cos\left(\frac{1}{2}\mathbf{c} \cdot \mathbf{r}\right) - \sin(\mathbf{c} \cdot \mathbf{x}) \sin\left(\frac{1}{2}\mathbf{c} \cdot \mathbf{r}\right) \right)$$

and

$$S_1\left(\mathbf{k}, \mathbf{x} - \frac{1}{2}\mathbf{r}\right) = 2S(\mathbf{k}) \left(\cos(\mathbf{c} \cdot \mathbf{x}) \cos\left(\frac{1}{2}\mathbf{c} \cdot \mathbf{r}\right) + \sin(\mathbf{c} \cdot \mathbf{x}) \sin\left(\frac{1}{2}\mathbf{c} \cdot \mathbf{r}\right) \right).$$

As a result, equation (3.67) becomes

$$\rho_1(\mathbf{x}, \mathbf{r}) = \int_{-\infty}^{\infty} 2S(\mathbf{k}) \cos(\mathbf{c} \cdot \mathbf{x}) \cos\left(\frac{1}{2}\mathbf{c} \cdot \mathbf{r}\right) e^{i(\mathbf{k}-\mathbf{k}_0)\cdot\mathbf{r}} d\mathbf{k}.$$

From this equation and equation (3.65), one will also get

$$2R(\mathbf{r}) = 2 \int_{-\infty}^{\infty} S(\mathbf{k}) \cos\left(\frac{1}{2}\mathbf{c} \cdot \mathbf{r}\right) e^{i(\mathbf{k}-\mathbf{k}_0)\cdot\mathbf{r}} d\mathbf{k}.$$

Since $2\cos\left(\frac{1}{2}\mathbf{c} \cdot \mathbf{r}\right) = e^{i\mathbf{c}\cdot\mathbf{r}/2} + e^{-i\mathbf{c}\cdot\mathbf{r}/2}$, above equation can be rewritten as

$$2R(\mathbf{r}) = \int_{-\infty}^{\infty} S(\mathbf{k}) \left(e^{i(\mathbf{k}-\mathbf{k}_0+\mathbf{c}/2)\cdot\mathbf{r}} + e^{i(\mathbf{k}-\mathbf{k}_0-\mathbf{c}/2)\cdot\mathbf{r}} \right) d\mathbf{k}. \quad (3.68)$$

Taking the \mathbf{r} to define χ Fourier transform of (3.68) yields,

$$2 \int_{-\infty}^{\infty} R(\mathbf{r}) e^{-i\mathbf{x}\cdot\mathbf{r}} d\mathbf{r} = \int_{-\infty}^{\infty} \int_{-\infty}^{\infty} S(\mathbf{k}) \left(e^{i(\mathbf{k}-\mathbf{k}_0+\frac{\mathbf{c}}{2}-\boldsymbol{\chi})\cdot\mathbf{r}} + e^{i(\mathbf{k}-\mathbf{k}_0-\frac{\mathbf{c}}{2}-\boldsymbol{\chi})\cdot\mathbf{r}} \right) d\mathbf{r} d\mathbf{k}. \quad (3.69)$$

Integrating the right hand side with respect to \mathbf{r} by using the following delta function property (Champeney, 1973),

$$\int_{-\infty}^{\infty} \int_{-\infty}^{\infty} S(\mathbf{k}) e^{\pm i(\mathbf{k}-\mathbf{k}_0)\cdot\mathbf{r}} d\mathbf{r} d\mathbf{k} = (2\pi)^2 \int_{-\infty}^{\infty} S(\mathbf{k}) \delta(\mathbf{k} - \mathbf{k}_0) d\mathbf{k} = (2\pi)^2 S(\mathbf{k}_0)$$

yields,

$$\begin{aligned} \int_{-\infty}^{\infty} \int_{-\infty}^{\infty} S(\mathbf{k}) \left(e^{i(\mathbf{k}-\mathbf{k}_0+\frac{\mathbf{c}}{2}-\boldsymbol{\chi})\cdot\mathbf{r}} + e^{i(\mathbf{k}-\mathbf{k}_0-\frac{\mathbf{c}}{2}-\boldsymbol{\chi})\cdot\mathbf{r}} \right) d\mathbf{r} d\mathbf{k} \\ = (2\pi)^2 \left(S\left(\mathbf{k}_0 - \frac{\mathbf{c}}{2} + \boldsymbol{\chi}\right) + S\left(\mathbf{k}_0 + \frac{\mathbf{c}}{2} + \boldsymbol{\chi}\right) \right). \end{aligned}$$

Therefore, equation (3.69) becomes

$$\frac{1}{2\pi^2} \int_{-\infty}^{\infty} R(\mathbf{r}) e^{-i\mathbf{x}\cdot\mathbf{r}} d\mathbf{r} = S\left(\mathbf{k}_0 - \frac{\mathbf{c}}{2} + \boldsymbol{\chi}\right) + S\left(\mathbf{k}_0 + \frac{\mathbf{c}}{2} + \boldsymbol{\chi}\right).$$

Let $\boldsymbol{\chi} = \mathbf{k} - \mathbf{k}_0$, then above equation becomes

$$\frac{1}{2\pi^2} \int_{-\infty}^{\infty} R(\mathbf{r}) e^{-i(\mathbf{k}-\mathbf{k}_0)\cdot\mathbf{r}} d\mathbf{r} = S\left(\mathbf{k} - \frac{\mathbf{c}}{2}\right) + S\left(\mathbf{k} + \frac{\mathbf{c}}{2}\right).$$

Furthermore, applying Taylor series for the right hand side of the previous equation and neglecting the second order of \mathbf{c} gives,

$$S\left(\mathbf{k} - \frac{\mathbf{c}}{2}\right) + S\left(\mathbf{k} + \frac{\mathbf{c}}{2}\right) = 2 S(\mathbf{k}).$$

Thus, the equation for $S(\mathbf{k})$ can be written as

$$S(\mathbf{k}) = \frac{1}{(2\pi)^2} \int_{-\infty}^{\infty} R(\mathbf{r}) e^{-i(\mathbf{k}-\mathbf{k}_0)\cdot\mathbf{r}} d\mathbf{r}. \quad (3.70)$$

Equations (3.62), (3.66) and (3.70) give the initial spectrum.

One has to note that the similarities between the pair $(\rho_h(\mathbf{r}), S_h(\mathbf{k}))$ and the pair $(R(\mathbf{r}), S(\mathbf{k}))$ are demonstrated by their interrelations as shown in the following

$$\rho_h(\mathbf{r}) = \int_{-\infty}^{\infty} S_h(\mathbf{k}) e^{i(\mathbf{k}-\mathbf{k}_0)\cdot\mathbf{r}} d\mathbf{k}, \quad (3.71)$$

$$S_h(\mathbf{k}) = \frac{1}{(2\pi)^2} \int_{-\infty}^{\infty} \rho_h(\mathbf{r}) e^{-i(\mathbf{k}-\mathbf{k}_0)\cdot\mathbf{r}} d\mathbf{r}, \quad (3.72)$$

$$R(\mathbf{k}) = \int_{-\infty}^{\infty} S(\mathbf{k}) e^{i(\mathbf{k}-\mathbf{k}_0)\cdot\mathbf{r}} d\mathbf{k}, \quad (3.73)$$

$$S(\mathbf{k}) = \frac{1}{(2\pi)^2} \int_{-\infty}^{\infty} R(\mathbf{r}) e^{-i(\mathbf{k}-\mathbf{k}_0)\cdot\mathbf{r}} d\mathbf{r}. \quad (3.74)$$

3.5.2 Connection to the initial surface elevation

It is important to show the connection of the initial disturbance to the initial surface elevation. Therefore, in this subsection, calculation of the initial surface elevation, η , will be derived. Starting from the equation (3.4) which is evaluated at $t = 0$ yields,

$$2\eta(\mathbf{x}) = \int_{-\infty}^{\infty} e^{i(\mathbf{k}\cdot\mathbf{x}+\theta(\mathbf{k}))} \sqrt{S(\mathbf{k}, \mathbf{x})} d\mathbf{k} + c. c. \quad (3.75)$$

Moreover, from equation (3.62) and (3.66), one will get

$$S(\mathbf{x}, \mathbf{k}) = S_h(\mathbf{k}) + 2\delta S(\mathbf{k}) \cos(\mathbf{c} \cdot \mathbf{x})$$

and then,

$$\sqrt{S(\mathbf{x}, \mathbf{k})} = \sqrt{S_h(\mathbf{k}) + 2\delta S(\mathbf{k}) \cos(\mathbf{c} \cdot \mathbf{x})}.$$

Substituting this result into (3.75) gives

$$2\eta(\mathbf{x}) = \int_{-\infty}^{\infty} e^{i(\mathbf{k}\cdot\mathbf{x}+\theta(\mathbf{k}))} \sqrt{(S_h(\mathbf{k}) + 2\delta S(\mathbf{k}) \cos(\mathbf{c} \cdot \mathbf{x}))} \sqrt{d\mathbf{k}} + c. c.$$

Furthermore, approximating the value under the square root, yields,

$$\sqrt{(S_h(\mathbf{k}) + 2\delta S(\mathbf{k}) \cos(\mathbf{c} \cdot \mathbf{x}))} = \sqrt{S_h(\mathbf{k})} + \cos(\mathbf{c} \cdot \mathbf{x}) \sqrt{\frac{\delta^2 S^2(\mathbf{k})}{S_h(\mathbf{k})}}.$$

As a result, the surface elevation can be written as

$$2\eta(\mathbf{x}) = \int_{-\infty}^{\infty} e^{i(\mathbf{k} \cdot \mathbf{x} + \theta(\mathbf{k}))} \left(\sqrt{S_h(\mathbf{k})} + \cos(\mathbf{c} \cdot \mathbf{x}) \sqrt{\frac{\delta^2 S^2(\mathbf{k})}{S_h(\mathbf{k})}} \right) \sqrt{d\mathbf{k}} + c. c.$$

For convenient, this equation can be rewritten as

$$2\eta(\mathbf{x}) = \int_{-\infty}^{\infty} e^{i(\mathbf{k} \cdot \mathbf{x} + \theta(\mathbf{k}))} \sqrt{S_h(\mathbf{k})} d\mathbf{k} + \cos(\mathbf{c} \cdot \mathbf{x}) \int_{-\infty}^{\infty} e^{i(\mathbf{k} \cdot \mathbf{x} + \theta(\mathbf{k}))} \sqrt{\frac{\delta^2 S^2(\mathbf{k})}{S_h(\mathbf{k})}} d\mathbf{k} + c. c. \quad (3.76)$$

This result shows that the phases $\theta(\mathbf{k})$ of the inhomogeneous disturbance are not free, and are related to the phases of the homogeneous spectrum. In addition, since $\cos(\mathbf{c} \cdot \mathbf{x}) = (e^{i\mathbf{c} \cdot \mathbf{x}} + e^{-i\mathbf{c} \cdot \mathbf{x}})/2$, equation (3.76) can be rewritten as

$$2\eta(\mathbf{x}) = \int_{-\infty}^{\infty} \left(e^{i(\mathbf{k} \cdot \mathbf{x} + \theta(\mathbf{k}))} \sqrt{S_h(\mathbf{k})} + \frac{1}{2} e^{i(\mathbf{k} \cdot \mathbf{x} + \mathbf{c} \cdot \mathbf{x} + \theta(\mathbf{k}))} \sqrt{\frac{\delta^2 S^2(\mathbf{k})}{S_h(\mathbf{k})}} + \frac{1}{2} e^{i(\mathbf{k} \cdot \mathbf{x} - \mathbf{c} \cdot \mathbf{x} + \theta(\mathbf{k}))} \sqrt{\frac{\delta^2 S^2(\mathbf{k})}{S_h(\mathbf{k})}} \right) \sqrt{d\mathbf{k}} + c. c. \quad (3.77)$$

A shift of integration variables in the last two terms on the right-hand side gives

$$2\eta(\mathbf{x}) = \int_{-\infty}^{\infty} \left(e^{i(\mathbf{k} \cdot \mathbf{x} + \theta(\mathbf{k}))} \sqrt{S_h(\mathbf{k})} + \frac{1}{2} e^{i(\mathbf{k} \cdot \mathbf{x} + \theta(\mathbf{k} - \mathbf{c}))} \sqrt{\frac{\delta^2 S^2(\mathbf{k} - \mathbf{c})}{S_h(\mathbf{k} - \mathbf{c})}} + \frac{1}{2} e^{i(\mathbf{k} \cdot \mathbf{x} + \theta(\mathbf{k} + \mathbf{c}))} \sqrt{\frac{\delta^2 S^2(\mathbf{k} + \mathbf{c})}{S_h(\mathbf{k} + \mathbf{c})}} \right) \sqrt{d\mathbf{k}} + c. c. \quad (3.78)$$

where $\mathbf{c} = (p, q)$.

Finally, from equation (3.78) one can see that the phases of the right and left disturbances are identical to those of the homogeneous spectrum, which are random.

For one-dimensional case, one can refer to Figure 4 of Stiassnie et al. (2008) as shown in Figure 3.23.

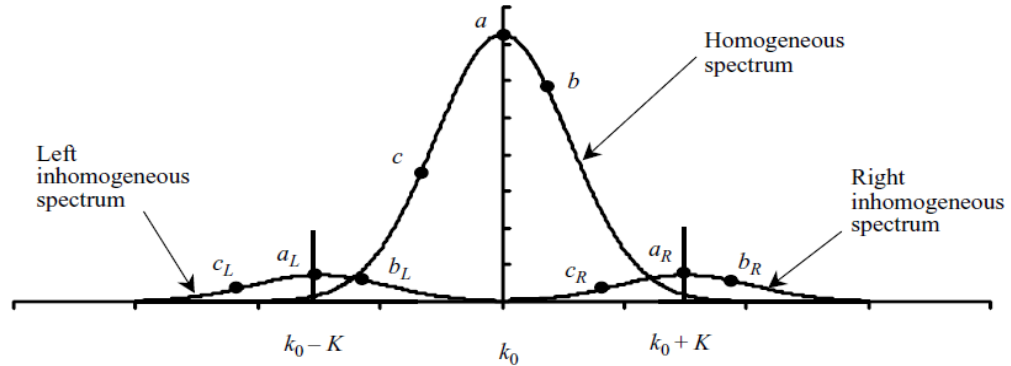


Figure 3.23: Schematic description of the main homogeneous spectrum and the inhomogeneous disturbances (see Fig. 4 of Stiassnie et al. (2008)).

3.6 Concluding remarks

Linear stability analysis of narrow spectra homogeneous seas for two spatial dimensions subject to inhomogeneous disturbances by means of the Alber equation is studied in this Chapter. The actual growth rate and the point of maximum growth rate of both symmetric and asymmetric spectra were studied. The symmetric spectra are square spectra, rectangular spectra and Lorentz spectra as well as the Lorentzian spectra which was obtained by approximating a JONSWAP spectrum, while the asymmetric spectra are the well-known JONSWAP spectra with and without directional distributions.

The key parameters for symmetric spectra are the spectral width in directions parallel and perpendicular to the carrier wave. It is found numerically from square spectra and rectangular spectra and analytically from the Lorentz spectra that the maximum growth rate is independent of the spectral width which is perpendicular to carrier wave. Besides that, it was also shown that the role of the spectral width in direction perpendicular to the carrier wave is to shrink the area of instability.

For JONSWAP spectrum, which is asymmetric spectrum, the key parameters are the energy scale, α , and the peak enhancement factor, γ , for unidirectional spectrum and also the degree of the directional distributions for directional wave spectrum. Since these spectra are asymmetric and cannot be integrated analytically, it is necessary to

seek an approximate solution. To this end, a “general method” has been established by replacing the original spectrum by a sum of weighted Dirac-delta functions. Seeking the root of Ω , which is the frequency of the disturbance, with the largest imaginary contribution will give the maximum growth rate of the given spectrum. Based on this result, one can also get the point of maximum growth rate. The validity of this method is demonstrated by using a Lorentz spectrum that can be solved analytically.

For unidirectional JONSWAP spectra, it is found that increasing the energy scale while keeping the peak enhancement factor constant will increase the maximum growth rate. Similarly, keeping the energy scale constant and increasing the peak enhancement factor will increase the maximum growth rate. For JONSWAP spectrum with directional distributions, the degree of the directional spreading is an additional parameter to the unidirectional spectrum. It is found that increasing the directionality of the spectrum will decrease the maximum growth rate or even stop the instability. This conclusion agrees with the measurements in the tanks which are in the literature.

Furthermore, the instability criterion for JONSWAP spectra with and without directional spreading was introduced. The criterion is determined by a dimensionless “width parameter”, Π_1 , for unidirectional JONSWAP spectrum and a slightly corrected dimensionless “width parameter”, Π_2 , for JONSWAP spectrum with directional distributions. Specifically, a unidirectional JONSWAP spectrum is unstable to inhomogeneous disturbance if

$$\Pi_1 = \frac{\varepsilon}{\alpha\gamma} < 1,$$

where ε is the typical wave steepness.

Similarly, a JONSWAP spectrum with directional distributions is unstable to inhomogeneous disturbance if

$$\Pi_2 = \frac{\varepsilon}{\alpha\gamma} + \frac{0.0256}{\varepsilon A_d} < 1.1,$$

where A_d is the normalization factor of the directional distribution.

It appears that the conclusion from two-dimensional Lorentz spectra is different from the conclusion obtained based on JONSWAP spectra with directional distributions in

terms of dependency on the transverse width of the spectrum. However, one can easily compare these spectra, namely Lorentz spectra and JONSWAP spectra by maintaining that both spectra have the same total energy and momentum. One will find that changing the power of the directional distribution of JONSWAP spectra will not only change the spectral width which is perpendicular to the carrier wave of the Lorentz spectra but also the spectral width which is parallel to the carrier wave.

Finally, the spectral interpretation of the inhomogeneous disturbance was derived and the intercorrelation between the homogeneous spectrum and homogeneous correlation function were shown. Moreover, the connection to the initial surface elevations was also derived.

Chapter 4

Long-time evolution in two spatial dimensions

4.1 Introduction

It is known from the cubic Schrödinger equation that Benjamin–Feir instability in one dimensional solution does not lead to a permanent end state, but to an unsteady series of modulation and demodulation cycles, called the Fermi–Pasta–Ulam recurrence phenomenon (Fermi et al., 1965). This interesting behaviour has been shown experimentally, numerically and analytically. Lake et al. (1977), for example, demonstrated in their wave-flume experiments how the modulation periodically increases and decreases at some stages of the evolution. They also have confirmed their experimental results by a numerical simulation using the nonlinear Schrödinger equation derived by Hasimoto and Ono (1972) for the water of finite depth. Another experiment investigating this recurrent behaviour was done by Tulin and Waseda (1999).

Based on the numerical solutions of one-dimensional nonlinear Schrödinger equation, Yuen and Ferguson (1978b), showed a simple relationship between the Benjamin–Feir instability and the long-time evolution of the unstable solution of nonlinear Schrödinger equation. In particular, they studied the influence of the initial condition on the long-time evolution, and defined two types of recurrence, namely, simple recurrence and complex recurrence. They explained that modulations with the perturbation wavenumber Δ in the range $\sqrt{2}a_0 \leq \Delta < 2\sqrt{2}a_0$ give a simple recurrence because all the higher harmonics of the prescribed modulation are stable while modulations with the perturbation wavenumber Δ in the range $0 \leq \Delta < \sqrt{2}a_0$ give a complex recurrence because at least one higher harmonic of the prescribed mode lies in the unstable region. In order to confirm the numerical results obtained by Yuen and Ferguson (1978b), Rowlands (1980) attempted to estimate the period of the evolution based on Yuen and Ferguson (1978b) numerical simulation analytically. He found that the time evolution is

periodic for the case of simple recurrence. Working independently, Janssen (1981) studied the long-time behaviour of the modulational instability near the instability threshold by means of the multiple time scaled method. He found that a weakly unstable modulation of a uniform wave train exhibits the Fermi-Pasta-Ulam recurrence phenomenon. Both authors studied the long-time evolution for the wavenumber of the disturbance Δ limited to very near $\Delta = 2\sqrt{2}a_0$. Pointing out this limitation, Infeld (1981) removed this restriction made by two previous authors and, then, gave a more general calculation where the wavenumber of the disturbance is not restricted to very near $2\sqrt{2}a_0$. As a results, he obtained a quantitative theory of the Fermi-Pasta-Ulam recurrence for the nonlinear Schrödinger equation, at least for $\sqrt{2}a_0 \leq \Delta < 2\sqrt{2}a_0$. Another numerical solution that shows the long-time evolution from nonlinear Schrödinger equation was done by Martin and Yuen (1980b) who show the spreading energy during the evolution are computed. Moreover, the more general study of long-time evolution of an unstable water-wave train based on cubic Schrödinger equation theoretically albeit for simplified system was done by Stiassnie and Kroszynski (1982).

For two spatial dimensions of the nonlinear Schrödinger equation, Yuen and Ferguson (1978a) investigated influence of the initial condition on the long-time evolution in two spatial dimensions of the nonlinear Schrödinger equation and also found that such evolution exhibits the Fermi-Pasta-Ulam recurrence phenomenon. Moreover, based on the works of Yuen and Ferguson (1978a, 1978b), Martin and Yuen (1980a) found the energy leakage from lower mode to unstable higher harmonics in a quasi-recurring manner.

A stochastic generalization of cubic Schrödinger equation was designed by Alber (1978) which is now known as the Alber equation. His finding is, therefore, the stochastic counterpart of the well-known deterministic Benjamin-Feir instability obtained for cubic Schrödinger equation. Since this equation cannot be solved analytically (at least up to this stage), in order to study a stochastic parallel to Fermi-Pasta-Ulam recurrence phenomenon, a numerical method will be used. Specifically, the Alber equation will be integrated numerically.

The only known attempt to obtain subsequent evolution for the solution of the one dimensional Alber equation is that of Janssen (1983). He used an asymptotic method to solve the problem near the threshold of instability and obtained a solution which is

characterized by an initial small overshoot followed by an oscillation around its time asymptotic value. Recently, Stiassnie et al. (2008) also used one-dimensional Alber equation to study the linear instability of narrow-spectra homogeneous seas and its subsequent evolution in time, subject to inhomogeneous disturbances. They found that in the region of instability, recurrent evolution, which is the stochastic counterpart of the Fermi–Pasta–Ulam recurrence obtained for the cubic Schrödinger equation, occurs. Their initial homogeneous wave fields have simple one-dimensional spectra of three different types, namely, square, Lorentz and Gaussian.

These two aforementioned findings are limited to unidirectional wave fields. Real sea states, however, are characterized by wave components propagating along different directions. Numerical simulations (e.g. Onorato et al. 2002, Socquet-Juglard et al. 2005, Gramstad and Trulsen 2007, Eliasson and Shukla 2010) have revealed that wave directional spreading reduces the effect of instability. Furthermore, Onorato et al. (2009a, 2009b) and Waseda et al. (2009) performed two independent experimental investigations, in order to study statistical properties of surface elevations for different degrees of directional energy spreading. The experimental facilities used had different sizes and they were equipped with different wave makers. Nevertheless, they reported consistent results and claimed that the modulational instability process, which is one of the main mechanisms of formation of extreme and breaking waves in deep-water, random, long-crested waves, seems to be quenched when directional waves are considered. Babanin et al. (2010, 2011b), however, argued that, for a given bandwidth, directional spreading is not the only property of surface wave fields to influence the modulational instability. If the directional spreading becomes too broad and wave field stabilizes, increase of the steepness can re-activate the instability. Although some experimental estimations have been made (Babanin et al., 2010, 2011a), it is not yet clear what is the role of wave instability in the evolution of directional wave fields (Babanin, 2011, 2011b).

Therefore, extending the work of Stiassnie et al. (2008), we will be working with realistic asymmetric JONSWAP spectra of ocean waves, for both unidirectional waves and JONSWAP spectra with directional distributions. We will show that they can reproduce a stochastic recurrence which is parallel to Fermi-Pasta-Ulam recurrence in the unstable conditions. These unstable conditions will occur (see previous Chapter)

when the dimensionless “width parameter”, $\Pi_1 < 1$ for unidirectional JONSWAP spectra and $\Pi_2 < 1.1$, for JONSWAP spectra with directional distributions.

4.2 Numerical solution of the Alber equation

There are several methods to solve partial differential equations numerically such as finite difference method (FDM), boundary element method (BEM) and finite element method (FEM). However, in order to solve the Alber equation, a finite difference method will be used because of its simplicity. We start from the non-dimensional Alber equation, then a simplified problem will be considered due to the high computational cost. Note that the Alber equation consists of five parameters that require huge computer memory and long computational time. Therefore, we consider a simplification by reducing the equation to four parameters. As a result, this can reduce computing resources significantly. Based on the simplified equation, a numerical scheme is derived. Furthermore, the initial conditions and the boundary conditions are also determined.

4.2.1 Non-dimensional Alber equation

It is convenient to change the two-spatial-dimensions Alber equation on the infinitely deep water from the dimensional form as in the equation (3.1) to non-dimensional variables using the following relations

$$\tilde{\rho} = \frac{k_0^2}{\varepsilon^2} \rho; \quad \tilde{x} = \varepsilon k_0 \left(x - \frac{1}{2} \sqrt{\frac{g}{k_0}} t \right); \quad \tilde{y} = \varepsilon k_0 y; \quad \tilde{r}_1 = \varepsilon k_0 r_1; \quad \tilde{r}_2 = \varepsilon k_0 r_2; \quad \tilde{t} = \varepsilon^2 \sqrt{g k_0} t,$$

which yields

$$i \frac{\partial \tilde{\rho}}{\partial \tilde{t}} + 2\lambda \frac{\partial^2 \tilde{\rho}}{\partial \tilde{x} \partial \tilde{r}_1} + 2\mu \frac{\partial^2 \tilde{\rho}}{\partial \tilde{y} \partial \tilde{r}_2} - 2v \tilde{\rho} \left(\tilde{\rho} \left(\tilde{\mathbf{x}} + \frac{1}{2} \tilde{\mathbf{r}}, \mathbf{0}, \tilde{t} \right) - \tilde{\rho} \left(\tilde{\mathbf{x}} - \frac{1}{2} \tilde{\mathbf{r}}, \mathbf{0}, \tilde{t} \right) \right) = 0 \quad (4.1)$$

$$\text{where } \lambda = -\frac{1}{8}; \quad \mu = \frac{1}{4}; \quad v = \frac{1}{2}.$$

In order to study the long-time evolution which is a stochastic counterpart of the Fermi–Pasta–Ulam recurrence obtained for the cubic Schrödinger equation, the Alber equation will be integrated numerically. To this end, a two-dimensional perturbation and a two-

dimensional spectrum are required. However, since the equation includes five-dimensional space, it will be computationally expensive even for a supercomputer. Therefore, a simplified case will be considered where only a two-dimensional spectrum and one-dimensional perturbation will be used. This is based on the assumption made and supported in Chapter 3 that the most unstable mode occurs at $q = 0$ which is the wavenumber of the disturbance in direction perpendicular to the carrier wave. As a result, the third term of the equation (4.1) vanishes automatically and, therefore, the dimensionless Alber equation can be rewritten as follows:

$$i \frac{\partial \tilde{\rho}}{\partial \tilde{\tau}} + 2\lambda \frac{\partial^2 \tilde{\rho}}{\partial \tilde{x} \partial \tilde{r}_1} - 2\nu \tilde{\rho} \left(\tilde{\rho} \left(\tilde{x} + \frac{1}{2} \tilde{r}_1, \mathbf{0}, \tilde{\tau} \right) - \tilde{\rho} \left(\tilde{x} - \frac{1}{2} \tilde{r}_1, \mathbf{0}, \tilde{\tau} \right) \right) = 0 \quad (4.2)$$

where $\tilde{\rho}$ is the dimensionless two-point correlation function which depends on four dimensionless variables namely \tilde{x} , \tilde{r}_1 , \tilde{r}_2 and $\tilde{\tau}$. In order to solve this equation numerically, the following procedures will be carried out.

4.2.2 Numerical scheme

In order to solve equation (4.2) numerically, a finite difference method will be used where the dimensionless time derivative is approximated by a forward difference, that is,

$$\left(\frac{\partial \tilde{\rho}}{\partial \tilde{\tau}} \right)_{(n,j,k,l)} = \frac{\tilde{\rho}_{(n,j,k,l+1)} - \tilde{\rho}_{(n,j,k,l)}}{\Delta \tilde{\tau}}.$$

This approximation has the accuracy $O(\Delta \tilde{\tau})$. The dimensionless spatial derivatives in \tilde{x} and \tilde{r}_1 are approximated by central differences with accuracy $O(\Delta \tilde{x}^2, \Delta \tilde{r}_1^2)$ giving

$$\left(\frac{\partial^2 \tilde{\rho}}{\partial \tilde{x} \partial \tilde{r}_1} \right)_{(n,j,k,l)} = \frac{\tilde{\rho}_{(n+1,j+1,k,l)} - \tilde{\rho}_{(n-1,j+1,k,l)} - (\tilde{\rho}_{(n+1,j-1,k,l)} - \tilde{\rho}_{(n-1,j-1,k,l)})}{4\Delta \tilde{x} \Delta \tilde{r}_1},$$

$$(\tilde{\rho}(\tilde{x}, \tilde{r}_1, \tilde{r}_2, \tilde{\tau}))_{(n,j,k,l)} = \tilde{\rho}_{(n,j,k,l)},$$

and

$$\left(\tilde{\rho} \left(\tilde{x} \pm \frac{1}{2} \tilde{r}_1, 0, 0, \tilde{\tau} \right) \right)_{(n,j,k,l)} = \tilde{\rho}_{(n \pm \frac{j \Delta \tilde{r}_1}{2 \Delta \tilde{x}}, 0, 0, l)}.$$

Index n belongs to points along the \tilde{x} axis, $\tilde{x} = n\Delta\tilde{x}$, $n = 0, 1, 2, \dots, N$ and $N+1$ is the number of points along this axis. Index j represents points along the \tilde{r}_1 axis, $\tilde{r}_1 = j\Delta\tilde{r}_1$, $j = 0, 1, 2, \dots, M_1$ and $M_1 + 1$ is the number of points along the \tilde{r}_1 axis. Similarly, index k represents points along the \tilde{r}_2 axis, $\tilde{r}_2 = k\Delta\tilde{r}_2$; $k = 0, 1, 2, \dots, M_2$, $M_2 + 1$ is the number of points along the \tilde{r}_2 axis, and l represents time steps by $\tilde{t} = l\Delta\tilde{t}$, where $l = 0, 1, 2, \dots, T$. $\Delta\tilde{t}$, $\Delta\tilde{x}$, $\Delta\tilde{r}_1$ and $\Delta\tilde{r}_2$ are the differential steps in time direction and the space directions respectively.

Substituting all above approximations into equation (4.2) gives,

$$\begin{aligned}
& i \left(\frac{\tilde{\rho}_{(n,j,k,l+1)} - \tilde{\rho}_{(n,j,k,l)}}{\Delta\tilde{t}} \right) \\
& + \frac{2\lambda}{4\Delta\tilde{x}\Delta\tilde{r}_1} \left(\tilde{\rho}_{(n+1,j+1,k,l)} - \tilde{\rho}_{(n-1,j+1,k,l)} \right. \\
& \quad \left. - \left(\tilde{\rho}_{(n+1,j-1,k,l)} - \tilde{\rho}_{(n-1,j-1,k,l)} \right) \right) \\
& - 2v\tilde{\rho}_{(n,j,k,l)} \left(\tilde{\rho}_{(n+\frac{j\Delta\tilde{r}_1}{2\Delta\tilde{x}}, 0, 0, l)} - \tilde{\rho}_{(n-\frac{j\Delta\tilde{r}_1}{2\Delta\tilde{x}}, 0, 0, l)} \right) = 0.
\end{aligned} \tag{4.3}$$

After simplification, the numerical time-stepping scheme is formulated as follows:

$$\begin{aligned}
\tilde{\rho}_{(n,j,k,l+1)} &= \tilde{\rho}_{(n,j,k,l)} \\
& + \frac{i\lambda\Delta\tilde{t}}{2\Delta\tilde{x}\Delta\tilde{r}_1} \left(\tilde{\rho}_{(n+1,j+1,k,l)} - \tilde{\rho}_{(n-1,j+1,k,l)} \right. \\
& \quad \left. - \left(\tilde{\rho}_{(n+1,j-1,k,l)} - \tilde{\rho}_{(n-1,j-1,k,l)} \right) \right) \\
& - 2i\Delta\tilde{t}v\tilde{\rho}_{(n,j,k,l)} \left(\tilde{\rho}_{(n+\frac{j\Delta\tilde{r}_1}{2\Delta\tilde{x}}, 0, 0, l)} - \tilde{\rho}_{(n-\frac{j\Delta\tilde{r}_1}{2\Delta\tilde{x}}, 0, 0, l)} \right).
\end{aligned} \tag{4.4}$$

The following values for differential steps were taken after several attempts. For the unidirectional JONSWAP spectra as a special case, the differential steps are: $\Delta\tilde{x} = \pi/100$, $\Delta\tilde{r}_1 = \pi/44$ and $\Delta\tilde{t} = 5 \times 10^{-5}$ while for the JONSWAP spectra with different degrees of the directional spreading the differential steps are: $\Delta\tilde{x} = \pi/75$, $\Delta\tilde{r}_1 = \pi/35$, $\Delta\tilde{r}_2 = \pi/25$ and $\Delta\tilde{t} = 4 \times 10^{-5}$. Taking smaller values will not give a significant effect. In addition, the size of the domain along \tilde{x} axis is $\tilde{x} \in (0, 2\pi/\tilde{P}^{(max)})$ where $\tilde{P}^{(max)}$ is the dimensionless wavenumber of the disturbance which is parallel to the carrier wave and is the point of maximum growth rate. The size of the dimensions of \tilde{r}_1 and \tilde{r}_2 will be determined later. In general the schematic description of the domain for

one dimensional case is shown in the following Figure 4.1 which is the same as given in the Figure 5 of Stiasnie et al. (2008). For given value of \tilde{P} , we can obtain the values of \tilde{x}_{end} and $(\tilde{r}_1)_{end}$ straightforward, respectively. However, the schematic description of the domain for two-dimensional cases cannot be shown as it contains more than three variables. Furthermore, the boundary conditions will be determined in the following sections.

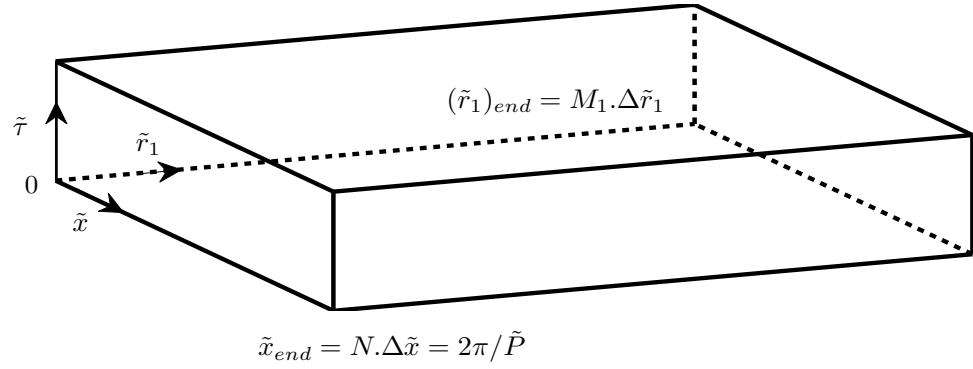


Figure 4.1: Schematic description of the numerical domain for one-dimensional case (see Fig. 5 of Stiasnie et al., 2008).

4.2.3 Periodicity in \tilde{x}

We limit the discussion to periodic solution in \tilde{x} so that on the boundaries $\tilde{x} = \tilde{x}_{end}$, $\tilde{\rho}_{(N,j,k,l)} = \tilde{\rho}_{(0,j,k,l)}$. Moreover, the last term on the right hand side of equation (4.4) depends on the values of $\tilde{\rho}$ at $\tilde{x} = n + j\Delta\tilde{r}_1/(2\Delta\tilde{x})$ which can be larger than $\tilde{x}_{end} = N\Delta\tilde{x}$. In this condition, the periodicity, again, is used, that is $\tilde{\rho}(\tilde{x} + 2q\pi, \tilde{\mathbf{r}}, \tilde{\tau}) = \tilde{\rho}(\tilde{x}, \tilde{\mathbf{r}}, \tilde{\tau})$ where $q = 1, 2, 3, \dots$. This equation can be rewritten as $\tilde{\rho}_{(n+qN,j,k,l)} = \tilde{\rho}_{(n,j,k,l)}$. Similarly, the values of $\tilde{\rho}$ along $\tilde{\mathbf{r}} = \mathbf{0}$, depend on points outside the domain $0 \leq \tilde{r}_1 \leq (\tilde{r}_1)_{end}$; $0 \leq \tilde{r}_2 \leq (\tilde{r}_2)_{end}$. In particular, the second term on the right hand side of equation (4.4) depends on $\tilde{\rho}_{(n+1,-1,k,l)}$. In order to deal with this problems, the definition of $\tilde{\rho}$ which is the two-point correlation function in equation (3.2) will be used, that is $\tilde{\rho}(\tilde{x}, -\tilde{\mathbf{r}}, \tilde{\tau}) = \tilde{\rho}^*(\tilde{x}, \tilde{\mathbf{r}}, \tilde{\tau})$. Therefore, the values of $\tilde{\rho}$ along $\tilde{\mathbf{r}} = \mathbf{0}$, can be calculated from the conditions $\tilde{\rho}_{(n+1,-1,k,l)} = \tilde{\rho}_{(n+1,1,k,l)}^*$ where asterisk stands for the complex conjugate.

4.2.4 Condition at large $\tilde{\mathbf{r}}$

Another condition that has to be defined for the numerical scheme is the condition at large $\tilde{\mathbf{r}}$. Following a procedure similar to Stiassnie et al. (2008), the boundary condition for large $\tilde{\mathbf{r}}$ will be derived as follows. We start from equation (3.63) and approximate $S(\mathbf{k}, x)$ by a two-dimensional rectangular spectrum in $(k_1 - k_0) \in (-W_l, W_r)$ and $k_2 \in (-W, W)$ where W_l and W_r are the spectral width on the left hand side and on the right hand side of k_0 , which is the carrier, respectively, whilst W is the spectral width in direction perpendicular to the carrier wave, that is,

$$\rho(x, \mathbf{r}, \tau) = \int_{-\infty}^{\infty} e^{i(\mathbf{k}-\mathbf{k}_0)\cdot\mathbf{r}} \sqrt{S\left(\mathbf{k}, x + \frac{1}{2}r_1, \tau\right) S\left(\mathbf{k}, x - \frac{1}{2}r_1, \tau\right)} d\mathbf{k}. \quad (4.5)$$

Since a two-dimensional rectangular spectrum is independent of \mathbf{k} , equation (4.5) can be rewritten as

$$\rho(x, \mathbf{r}, \tau) = \sqrt{S\left(\mathbf{k}, x + \frac{1}{2}r_1, \tau\right) S\left(\mathbf{k}, x - \frac{1}{2}r_1, \tau\right)} \int_{-\infty}^{\infty} e^{i(\mathbf{k}-\mathbf{k}_0)\cdot\mathbf{r}} d\mathbf{k}. \quad (4.6)$$

Calculating the integrals yields,

$$\begin{aligned} \int_{-\infty}^{\infty} e^{i(\mathbf{k}-\mathbf{k}_0)\cdot\mathbf{r}} d\mathbf{k} &= \int_{-W}^W \int_{k_0-W_l}^{k_0+W_r} e^{i[(k_1-k_0)r_1+k_2r_2]} dk_1 dk_2 \\ &= \left(\int_{-W}^W e^{ik_2r_2} dk_2 \right) \left(\int_{k_0-W_l}^{k_0+W_r} e^{i(k_1-k_0)r_1} dk_1 \right) \end{aligned}$$

and then finally gives,

$$\int_{-\infty}^{\infty} e^{i(\mathbf{k}-\mathbf{k}_0)\cdot\mathbf{r}} d\mathbf{k} = -\frac{1}{r_1 r_2} (e^{iWr_2} - e^{-iWr_2}) (e^{ir_1W_r} - e^{-ir_1W_l}). \quad (4.7)$$

Using the fact that $e^{iWr_2} - e^{-iWr_2} = 2i \sin(Wr_2)$, equation (4.7) can be rewritten as

$$\int_{-\infty}^{\infty} e^{i(\mathbf{k}-\mathbf{k}_0)\cdot\mathbf{r}} d\mathbf{k} = \left(\frac{2 \sin(Wr_2)}{r_2} \right) \left(\frac{e^{ir_1W_r} - e^{-ir_1W_l}}{ir_1} \right). \quad (4.8)$$

Substituting equation (4.8) into equation (4.6), gives

$$\rho(x, \mathbf{r}, \tau) = 2 \sqrt{S\left(\mathbf{k}, x + \frac{1}{2}r_1, \tau\right) S\left(\mathbf{k}, x - \frac{1}{2}r_1, \tau\right)} \left[\frac{\sin(Wr_2)}{r_2} \right] \left[\frac{e^{ir_1W_r} - e^{-ir_1W_l}}{ir_1} \right]. \quad (4.9)$$

For $\mathbf{r} = \mathbf{0}$, equation (4.9) becomes

$$\rho(x, \mathbf{0}, \tau) = 2S(\mathbf{k}, x, \tau) \left(\lim_{r_1 \rightarrow 0} \frac{e^{ir_1W_r} - e^{-ir_1W_l}}{ir_1} \right) \left(\lim_{r_2 \rightarrow 0} \frac{\sin(Wr_2)}{r_2} \right).$$

Moreover, since

$$\lim_{r_1 \rightarrow 0} \frac{e^{ir_1W_r} - e^{-ir_1W_l}}{ir_1} = W_l + W_r \quad \text{and} \quad \lim_{r_2 \rightarrow 0} \frac{\sin(Wr_2)}{r_2} = W,$$

equation (4.9) can then be rewritten as

$$\rho(x, \mathbf{0}, \tau) = 2S(\mathbf{k}, x, \tau)(W_l + W_r)W.$$

Solving this equation for $S(\mathbf{k}, x, \tau)$ yields,

$$S(\mathbf{k}, x, \tau) = \frac{\rho(x, \mathbf{0}, \tau)}{2(W_l + W_r)W}.$$

Furthermore, making use of this result, equation (4.9) finally becomes

$$\rho(x, \mathbf{r}, \tau) = \sqrt{\rho\left(x + \frac{1}{2}r_1, \mathbf{0}, \tau\right) \rho\left(x - \frac{1}{2}r_1, \mathbf{0}, \tau\right)} \left[\frac{\sin(Wr_2)}{Wr_2} \right] \left[\frac{e^{ir_1W_r} - e^{-ir_1W_l}}{i(W_l + W_r)r_1} \right]. \quad (4.10)$$

Switching to non-dimensional quantities where

$$\tilde{r}_1 = \varepsilon k_0 r_1; \quad \tilde{r}_2 = \varepsilon k_0 r_2; \quad \tilde{W} = \frac{W}{\varepsilon k_0}; \quad \tilde{W}_l = \frac{W_l}{\varepsilon k_0}; \quad \tilde{W}_r = \frac{W_r}{\varepsilon k_0}, \quad (4.11)$$

gives,

$$\tilde{\rho}(\tilde{x}, \tilde{\mathbf{r}}, \tilde{\tau}) = \sqrt{\tilde{\rho}\left(\tilde{x} + \frac{1}{2}\tilde{r}_1, \mathbf{0}, \tilde{\tau}\right) \tilde{\rho}\left(\tilde{x} - \frac{1}{2}\tilde{r}_1, \mathbf{0}, \tilde{\tau}\right)} \left(\frac{\sin(\tilde{W}\tilde{r}_2)}{\tilde{W}\tilde{r}_2} \right) \left(\frac{e^{i\tilde{r}_1\tilde{W}_r} - e^{-i\tilde{r}_1\tilde{W}_l}}{i(\tilde{W}_l + \tilde{W}_r)\tilde{r}_1} \right) \quad (4.12)$$

which is the boundary condition used at larger \tilde{r}_1 or \tilde{r}_2 .

In order to determine the values of \tilde{W} , \tilde{W}_l and \tilde{W}_r , one needs to compare the rectangular spectrum with the JONSWAP spectrum in a way that maintains the total energy and momentum. Such comparison is shown below. As given in Chapter 3, for one-dimensional problem, the unidirectional JONSWAP spectrum, $S(k_1)$, and the rectangular spectrum, $S_{rec}(k_1)$, as a function of the wavenumber can be written as

$$S(k_1) = \frac{\alpha}{2k_1^3} e^{-\left(\frac{5k_0^2}{4k_1^2}\right)} \gamma e^{-\left[\frac{1}{2\sigma^2 k_0}(\sqrt{k_1} - \sqrt{k_0})^2\right]} \quad (4.13)$$

and

$$S_{rec}(k_1) = s_0 ; \quad k_0 - W_l < k_1 < k_0 + W_r$$

respectively, where s_0 is the energy spectrum.

Now, for unidirectional JONSWAP spectrum, since the limit of k_1 is from 0 to infinity, it will be divided into two components, namely, from $k_1 = 0$ to $k_1 = k_0$ as the first component and from $k_1 = k_0$ to $k_1 = \infty$ as the second component. However, for the numerical purposes, the upper limit of k_1 has to be truncated. Hence, the total energy and the momentum of the unidirectional JONSWAP spectrum for the first component are respectively

$$m_{0l} = \int_0^{k_0} S(k_1) dk_1, \quad \text{and} \quad m_{1l} = \int_0^{k_0} (k_1 - k_0) S(k_1) dk_1 \quad (4.14)$$

while for the rectangular spectrum we have

$$m_{0l} = s_0 W_l, \quad \text{and} \quad m_{1l} = -\frac{s_0 W_l^2}{2}. \quad (4.15)$$

Hence, from (4.15), the spectral width on the left hand side of the carrier-wave, k_0 , is given by

$$W_l = -\frac{2m_{1l}}{m_{0l}} \quad (4.16)$$

and the energy spectrum is defined as

$$s_0 = \frac{m_{0l}}{W_l}.$$

Also, from the second component of a unidirectional JONSWAP spectrum we have

$$m_{0r} = \int_{k_0}^{\infty} S(k_1) dk_1$$

and for the rectangular spectrum

$$m_{0r} = \int_{k_0}^{k_0+W_r} s_0 dk_1 = s_0 W_r.$$

Therefore, one can easily get the spectral width on the right hand side as follows

$$W_r = \frac{m_{0r}}{s_0}. \quad (4.17)$$

Using equation (4.11), above variables (equations (4.16) and (4.17)) can be transformed to non-dimensional variables.

For the two-dimensional case, we assume JONSWAP spectrum with a directional distribution as a function of wavenumber, $S(k_1, k_2)$, as symmetric in k_2 . Therefore, the spectrum can then be written as

$$S_1(k_1) = 2 \int_0^{\infty} S(k_1, k_2) dk_2$$

and the location of the peak of the $S_1(k_1)$ is k_0 .

Following a similar procedure to that used for one-dimensional case, the total energy and the momentum of JONSWAP spectrum with directional distribution of the first component are given by

$$m_{0l} = \int_0^{k_0} S_1(k_1) dk_1 \quad \text{and} \quad m_{1l} = \int_0^{k_0} (k_1 - k_0) S_1(k_1) dk_1,$$

respectively, while a two-dimensional rectangular spectrum gives

$$m_{0l} = 2 \int_{k_0-W_l}^{k_0} \int_0^W s_0 dk_2 dk_1 = 2s_0 W_l W$$

and

$$m_{1l} = 2 \int_{k_0-W_l}^{k_0} \int_0^W (k_1 - k_0) s_0 dk_2 dk_1 = -s_0 W W_l^2.$$

Thus, one can get the spectral width on the left hand side of the carrier wave as

$$W_l = -\frac{2m_{1l}}{m_{0l}} \quad (4.18)$$

and the relation as follows

$$s_0 W = \frac{m_{0l}}{2W_l}.$$

Moreover, for the second component of the JONSWAP spectrum with a directional distribution, the total energy is defined as

$$m_{0r} = \int_{k_0}^{\infty} S_1(k_1) dk_1$$

while the second component of the two-dimensional rectangular spectrum is given by

$$m_{0r} = 2 \int_{k_0}^{k_0+W_r} \int_0^W s_0 dk_2 dk_1 = 2s_0 W_r W.$$

Thus, the spectral width on the right hand side of the carrier wave leads to

$$W_r = \frac{m_{0r}}{2s_0 W}. \quad (4.19)$$

Also, defining

$$S_2(k_2) = \int_0^{\infty} S(k_1, k_2) dk_1,$$

the wave momentum for JONSWAP spectrum with directional spreading and for two-dimensional rectangular spectrum are defined as

$$m_1 = \int_0^{\infty} k_2 S_2(k_2) dk_2$$

and

$$m_1 = \frac{s_0(W_l + W_r)W^2}{2},$$

respectively. Therefore, spectral width of the two-dimensional rectangular spectrum in direction perpendicular to the carrier wave is given by

$$W = \frac{2m_1}{s_0 W(W_r + W_l)}. \quad (4.20)$$

Again, using equation (4.11), spectral widths of the rectangular spectra can be switched to non-dimensional forms.

Furthermore, as seen from equation (4.4), this problem contains four indexes, namely n, j, k and l where each of them represents a spatial dimension and thus the equation leads to a four-dimensional space. Therefore, it requires a huge computer memory and long computational time. Thus, a parallel programming solution is necessary. To this end, we use OpenMP (Open Multi-Processing) which allows us to spread the jobs over the processors in one node. For more details of this type of parallel programming including its advantages and disadvantages, one can refer to parallel programming books such as Chandra (2001) or refer to the openMP website (www.openMP.org). For the one-dimensional problem, one will solve the Alber equation only in a three-dimensional space $(\tilde{x}, \tilde{r}_1, \tilde{\tau})$ as variables \tilde{y} and \tilde{r}_2 in (4.1) vanish automatically, which reduces the required computation resources significantly. For example, taking $\alpha = 0.016$, $\gamma = 10$ and $\sigma = 0.08$, for unidirectional JONSWAP spectrum, it requires $N = 140$, $M_1 = 922$ and about 1,600,000 time steps to obtain a recurrence solution. Moreover, it needs more than 8 megabytes of computer memory. Using 8 processors in one node of the supercomputer, it takes a few hours for a computer to complete the job. Note that OpenMP does not work over the nodes of supercomputer. Therefore, with this type of parallel programming, only one node will be used. However, for the simplified two-dimensional case, one has to solve the Alber equation in a four-dimensional domain $(\tilde{x}, \tilde{r}_1, \tilde{r}_2, \tilde{\tau})$ as in the equation (4.2) since variable \tilde{y} in (4.1) vanishes automatically, which requires substantial computing resources. Taking $\alpha = 0.016$, $\gamma = 10$ and $\sigma = 0.08$, for JONSWAP spectrum with the degree of directional spreading $n = 50$, for instance, it requires $N = 100$, $M_1 = 690$, $M_2 = 500$ and about 1,908,000 time steps to obtain a recurrence solution. Moreover, it needs about 1.12 gigabytes of computer memory. Furthermore, using 16 processors in one node of the supercomputer, it needs more than two weeks to complete one job. Note that one node of the supercomputer contains either 8 processors or 16 processors. In this research, a node with 8 processors has been used for unidirectional JONSWAP spectra while a node with 16 processors has been used for JONSWAP spectra with directional distribution.

4.3 Stochastic recurrence

In order to apply the numerical scheme, as given in the equation (4.4), to study the long-time evolution and the stochastic recurrence, which is parallel to the Fermi-Pasta-Ulam recurrence obtained from the cubic Schrödinger equation, the initial values have to be given. Therefore, in the following subsections, the initial condition will be derived then following by the derivation of the invariants of motion as a quality control of the numerical solution. Furthermore, the justification for truncating the $\tilde{\mathbf{r}}$ -axis will be determined and then finally, the stochastic recurrence for JONSWAP spectrum with and without directional distributions will be simulated.

4.3.1 Description of the initial conditions

The initial conditions of the numerical scheme as in the equation (4.4) are determined by equation (3.7) and equation (3.9) in Chapter 3 and there are some degrees of freedom, namely, the value of the inhomogeneous disturbance wavenumber $\tilde{P} = p/\varepsilon k_0$, the inhomogeneous parameter δ and the decay $\tilde{R}(\tilde{r}_1)$. In this research, we take $\delta = 0.1$ which is the typical order of wave steepness ε , $\tilde{R}(\tilde{r}_1) = \tilde{\rho}_h(\tilde{r}_1) = k_0^2 \rho_h(r_1)/\varepsilon^2$ as in the equation (3.6) in Chapter 3 and \tilde{P} is chosen from the most unstable mode which is $\tilde{P}^{(max)}$. Note that for some different choices of $\tilde{P} = p/\varepsilon k_0$, one can refer to the work of Stiassnie et al. (2008). In addition, in order to obtain $\tilde{\rho}_h(\tilde{r}_1) = k_0^2 \rho_h(r_1)/\varepsilon^2$, one has to define a spectrum and for this special case unidirectional JONSWAP spectrum as a function of wavenumber as in equation (4.13) will be used. However, since equation (3.7) cannot be integrated analytically for unidirectional JONSWAP spectrum, again, the spectrum will be replaced by a sum of weighted Dirac-delta functions. Moreover, as shown in Chapter 3, unidirectional JONSWAP spectrum is unstable for the dimensionless “width-parameter” $\Pi_1 < 1$. Therefore, values of α and γ such that the unstable condition is satisfied, will be chosen. To this end, the initial spectra (4.13) where $\gamma = 20$, $\sigma = 0.08$, with various values of $\alpha = 0.01, 0.016, 0.02, 0.025$ and 0.03 and $\gamma = 10$, $\sigma = 0.08$, with $\alpha = 0.016, 0.02, 0.025$ and 0.03 will be taken. Summary of these values is given in the following Table 4.1. One should note that the steepness is calculated as $\varepsilon = k_0 \sqrt{2m_0}$, where k_0 is the peak wavenumber and m_0 is the total energy of the spectrum. The dimensionless “width parameter” is calculated as $\Pi_1 =$

$\varepsilon/(\alpha\gamma)$ and the most unstable mode is determined by $\tilde{P}_1^{(max)} = 2.313 - 0.976\Pi_1$ while the actual point of maximum growth rate can be found in Table 3.1 or Table 3.2 in Chapter 3. Moreover, the spectral widths of the rectangular spectrum, which are \tilde{W}_l and \tilde{W}_r , were calculated based on the equation (4.16) and (4.17), respectively.

Table 4.1: Values of parameters of initial conditions for unidirectional JONSWAP spectrum.

Case	α	γ	ε	Π_1	$\tilde{P}_1^{(max)}$	\tilde{W}_l	\tilde{W}_r
A	0.01	20	0.13	0.65	1.68	1.53	1.79
B	0.016	20	0.16	0.50	1.83	1.21	1.43
C	0.02	20	0.18	0.45	1.87	1.08	1.28
D	0.025	20	0.20	0.40	1.92	0.97	1.13
E	0.03	20	0.22	0.37	1.95	0.88	1.04
B_1	0.016	10	0.13	0.81	1.52	1.88	2.16
B_2	0.02	10	0.14	0.70	1.63	1.63	2.08
B_3	0.025	10	0.16	0.64	1.69	1.46	1.86
B_4	0.03	10	0.18	0.60	1.73	1.33	1.70

Details of the spectra are shown in Figure 4.2 and Figure 4.3. Note that all of these cases have the same peak wavenumber of JONSWAP spectra, that is $k_0 = 1$. As seen from the figures, the higher is the value of the energy scale, α , the higher is the energy of the spectrum.

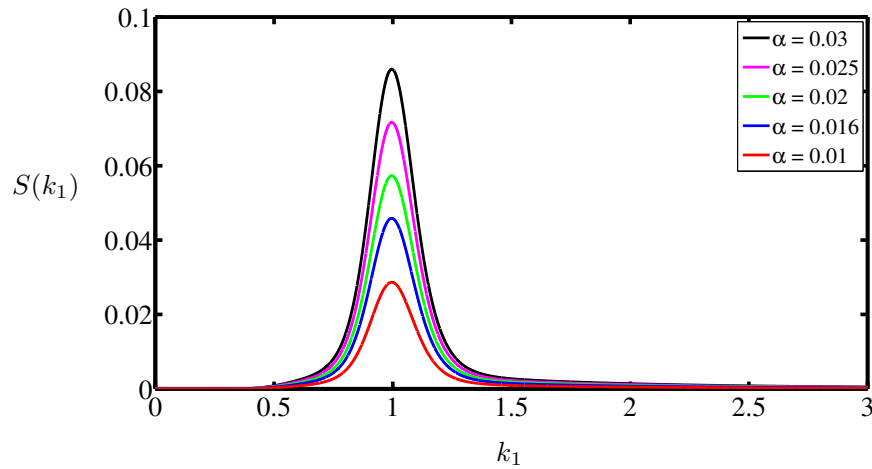


Figure 4.2: The energy spectrum for the peak enhancement factor $\gamma = 20$ with different values of the energy scale α .

For JONSWAP spectrum with directional distributions, the initial condition is determined by following a similar procedure in order to determine the initial condition of the unidirectional JONSWAP spectrum. Again, in this case $\delta = 0.1$ and $\tilde{R}(\tilde{\mathbf{r}}) = \tilde{\rho}_h(\tilde{\mathbf{r}})$ are taken.

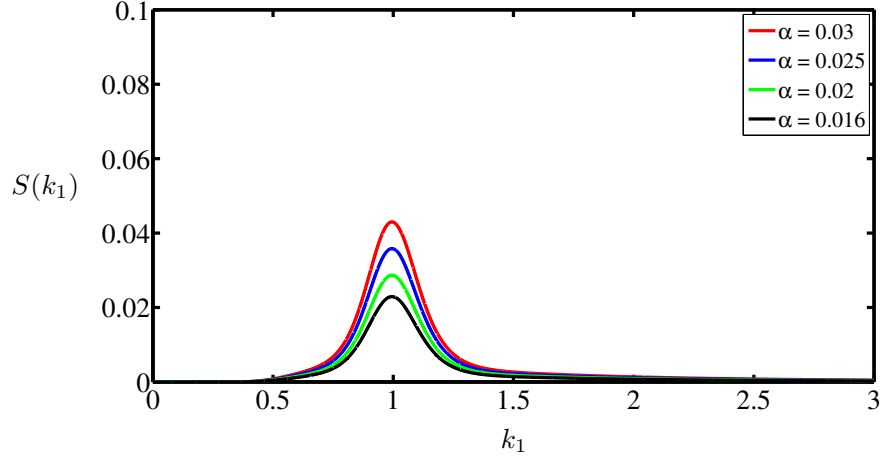


Figure 4.3: The energy spectrum for the peak enhancement factor $\gamma=10$ with different values of the energy scale α .

It is important to mention that the initial inhomogeneous disturbances that are used in this research were taken to depend on the homogeneous spectra themselves. Note that the influence of different choices of disturbances is demonstrated in Stiassnie et al. (2008), Regev et al. (2008) and more recently in Eliasson and Shukla (2010). Now, recall the initial homogeneous distribution (ρ_h) as given by

$$\rho_h(\mathbf{r}, \tau = 0) = \int_{-\infty}^{\infty} S(\mathbf{k}) e^{i(\mathbf{k}-\mathbf{k}_0) \cdot \mathbf{r}} d\mathbf{k} \quad (4.21)$$

where

$$S(\mathbf{k}) = \frac{\alpha \Gamma\left(1 + \frac{n}{2}\right) k_1^n}{2\sqrt{\pi} \left(\sqrt{k_1^2 + k_2^2}\right)^{4+n} \Gamma\left(\frac{1+n}{2}\right)} e^{-\left(\frac{5k_0^2}{4(k_1^2+k_2^2)}\right)} \gamma e^{\left[\frac{1}{2\sigma^2} \left(\sqrt{\frac{k_1^2+k_2^2}{k_0}} - 1\right)\right]^2} \quad (4.22)$$

for

$$0 < k_1 < k, \quad -k < k_2 < k.$$

Again, since equation (4.21) cannot be integrated analytically, this equation will be integrated numerically by using Dirac–delta functions, and therefore the initial condition is given by

$$\rho(x, \mathbf{r}, 0) = \rho_h(\mathbf{r})[1 + \delta \cos(px)]$$

where $\delta = o(1)$ is the dimensionless inhomogeneity parameter and p is the wavenumber of the disturbance in direction parallel to the carrier waves. In this study, the wavenumber of the disturbance is chosen from the most unstable mode. Turning to the dimensionless parameters gives

$$\tilde{\rho}(\tilde{x}, \tilde{\mathbf{r}}, 0) = \tilde{\rho}_h(\tilde{\mathbf{r}})[1 + \delta \cos(\tilde{P}\tilde{x})].$$

As we know, a unidirectional JONSWAP spectrum depends on two parameters γ and α while a JONSWAP spectrum with a directional distribution is a function of three parameters γ , α and n . In order to study the influence of the directional spreading for long-time evolution, the unidirectional JONSWAP spectrum parameters $\gamma = 10$, $\alpha = 0.016$ with various values of the degree of the directional energy distributions, namely, $n = 90, 50, 10$ and $n = 2$; which are from fairly narrow to very broad directional distribution were chosen. The energy directional distribution as a function of angle θ for different values of the parameter n is shown in Figure 4.4. As seen, the higher is the degree of the directional spreading, the narrower is the directional distribution.

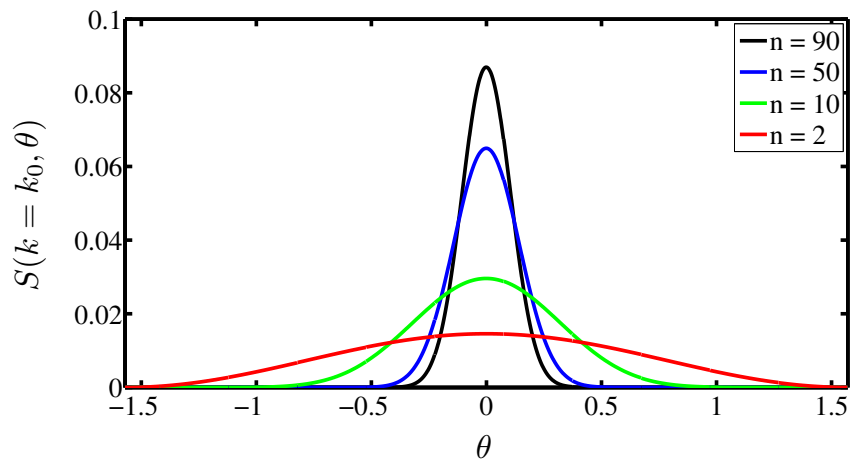


Figure 4.4: Energy directional spreading as a function of angle θ for different values of the parameter n .

4.3.2 Invariants of motion

There are several ways to clarify the results based on such numerical method. In this section, the invariants of motion as a quality control for our numerical results will be used. Following Janssen (1983), the solution of our problem has to satisfy certain conservation laws. He specifies the first three of the invariants which are the same as mentioned in Janssen (2003). Moreover, as mentioned in Stiassnie et al. (2008), the integrability of the Alber equation could mean existence of the more than three invariants. All the previous invariants, however, are for one-dimensional case, and the invariants for two-dimensional case are not yet available. Therefore, in the Appendix A the invariants for two-spatial-dimensions Alber equation were derived namely the wave action, wave momentum and the energy of the system. Note that the following invariants are for simplified problem where the variable y has been eliminated. Moreover, in order to calculate these following invariants numerically, the fifth order Taylor expansion has been used.

The first invariant which is related to the wave action is obtained by evaluating the dimensional Alber equation at $\mathbf{r} = \mathbf{0}$, then integrating it with respect to x and using the periodicity properties, and yields

$$I_1 = \int_0^{\frac{2\pi}{p}} \rho(x, \mathbf{0}, t) dx. \quad (4.23)$$

For all study cases in this research, the first invariant, I_1 , did not change at all times from its value at $t = 0$ throughout the calculations.

The second invariant which is related to the wave momentum consists of two components namely the invariant which depends on the values along r_1 and the invariant which depends on the values along r_2 . The first component of this invariant is defined by differentiating the dimensional Alber equation with respect to r_1 , then evaluating it at $\mathbf{r} = \mathbf{0}$ and integrating with respect to x as well as using the periodicity properties. It gives

$$I_{21} = \int_0^{\frac{2\pi}{p}} \frac{\partial \rho(x, \mathbf{0}, t)}{\partial r_1} dx. \quad (4.24)$$

Following the similar procedure to determine the first component of the second invariant, we obtain

$$I_{22} = \int_0^{\frac{2\pi}{p}} \frac{\partial \rho(x, \mathbf{0}, t)}{\partial r_2} dx. \quad (4.25)$$

For the first component of the second invariant, one can easily show that its value at $t = 0$ is imaginary. Moreover, it is found that the relative deviation of the imaginary part of I_{21} from its value at $t = 0$ at all times did not exceed 1.0% for the unidirectional JONSWAP spectra and did not exceed 1.5% for the JONSWAP spectrum with directional distributions. Moreover, for the second component of the second invariant for the JONSWAP spectrum with directional spreading, $I_{22} = 0$, since $\rho(t = 0)$ is real and symmetric in r_2 . Thus, we cannot compare running values of I_{22} to the initial value.

The third invariant which is interpreted as the energy of the system, is much more complicated as it depends on the values at $\mathbf{r} = \mathbf{0}$, the values along r_1 and the values along r_2 . To obtain an explicit formula for this invariant, we first take the second partial derivative of the dimensional Alber equation with respect to r_1 and also with respect to r_2 . After that, evaluating them at $\mathbf{r} = \mathbf{0}$ and integrating with respect to x will give the following invariant

$$I_3 = \int_0^{\frac{2\pi}{p}} \rho^2(x, \mathbf{0}, t) dx + \frac{1}{4k_0^4} \int_0^{\frac{2\pi}{p}} \frac{\partial^2 \rho(x, \mathbf{0}, \tilde{t})}{\partial r_1^2} dx. \quad (4.26)$$

It is found that relative deviation of I_3 at all times from its value at $t = 0$ did not exceed 1.0% for the unidirectional JONSWAP spectra throughout all calculated evolutions and did not exceed 1.1% for the JONSWAP spectra with different degrees of the directional energy distribution.

4.3.3 Justification for truncating the $\tilde{\mathbf{r}}$ -axis

As has been shown in section 3.5.1 of Chapter 3, the values of spacing $\tilde{\mathbf{r}}$ are from negative infinity to infinity, or all real numbers. However, using the symmetrical properties, the values of $\tilde{\mathbf{r}}$ can be taken from zero to infinity. Moreover, for the numerical purposes, $\tilde{\mathbf{r}}$ has to be truncated. However, it has to be truncated correctly. Here, we will show a reasonable way to truncate the $\tilde{\mathbf{r}}$ domain. In this regards, the

unidirectional JONSWAP spectrum with $\alpha = 0.016$, $\gamma = 10$ and $\sigma = 0.08$ were chosen. Furthermore, applying the procedure of section 4.2.4, we can obtain the spectral width on the left hand side and the right hand side of the rectangular spectrum which are $\tilde{W}_l = 1.88$ (see equation (4.16)) and $\tilde{W}_r = 2.16$ (see equation (4.17)), respectively. Moreover, applying the formula for the dimensionless “width parameter” gives $\Pi_1 = 0.81$ which is less than 1 (see equation (3.54)). This means that the chosen unidirectional JONSWAP spectrum falls into the unstable conditions. Based on the linear stability analysis, the growth rate of the instability is shown in Figure 4.5 and as we can see, the maximum growth rate occurs at $\tilde{P}^{(max)} = 1.52$. However, for $\tilde{P} > 2.1$, the line is not smooth enough and therefore, it has to be refined.

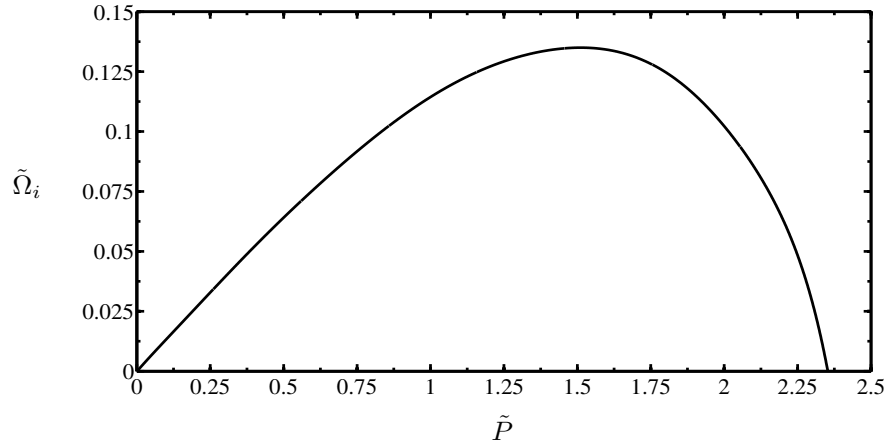


Figure 4.5: Non-dimensional growth rate, $\tilde{\Omega}_i$, for $\alpha=0.016$, $\gamma=10$ and $\sigma=0.08$ where the horizontal axis represents the dimensionless wavenumber of the disturbance in direction parallel to the carrier wave.

In order to justify the truncation of the \tilde{r}_1 axis, the influence of the extent of the \tilde{r}_1 domain has been checked. To this end, there are several values that were tested, namely, $(\tilde{r}_1)_{end} = 10\tilde{x}_{end}$, $15\tilde{x}_{end}$, $20\tilde{x}_{end}$ and $30\tilde{x}_{end}$. The dimensionless maximum correlation function evaluated at $\tilde{r}_1 = 0$, is shown in Figure 4.6. All four cases are not distinguishable. Therefore, the justification for the influence of the extent of the \tilde{r}_1 domain cannot be made based on these results. However, using the invariants of motion, the influence of the extent of the \tilde{r}_1 domain can be justified except for the first invariant which is related to the wave action. This is because, the relative deviation of the first invariant at all times from its values at $\tilde{\tau} = 0$ for all cases do not change throughout the calculated evolutions.

Comparing the second invariant for all the cases shows the justification for the extent of the \tilde{r}_1 domain as shown in Figure 4.7 and Figure 4.8 for real part of I_2 and its imaginary part, respectively. As seen from these figures, all studied cases overlap from the beginning until about $\tilde{\tau} = 44$. After that, the results for $(\tilde{r}_1)_{end} = 10\tilde{x}_{end}$ deviates significantly from others and reaches the maximum deviation at about $\tilde{\tau} = 57$. On the other hand, the second invariant for the case $(\tilde{r}_1)_{end} = 15\tilde{x}_{end}$ overlaps with the cases $(\tilde{r}_1)_{end} = 20\tilde{x}_{end}$ and $(\tilde{r}_1)_{end} = 30\tilde{x}_{end}$ until $\tilde{\tau} = 57$ and then deviated slightly. The last two cases overlap throughout the calculation time.

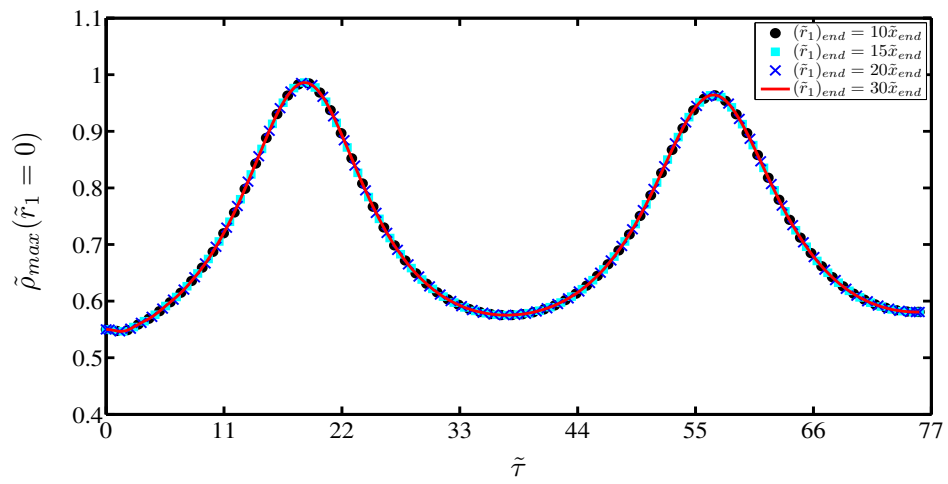


Figure 4.6: The influence of the extent of the \tilde{r}_1 domain on the maximum value of $\tilde{\rho}$ at $\tilde{r}_1 = 0$ as a function of non-dimensional time $\tilde{\tau}$, for $(\tilde{r}_1)_{end} = 10\tilde{x}_{end}$, $(\tilde{r}_1)_{end} = 15\tilde{x}_{end}$, $(\tilde{r}_1)_{end} = 20\tilde{x}_{end}$ and $(\tilde{r}_1)_{end} = 30\tilde{x}_{end}$. These calculations are for a homogeneous unidirectional JONSWAP spectrum and an inhomogeneous unidirectional JONSWAP disturbance with $\alpha = 0.016$, $\gamma = 10$, $\tilde{P}_1^{(max)} = 1.52$, $\delta = 0.1$.

Based on the second invariant, we may say that taking $(\tilde{r}_1)_{end} = 10\tilde{x}_{end}$ is not sufficient for the truncation of the \tilde{r}_1 axis. In order to strengthen our decision, it is important to check the results of the third invariant. Therefore, comparing the third invariant with different formulation will give different relative deviations from its value at $\tilde{\tau} = 0$ as shown in Figure 4.9. Generally speaking, the behaviour of the third invariant is similar to the second invariant.

For all cases, the relative deviation of I_3 from its value at $\tilde{\tau} = 0$ over the computational period is summarized in Table 4.2. As seen, the case $(\tilde{r}_1)_{end} = 10\tilde{x}_{end}$ gives the highest deviation of the third invariant while other cases have the same result.

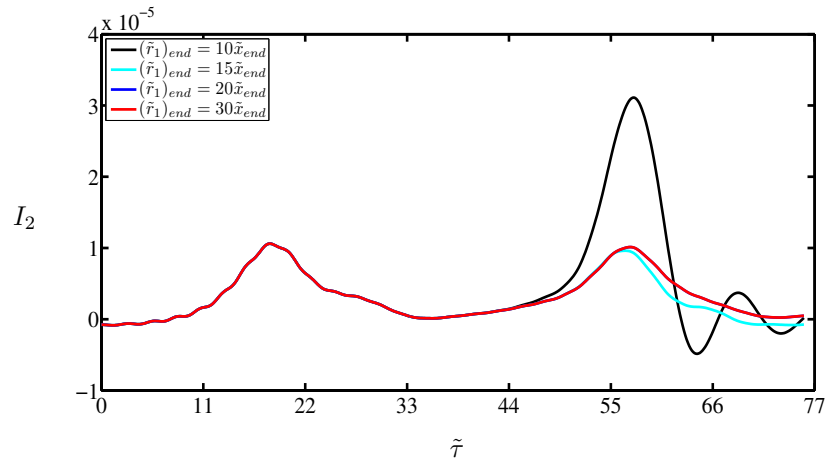


Figure 4.7: The influence of the extent of the \tilde{r}_1 domain on the real part of the second invariant I_2 as a function of non-dimensional time $\tilde{\tau}$. These cases are the same as in Figure 4.6.

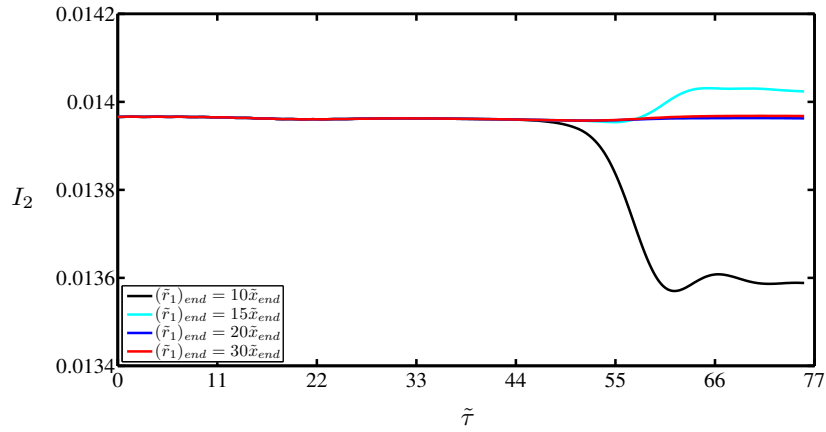


Figure 4.8: The influence of the extent of the \tilde{r}_1 domain on the imaginary part of the second invariant I_2 as a function of non-dimensional time $\tilde{\tau}$. These cases are the same as in Figure 4.6.

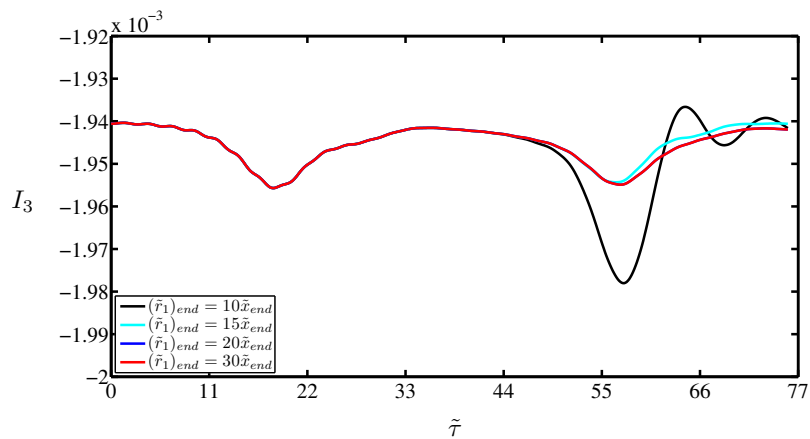


Figure 4.9: The influence of the extent of the \tilde{r}_1 domain of the third invariant I_3 as a function of non-dimensional time $\tilde{\tau}$. These cases are the same as in Figure 4.6.

Table 4.2: Comparison for the maximum deviation of I_3 (in percents) from its value at $\tilde{\tau}=0$ for all four cases throughout the calculated evolutions.

Cases	Maximum deviation (%)
$(\tilde{r}_1)_{end} = 10\tilde{x}_{end}$	1.9295
$(\tilde{r}_1)_{end} = 15\tilde{x}_{end}$	0.7788
$(\tilde{r}_1)_{end} = 20\tilde{x}_{end}$	0.7788
$(\tilde{r}_1)_{end} = 30\tilde{x}_{end}$	0.7788

Based on the above comparison, it can be concluded that taking $(\tilde{r}_1)_{end} > 15\tilde{x}_{end}$ will not give a significant effect in our computations. Therefore, all of the simulations presented in the sequel are with $(\tilde{r}_1)_{end} = 15\tilde{x}_{end}$ for unidirectional JONSWAP spectrum and $(\tilde{r}_1)_{end} = 15\tilde{x}_{end}$ and $(\tilde{r}_2)_{end} = 15\tilde{x}_{end}$ for JONSWAP spectrum with directional distributions.

4.3.4 Recurrence for unidirectional JONSWAP spectrum

Recurrent results for five different unidirectional JONSWAP spectra with $\gamma = 20$ are shown in Figure 4.10. Note that $\tilde{\rho}_{max}(\tilde{r}_1 = 0)$ signifies the maximum values of $k_0^2\rho(r_1 = 0)/\varepsilon^2$ within the interval $\tilde{x} \in (0, 2\pi/\tilde{P}_1^{(max)})$. Here it is plotted as a function of $\tilde{\tau} = (\varepsilon^2\sqrt{gk_0})t$. The various parameters, as well as the main features of the evolution are summarized in Table 4.3 where $\tilde{P}_1^{(max)}$ and $\tilde{\Omega}_1^{(max)}$ were calculated using equations (3.55) and (3.56), respectively, in Chapter 3 while peak enhancements of the recurrence were calculated by taking the maximum value of $\tilde{\rho}_{max}(\tilde{r}_1 = 0)$ divided by $\tilde{\rho}_h(0)$.

It is clear that the decrease in the “width-parameter” Π_1 is accompanied by an increase in the peak enhancement of the recurrence and a decrease in the numerical recurrence duration. In addition, the higher is the value of the energy scale α while keeping the peak enhancement factor γ constant, the higher is its maximum growth rate. From all five cases, case *E* has the highest maximum growth rate while case *A* has the lowest maximum growth rate. This can be seen in Figure 4.10 where case *E* has the highest maximum correlation function evaluated at $\tilde{r}_1 = 0$ as opposed to the case *A*. A more general picture of the values of $\tilde{\rho}(\tilde{x}, 0, \tilde{\tau})$ is given in Figure 4.11 where contour plot

are shown. As can be seen from the figure, the maximum correlation function evaluated at $\tilde{r}_1 = 0$ are at $\tilde{x} = 0$ and $\tilde{x} = 2\pi/\tilde{P}_1^{(max)}$.

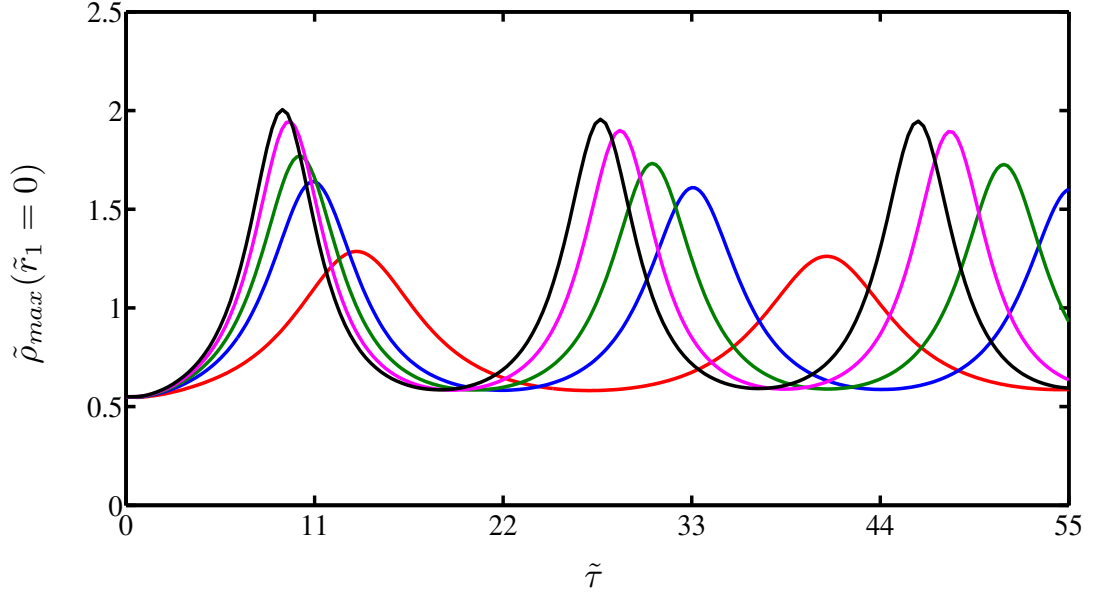


Figure 4.10: Recurrence solutions for unidirectional JONSWAP spectra with $\gamma = 20$; A, —; B, —; C, —; D, —; E, — (see Table 4.3).

In addition, the energy is distributed from a nearly even distribution at $\tilde{\tau} = 0$ to the case where most of the energy is concentrated at the end of the region and then back to (almost) the initial distribution of $\tilde{\rho}$ after one recurrence cycle for all cases. This is similar to Figure 8 in Stiassnie et al. (2008). Interestingly, as one can see from Figure 4.11, for the case where $\gamma = 20$ and $\alpha = 0.016$, which is case B, the maximum growth rate is the same as in the case C of Regev et al. (2008) whose result was obtained from a Gaussian spectrum with the influence of swell. This indicates that the shape of the spectrum does not necessary influence the results of the long-time evolution.

Changing the peak enhancement factor of the unidirectional JONSWAP spectrum from $\gamma = 20$ to $\gamma = 10$ and following a similar procedure, while keeping the same energy scale for four cases, also exhibits the stochastic recurrence as shown in Figure 4.12. All of the features of Figure 4.12 are similar to Figure 4.10 and are also summarized in Table 4.3. For instance, the decrease in the “width-parameter” Π_1 is accompanied by an increase in the peak enhancement and a decrease in the numerical recurrence duration.

Table 4.3: Spectral parameters and evolution features for unidirectional JONSWAP spectra.

Case	α	γ	ε	Π_1	$\tilde{P}_1^{(max)}$	$2\pi / \tilde{\Omega}_1^{(max)}$	Numerical recurrence time	Peak enhancement
<i>A</i>	0.01	20	0.13	0.65	1.68	30	27	2.3
<i>B</i>	0.016	20	0.16	0.50	1.83	21	22	3.0
<i>C</i>	0.02	20	0.18	0.45	1.87	20	20	3.2
<i>D</i>	0.025	20	0.20	0.40	1.92	18	19	3.5
<i>E</i>	0.03	20	0.22	0.37	1.95	17	18	3.6
<i>B₁</i>	0.016	10	0.13	0.81	1.52	47	37	1.8
<i>B₂</i>	0.02	10	0.14	0.70	1.63	37	33	2.0
<i>B₃</i>	0.025	10	0.16	0.64	1.69	30	28	2.3
<i>B₄</i>	0.03	10	0.18	0.60	1.73	26	26	2.6

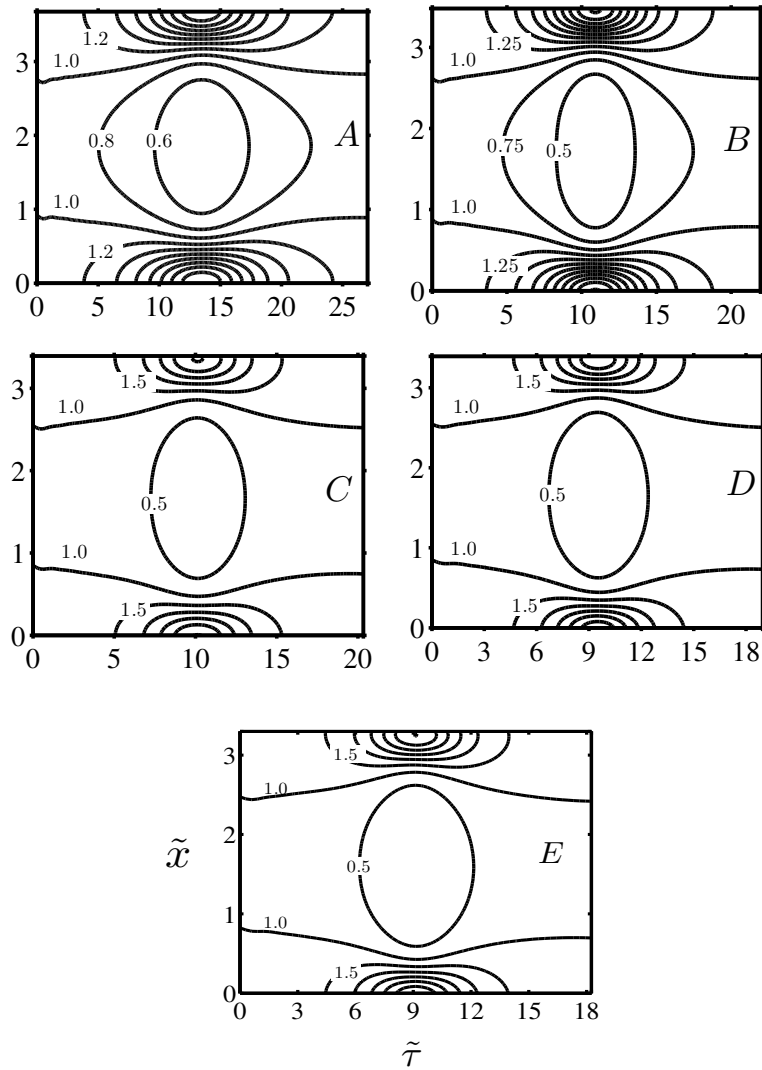


Figure 4.11: Isolines of $\tilde{\rho}(\tilde{x}, 0, \tilde{\tau}) / \tilde{\rho}_h(0)$. Each case refers to Table 4.3 for $\gamma = 20$.

Moreover, identical dimensionless “width-parameter” Π_1 gives the same maximum growth, the same point of maximum, as well as the same peak enhancement of the recurrence. Furthermore, contour plots of $\tilde{\rho}(\tilde{x}, 0, \tilde{\tau})$ are given in Figure 4.13. Again, it is clearly seen that the maximum values are at $\tilde{x} = 0$ and $\tilde{x} = 2\pi/\tilde{P}_1^{(max)}$ which is similar to Figure 4.11. In addition, looking at the case A from Figure 4.11 and case B_3 in Figure 4.13, one can see that they are almost the same. This is apparently because both cases have almost the same value of the dimensionless “width-parameter”, Π_1 , even though the spectra are not the same.

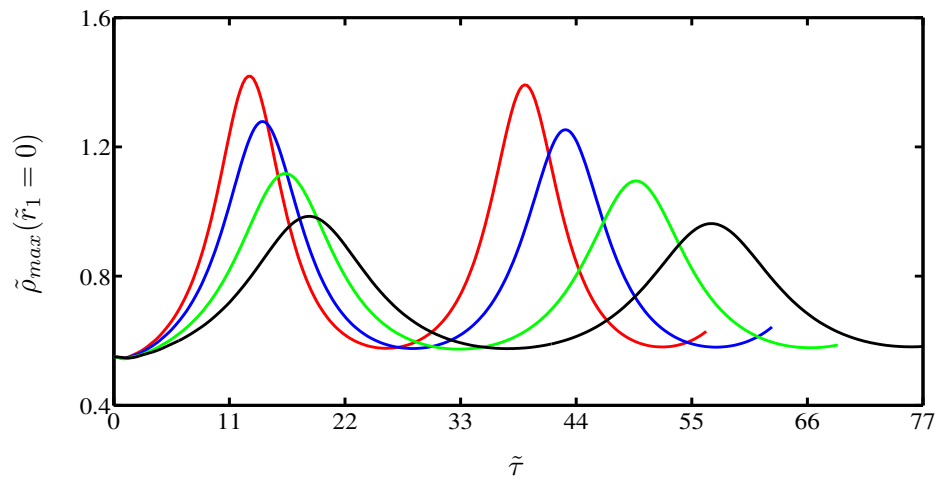


Figure 4.12: Recurrence solutions for unidirectional JONSWAP spectra with $\gamma=10$; B_4 , —; B_3 , —; B_2 , —; B_1 , — (see Table 4.3).

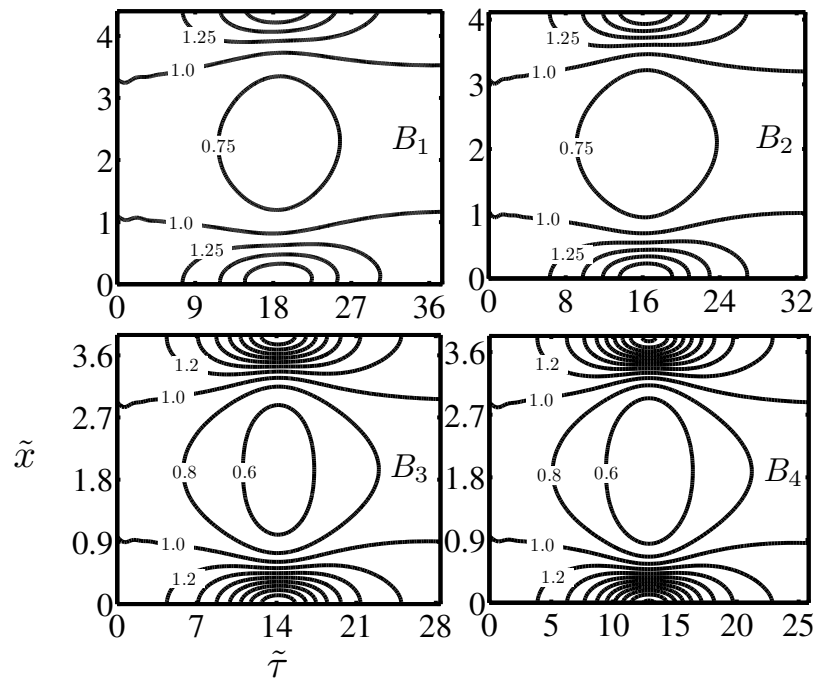


Figure 4.13: Isolines of $\tilde{\rho}(\tilde{x}, 0, \tilde{\tau}) / \tilde{\rho}_h(0)$. Each case refers to Table 4.3 for $\gamma=10$.

As aforementioned, Janssen (1983) used an asymptotic method to solve the Alber equation near the threshold of instability and obtained a solution which is characterized by an initial small overshoot followed by an oscillation around its time-asymptotic value. Stiassnie et al. (2008) recovered Janssen's results at the threshold of the instability using an initial Lorentz spectrum with a small inhomogeneous square disturbance. In Figure 4.14, results from the numerical simulations at the threshold of the instability for the case of an initial unidirectional JONSWAP spectrum with a small inhomogeneous unidirectional JONSWAP disturbance are presented.

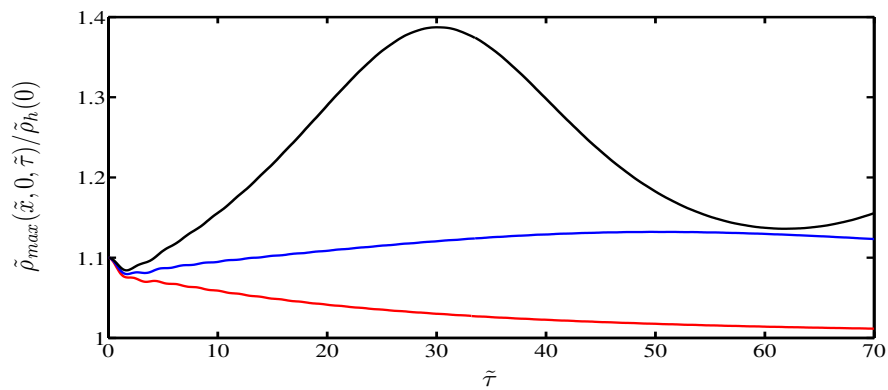


Figure 4.14: Values of $\hat{\rho}_{max}(\tilde{x}, 0, \tilde{\tau}) / \hat{\rho}_h(0)$ as a function of non-dimensional time, $\tilde{\tau}$, for three cases near the threshold of instability for $\gamma=10$, $\sigma=0.08$, $\delta=0.1$; P_1 , —; P_2 , —; P_3 , —.

It shows the behaviour of such numerical solution, with the initial homogeneous spectrum and an inhomogeneous disturbance are both unidirectional JONSWAP spectra for $\gamma = 10$, $\sigma = 0.08$ and $\delta = 0.1$ with three different values of the energy scale $\alpha = 0.0075$ (P_1), 0.009 (P_2) and 0.011 (P_3). These cases correspond to the value of $\Pi_1 = 1.1$, 1.0 and 0.9 . As seen from Figure 4.14, case P_1 which is outside the instability criterion does not exhibit recurrence behaviour at all, while case P_2 which is on the marginal instability criterion almost shows a recurrent behaviour with an extremely long period. These are in contrast with the case P_3 which is inside the instability criterion. The latter case exhibits the recurrent behaviour but with very long period. In addition, this figure is also similar to Figure 14 in Stiassnie et al. (2008). These three cases are further investigated in Figure 4.15. Here, the marginal instability line is plotted based on the equation (3.52) in Chapter 3.

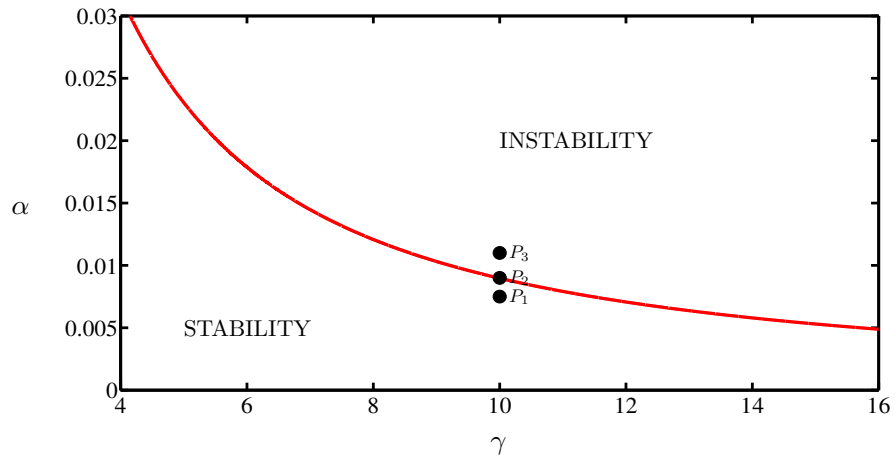


Figure 4.15: α versus γ , three cases near the marginal stability where red line represents the marginal-instability line.

Furthermore, Yuen and Ferguson Jr (1978b) investigated the long-time evolution of the unstable solution based on the nonlinear Schrödinger equation. They defined two types of the recurrence namely simple recurrence and complex recurrence. Recently, Stiassnie et al. (2008) used a Gaussian spectrum to investigate these types of recurrence based on the one-dimensional Alber equation and also found the two aforementioned types of recurrence. In the following, these types of recurrence are shown using a more realistic ocean wave JONSWAP spectrum. Four different cases for simple and complex recurrence are shown in Figure 4.16 for $\alpha = 0.016$, $\gamma = 10$ and $\sigma = 0.08$ as given in Figure 4.5.

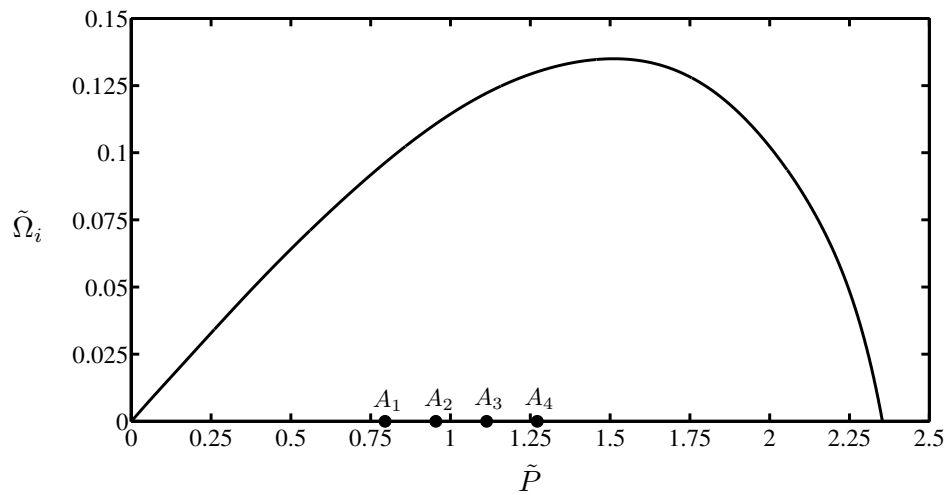


Figure 4.16: $\tilde{\Omega}_i$ versus \tilde{P} , four cases of simple and complex recurrence, $A_1(\tilde{P} = 0.795)$, $A_2(\tilde{P} = 0.954)$, $A_3(\tilde{P} = 1.113)$ and $A_4(\tilde{P} = 1.272)$. All other parameters are the same as in Figure 4.5.

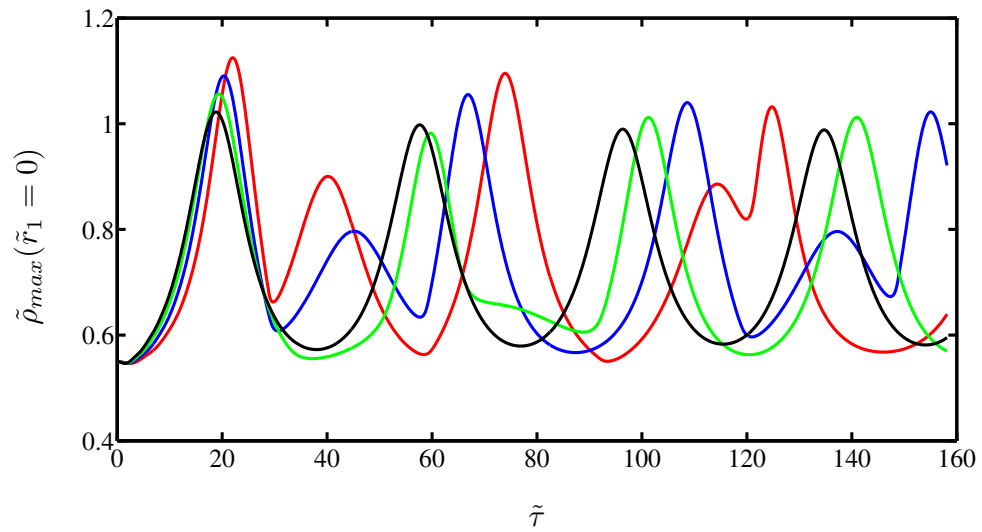


Figure 4.17: Values of $\tilde{\rho}_{max}(\tilde{r}_1 = 0)$ as a function of non-dimensional time, $\tilde{\tau}$, for three cases in the complex recurrence and one case in the simple recurrence. A_1 , —, A_2 , —, A_3 , —, A_4 , —. A_1, A_2, A_3 and A_4 as shown in Figure 4.16.

The results from the numerical solution of the four study cases are shown in Figure 4.17. In this figure, cases A_1, A_2 and A_3 are very different from A_4 which exhibits the recurrence. As was demonstrated in Stiassnie et al. (2008) using a Gaussian spectrum, the reason for the cases A_1, A_2 and A_3 not showing full recurrence is because the double harmonic, $2\tilde{P}$, in each of this cases is still inside the instability area. Using the terminology of previous authors, the first three cases are called complex recurrence while the case A_4 is simple recurrence.

As has been mentioned in the introduction, the real sea states are not unidirectional but are characterized by wave components propagating along different directions (directional distribution). Therefore, in the following section, these kinds of waves will be studied by including different directional distributions.

4.3.5 Recurrence for JONSWAP spectrum with directional distribution

In this section, we will be showing that whenever the dimensionless “width-parameter” $\Pi_2 < 1.1$ (see equation (3.59) in Chapter 3), the Alber equation yields recurring solutions. Note, however, for practical purposes, that the results for unidirectional waves with an initial unidirectional JONSWAP spectrum as given in (4.13) with $\gamma = 20, \varepsilon = 0.13$ ($\alpha = 0.01$) and $k_0 = 1$ are identical to those of a JONSWAP

spectrum with a directional distribution as given in equation (4.22) with the same values of parameters α and γ , and the degree of the directional spreading $n = 90$. The dimensionless maximum correlation functions for unidirectional JONSWAP spectrum evaluated at $\tilde{r}_1 = 0$ ($\tilde{\rho}_{max}(\tilde{r}_1 = 0)$) and for the JONSWAP spectrum with directional distribution $n = 90$ evaluated at $\tilde{\mathbf{r}} = \mathbf{0}$ ($\tilde{\rho}_{max}(\tilde{\mathbf{r}} = \mathbf{0})$) are shown in Figure 4.18. As one can see, they are hardly distinguished.

In order to show the influence of the directional spreading on the long-time evolution, we use the initial spectra as in equation (4.22) which share the same values of $\gamma = 10$, $\varepsilon = 0.126$ and $\alpha = 0.016$. The spectra only differ by their angular spread, having $n = 2, 10$ and 50 which range from very broad (small n) to fairly narrow (large n) directional spreading, and thus the normalization factor as given in the equation (3.57) of Chapter 3 yields $A_d = 0.64, 1.29$ and 2.84 , respectively. These conditions are summarized in Table 4.4 where the dimensionless spectral widths of the rectangular spectrum that are used for large $\tilde{\mathbf{r}}$ are also included. Moreover, their dimensionless “width-parameters”, as given in the section 3.4.4.3 of Chapter 3 with $\beta = 0.0256$ are $\Pi_2 = 1.11, 0.95$ and 0.86 , respectively. The isolines of these three spectra are shown in Figure 4.19, Figure 4.20 and Figure 4.21. The spectral widths of the two-dimensional rectangular spectrum, \tilde{W}_l , \tilde{W}_r and \tilde{W} , that will be used for the condition at large $\tilde{\mathbf{r}}$ are calculated based on the equations (4.18), (4.19) and (4.20). Moreover, the “width parameter”, Π_2 , is calculated by $\varepsilon/(\alpha\gamma) + \beta/(\varepsilon A_d)$ (see Chapter 3 for more details).

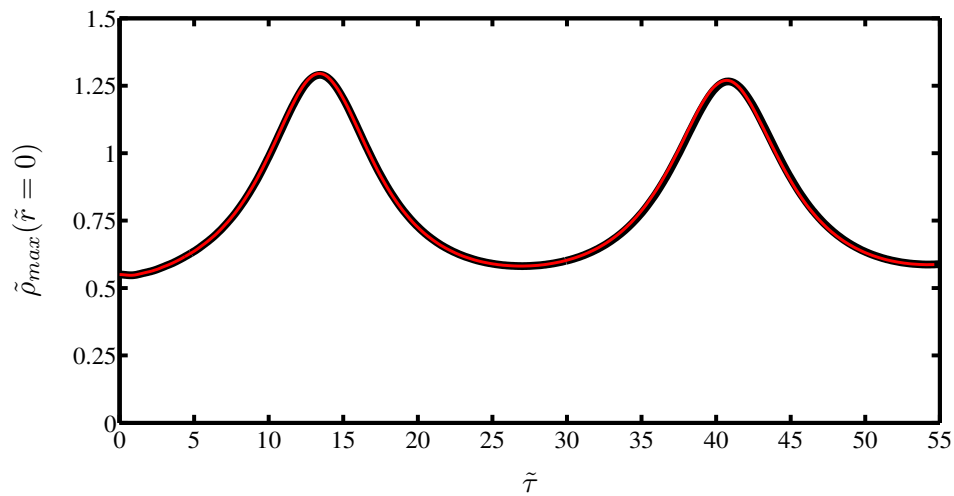


Figure 4.18: Comparison between the solution for unidirectional JONSWAP spectrum —, and JONSWAP spectrum with degree of directional distribution $n = 90$, —. Both spectra have the same $\gamma = 20$ and $\varepsilon = 0.13$ ($\alpha = 0.01$).

Table 4.4: Spectral parameters for JONSWAP spectra with directional distribution, with $\gamma=10$, $\alpha=0.016$. n is the degree of the directional distribution and A_d is the normalization factor (equation (3.57)), $\tilde{P}_2^{(max)}$, \tilde{W} , \tilde{W}_l and \tilde{W}_r are dimensionless wavenumber of the disturbance which is the point of maximum growth rate and dimensionless spectral widths of the rectangular spectra, respectively.

Case	n	A_d	Π_2	$\tilde{P}_2^{(max)}$	\tilde{W}	\tilde{W}_l	\tilde{W}_r
A_1	50	2.84	0.86	1.501	1.843	1.913	1.961
A_2	10	1.29	0.95	1.427	3.838	2.213	1.625
A_3	2	0.64	1.11	1.28*	6.949	3.756	1.276

Note: * indicates the stable condition.

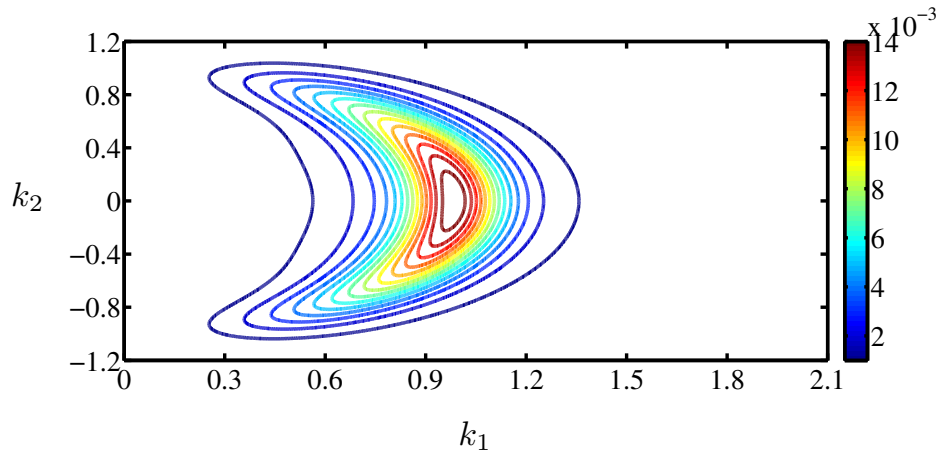


Figure 4.19: Isolines for JONSWAP spectrum with $\gamma=10$, $\alpha=0.016$, $\sigma=0.08$, $n=2$ and $k_0=1$. k_1 and k_2 are the wavenumbers in direction perpendicular and parallel to the carrier wave, respectively.

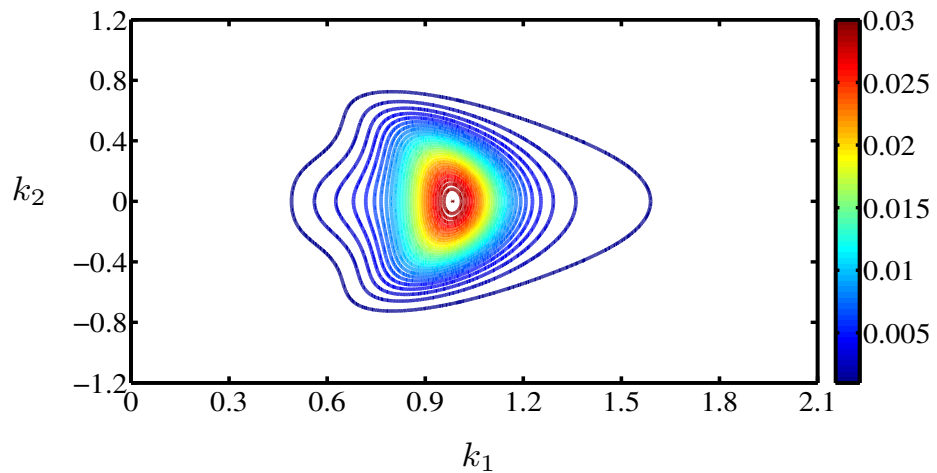


Figure 4.20: Isolines for JONSWAP spectrum with $\gamma=10$, $\alpha=0.016$, $\sigma=0.08$, $n=10$ and $k_0=1$. k_1 and k_2 are the wavenumbers in direction perpendicular and parallel to the carrier wave, respectively.

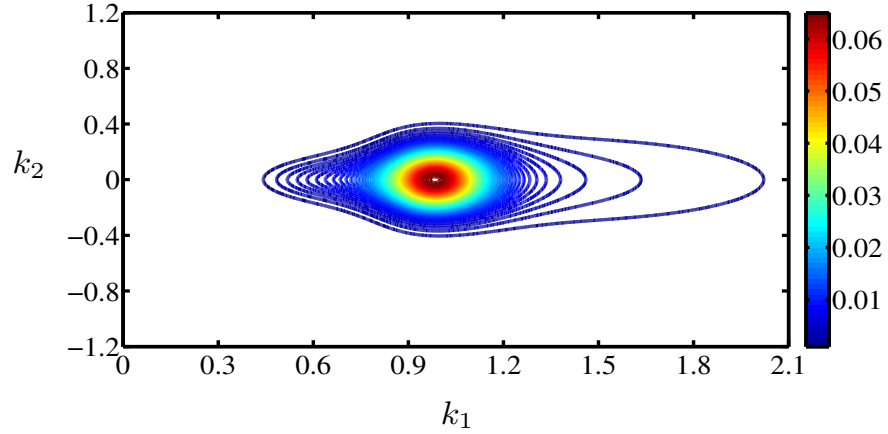


Figure 4.21: Isolines for JONSWAP spectrum with $\gamma=10$, $\alpha=0.016$, $\sigma=0.08$, $n=50$ and $k_0=1$. k_1 and k_2 are the wavenumbers in direction perpendicular and parallel to the carrier wave, respectively.

In addition, it is also important to show the initial homogeneous correlation function of these cases, i.e. at $\tilde{\tau} = 0$ (Figure 4.22 and Figure 4.23). As an example, the degree of the directional distribution $n = 50$ has been chosen. Substituting $n = 50$ into equation (4.22) and then solving the integral as given in (4.21) by using a sum of weighted Dirac-delta functions gives the initial homogeneous correlation function. However, since this function depends on two variables, namely, \tilde{r}_1 and \tilde{r}_2 , there are at least three possibilities for solution such as along \tilde{r}_1 at $\tilde{r}_2 = 0$, along \tilde{r}_2 at $\tilde{r}_1 = 0$ and along \tilde{r}_1 and \tilde{r}_2 . Note that the blue line and the red line represent the real part and the imaginary part of the homogeneous correlation function, respectively. As seen, Figure 4.22 shows the homogeneous correlation function along \tilde{r}_1 at $\tilde{r}_2 = 0$. Similarly, Figure 4.23 reveals the homogeneous correlation function along \tilde{r}_2 at $\tilde{r}_1 = 0$. Furthermore, the homogeneous correlation function along \tilde{r}_1 and along \tilde{r}_2 is shown in Figure 4.24. One can actually see from these initial conditions that it is reasonable to take $\tilde{R}(\tilde{\mathbf{r}}) = \tilde{\rho}_h(\tilde{\mathbf{r}})$ as the properties of $\tilde{R}(\tilde{\mathbf{r}})$ are satisfied by the behaviour of $\tilde{\rho}_h(\tilde{\mathbf{r}})$ (see Chapter 3 for these properties).

It is clearly seen from Figure 4.23 that the imaginary part of the homogeneous correlations function is zero as expected. This is because the spectrum is symmetric with respect to \tilde{r}_2 . This is in contrast with the imaginary part of the homogeneous correlation function as shown in Figure 4.22 which is not zero. This is, again as expected, because the spectrum is not symmetric with respect to k_1 for the case. In addition, these initial homogeneous correlation functions are very consistent with the

definition of the correlation function where the larger the spacing, the smaller its correlation function.

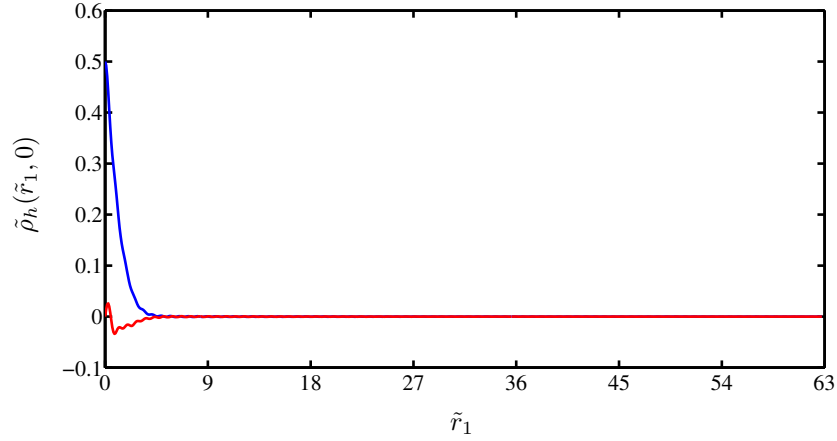


Figure 4.22: The initial homogeneous correlation function with respect to \tilde{r}_1 . The red line represents the imaginary part and the blue line represents the real part.

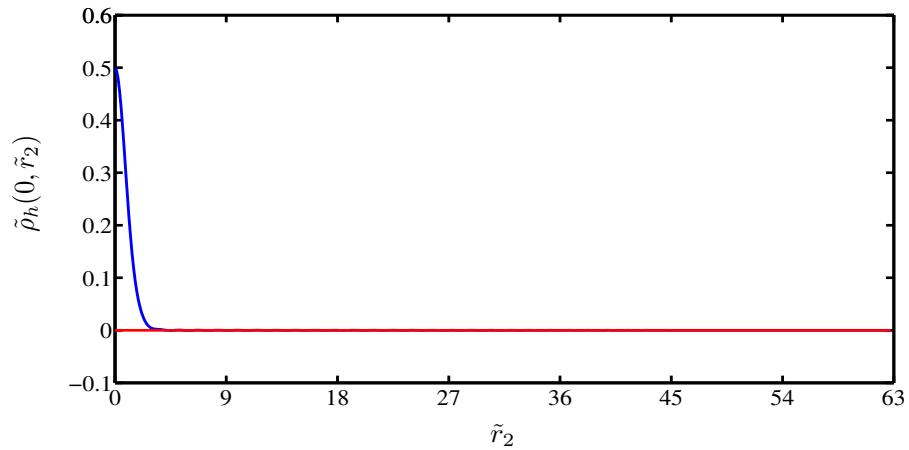


Figure 4.23: The initial homogeneous correlation function with respect to \tilde{r}_2 . The red line represents the imaginary part and the blue line represents the real part.

Further results are shown in Figure 4.25 for $\tilde{\rho}_{max}(\tilde{\mathbf{r}} = \mathbf{0})$, which signifies the maximum values of $k_0^2 \rho(\mathbf{r} = \mathbf{0})/\varepsilon^2$ within the interval $\tilde{x} \in (0, 2\pi/\tilde{P}_2^{(max)})$, as a function of $\tau = \varepsilon^2 \sqrt{gk_0} t$. It clearly demonstrates the recurrent nature of the solution for the degrees of the directional spreading $n = 10$ and $n = 50$ which is from fairly broad directional spreading to fairly narrow directional spreading.

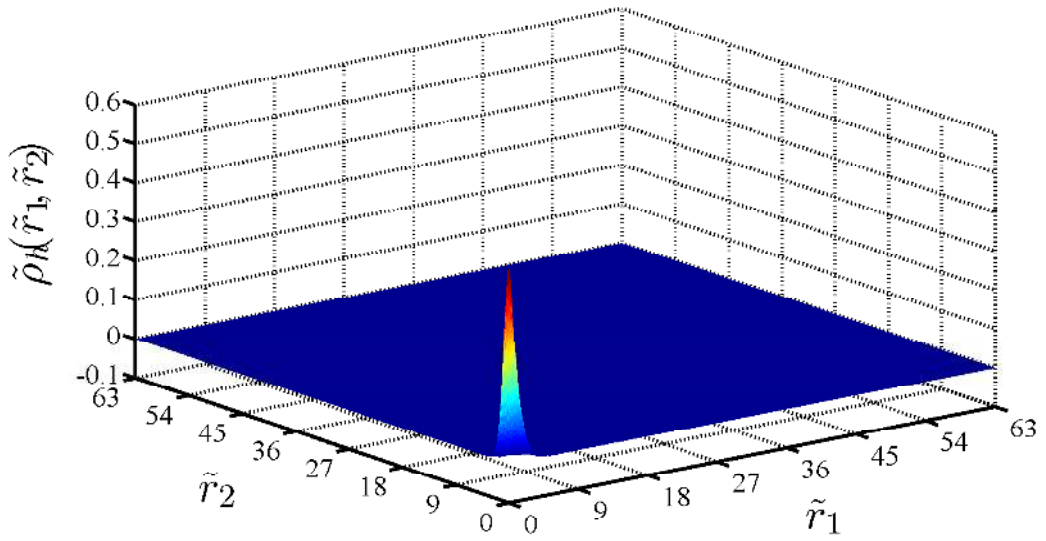


Figure 4.24: Three-dimensional image of the real part of the initial homogeneous correlation function.

This is in sharp contrast to the solution for $n = 2$ which is for a very broad directional spread and has no recurrence. Note that case A_3 is stable (see equation (3.61)) and therefore the chosen disturbance $\tilde{P}_2^{(max)}$ does not have any particular physical meaning. Note that the increase of the peak value and the shortening of the recurrence duration are the result of the decrease in Π_2 (see Table 4.5). A more general picture of the $\tilde{\rho}(\tilde{x}, \mathbf{0}, \tilde{\tau})$ values is given in Figure 4.26. In the figure, the values were shifted along the \tilde{x} axis so that the dimensionless maximum correlation function evaluated at $\tilde{\mathbf{r}} = \mathbf{0}$ are at $\tilde{x} = 0$ and $\tilde{x} = 2\pi/\tilde{P}_2^{(max)}$. The curves were also slightly smoothed.

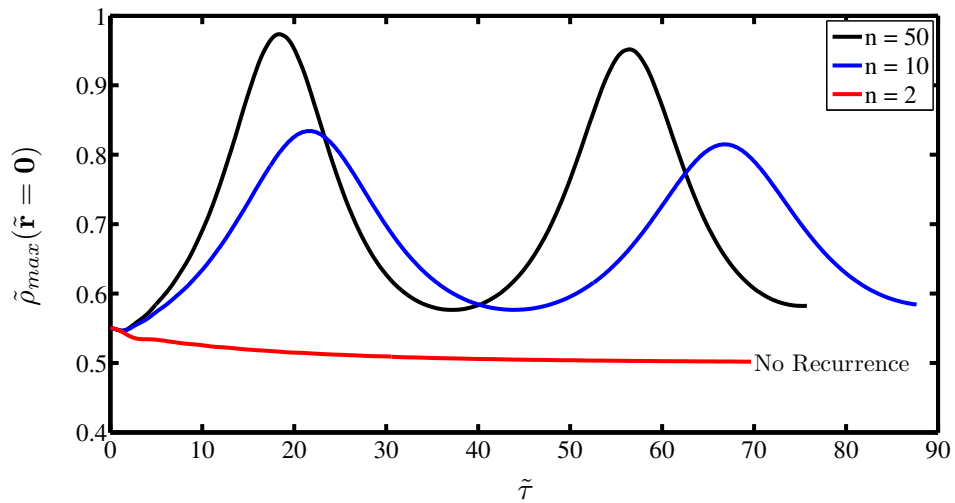


Figure 4.25: The influence of the directional spreading on the variation of the maximum value of $\tilde{\rho}$ at $\tilde{\mathbf{r}} = \mathbf{0}$, as a function of non-dimensional time, $\tilde{\tau}$.

Features of the long-time evolution for JONSWAP spectra with directional distributions are summarised in Table 4.5. As seen from Table 4.5, the narrower is the directional distribution, the smaller the value of Π_2 , i.e. the more unstable the wave trains are. Looking at Table 4.4 and Table 4.5, one can see that the discrepancy between the numerical recurrence time and $2\pi/\tilde{\Omega}_2^{(max)}$ increases with the increase of Π_2 .

Table 4.5: Spectral parameters and evolution features for JONSWAP spectra with three different degrees of the directional distributions, n , and $\gamma=10$, $\alpha=0.016$. A_i is the normalization factor of the directional spreading.

Case	n	A_d	Π_2	$\tilde{P}_2^{(max)}$	$2\pi/\tilde{\Omega}_2^{(max)}$	Numerical recurrence time	Peak enhancement
A_1	50	2.84	0.86	1.53	49	37	1.77
A_2	10	1.29	0.95	1.43	73	44	1.52
A_3	2	0.64	1.11	1.28*	--	--	--

Note: * indicates the stable condition.

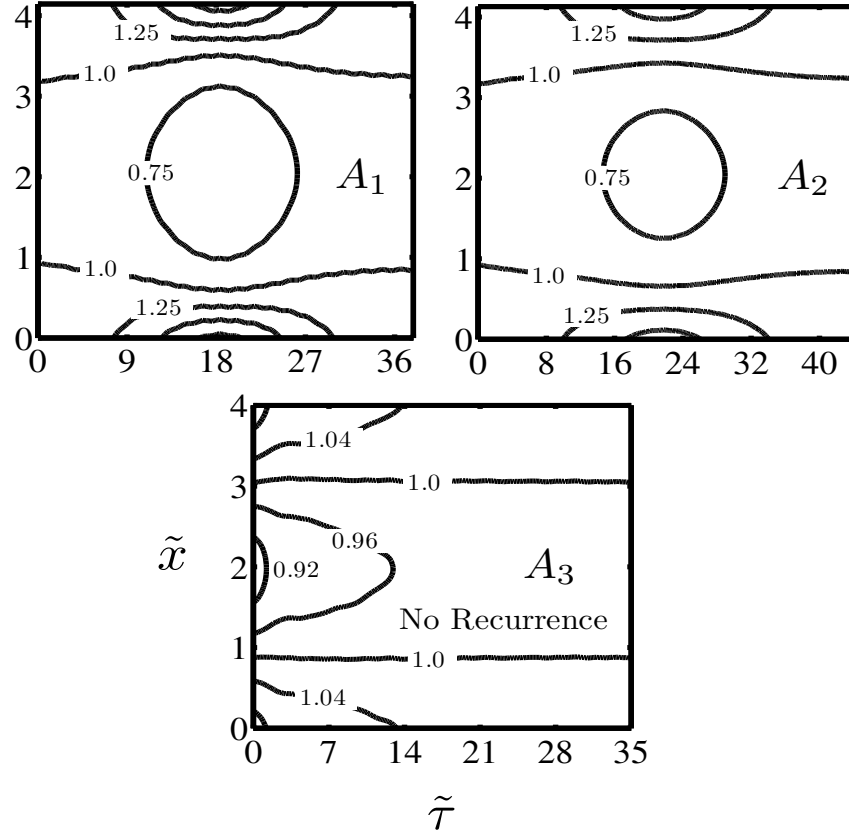


Figure 4.26: Isolines of $\tilde{\rho}(\tilde{x}, \mathbf{0}, \tilde{\tau}) / \tilde{\rho}_h(\mathbf{0})$. Each case refers to Figure 4.25.

4.4 Concluding remarks

A stochastic recurrence for waves with continuous spectrum, which is parallel to the well-known Fermi-Pasta-Ulam recurrence for monochromatic wave trains in the unstable condition initialized by realistic ocean JONSWAP spectra with and without directional distribution, is shown in this Chapter. For unidirectional JONSWAP spectra, whenever the dimensionless “width parameter”, $\Pi_1 < 1$, the Alber equation yields recurring solutions. It is found that the decrease in the “width parameter” is accompanied by an increase in the peak enhancement of the recurrence and a decrease in the numerical recurrence duration. Moreover, the narrower the spectrum, the higher the maximum correlation function evaluated at spacing equal to zero. At the threshold of instability, long-time evolutions are simulated and the previous results in the literature are recovered. It is found that in the stable condition, no recurrence occurs as well as at the marginal instability line. In the unstable condition, but close to the marginal instability line, the recurrence period is very long.

For JONSWAP spectra with directional distributions, whenever the slightly corrected dimensionless “width parameter”, $\Pi_2 < 1.1$, the Alber equation produces recurrence solution. It is found that decreasing the degree of the directional spreading will decrease the peak enhancement of the recurrent solution and for a certain limit of the directional spread, the recurrence solution stops. This is one of the most important results in this research.

In order to have a quality control of the numerical simulation, the first three invariants for two-dimensional Alber equation were derived which is also a new outcome of this research. The first invariant is related to the wave action, the second invariant to the wave momentum and the third invariant to the energy of the system. The deviations of the invariants throughout the simulation did not exceed 1.0% for unidirectional JONSWAP spectra and did not exceed 1.5% for the JONSWAP spectra with directional distributions.

Furthermore, the question of possible manifestation of such inhomogeneous disturbances in nature has to be answered. One positive answer for this question is this behaviour can be used to study the development of freak waves. Therefore, in the next Chapter of this thesis, we will be showing the application of these new results to the statistics of freak waves.

Chapter 5

Application to the statistics of freak waves in directional sea states

5.1 Introduction

Janssen and Alpers (2006) argued that with modern wave forecasting systems it is not possible to predict individual wave events. The reason for this problem is because modern wave forecasting systems only determine the evolution of the ocean wave spectrum but they do not provide information on the phases of the waves. On the other hand, ships or vessels, oil rigs, etc. have not been designed to withstand these exceptional high surface waves (see also: Janssen and Bidlot, 2009). Therefore, it is important to predict the probability of occurrence of freak waves. As has been mentioned in Chapter 1, there is no standard definition of a freak wave. However, the most popular definition is based on the significant wave height where freak waves or rogue waves are defined as waves whose heights are more than twice the significant wave height, e.g. from 2.0 to 2.2 times the significant wave height (Dean, 1990, Kharif and Pelinovsky, 2003, Janssen, 2003). So, if the significant wave height is 2 meters, then all waves whose heights exceeding 4 meters should be categorized as freak waves or rogue waves (see also: Chalikov, 2009). In addition, a wave whose height exceeded the significant wave height more than three times is called an exceptionally high freak wave. Note, however, that there is a limit of waves steepness beyond where the waves will break (Babanin et al., 2010, Toffoli et al., 2010a). Based on the known physical mechanisms, as shown in Chapter 1, which responsible for the formation of freak waves, up to this days, it is impossible to predict the occurrence of the freak waves unless by means of the statistics.

Based on the theory of linear waves, Longuet-Higgins (1952) showed that the probability distribution of wave heights is given by the Rayleigh distribution if the wave

spectrum contains a single narrow band of frequencies and if the wave energy is being received from a large number of different sources whose phases are random. From this distribution, it is a straightforward calculation to obtain the probability of waves whose heights are higher than twice or three times the significant wave heights which are 3×10^{-4} and 10^{-8} , respectively. For a typical sea wave period of 10 seconds, a wave whose height is higher than two times the significant wave height should appear once among about 3333 waves. Moreover, based on this probability, for waves with period of 10 seconds one should meet this kind of a freak wave every 9 to 10 hours. Similarly, a wave whose height is higher than three times the significant wave height may occur once in 31 years as also reported by Regev et al. (2008). This is provided that the storm is stationary and continues for 31 years. It is hard to believe that this very unrealistic event can happen in the real ocean. First, storms do not last that long and second, the wave will break for this very unlikely wave height (Babanin et al., 2010). It is evident that such very exceptional wave height does occur in the real sea. As reported by Didenkulova et al. (2006), for example, a freak wave which occurred on 14 February 2005 has damaged the cruiser “Grand Voyager”. It was reported that the estimation of freak wave height was 14 metres, while the maximum significant wave height estimation was 2.4 metres. This clearly shows that the freak wave height was about 5.8 times the significant wave height. Similarly, cruiser “Norwegian Dawn” accident on 16 February 2005 was hit by a freak wave whose height was approximately 21 metres while the significant wave height at the time was about 4 metres. This, again, indicates that wave whose height is greater than three times the significant wave height may occur in the real ocean.

As have been mentioned in Chapter 1, one of the several mechanisms that can be responsible for the generation of freak waves is the modulational instability such as the well-known Benjamin-Feir instability (Zakharov 1966; Benjamin and Feir, 1967, McLean et al., 1981). Moreover, Zakharov et al. (2010) argued that freak waves appear inevitably as a result of nonlinear evolution of modulation instability not only for monochromatic Stokes waves, but also for stochastic spectra with a narrow enough spectral band (see also Zakharov and Shamin (2010)). Classical Benjamin Feir instability was derived for quasi-monochromatic wave trains and later, by analogy, Onorato et al. (2001) and Janssen (2003) introduced a so-called Benjamin-Feir index

(BFI) in continuous spectra which is the ratio of steepness to bandwidth of the spectrum for the unidirectional sea states and it can be written as:

$$BFI = \frac{\varepsilon}{\Delta\omega/\omega_0} \quad (5.1)$$

where ω_0 and $\Delta\omega$ are the peak frequency and the bandwidth in the frequency spectrum, respectively. It is found that if BFI is greater than one, then the random wave fields can experience modulational instability, while in the opposite side where if BFI is less than one, then the random wave field is stable.

As shown in Chapter 2, for directional sea states, some experiments (see, for example, Onorato et al., 2009a, 2009b) revealed that modulational instability depends on the directional distributions. However, Babanin et al. (2010, 2011a, 2011b) argued that directional spreading is not the only parameter of surface wave fields which influences modulational instability. Based on their experiments in the wave flume, they found that if the directional spreading becomes too broad and wave field stabilizes, an increase of the steepness can re-activate the instability. Moreover, they introduced their version of the directional Benjamin-Feir Index (BFI) in which they called a directional Modulational Index, M_{Id} , which is a product of the normalization factor of the directional distribution, A_d , and the wave steepness, ε , i.e.

$$M_{Id} = A_d \cdot \varepsilon. \quad (5.2)$$

Another version of BFI which include the directional effect has been introduced by Mori et al. (2011) which is

$$BFI_{2D} = \frac{\varepsilon}{\sqrt{\delta_\omega^2 + \frac{\alpha_2 \delta_\theta^2}{2}}} \quad (5.3)$$

where ε , δ_ω and δ_θ are the steepness, frequency bandwidth and directional bandwidth, respectively, while α_2 is a constant.

One interesting thing of the directional Modulational Index introduced by Babanin et al. is the use of parameter A_d which corresponds to narrower directional distribution. This parameter is convenient property to use as a proxy of the directional spread because there is an intensive parameterization available for its dependence (Babanin and

Soloviev, 1987, 1998b) and it is unambiguously analytically connected with other existing directional spread characteristics used in the literature, even for bimodal directional spectra.

The role of the modulational instability on the generation of freak waves has been demonstrated numerically (e.g. Toffoli et al., 2010b, Gramstad and Trulsen, 2010) as well as experimentally (e.g. Onorato et al., 2009b, Babanin et al., 2011a) in the wave flumes. These results will be discussed below where both unidirectional random wave fields and with directional spreading will be considered, respectively. Note that a similar review can be found in Gramstad and Trulsen (2007).

For unidirectional sea states, Onorato et al. (2001) performed numerical simulation based on the nonlinear Schrödinger equation initialized by a JONSWAP spectrum in order to study freak waves. They found that the probability occurrence of freak waves increases for large values of both Phillips parameter, α , and the peak enhancement factor, γ , of a JONSWAP spectrum. As seen from equation (5.1), the Benjamin Feir Index is proportional to the steepness of the spectrum. By assuming that bandwidth of the spectrum is constant, increasing the Phillips parameter or the peak enhancement factor of the JONSWAP spectrum both will lead to increase of the steepness. This will cause to the BFI increase and as a result, it will increase the probability of occurrence of freak waves.

Specifically, If α is increased, then to keep the steepness constant γ should be decreased. This means that spectra become broader and this leads to corresponding implications for the instability of nonlinear groups – i.e. the growth rates of most unstable modes are expected to decrease or even be suppressed. If γ is increased, then to keep the steepness constant α should be decreased. Such combination will instigate rapid narrowing of the spectral bandwidth of dominant waves, which we expect to be associated with their instability, and which is the most important outcome in practical sense, e.g. for wave breaking or freak wave probability.

Using the Zakharov equation, Janssen (2003) showed the freak waves occurrence as a result for a four-wave interaction where Benjamin-Feir instability plays a key role. Moreover, Onorato et al. (2004) performed experiments in one of the largest wave tank facilities in the world and found that the tail of the probability density function for wave height strongly depends on the Benjamin-Feir index. They also found that for large BFI

the Rayleigh distribution clearly underestimates the probability of large events. Furthermore, Onorato et al. (2005) found that the presence of the modulational instability is responsible for the departure from a Gaussian behaviour, indicating that, for particular parameters in the wave spectrum, coherent unstable modes are quite prevalent, leading to the occurrence of what might be called a “rogue sea”. In addition, Onorato et al. (2006) showed the statistical properties of the surface elevation for long crested waves characterized by JONSWAP spectra with random phases. They found that for unidirectional waves and for large values of the Benjamin–Feir index, the second order theory is not adequate to describe the tails of the probability density function of wave crests and wave heights.

For more realistic sea states (i.e. directional sea states) which are characterized by wave components propagating along different directions, numerical (e.g. Gramstad and Trulsen, 2010, Toffoli et al., 2010b) and experimental evidence (e.g. Onorato et al., 2009b, Babanin et al., 2011b) shown that directional spreading plays an important role on the probability of occurrence of freak waves. Onorato et al. (2002), for example, numerically integrated a two-dimensional modified nonlinear Schrodinger equation initialized by JONSWAP spectra and reported that the number of extreme wave events was reduced when the directionality of the initial spectrum was increased. Likewise, Socquet-Juglard et al. (2005) also performed numerical simulations by using a modified nonlinear Schrödinger equation and found that for broad directional distribution, deviation from Gaussian statistics are only due to bound nonlinear contributions to the wave field, while free waves preserve the Gaussian statistics despite the third-order nonlinear evolution. The statistics of the numerically simulated sea surface thus showed an excellent agreement with Tayfun distributions (Tayfun, 1980). In addition, Gramstad and Trulsen (2007) performed a large number of simulations in order to investigate the occurrence of freak wave in deep water and found that it depends on the group length and directionality for a fixed steepness. They reported that Benjamin-Feir index is a useful parameter to indicate the increase of the freak wave activity. Moreover, Eliasson and Shukla (2010) derived a nonlinear wave-kinetic equation for gravity waves in 2+2 dimensions (two spatial dimensions and two velocity dimensions) and carried out numerical simulations to study the stability and nonlinear spatiotemporal evolution of narrow-banded waves. They also found that narrower directional spectra lead to self-focusing of ocean waves and an enhanced probability of extreme events. Furthermore,

Onorato et al. (2009a) and Waseda et al. (2009) performed two independent experimental investigations, in order to study the statistical properties of surface-elevation for different degrees of directional energy distribution. The experimental facilities used had different sizes and they were equipped with different wave-makers. Nevertheless, they reported consistent results that the probability of the formation of large amplitude waves strongly depends on the directional properties of the waves (Onorato et al., 2009b). All of these numerical and experimental results are very consistent to reveal that wave directional spreading reduces the effect of instability and concurrently reduces the probability of occurrence of freak waves. In relation to the instability, however, none of the aforementioned experiments provides the deterministic marginal instability. Therefore, the question that still unanswered is when the instability stops. In order to answer this question, Babanin et al. (2010, 2011a) conducted experiments for quasi-monochromatic waves and as a results, they introduced what so-called directional Modulational Index which depends on two parameters, namely directional spreading and the steepness (see equation 5.2). They have shown that the modulational instability stops when the directional modulational index is $M_{Id} \approx 0.18$. This indicates that the instability condition for unidirectional sea states is well established (Babanin 2011, 2011b). However, for directional wave fields, it is much less certain although quantitative guidance exists. This is including the role of the instability on the formation of freak waves.

Most of numerical studies are based on the nonlinear Schrödinger equation and its extensions which are the most popular tool to investigate the nonlinear waves albeit for their limitation on narrow spectra (Chalikov, 2009, Zakharov et al., 2010). The stochastic version of the nonlinear Schrödinger equation has been derived by Alber (1978) which is now called Alber equation. This equation is designed for treating inhomogeneous wave fields albeit for narrow spectra. In Chapter 3, new instability conditions for more realistic ocean wave spectra with and without directional distributions have been introduced. In addition, it has been shown in Chapter 4 that in the unstable condition, recurrent evolutions which are parallel to the well-known Fermi-Pasta-Ulam recurrence phenomenon are obtained. Here we show the physical significance of the recurrent behaviour to study the statistics of freak waves in directional sea states. Specifically, we took advantage of the periodicity imposed by the initial disturbance and the consequent recurrent evolution of unstable spectra to

calculate the probability of freak waves, implying that for stable spectra the freak waves probability will be given by the Rayleigh distribution. The preliminary attempt to this regard has been done by Regev et al. (2008) using unidirectional Gaussian spectra. In addition, the comparison between the results obtained from the Alber equation and the second order theory of the Forristall distribution (Forristall, 2000) will be shown.

5.2 Theoretical background

In order to study the statistics of freak waves, a formula for the probability of wave height will be determined in this section. To do so, the method used by Regev et al. (2008) will be adopted. Starting from the Rayleigh distribution, the probability distribution of wave height will be formulated. Furthermore, the review of the Forristall distribution on the deep water will be presented.

5.2.1 The Rayleigh distribution

Following Young (1999) and adopting the basic theory for the distribution of wave heights that was originally developed by Rice (1944), it is assumed that the spectrum of the water surface elevation is narrow banded where the energy of spectrum is concentrated in the vicinity of the carrier waves. The probability density function for wave heights of such a spectrum follows the Rayleigh distribution

$$p(H) = \frac{H}{4\sigma^2} e^{-\frac{H^2}{8\sigma^2}} \quad (5.4)$$

where $\sigma^2 = \int S(k) dk$ is the variance of the record, $S(k)$ is the spectrum as a function of wavenumber and H is the wave height. Moreover, since equation (5.4) is the probability density function, it must satisfy the following condition

$$\int p(H) dH = 1. \quad (5.5)$$

In order to obtain the mean of the Rayleigh distribution, one can take an expected value of H , that is

$$\bar{H} = E[H] = \int_0^{\infty} H p(H) dH = \int_0^{\infty} \frac{H^2}{4\sigma^2} e^{-\frac{H^2}{8\sigma^2}} dH = \sqrt{2\pi\sigma^2} \quad (5.6)$$

and the root mean square (rms) wave height is calculated by taking an expected value of H^2 , that is

$$H_{rms}^2 = E[H^2] = \int_0^{\infty} H^2 p(H) dH = \int_0^{\infty} \frac{H^3}{4\sigma^2} e^{-\frac{H^2}{8\sigma^2}} dH = 8\sigma^2. \quad (5.7)$$

Note that $E[\]$ stands for the expected value.

Making use of the equation (5.7), the probability density function of the Rayleigh distribution can be rewritten as

$$p(H) = \frac{2H}{H_{rms}^2} e^{-\frac{H^2}{H_{rms}^2}}. \quad (5.8)$$

Furthermore, the relation between the significant wave height, H_s , with the variance of the wave record as shown in Chapter 2 is given by (see Boccotti, 2000, Ochi, 2005, Holthuijsen, 2007)

$$H_s = 4\sigma. \quad (5.9)$$

Therefore, from equation (5.7) and equation (5.9), one can obtain the relation between the significant wave height and the root mean square wave height that is

$$H_s = \sqrt{2}H_{rms}. \quad (5.10)$$

Note that theoretical derivations of equations (5.9) and (5.10) can also be found in Chapter 2.

5.2.2 The Forristall distribution on infinitely deep water

As given in Chapter 2, Forristall (2000) fitted the Weibull distribution which is the general form of the Rayleigh distribution obtained from the linear waves, to the second order simulation with a wide variety of wave steepness and Ursell number. This result is now known as Forristall distribution/model. One advantage of this model is that it can be applied for arbitrary water depths. Specifically, he fits the Weibull distribution as given by (i.e. probability that H is greater than a value \hat{H})

$$P(H > \hat{H}) = \exp \left[- \left(\frac{\hat{H}}{2\sqrt{2}\alpha H_{rms}} \right)^\beta \right], \quad (5.11)$$

where H is the wave height, H_{rms} is the root mean square wave height and the parameters α and β for the deep water are given in the following. For the unidirectional sea simulations (1D), the values of parameters are

$$\alpha_1 = 0.3536 + 0.2892S_1, \quad (5.12)$$

$$\beta_1 = 2 - 2.1597S_1, \quad (5.13)$$

and for the directional sea simulations (2D), the values of parameters are

$$\alpha_2 = 0.3536 + 0.2568S_1, \quad (5.14)$$

$$\beta_2 = 2 - 1.7912S_1, \quad (5.15)$$

where $S_1 = 2\pi H_s / (gT_1^2)$ is the steepness, H_s is the significant wave height and is calculated by four times the square root of the variance of the wave spectrum, i.e. $H_s = 4\sqrt{m_0}$, where m_0 is the variance of the wave spectrum. T_1 is the mean wave period which is determined by $T_1 = m_0/m_1$, where m_1 is the first order moment.

As seen from the Forristall parameters, the Forristall distribution on infinitely deep water is only a function of wave steepness. Taking for example, a unidirectional JONSWAP spectrum with the energy scale $\alpha = 0.016$, the peak enhancement factor $\gamma = 10$ and the peak width parameter $\sigma = 0.08$, gives the following values of Forristal parameters

$$S_1 = 0.0589,$$

$$\alpha_1 = 0.3706, \quad \beta_1 = 1.8728,$$

$$\alpha_2 = 0.3687, \quad \beta_2 = 1.8945.$$

Using the equation (5.11), the plot of these results and the comparison with the classical value given by the Rayleigh distribution are shown in Figure 5.1. It is clearly seen that the probability of wave height obtained from the Forristal distribution, which is based on the second order theory, is higher than the probability of wave height given by the

classical values of the Rayleigh distribution. In addition, the probability of wave height for the directional wave fields is lower compared to probability of wave height for the unidirectional sea states as expected. One should note, however, that even though Forristall distribution is in a good agreement with the observations, it also has some limitations as shown in Chapter 2. Such limitations will also be shown in this research.

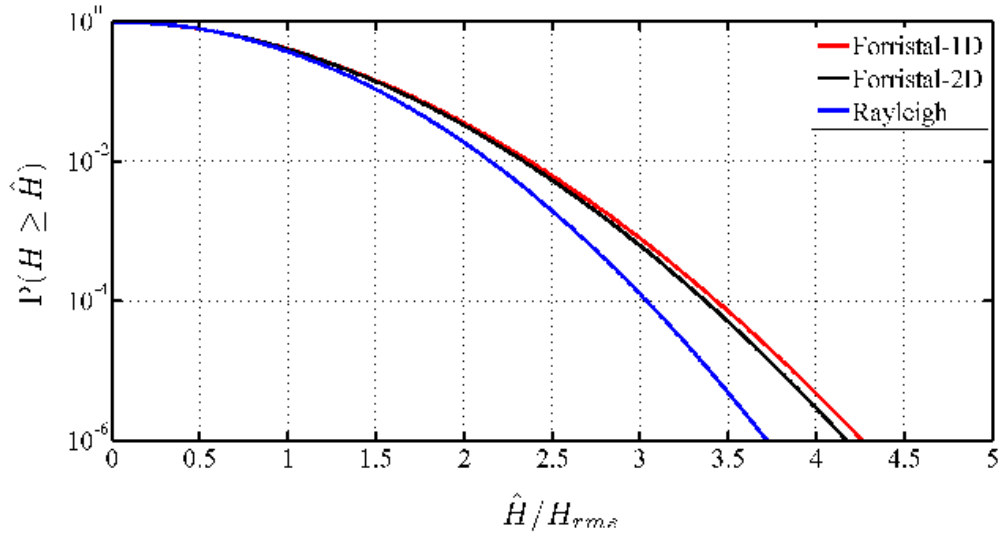


Figure 5.1: Comparison between the probability of wave height for the unidirectional and directional sea states based on the Forristall distribution and the probability of wave height given by the Rayleigh distribution.

5.2.3 Probability distribution of the wave height

A two-dimensional Alber equation, which is the equation for narrow-banded random surface waves on the infinitely deep water, has been given in Chapter 3. The two-point spatial correlation function is defined as the ensemble average of the complex envelope of the narrow banded sea. Besides that, it has been shown that the correlation function for homogeneous sea only depends on the spacing \mathbf{r} . Therefore, for homogeneous sea, the correlation function at $\mathbf{r} = \mathbf{0}$ is given by the integral of the energy spectrum and it can be written as

$$\rho_h(\mathbf{r} = \mathbf{0}) = \int S(\mathbf{k}) d\mathbf{k}. \quad (5.16)$$

Now, following a procedure similar to that in Regev et al. (2008), let H_{rms0} be the root mean square wave height of the homogeneous sea and thus the correlation for homogeneous sea at $\mathbf{r} = \mathbf{0}$ is proportional to H_{rms0}^2 and it can be written as

$$\rho_h(\mathbf{r} = \mathbf{0}) \propto H_{rms0}^2. \quad (5.17)$$

Similarly, based on the equation (3.63) of Chapter 3, we can assume that the correlation for an inhomogeneous sea can be written as

$$\rho(\mathbf{x}, \mathbf{r} = \mathbf{0}, t) \propto H_{rms}^2 \quad (5.18)$$

where H_{rms}^2 is a measure of the average energy density at the point $\rho(\mathbf{x}, t)$.

From equation (5.17) and equation (5.18), we have the following relation

$$\frac{H_{rms0}^2}{H_{rms}^2} = \frac{\rho_h(\mathbf{r} = \mathbf{0})}{\rho(\mathbf{x}, \mathbf{r} = \mathbf{0}, t)}. \quad (5.19)$$

Moreover, the cumulative form of the Rayleigh distribution in the equation (5.8) (Young, 1999) is given by

$$P(H \geq \hat{H}) = e^{-\left(\frac{\hat{H}}{H_{rms}}\right)^2}, \quad (5.20)$$

that is probability that H is greater than a value \hat{H} . Equation (5.20) can then be rewritten as

$$P(H/H_{rms0} \geq \hat{H}/H_{rms0}) = e^{-[(\hat{H}/H_{rms0})(H_{rms0}/H_{rms})]^2}. \quad (5.21)$$

Making use of equation (5.19), equation (5.21) for a chosen value of ρ can then be rewritten as

$$P(H/H_{rms0} \geq \hat{H}/H_{rms0}) = \exp \left[- \left(\frac{\hat{H}}{H_{rms0}} \right)^2 \left(\frac{\rho_h}{\rho} \right) \right]. \quad (5.22)$$

However, the probability density function (pdf) of $\rho(\mathbf{x}, \mathbf{r} = \mathbf{0}, t)$ is required to determine the probability to obtain values of ρ in the interval $(\rho, \rho + \Delta\rho)$. Therefore, the probability to obtain $H \geq \hat{H}$ throughout the spatial and temporal evolution of ρ is given by

$$P(H/H_{rms0} \geq \hat{H}/H_{rms0}) = \int \text{pdf} \left(\frac{\rho}{\rho_h} \right) e^{\left[- \left(\frac{\hat{H}}{H_{rms0}} \right)^2 \left(\frac{\rho_h}{\rho} \right) \right]} d \left(\frac{\rho}{\rho_h} \right) \quad (5.23)$$

where $\text{pdf}(\rho/\rho_h)$ stands for the probability density function of $\rho(\mathbf{x}, \mathbf{r} = \mathbf{0}, t)/\rho_h(\mathbf{0})$.

5.3 Recurrent solutions

As has been shown in Chapter 4, if the dimensionless “width parameter” Π where $\Pi = \Pi_1 < 1$ for the unidirectional spectra and $\Pi = \Pi_2 < 1.1$ for the directional spectra, the Alber equation yields recurring solutions. One advantage of this recurrent behaviour is that it enables us to study the probability of occurrence of freak waves. This is because one can take one cycle of the recurrent solution and establish the probability density function. It then allows us to determine the probability of wave height and based on this, by definition of freak waves, one can determine its occurrence probability. Therefore, a further step to calculate the probability of wave height is to determine the probability density function of $\rho(\mathbf{x}, \mathbf{r} = \mathbf{0}, t)/\rho_h(\mathbf{0})$ which is $\text{pdf}(\rho/\rho_h)$. To this end, as aforementioned, one cycle of the stochastic recurrence will be taken. For convenience, however, all the parameters will be transformed into the non-dimensional forms as defined in Chapter 4, that is

$$\tilde{\rho} = \frac{k_0^2}{\varepsilon^2} \rho; \tilde{x} = \varepsilon k_0 \left(x - \frac{1}{2} \sqrt{\frac{g}{k_0}} t \right); \tilde{y} = \varepsilon k_0 y; \tilde{r}_1 = \varepsilon k_0 r_1; \quad (5.24)$$

$$\tilde{r}_2 = \varepsilon k_0 r_2; \tilde{t} = \varepsilon^2 \sqrt{g k_0} t.$$

A typical cycle of the recurrence as given in Chapter 4 for a unidirectional wave field is given in Figure 5.2 and Figure 5.3 for the peak enhancements, $\gamma = 20$ and $\gamma = 10$, respectively, with different values of the energy scale (see Table 5.1). For JONSWAP spectra with directional distributions, a typical cycle of the long-time recurring evolution is shown in Figure 5.4 with different values of the degree of the directional spreading, namely $n = 10$ and $n = 50$. This is, again, the same as the case study in Chapter 4, where $\alpha = 0.016$ and $\gamma = 10$ (see Table 5.2). In Figure 5.2 and Figure 5.3, $\tilde{\rho}_m(\tilde{t})$ is the maximum value of dimensionless correlation function evaluated at $r_1 = 0$, $\tilde{\rho}(\tilde{x}, 0, \tilde{t})$, for chosen dimensionless time \tilde{t} and for all possible values of \tilde{x} while $\tilde{\rho}_m(\tilde{t})$ in Figure 5.4 is the maximum value of dimensionless correlation function evaluated at $\tilde{\mathbf{r}} = \mathbf{0}$, $\tilde{\rho}(\tilde{\mathbf{x}}, \mathbf{0}, \tilde{t})$, also for chosen dimensionless time \tilde{t} and for all possible values of $\tilde{\mathbf{x}}$.

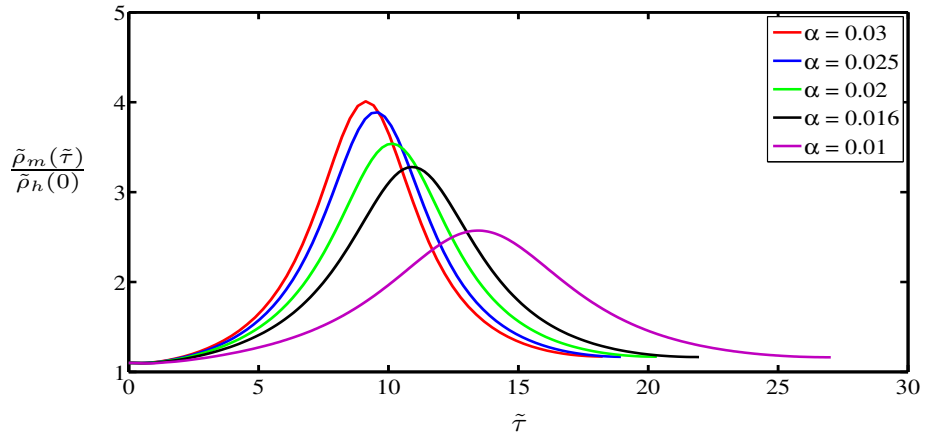


Figure 5.2: A typical cycle of the long-time recurring evolution of $\tilde{\rho}_m(\tilde{\tau}) / \tilde{\rho}_h(0)$ as a function of the dimensionless time for unidirectional JONSWAP spectra with $\gamma=20$ and five different values of the energy scale.

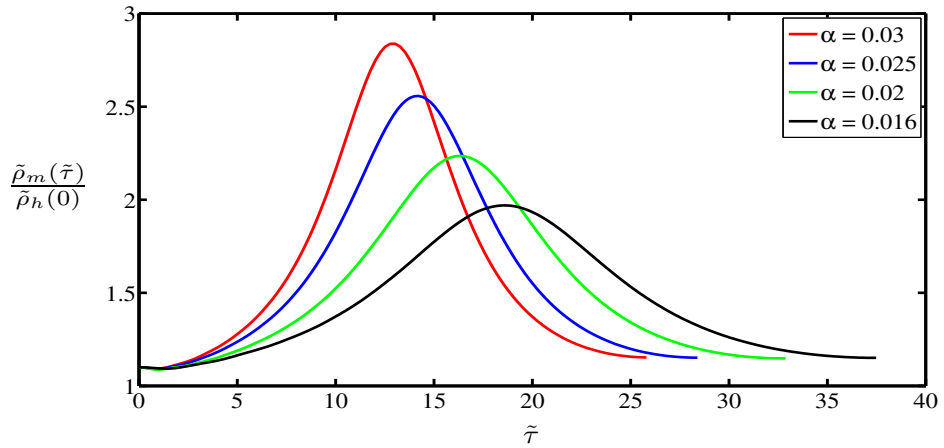


Figure 5.3: A typical cycle of the long-time recurring evolution of $\tilde{\rho}_m(\tilde{\tau}) / \tilde{\rho}_h(0)$ as a function of the dimensionless time for unidirectional JONSWAP spectra with $\gamma=10$ and four different values of the energy scale.

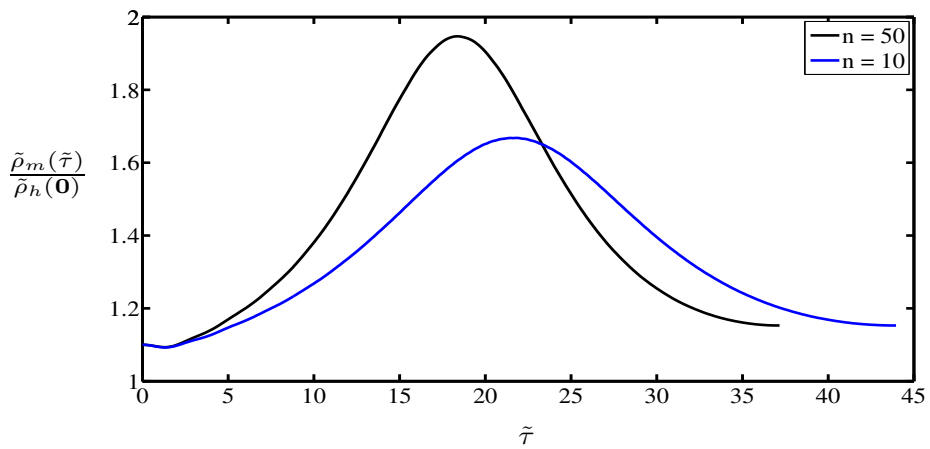


Figure 5.4: A typical cycle of the long-time recurring evolution of $\tilde{\rho}_m(\tilde{\tau}) / \tilde{\rho}_h(\mathbf{0})$ as a function of the dimensionless time for JONSWAP spectra with two different degrees of the directional distribution $\cos^n(\theta)$ and with $\alpha=0.016$ and $\gamma=10$.

5.4 The probability of freak waves

The stochastic recurrence facilitates the study of the probability of freak waves. This is because the stochastic recurrence can be used to establish the probability density function and then to determine the freak waves probability in a straightforward fashion. The wave height probability is given in equation (5.23). In the following two sections we will show the probability of freak waves in unidirectional wave fields (based on JONSWAP spectrum) and directional wave fields (described by JONSWAP spectrum and a $\cos^n(\theta)$ directional function).

5.4.1 Unidirectional sea states

As a special case, a JONSWAP spectrum with $\gamma = 20$ and five different values of the energy scale is used to describe a variety of unidirectional sea states (see Table 5.1). Furthermore, in order to find the probability density function, $\text{pdf}(\tilde{\rho}/\tilde{\rho}_h)$, again, we adopted the method used in Regev et al. (2008). Firstly, more than 100 locations evenly distributed along the \tilde{x} axis from 0 to $2\pi/\tilde{P}^{(max)}$ were taken. Over one recurrence cycle, $\tilde{\rho}/\tilde{\rho}_h$ was sampled at 100 evenly distributed sampling times, so that more than ten thousand $\tilde{\rho}(\tilde{x}, 0, \tilde{\tau})/\tilde{\rho}_h(0)$ values were used to establish $\text{pdf}(\tilde{\rho}/\tilde{\rho}_h)$ (see Figure 5.2). The isolines of these $\tilde{\rho}/\tilde{\rho}_h$ are plotted in Figure 4.11 of Chapter 4 for the above-mentioned five different cases (see Table 5.1).

Secondly, all of the values were arranged from the lowest to the highest and then divided into 100 evenly spaced increments in $\tilde{\rho}/\tilde{\rho}_h$, e.g. from 0.26 to 4 for $\gamma = 20$ and from 0.5 to 2.8 for $\gamma = 10$. The probability of each increment was calculated as the number of elements within the increment divided by the total number of values used. Figure 5.5 presents the probability density function of $\tilde{\rho}/\tilde{\rho}_h$ in the form of a bar diagram (to ease comparison, the widths of the bins in all bar diagrams are equal) and the probability function (the probability of obtaining a value smaller or equal to $\tilde{\rho}/\tilde{\rho}_h$) is given by the solid line for the five different cases. Note that the probability function in this research is commonly called cumulative distribution function (cdf) in general statistics. From isolines as shown in Figure 4.11 in Chapter 4 and Figure 5.5 one can see that for cases *D* and *E* many bins are activated and that the number of active bins reduces when the dimensionless “width-parameter” Π_1 increases as shown in Table 5.1.

The probability function for the wave height given by equation (5.23) is calculated on the basis of the known values of pdf($\tilde{\rho}/\tilde{\rho}_h$) as shown in Figure 5.5. Some different features that will be shown in relation to this probability, such as the comparison with the classical value given by Rayleigh distribution as given in the equation starting from zero wave height and at the tail of the probability, the probability of waves whose heights are higher than two times and three times the significant wave height respectively. Figure 5.6 shows two different features of the probability in comparison to homogenous seas according to the Rayleigh distribution. The first feature is the tail of the probability. As can be seen from Figure 5.6, the results obtained from the Alber equation are higher than obtained from the Rayleigh distribution as expected. This is because, as known, Rayleigh distribution was established based on the linear waves theory (Longuet-Higgins, 1952) while Alber equation is the equation for the nonlinear ocean surface waves. In addition, in the figure, probability values of freak waves, that is the probability for waves with $\hat{H} \geq 2.84H_{rms0}$; i.e. $\hat{H} \geq 2H_s$ is plotted (note that our H_{rms0} and significant wave height H_s are connected as $H_s = \sqrt{2}H_{rms0}$ as shown in Section 5.2.1). Another feature as shown in the inset of Figure 5.6 is a full comparison (starting from zero wave height) between the probability of the homogeneous sea and the probability obtained from the Alber equation for case *E*. As can be seen from the inset, the probability up to $\hat{H} \geq 1.46H_{rms0}$ is greater for the Rayleigh distribution, but after the intersection point the probability is greater for the results obtained from the Alber equation. For other cases, namely for cases *A*, *B*, *C* and *D* one can obtain that the intersection values in the range $\hat{H}/H_{rms0} \in (1.46, 1.53)$.

In order to obtain the exact values of the probability, it is necessary to change the scale of the vertical axis of the figure from logarithmic scale to linear scale. Then, the probability of waves whose heights are more than two times the significant wave height are shown in Figure 5.7. As can be seen from the figure, case *E* gives 40 out of 10000 waves higher than $2.84H_{rms0}$, which is equivalent to two times the significant wave height, as opposed to case *A* where about 17 out of 10000 are higher than $2.84H_{rms0}$ ($\approx 2H_s$) which is closer to the Rayleigh distribution.

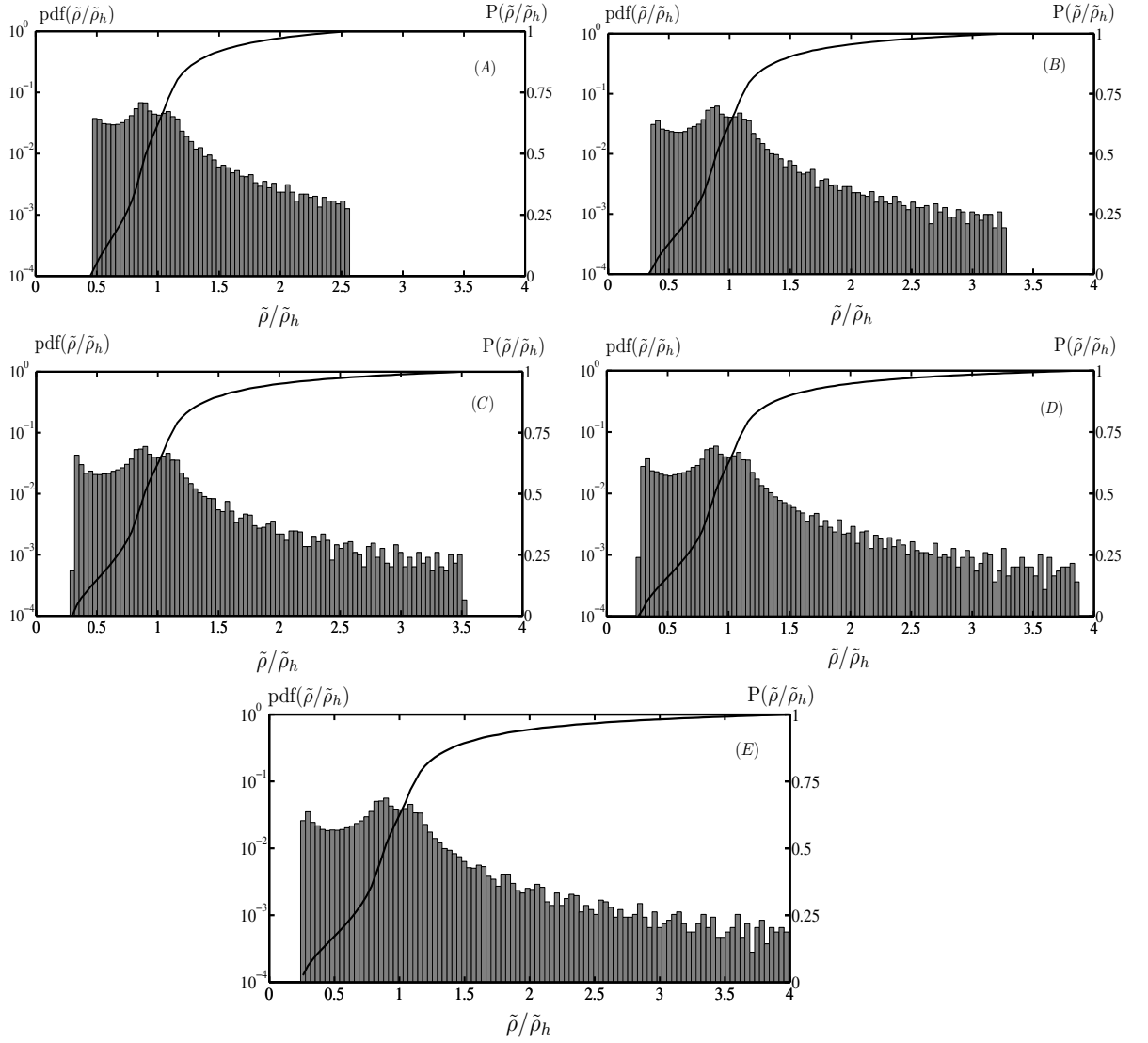


Figure 5.5: Probability density function $\text{pdf}(\tilde{\rho}/\tilde{\rho}_h)$ and probability function $P(\tilde{\rho}/\tilde{\rho}_h)$ (solid line) as functions of $\tilde{\rho}/\tilde{\rho}_h$ for unidirectional JONSWAP spectra with $\gamma = 20$.

Note that the Rayleigh distribution only gives about 3 out of 10000 waves higher than two times the significant wave height. Moreover, there are about 27, 32 and 37 over 10000 waves whose heights are higher than two times significant wave height for the cases *B*, *C* and *D*, respectively. Furthermore, the probabilities of waves whose height are higher than three times the significant wave height are shown in Figure 5.8. As we can see from the figure, the probability values increase from “almost never” value of 10^{-8} for the Rayleigh distribution to 10^{-5} for case *A*, 5×10^{-5} for case *B*, 7×10^{-5} for case *C*, 11×10^{-5} for case *D* and 13×10^{-5} for case *E*. These are about 10000 times higher probabilities. It should be mentioned in this regard that the Alber equation does not have any dissipation mechanisms and in theory allows for infinite wave heights

to occur. In reality, there is a limit of wave steepness beyond which the waves will break (Babanin et al., 2010), and this limit indicates the maximum ratio of individual wave height to the significant wave height of ~ 2.0 (Babanin et al., 2011a). Note, however, this maximum ratio was obtained from a one dimensional quasi-monochromatic waves experiment.

Now, it is also important to show the influence of the peak enhancement factor on the probability of occurrence of freak waves. In this regard, the previous peak enhancement factor, i.e. $\gamma = 20$, will be changed to $\gamma = 10$ for four cases as shown in Table 5.1. Furthermore, a similar procedure that was used to determine the probability of freak waves for the case $\gamma = 20$ will be applied for these cases including the determination of the probability density function. To this end, one typical cycle of the stochastic recurrence as shown in Figure 5.3 will be used. The probability density functions of these cases are shown in Figure 5.9. As seen from the figures, the number of active bins increase by increasing the energy scale, which is consistent with the cases for $\gamma = 20$. Also, in terms of the dimensionless “width parameter”, Π_1 , the decrease of value of this parameter is accompanied by an increase of active bins. Likewise, using the probability density function as shown in Figure 5.9, one will obtain the probability of wave heights by using equation (5.23).

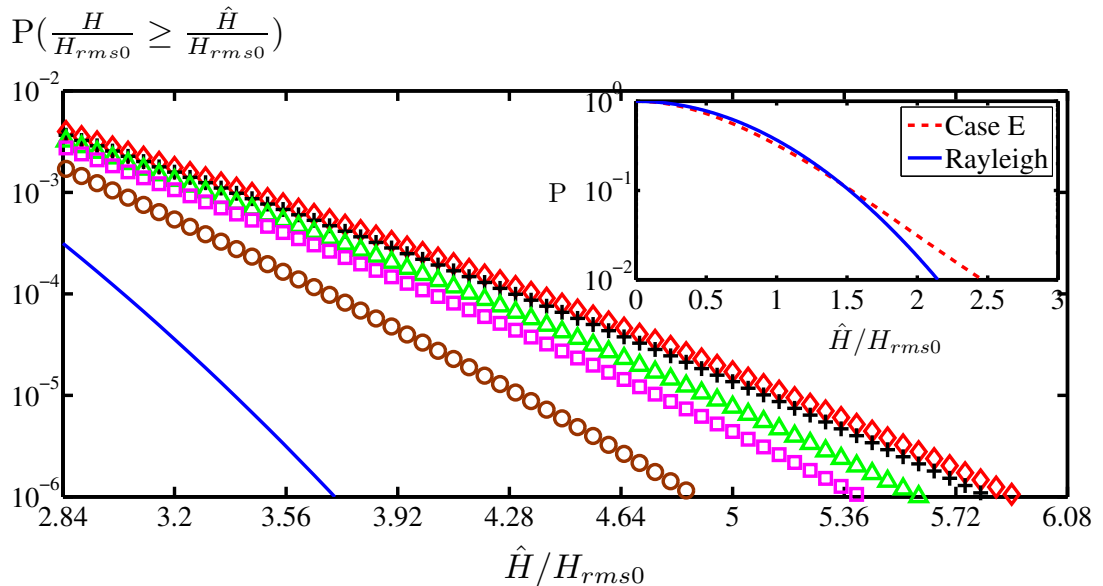


Figure 5.6: The probability of freak waves ($\hat{H}/H_{rms0} \geq 2.84; \hat{H} \geq 2H_s$) for the Rayleigh distribution, —, and the probability obtained from the Alber equation for unidirectional JONSWAP spectra with $\gamma = 20$: case A (\circ), case B (\square), case C (\triangle), case D ($+$) and case E (\diamond) (see Table 5.1). The inset shows probability function for the Rayleigh distribution (solid line) and case E (dashed line) starting from zero wave height.

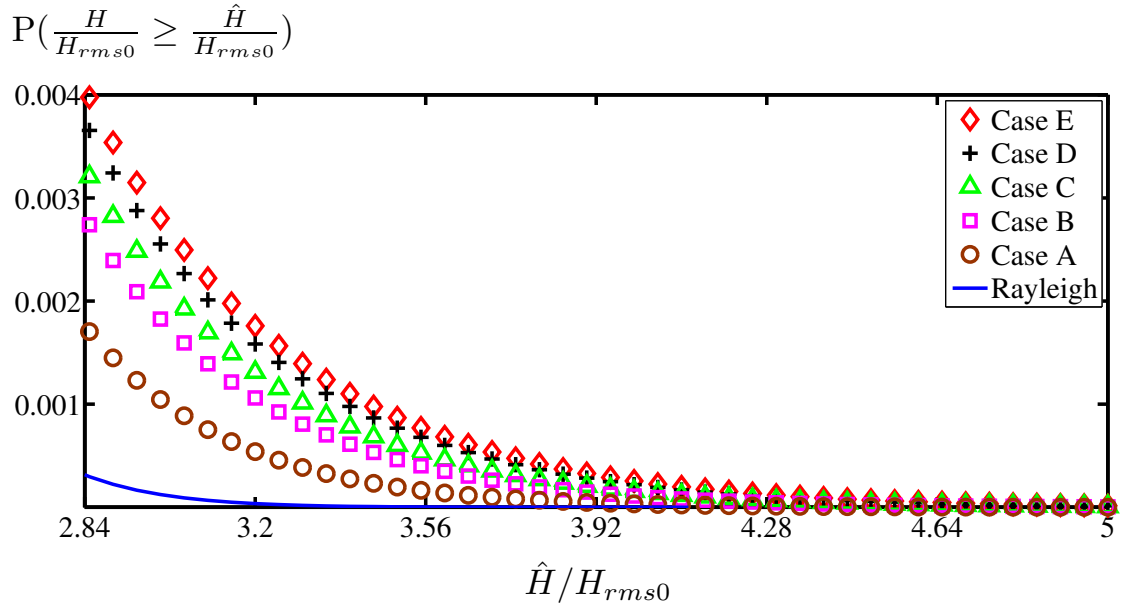


Figure 5.7: The probability of freak waves ($\hat{H}/H_{rms0} \geq 2.84; \hat{H} \geq 2H_s$) for the Rayleigh distribution and for unidirectional JONSWAP spectra with $\gamma=20$ as in Figure 5.6, linear scales.

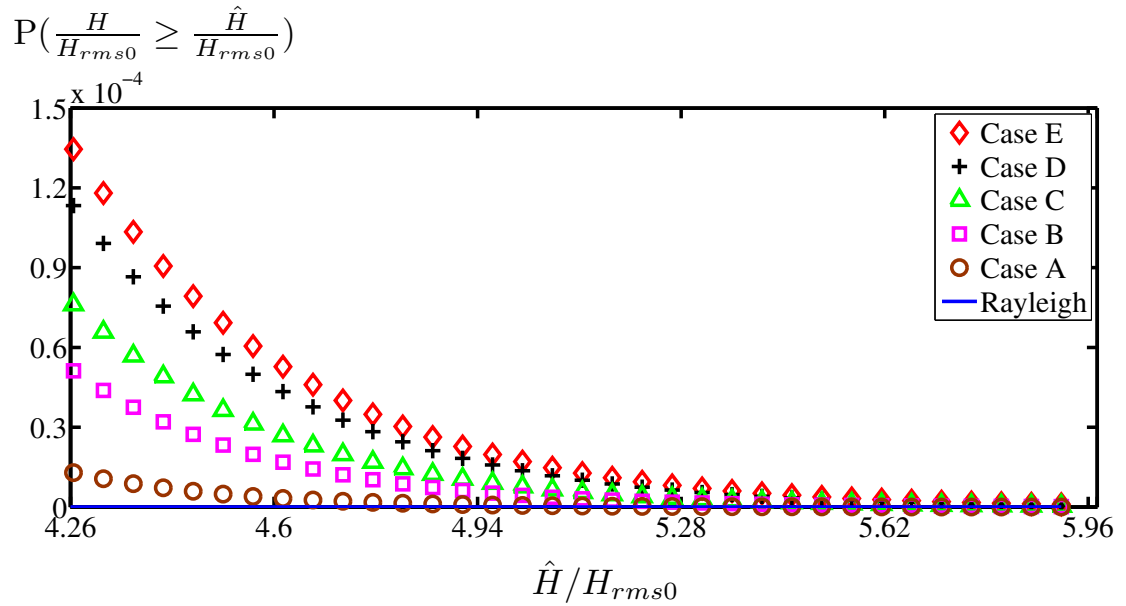


Figure 5.8: The probability of freak waves ($\hat{H}/H_{rms0} \geq 4.26; \hat{H} \geq 3H_s$) for the Rayleigh distribution and the probability obtained from the Alber equation for unidirectional JONSWAP spectra with $\gamma=20$ as in Figure 5.6, linear scales.

Figure 5.10 shows the probability of waves whose heights are higher than two times the significant wave height. As seen from the figure, the tails of the probability obtained from the Alber equation are higher compared to the classical value given by the Rayleigh distribution. Again, in order to show the exact values of the probability, it is

necessary to change the vertical axis scale from logarithmic scale to linear scale as shown in Figure 5.11.

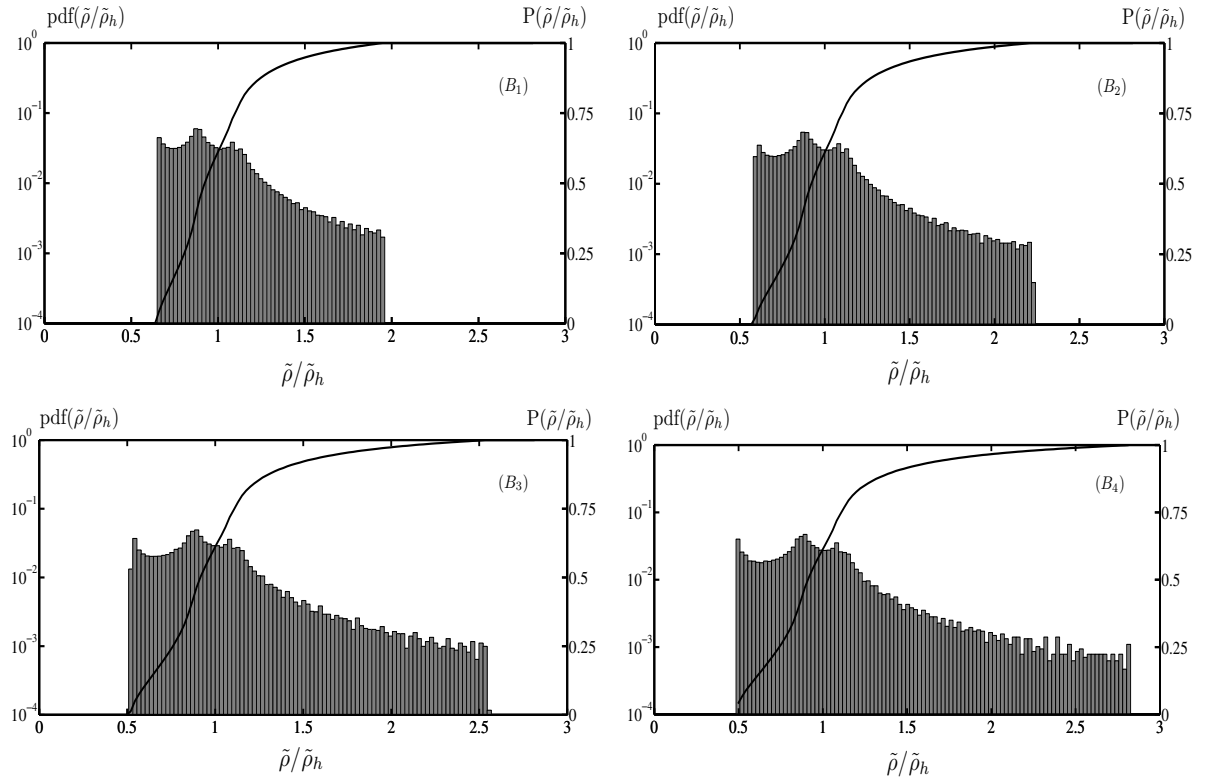


Figure 5.9: Probability density function $\text{pdf}(\tilde{\rho} / \tilde{\rho}_h)$ and probability function $P(\tilde{\rho} / \tilde{\rho}_h)$ (solid line) as functions of $\tilde{\rho} / \tilde{\rho}_h$ for unidirectional JONSWAP spectra with $\gamma=10$.

It is clearly seen from the figure that the case with the highest energy scale (the smallest value of the dimensionless “width parameter”, Π_1) gives the highest probability of waves whose heights are more than two times the significant wave height. In more details, case B_4 gives about 21 over 10^4 waves being higher than two times the significant wave height, as opposed the case B_1 where it is only about 10 over 10^4 . The latter case is closer to the Rayleigh distribution with 3 over 10^4 . The case B_2 and B_3 give about 12 and 17 over 10^4 waves whose heights are more than two times the significant wave height, respectively. In addition, the probability of waves whose heights are higher than three times the significant wave height as shown in Figure 5.12, increases from values of 10^{-8} for the Rayleigh distribution to 2×10^{-6} for case B_1 , 5×10^{-6} for case B_2 , 11×10^{-6} for case B_3 and 21×10^{-6} for case B_4 . Note that case B_1 is about 200 times higher probability compared to the Rayleigh distribution.

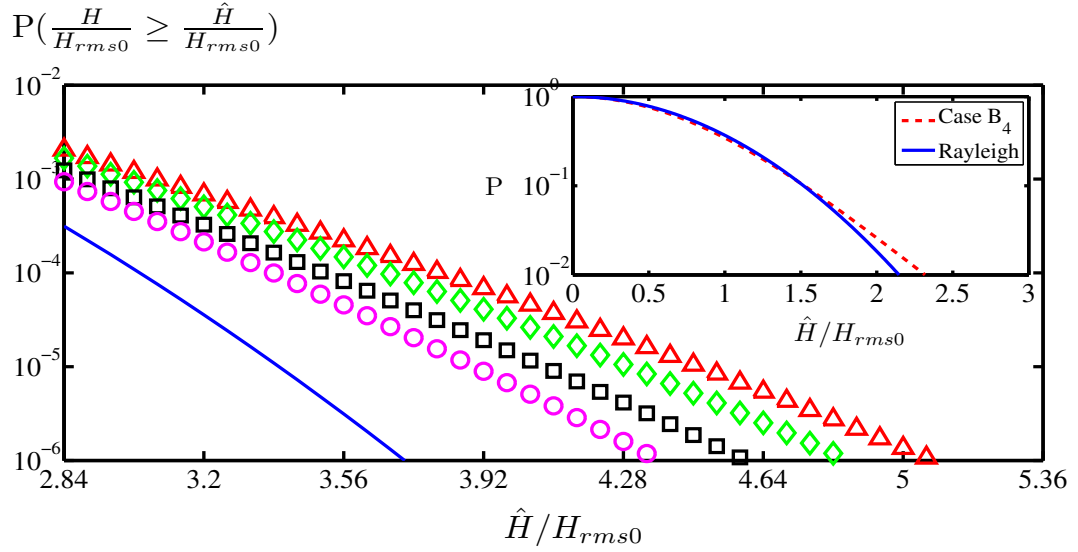


Figure 5.10: The probability of freak waves ($\hat{H}/H_{rms0} \geq 2.84; \hat{H} \geq 2H_s$) for the Rayleigh distribution, —, and the probability obtained from the Alber equation for unidirectional JONSWAP spectra with $\gamma=10$: case B_1 (\circ), case B_2 (\square), case B_3 (\diamond) and case B_4 (\triangle). The inset shows probability function for the Rayleigh distribution (solid line) and case B_4 (dashed line) starting from zero wave height.

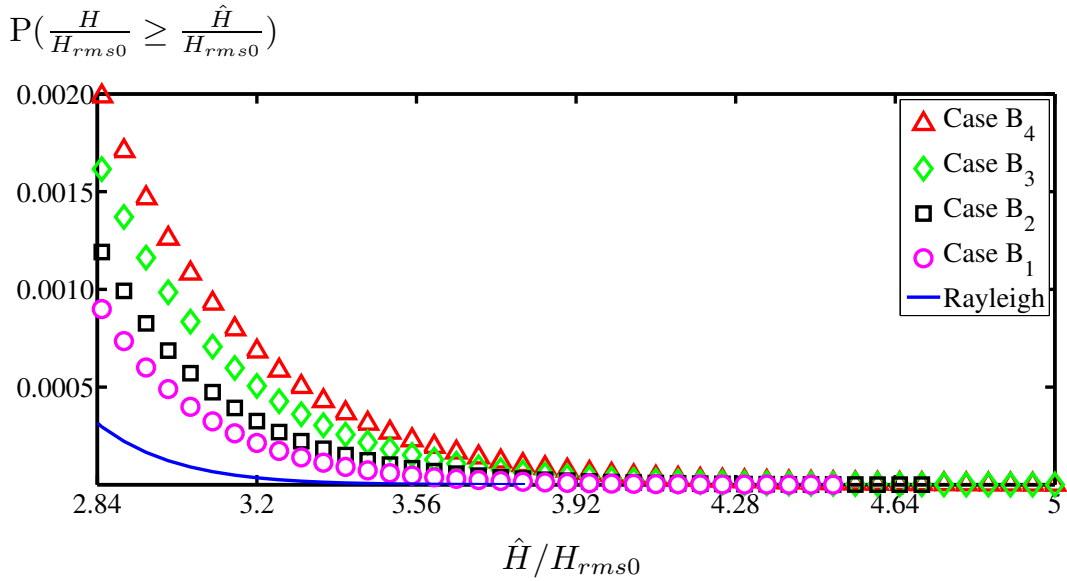


Figure 5.11: The probability of freak waves ($\hat{H}/H_{rms0} \geq 2.84; \hat{H} \geq 2H_s$) for the Rayleigh distribution and for unidirectional JONSWAP spectra with $\gamma=10$ as in Figure 5.10, linear scales.

In short, it can be noted that for the higher value of the peak enhancement while keeping the energy scale constant, the higher the probability of freak waves will be expected. For example, the probability of waves whose heights are higher than two times the significant wave height for the case $\gamma = 20$ and $\alpha = 0.03$ is higher than the probability

for the case $\gamma = 10$ with the same energy scale, i.e. $\alpha = 0.03$. In other words, the narrowness of spectrum affects the probability of freak waves.

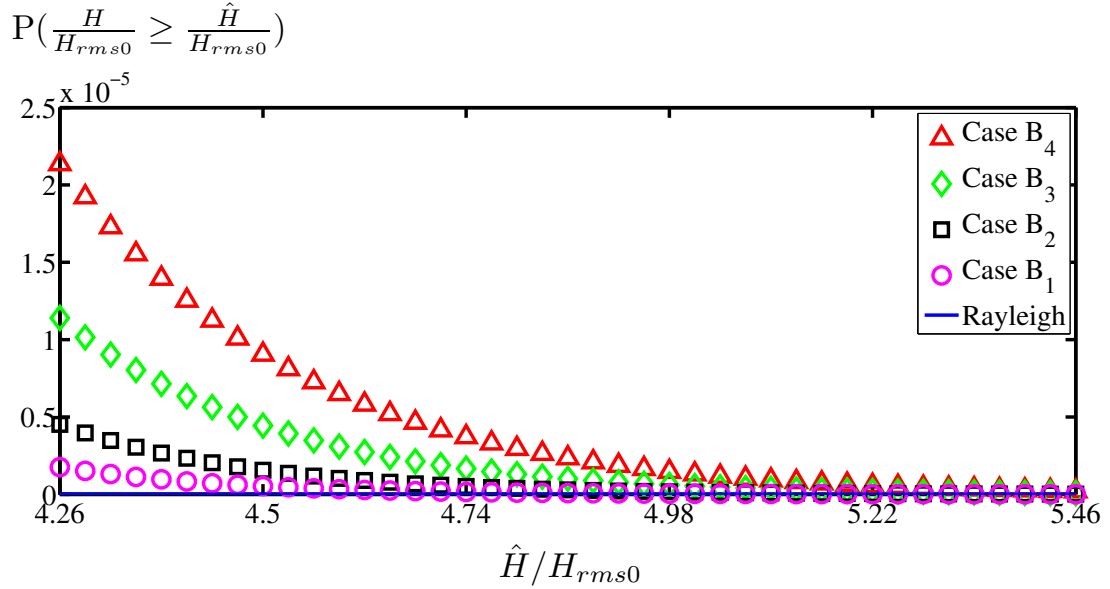


Figure 5.12: The probability of freak waves ($\hat{H}/H_{rms0} \geq 4.26; \hat{H} \geq 3H_s$) for the Rayleigh distribution and the probability obtained from the Alber equation for unidirectional JONSWAP spectra with $\gamma=10$ as in Figure 5.10, linear scales.

In particular, for the smaller value of the dimensionless “width parameter”, Π_1 , the value of the probability of freak waves will be higher. The results for unidirectional JONSWAP spectra are summarized in Table 5.1.

Table 5.1: The probability of wave height for unidirectional JONSWAP spectra where H_f stands for freak wave height and H_s is the significant wave height.

Case	α	γ	ε	Π_1	$\bar{P}_1^{(max)}$	$P(H_f \geq 2H_s)$ ($\times 10^{-4}$)	$P(H_f \geq 3H_s)$ ($\times 10^{-5}$)
A	0.01	20	0.13	0.65	1.68	17	1
B	0.016	20	0.16	0.50	1.83	27	5
C	0.02	20	0.18	0.45	1.87	32	7
D	0.025	20	0.20	0.40	1.92	37	11
E	0.03	20	0.22	0.37	1.95	40	13
B_1	0.016	10	0.13	0.81	1.52	10	0.2
B_2	0.02	10	0.14	0.70	1.63	12	0.5
B_3	0.025	10	0.16	0.64	1.69	17	1.1
B_4	0.03	10	0.18	0.60	1.73	21	2.1
Rayleigh distribution						3	0.001

5.4.2 Directional sea states

As aforementioned, the real sea states are not only limited to the unidirectional wave fields but also characterized by wave components propagation along different directions (directional wave fields). To this end, taking the peak enhancement factor of the unidirectional JONSWAP spectrum, $\gamma = 10$, and the energy scale, $\alpha = 0.016$, the probability of waves whose heights are more than two times and three times the significant wave height will be determined for two different degrees of the directional distributions which are $n = 10$ and $n = 50$ in the next subsection (see Table 5.2).

Following a similar procedure to that used to determine the probability density function, as for the unidirectional case, the probability density functions for the JONSWAP spectrum with directional distributions are shown in Figure 5.13. Note that one cycle of the long-time recurring evolution as shown in Figure 5.4 has also been used. As can be seen from Figure 5.13, the decrease in the value of the degree of the directional spreading is accompanied by the decrease in the number of active bins. Note that spaced increments in $\tilde{\rho} / \tilde{\rho}_h$ is from 0.65 to 1.95. In particular, the number of active bins reduces when the “width-parameter” Π_2 increases. This trend is very consistent with the unidirectional case.

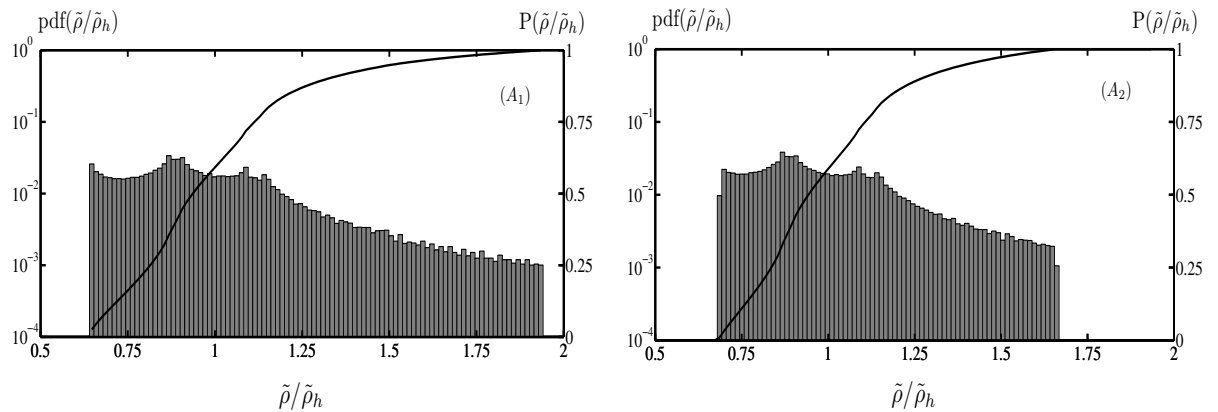


Figure 5.13: Probability density function $\text{pdf}(\tilde{\rho} / \tilde{\rho}_h)$ and probability function $P(\tilde{\rho} / \tilde{\rho}_h)$ (solid line) as functions of $\tilde{\rho} / \tilde{\rho}_h$ cases A_1 (left) and A_2 (right) of Table 5.2.

Figure 5.14 shows the wave-height probability for an inhomogeneous ocean obtained from the Alber equation and for homogeneous sea given by the Rayleigh distribution. These results are for the JONSWAP spectra with the degrees of the directional distribution set at $n = 10$ (case A_2) and $n = 50$ (case A_1) and parameters $\gamma = 10$ and

$\alpha = 0.016$. The steepness of this case were calculated by using the formula in Chapter 3, i.e. $\varepsilon = k_0 \sqrt{2 \int s(k) dk}$ where $s(k)$ is the wavenumber spectrum and yielded $\varepsilon = 0.126$. Similar to the unidirectional case, it can be seen from the inset of Figure 5.14 that the probability up to $\hat{H} \geq 1.49 H_{rms0}$ is greater for the Rayleigh distribution. After the intersection point, however, the probability is greater for the results obtained from the Alber equation (note that our H_{rms0} and significant wave height H_s are connected as $H_s = \sqrt{2} H_{rms0}$ (see Subsection 5.2.1)). Moreover, the probability of waves with wave height larger than two times the significant wave height is 9×10^{-4} when the degree of the directional distribution is 50 and decreases down to 7×10^{-4} when the degree of the directional distribution decreases to 10 while for homogenous seas according to the Rayleigh distribution is 3×10^{-4} .

The reduction is even more significant for the probability of exceptionally high waves, with wave heights are higher than three times the significant wave height as shown in Figure 5.16. It is of the order of 10^{-8} for the Rayleigh distribution, 16×10^{-7} for case A_1 and 5×10^{-7} for case A_2 . Now, it is only about 160 times higher than given by the Rayleigh distribution (was 200 times for unidirectional seas).

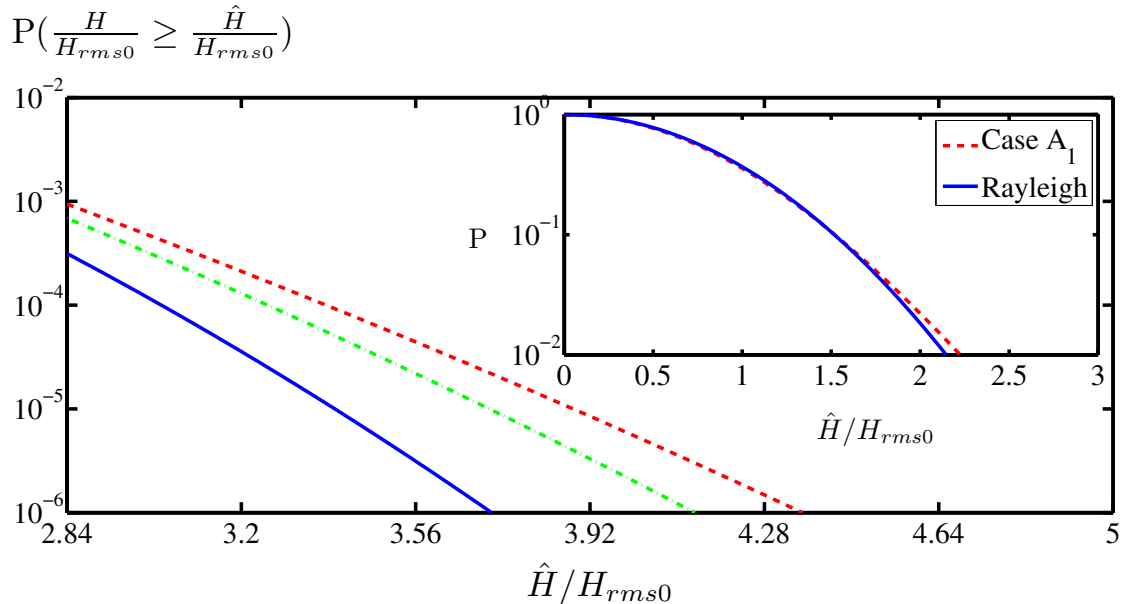


Figure 5.14: The probability of freak waves ($\hat{H}/H_{rms0} \geq 2.84; \hat{H} \geq 2H_s$) for the Rayleigh distribution, —, and the probability obtained from the Alber equation for JONSWAP spectra with different degrees of the directional distributions: case A_1 (- - -) and case A_2 (- - -), (see Table 5.2). The inset shows probability function for the Rayleigh distribution (solid line) and case A_1 (dashed line) starting from zero wave height.

This result is very consistent with the results obtained by Onorato et al. (2002) who integrate a modified nonlinear Schrödinger equation numerically. They found that broadening the directional spread by decreasing the power of the directional spectrum of the initial spectrum would reduce the probability of freak waves. It should be noted that the maximum wave height limited by wave breaking changes for three-dimensional waves if compared with two-dimensional (increases), because both limiting steepness and limiting skewness of waves are different in three dimensions but the increase is not large (<10%) (Toffoli et al., 2010a, Babanin et al., 2011b).

Comparing the probability of freak waves, whose wave height is larger than two times the significant wave height for unidirectional JONSWAP spectrum with $\gamma = 10$ and $\alpha = 0.016$ as shown in Figure 5.10 or Figure 5.11, and for the JONSWAP spectrum with the degree of the directional distribution set at $n = 50$ with the other parameters being the same. One can see that the probability for the unidirectional JONSWAP spectrum is slightly higher than the probability for JONSWAP spectrum with directional distribution, as expected. This is because as shown in Figure 4.18 of Chapter 4, a unidirectional JONSWAP spectrum is almost identical to the JONSWAP spectrum with directional spreading when the degree of the directional distribution $n = 90$.

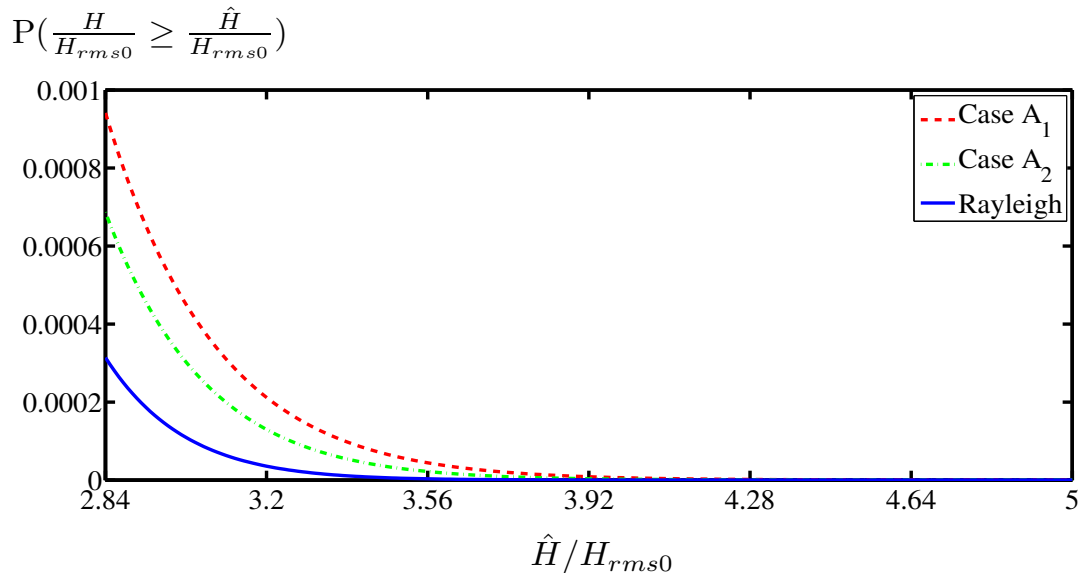


Figure 5.15: The probability of freak waves ($\hat{H}/H_{rms0} \geq 2.84; \hat{H} \geq 2H_s$) for the Rayleigh distribution and for JONSWAP spectra with different directional distributions with value of parameters $\gamma = 10$, $\alpha = 0.016$ and the linear vertical axis (see Table 5.2).

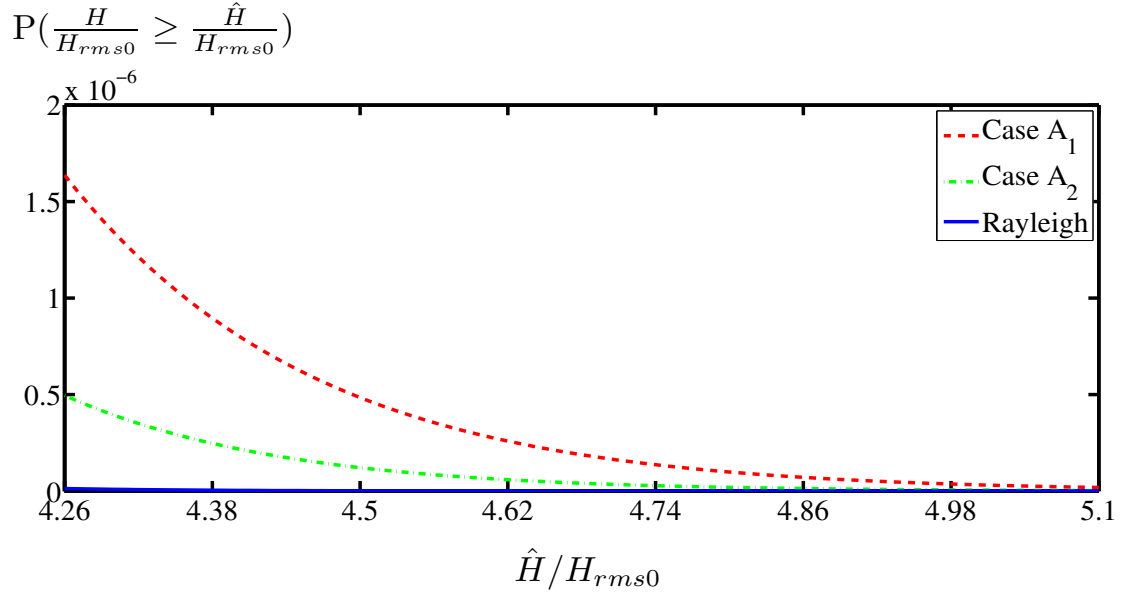


Figure 5.16: The probability of freak waves ($\hat{H}/H_{rms0} \geq 4.26; \hat{H} \geq 3H_s$) for the Rayleigh distribution and for JONSWAP spectra with different directional distributions and value parameters $\gamma=10$, $\alpha=0.016$ and the linear vertical axis (see Table 5.2).

In more details, as seen from Table 5.1, there are about 10 over 10000 waves whose height are more than two times the significant wave height for the unidirectional JONSWAP spectra with $\gamma = 10$ and $\alpha = 0.016$. On the other hand, there are 9 over 10000 waves whose heights are more than two times the significant wave height for JONSWAP spectra with the degree of the directional spreading 50 of other parameters are the same. Further results for JONSWAP spectra with different degrees of the directional spreading are summarized in Table 5.2.

Table 5.2: The probability of wave height for JONSWAP spectra with different degrees of the directional distributions where H_f stands for freak wave height and H_s is the significant wave height.

Case	n	A_d	Π_2	$\tilde{P}_2^{(max)}$	$P(H_f \geq 2H_s)$ ($\times 10^{-4}$)	$P(H_f \geq 3H_s)$ ($\times 10^{-7}$)
A_1	50	2.84	0.86	1.53	9	16
A_2	10	1.29	0.95	1.43	7	5
A_3	2	0.64	1.11	1.28*	--	--
Rayleigh distribution					3	0.1

Note: * indicates the stable condition.

Using all our results from Table 5.1, Table 5.2 and some other cases which are not shown here, the occurrence probability of freak waves can be estimated by simple relations using the best fit in Matlab:

$$P(H_f > 2H_s) = 10^{-(1.80+1.50\Pi)} \quad (5.25)$$

$$P(H_f > 3H_s) = 10^{-(2.00+4.65\Pi)} \quad (5.26)$$

where H_f is the freak wave height and H_s is the significant wave height. Moreover, $\Pi = \Pi_1 < 1$ and $\Pi = \Pi_2 < 1.1$ are used for unidirectional JONSWAP spectrum and JONSWAP spectrum with directional distribution, respectively. The plots of the equations (5.25) and (5.26) are shown in Figure 5.17.

The fact that almost any wave field, with a single peak frequency, can be approximated by a JONSWAP spectrum, adds to the applicability of the above-mentioned results. Finally, it has to be emphasized that the results for the probability of freak waves are in qualitative agreement with the results from both the laboratory experiments in the wave flumes such as Waseda et al. (2009), Onorato et al. (2009a) and Babanin et al. (2011b) and numerical simulations such as Eliasson and Shukla (2010) and Toffoli et al. (2010b).

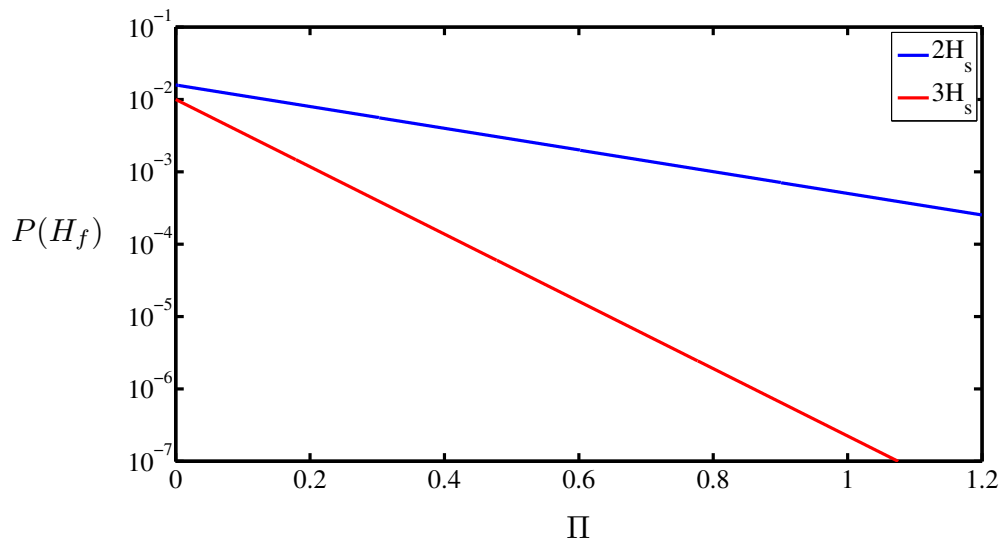


Figure 5.17: Simple relations between the probability of freak waves and the dimensionless “width parameter”, Π .

5.4.3 Comparison to the Forristall distribution

In the previous subsections, the probability of wave height obtained from the Alber equation was compared to the classical value given by the Rayleigh distribution established for linear waves. In this section, a comparison to the Forristall distribution is shown, which is based on the second order theory. Forristall distribution (Forristall, 2000) is actually the parameterization of the Weibull distribution which is a general form of the Rayleigh distribution.

The comparison is performed as follows: firstly, for unidirectional wave fields, the results for case B_1 (see: Table 5.1) will be compared to the Forristall distribution. Then, we change the shape of the spectrum while keeping the same steepness as per case A (see: Table 5.1). Finally, the influence of spectral shape will be discussed. Figure 5.18 shows the comparison between the probability of wave height obtained from the Forristall distribution and the probability obtained from the Alber equation for case B_1 .

As seen from Figure 5.18, the probability from the Forristall distribution is similar to the results from the homogeneous seas (i.e. the Rayleigh distribution). Both of them were higher than the probability obtained from the Alber equation until a certain point was reached. The probability for the Forristall distribution is greater for up to $\hat{H} \geq 3.7 H_{rms0}$. After the intersection point the probability is greater for the results obtained from the Alber equation. This indicates that the second order theory could not capture the extreme events as shown at the tail of the probability. In addition, it slightly improves the probability obtained from the Rayleigh distribution.

Changing the shape of the spectrum while keeping constant steepness gives a much clear comparison (see Figure 5.19). Note that case B_1 and case A have the same steepness, i.e. $\varepsilon \approx 0.13$ as given in Table 5.1. It is seen from Figure 5.19 that the intersection point between the probability obtained from the Forristall distribution and the probability obtained from the Alber equation is at about 2.75. This indicates that the spectral shapes do influence the probability of wave height particularly for the extreme events. This was also pointed out by Bitner-Gregersen and Magnusson (2004). However, these parameters cannot be captured by the second order theory such as the Forristall distribution.

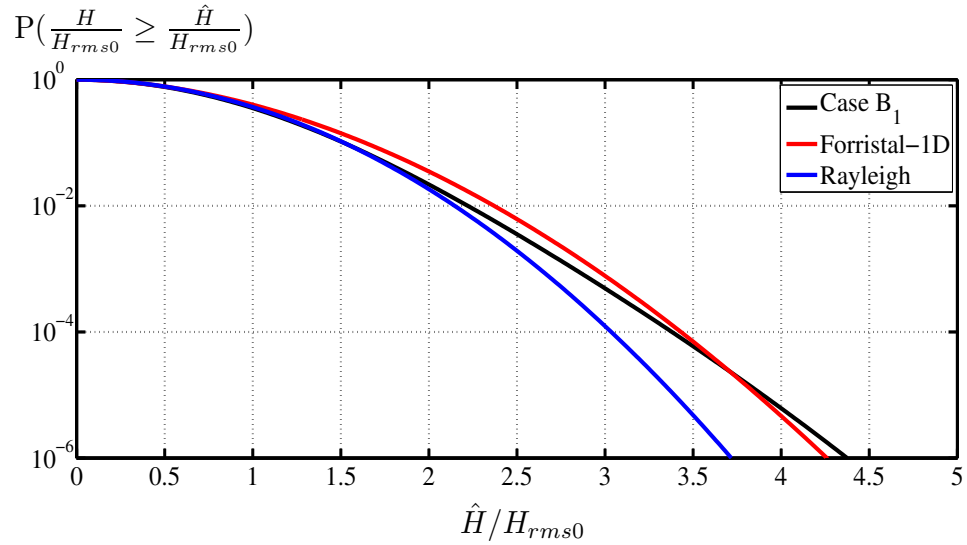


Figure 5.18: The comparison between the probability of wave height obtained from the Forristall distribution for the unidirectional sea states and the probability obtained from the Alber equation, i.e. case B_1 .

Further details of these comparisons are presented in Figure 5.20. While the results obtained from the Forristall distribution are the same for the two cases (A and B_1), the Alber equation gives an entirely different result. Still from Figure 5.20, the intersection point moves from about 3.7 for case B_1 to about 2.75 for case A .

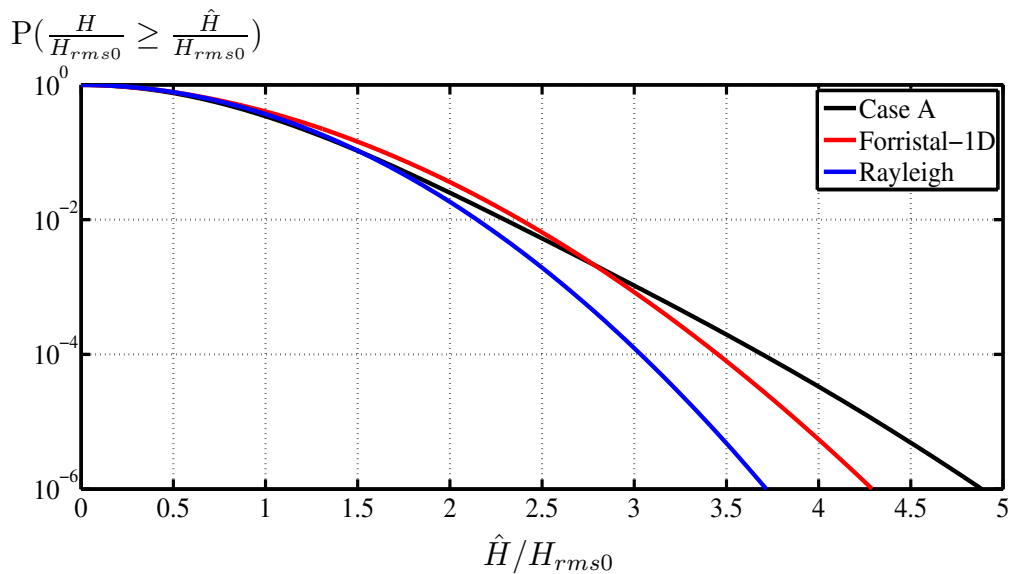


Figure 5.19: The comparison between the probability of wave height obtained from the Forristall distribution for the unidirectional sea states and the probability obtained from the Alber equation, i.e. case A .

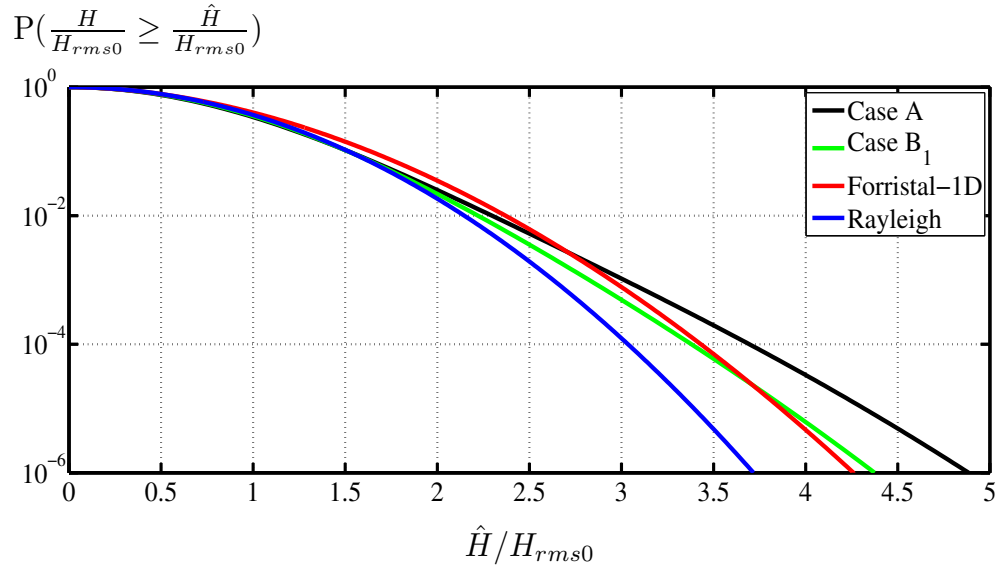


Figure 5.20: The comparison between the probability of wave height obtained from the Forristall distribution for the unidirectional sea states and the probability obtained from the Alber equation, i.e. cases A and B_1 .

For directional wave fields, firstly, the comparison between the results for unidirectional sea states based on the Alber equation (case B_1) and the results obtained from the Forristall distribution for directional sea states will be shown. Intuitively, it is expected that the probability obtained from the Alber equation is greater than the probability obtained from the Forristall distribution. This is clearly seen from Figure 5.21. The probability up to $\hat{H} \geq 3.3 H_{rms0}$ is greater for the Forristall distribution and greater for the Alber equation afterwards.

Furthermore, since Forristall distribution cannot be used to study the probability of wave height with variation of the directional distributions, in order to perform a comparison with the Forristall distribution, the results from the fairly narrow directional spreading obtained from the Alber equation will be used in this study. As can be seen from Figure 5.21 and Figure 5.22, the comparison between case B_1 and the Forristall distribution for directional sea states is similar to the comparison between case A_1 and the Forristall distribution for directional wave fields. However, the intersection point between case B_1 and the Forristall distribution for directional sea states is at about 3.35 (see Figure 5.22) which is slightly higher than the intersection point in Figure 5.21. This is actually to be expected as case B_1 is the unidirectional JONSWAP spectrum while case A_1 is the JONSWAP spectrum with fairly narrow directional spreading (see Table 5.2).

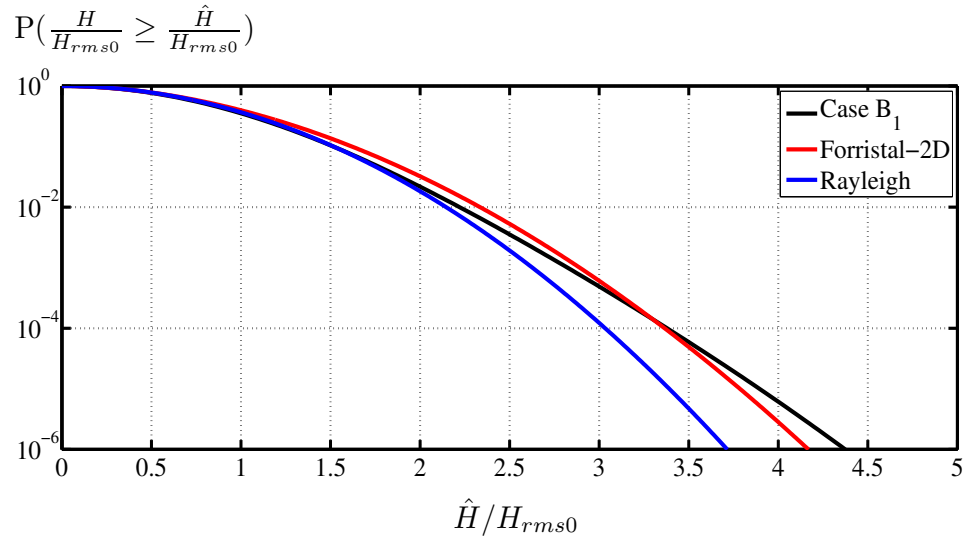


Figure 5.21: The comparison between the probability of wave height obtained from the Forristal distribution for directional sea states and the probability obtained from the Alber equation, i.e. case B_1 .

To summarize these comparisons, although Forristall distribution is simple and agree well with the observations, it is clearly shown, based on the Alber equation, that it does not capture the extreme events. This is seen in the tail of the distribution. Moreover, since Forristall distribution depends only on the wave steepness on infinitely deep water, it does not consider the spectral shape. It is argued in this research that the spectral shapes do play an important role in the probability of wave height particularly for the extreme events as Bitner-Gregersen and Magnusson (2004) also pointed out.

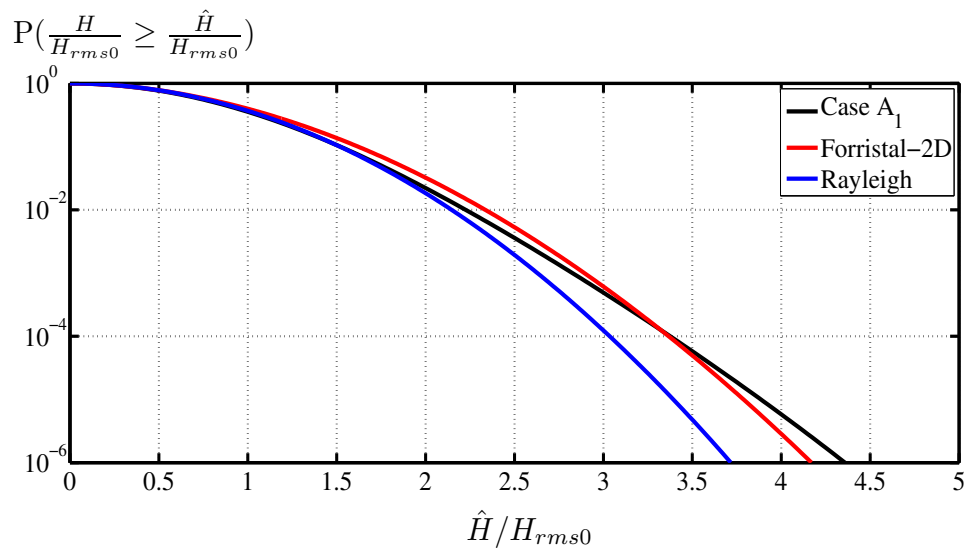


Figure 5.22: The comparison between the probability of wave height obtained from the Forristal distribution for directional sea states and the probability obtained from the Alber equation, i.e. case A_1 .

5.5 Concluding remarks

The Alber equation, which is an appropriate equation to study the random inhomogeneous wave fields with narrow spectra, was used to study the statistic of freak waves within wave fields defined by realistic ocean JONSWAP spectrum, with and without directional distributions. We start from defining the probability of wave height based on the homogeneous seas according to the Rayleigh distribution. After that, the advantage of the consequent recurrent evolution was taken to establish the probability density function and then to determine the probability of freak waves, which defined as the waves whose heights exceed two times the significant wave height in a straightforward fashion. The probability of wave height obtained from the Alber equation was compared to the probability obtained from the Rayleigh distribution which is based on the linear waves theory and the probability obtained from the Forristall distribution that was derived from the second order theory.

For unidirectional wave fields, it is found that the probability of freak waves obtained from the Alber equation is greater than the probability obtained from the Rayleigh distribution. For the peak enhancement factor of a JONSWAP spectrum that is 20 and the Phillips parameter that is 0.03, the probability of waves whose heights are more than two times the significant wave height increased up to about 13 times compared to the classical values given by the Rayleigh distribution. Similarly, for the peak enhancement factor of a JONSWAP spectrum that is 10 and a constant value of Phillips parameter, the probability of waves whose heights are more than two times the significant wave height increased up to about 7 times. This reveals that the narrower the spectrum, the higher the probability of freak waves. The increase is much more significant for the probability of wave whose heights are more than three times the significant wave height. For $\gamma = 20$ and $\alpha = 0.03$, the probability increased up to about 10000 compared to the Rayleigh distribution. The main parameters that play an important role in the JONSWAP spectrum in relation to the probability of freak waves are the energy scale and the peak enhancement factor. These two parameters are related through the dimensionless “width parameter”, Π_1 which is defined as $\Pi_1 = \varepsilon/(\alpha\gamma)$.

For directional sea states, the probability of freak waves depends on three parameters, namely the energy scale, α , the peak enhancement factor, γ , and the degree of the directional distribution, n . These three parameters are related through the dimensionless

“width parameter”, Π_2 , which is defined as $\Pi_2 = \varepsilon/(\alpha\gamma) + 0.0256/\varepsilon A_d$, where ε is the wave steepness and A_d is the normalization factor of the directional distribution.

The probability of wave heights obtained from the Alber equation was also compared with the Forristall distribution that was derived from the second order theory. It is clearly shown the difference between the probability obtained from the linear wave theory, the second order theory and the Alber equation. The latter is the stochastic version of the cubic Schrödinger equation at the tails of the probability. In addition, based on our simulation, it was confirmed that at least three features that cannot be captured by the Forristall distribution could be observed from the Alber equation. It seems that Forristall distribution cannot capture the extreme events such as the freak waves. Moreover, the influence of the spectral shapes that can be observed in the Alber equation cannot be observed for the Forristall distribution as it only depends on the wave steepness for the deep water that is considered in this research. Besides that, Forristal distribution cannot be used to study the effect of the variation of the directional spreading.

In short, it is found in this research that the probability of occurrence of the freak waves solely depends on the dimensionless “width parameter” Π , where $\Pi = \Pi_1 < 1$ is used for the unidirectional JONSWAP spectra and $\Pi = \Pi_2 < 1.1$ is used for JONSWAP spectra with directional distributions. Therefore, one could not expect any freak waves for $\Pi_1 \geq 1$ for unidirectional sea states and for $\Pi_2 \geq 1.1$ for directional sea states.

In addition, it should be mentioned that equations dealing with nonlinear evolution of water waves (i.e., the Alber equation, kinetic equation, Zakharov equation, etc.) do not have dissipation mechanisms and energy-input mechanisms. For example, the kinetic equation is most broadly employed by wave forecast models always combined with terms which represent wind energy input, wave-breaking dissipation, among others. Therefore, applying the outcomes of the Alber equation to the real waves in the ocean should be done with caution. Moreover, in theory the Alber equation and other equations based on higher-order terms in deep water allow for infinite wave heights to occur. In reality, there is a limit of wave steepness beyond which the waves will break.

Chapter 6

Summary and Conclusions

6.1 Summary

The cubic Schrödinger equation (see Zakharov, 1968) is a frequently used deterministic equation for describing nonlinear evolution in time and space of an ocean wave field with a narrow spectral band. This equation was used by Longuet-Higgins (1976) and Alber (1978) as their starting point to formulate two rather different stochastic evolution equations. Whereas Longuet-Higgins assumed that the wave field is a homogeneous and nearly Gaussian random process, Alber enabled the random process to be inhomogeneous, but requires Gaussianity. Although Crawford et al. (1980) provided a more general case where the phenomenon is considered an inhomogeneous and nearly Gaussian random process, their result is so cumbersome that it has never been used so far.

Longuet-Higgins (1976) result is actually the narrow-band limit of the Hasselmann (1962) kinetic equation. So far, the kinetic equation has been the most frequently used equation in stochastic models. However, the time scale is proportional to ε^{-4} , where ε is a typical small wave steepness (see also Janssen (2003) the non-resonant kinetic equation and Annenkov & Shrira (2006) for the extended kinetic equation). These equations were derived for homogeneous wave fields where the key step in the derivation is the assumption that the phases of the components are close to each other in wavenumber space and remain uncorrelated to the lowest order (Stiassnie et al. 2008).

Alber (1978) used his equation to study the instability of a homogeneous wave-field to inhomogeneous disturbances. Alber's findings are actually the stochastic counterpart of the well-known deterministic Benjamin–Feir instability, which can be described with the cubic Schrödinger equation. The growth rates of the inhomogeneous instabilities are proportional to ε^2 , reflecting the fact that the time scale of the Alber equation is

proportional to ε^{-2} . Although Alber does not state it explicitly, the choice of his initial small inhomogeneous disturbances discloses a certain correlation between their phases and those of the homogeneous base state.

Recently, Zuevsky (2008) and Stiassnie et al. (2008) used one spatial dimension of the Alber equation to study linear stability analysis for unidirectional wave fields. They determined the exact conditions of instability. One should note that the main difference between the work of Stiassnie et al. (2008) and the original work of Alber (1978) is the initial disturbance spectra, which are principally inhomogeneous through their phase relation to the homogenous spectrum in the Stiassnie et al. (2008) study. This is in contrast to the original work of Alber (1978) for which all initial phases were independent and randomly chosen.

From the cubic Schrödinger equation, it is known that the Benjamin–Feir instability does not lead to a permanent end state, but to an unsteady series of modulation and demodulation cycles, called the Fermi–Pasta–Ulam recurrence phenomenon (see Yuen & Ferguson Jr 1978a,b, Janssen 1981, Stiassnie & Kroszynski 1982). Janssen (1983) used an asymptotic method to obtain subsequent evolution for the solution of the Alber equation near the threshold of instability and obtained a solution which is characterized by an initial small overshoot followed by an oscillation around its time asymptotic value. Recently, Stiassnie et al. (2008) integrated one spatial dimension of the Alber equation and found that in the area of instability, recurrent evolution, which is the stochastic counterpart of the Fermi–Pasta–Ulam recurrence obtained for the cubic Schrödinger equation, is obtained. Furthermore, Regev et al. (2008) used the results of Stiassnie et al. (2008), which is the recurrent evolution of the Alber equation, to study the probability of freak waves occurrence.

Here we show an extension of the work of Stiassnie et al. (2008) and Regev et al. (2008) from one spatial dimension to two spatial dimensions. Essentially this thesis consists of three main parts. First, we performed the linear stability analysis of the two-dimensional symmetric spectra, namely, the square spectra, the rectangular spectra, the Lorentz spectra and both the one- and the two-dimensional asymmetric ocean wave JONSWAP spectra subject to two-dimensional inhomogeneous disturbances. We then determined the most unstable modes and their growth rates for all cases. However, since the dispersion relation for the disturbance (see equation 3.17) cannot be solved

analytically for the JONSWAP spectrum, it is necessary to seek an approximate solution. To this end, we replaced the original spectrum by a sum of weighted Dirac-functions and replaced the dispersion relation for the disturbance by a high order (up to 70) algebraic equation, seeking the root with the largest imaginary contribution. A Lorentz spectrum has been used to validate this rather “general method”.

Furthermore, we determined the marginal instability conditions for the disturbance and found that square spectra and rectangular spectra become stable to small inhomogeneous disturbance when the dimensionless spectral width, \tilde{W}_1 , in the direction parallel to the carrier wave is greater than 2.75. Similarly, we found that the Lorentz spectra become stable to inhomogeneous disturbance when the dimensionless spectral width, \tilde{W}_1 , is greater than $\sqrt{2}$.

For more realistic sea states represented by JONSWAP spectra, we defined a new parameter for the unstable conditions which is called a dimensionless “width parameter”. It is found that the unidirectional JONSWAP spectra become unstable to small inhomogeneous disturbances when the dimensionless “width parameter” is

$$\Pi_1 = \frac{\varepsilon}{\alpha\gamma} < 1,$$

where ε is the wave steepness and α and γ are the Phillips parameter and the peak enhancement factor of JONSWAP spectra, respectively. Similarly, the JONSWAP spectra with directional distribution become unstable to inhomogeneous disturbances when the slightly corrected dimensionless “width parameter” satisfies the condition of

$$\Pi_2 = \frac{\varepsilon}{\alpha\gamma} + \frac{0.0256}{\varepsilon A_d} < 1.1,$$

where A_d is the normalization factor of the directional spreading (see Chapter 3 for more details). Note that the defined dimensionless “width parameter” in this work was a further development of the unstable transition properties available in the literature.

In addition, we study the dependence of the most unstable mode wavenumbers and growth rates on the parameters of spectral width. We have shown, using the square spectra and the rectangular spectra numerically and using the Lorentz spectra analytically, that the maximum growth rate is independent of the spectral width in direction perpendicular to the carrier wave. On the other hand, using more realistic

ocean wave JONSWAP spectra with directional distributions, we found that the degree of the directional spreading influences the maximum growth rate of the disturbance. This is due to conservation of the total energy when using the JONSWAP parameterization of real spectra. We have shown that when the degree of the directional distribution is increased, then the maximum growth rates will also increase.

It appears that the conclusion from the two-dimensional symmetric spectra such as the square spectra, the rectangular spectra and the Lorentz spectra is different from the conclusion obtained based on the JONSWAP spectra with directional distributions in terms of dependency on the transverse width of the spectrum. However, one can easily compare these spectra, namely the Lorentz spectra and the JONSWAP spectra by maintaining that both spectra have the same total energy and momentum, and will find that changing the power of the directional distribution of the JONSWAP spectra will not only change the spectral width, which is perpendicular to the carrier-wave of the Lorentz spectra, but also the spectral width, which is parallel to the carrier wave.

In the second part of this thesis, we study the stochastic counterpart of the Fermi-Pasta-Ulam recurrence by integrating the Alber equation numerically. A finite difference method was used to integrate the Alber equation by prescribing initial conditions and boundary conditions. Moreover, we chose the most unstable modes obtained in the first part of this thesis for our simulation (see Chapter 3 for more details). These simulations are limited to the JONSWAP spectra with and without directional distributions. It is found that for unidirectional JONSWAP spectra, whenever the dimensionless “width parameter”, $\Pi_1 < 1$, the Alber equation yields recurring solutions. Specifically, the decrease in the “width parameter”, Π_1 , is accompanied by an increase in the peak enhancement of the recurrence and a decrease in the numerical duration. Similarly, for the JONSWAP spectra with directional spreading, the Alber equation yields recurrent solutions whenever the dimensionless “width parameter”, $\Pi_2 < 1.1$. Specifically, we study the influence of the directional spreading on the long-time evolution.

It was shown that for JONSWAP spectra with the degree of the directional distributions $n = 10$ and $n = 50$, which is from fairly broad directional spread to fairly narrow directional spread, the recurrence nature of the solutions is clearly manifested. These behaviours were in contrast to the solution for $n = 2$ which describes a very broad directional spread where there is no recurrence. Moreover, the derivation of the

invariants of motion, which are the quality control of the numerical solutions, for two-dimensional Alber equation was an additional development of this work (see Chapter 4 and Appendix A for more details).

Possible manifestations of such inhomogeneous disturbances in nature, which can be used to study the development of freak waves, are the third part of this thesis. Specifically, we took advantage of the periodicity imposed by the initial disturbance and the consequent recurrent evolution of unstable spectra to calculate the probability of freak waves. Firstly, we derived an equation for the wave height probability based on the Rayleigh distribution. However, in order to implement the equation, one needs a probability density function. To this end, we took one cycle of the recurrent solution to establish the probability density function. The probability of wave heights can be determined in the straightforward fashion. Note that a wave whose height exceeds two times the significant wave height is categorized as a freak wave and a wave whose height is more than three times the significant wave height is called an exceptionally freak wave.

For unidirectional JONSWAP spectra, we simulated nine cases which are for $\gamma = 20$ with $\alpha = 0.01, 0.016, 0.02, 0.025, 0.03$ and for $\gamma = 10$ with $\alpha = 0.016, 0.02, 0.025$ and 0.03 . In general, probability of freak waves obtained from the Alber equation is higher than the probability of freak waves given by the classical value of the Rayleigh distribution obtained for homogeneous seas. Specifically, the higher value of peak enhancement factor of JONSWAP spectrum will give a higher value of probability of occurrence of freak waves, while keeping the same energy scale α . Similarly, an increased value of the energy scale will give an increased value of probability of freak waves while keeping the same peak enhancement factor of JONSWAP spectrum. In this case, the main parameters are the energy scale and the peak enhancement factor. These two parameters are related through the dimensionless “width parameter” Π_1 . It is found that an increase in the value of Π_1 is accompanied by a decrease in the value of the probability of occurrence of freak waves.

For JONSWAP spectra with directional distributions, we chose the value of parameters $\alpha = 0.016$ and $\gamma = 10$ with two different values of the degree of the directional distributions, $n = 10$ and $n = 50$. It is found that the probability of waves whose heights are larger than two times the significant wave height is 9×10^{-4} when the degree

of the directional distribution is 50 and decreases down to 7×10^{-4} when the degree of the directional distribution decreases to 10. Overall, this probability is significantly lower than in the unidirectional case with the same value of parameters α and γ .

The reduction is even more significant for the probability of exceptionally high freak waves. It is of the order of 10^{-8} for the Rayleigh distribution, 16×10^{-7} for case $n = 50$ and 5×10^{-7} for case $n = 10$. Moreover, similar to the unidirectional case, it is found that an increased value of Π_2 is accompanied by a decreased value of the probability of occurrence of freak waves.

Finally, using all our results from the probability of occurrence of freak waves, the occurrence probability of freak waves can be estimated by simple relations using the best fit:

$$P(H_f > 2H_s) = 10^{-(1.80+1.50\Pi)}$$

$$P(H_f > 3H_s) = 10^{-(2.00+4.65\Pi)}$$

where H_f and H_s are the freak wave height and the significant wave height, respectively. In addition, $\Pi = \Pi_1 < 1$ and $\Pi = \Pi_2 < 1.1$ are used for the unidirectional JONSWAP spectrum and JONSWAP spectrum with the directional distribution, respectively as the indicators for the unstable conditions. The fact that almost any wave field, with a single peak frequency, can be approximated by a JONSWAP spectrum, adds to the applicability of the aforementioned result. Finally, we have to emphasize that our results for the probability of freak waves are in qualitative agreement with the results from both the laboratory experiments such as Waseda et al. (2009), Onorato et al. (2009a) and Babanin et al. (2011b) and numerical simulations (e.g. Eliasson and Shukla (2010), Toffoli et al. (2010b)). In particular, all previous results from the wave flumes and the numerical simulation concluded that the occurrence probability of freak waves decreases when the directional spread of the initial spectrum increases.

In order to complete our comparisons, the probability of wave heights obtained from the Alber equation was also compared with the Forristall distribution that was derived from the second order theory. It is clearly shown the difference between the probability obtained from the linear wave theory, the second order theory and the Alber equation.

The latter is the stochastic version of the cubic Schrödinger equation at the tails of the probability. Based on our simulation, it was confirmed that at least three features that cannot be captured by the Forristall distribution could be observed from the Alber equation. It seems that Forristall distribution cannot capture the extreme events such as the freak waves. Moreover, the influence of the spectral shapes that can be observed in the Alber equation cannot be observed for the Forristall distribution as it only depends on the wave steepness for the deep water that is considered in this research. Besides that, Forristal distribution cannot be used to study the effect of the variation of the directional spreading.

It is important to mention that the initial inhomogeneous disturbances that are used in this work were taken to depend on the homogeneous spectra themselves, namely: (i) the wavenumber of the most-unstable mode is a property of the spectrum (see equation (3.17)), (ii) the function $R(\mathbf{r})$ in equation (3.10) was taken as $\rho_h(\mathbf{r})$, and (iii) δ in equation (3.8) was assigned the value 0.1 which is typically of the order of ε . The influence of different choices of disturbances is demonstrated in Stiassnie et al. (2008), Regev et al. (2008) and more recently in Eliasson and Shukla (2010).

It is instructive to remind the various choices that we have made in this study. First, in order to enrich our knowledge about its possible physical consequences, we chose to explore the Alber equation rather than other possibilities listed in Table 2.1. Second, we decided to study the long-time evolution of unstable homogeneous spectra subject to their most unstable inhomogeneous disturbance; a choice which resulted in a recurrent solution. Taking either stable homogeneous spectra or other inhomogeneous disturbances is expected to yield a wealth of other types of solutions. To this end, one can refer to the recent work of Stiassnie et al. (2008). Third, the specific details of the initial inhomogeneous disturbance were taken to depend on the homogeneous spectra themselves. Other options are also possible (see Regev et al. (2008)). Finally, we took advantage of the periodicity imposed by the initial disturbance and the consequent recurrent evolution of unstable spectra in order to calculate the probability of freak waves, implying that for stable spectra the freak wave probability will be given by the Rayleigh distribution. Therefore, we are aware that alternative choices are available and we thus consider the interesting phenomenon of stochastic recurrence as opening a new avenue in the theory of stochastic weakly nonlinear wave fields.

6.2 Further work

In the theory of the Alber equation and other equations based on higher-order terms in deep water allow for infinite wave heights to occur. In reality, there is a limit of wave steepness beyond which the waves will break (Babanin et al., 2010), and for one-dimensional waves this limit indicates the maximum ratio of individual wave height to the significant wave height of the order of ~ 2.0 (Babanin et al., 2011a). This issue has to be quantitatively addressed for two-dimensional surfaces.

It should also be mentioned that equations dealing with nonlinear evolution of water waves (i.e., the Alber equation, kinetic equation, the Zakharov equation, etc.) do not have dissipation mechanisms and energy-input mechanisms. For example, the kinetic equation is most broadly employed by the wave forecast models, but always combined with terms which represent wind energy input, wave-breaking dissipation, among others. Therefore, applying the outcomes of the Alber equation to the real waves in the ocean should be done with caution. It is known, both from solutions of the nonlinear Schrödinger equation with energy sources/sinks added and from experiments, that instability of wave trains is altered due to such external forcing (Trulsen and Dysthe, 1992, Galchenko et al., 2012, Onorato and Proment, 2012). It will be interesting to investigate the ocean surface waves using the Alber equation under the influence of wind energy input and dissipation. Since the Alber equation was derived from the cubic Schrödinger equation, it is possible to include the external forcing.

References

- ABC. 2004. Seas awash with monster waves. *News in Science*, <http://www.abc.net.au/science/articles/2004/07/26/1161681.htm> [Online]. [Accessed 06 July 2012].
- Alber, I. E. 1978. The effects of Randomness on the Stability of Two-dimensional Surface Wavetrains. *Proc. R. Soc. Lond.*, A. 363, 525-546.
- Alber, I. E. & Saffman, P. G. 1978. Stability of random nonlinear deepwater waves with finite bandwidth spectra. *TRW Defense and Space System Group Rep.*, 31326-6035-RU-00, 89 pp.
- Annenkov, S. Y. & Shrira, V. I. 2006. Role of non-resonant interactions in the evolution of nonlinear random water wave fields. *Journal of Fluid Mechanics*, 561, 181-207.
- Babanin, A. 2011. *Breaking and dissipation of ocean surface waves*, Cambridge University Press.
- Babanin, A. V., Chalikov, D., Young, I. R. & Savelyev, I. 2010. Numerical and laboratory investigation of breaking of steep two-dimensional waves in deep water. *Journal of Fluid Mechanics*, 644, 433-463.
- Babanin, A. V. & Soloviev, Y. P. 1987. Parameterization of the Width of Angular-Distribution of the Wind Wave Energy at Limited Fetches. *Izvestiya Akademii Nauk Sssr Fizika Atmosfery I Okeana*, 23, 868-876.
- Babanin, A. V. & Soloviev, Y. P. 1998a. Field investigation of transformation of the wind wave frequency spectrum with fetch and the stage of development. *Journal of Physical Oceanography*, 28, 563-576.
- Babanin, A. V. & Soloviev, Y. P. 1998b. Variability of directional spectra of wind-generated waves, studied by means of wave staff arrays. *Marine and Freshwater Research*, 49, 89-101.
- Babanin, A. V., T. Waseda, I. Shugan & Hwung, H.-H. 2011a. Modulational instability in directional wave fields and extreme wave events. *Proceedings of the ASME 2011 30th International Conference on Ocean, Offshore and Arctic Engineering OMAE2011, July 19-24*, . Rotterdam, The Netherlands.
- Babanin, A. V., Waseda, T., Kinoshita, T. & Toffoli, A. 2011b. Wave breaking in directional fields. *Journal of Physical Oceanography*, 41, 145-156.
- Benjamin, T. B. & Feir, J. E. 1967. The Disintegration of Wave Trains on Deep Water. *J. Fluid Mech.*, 27, 417-430.
- Bitner-Gregersen, E. M. & Magnusson, A. K. 2004. Extreme Events in Field Data and in a Second Order Wave Model. *Proc. Rogue Waves 2004*, . Brest, France.
- Boccotti, P. 2000. *Wave Mechanics for Ocean Engineering*, Burlington, Elsevier Science.
- Buckingham, E. 1914. On physically similar systems; Illustrations of the use of dimensional equations. *Physical Review*, 4, 345-376.
- Cavaleri, L., Bertotti, L., Torrisi, L., Bitner-Gregersen, E., Serio, M. & Onorato, M. 2012. Rogue waves in crossing seas: The Louis Majesty accident. *Journal of Geophysical Research-Oceans*, 117.
- Chalikov, D. 2009. Freak waves: Their occurrence and probability. *Physics of Fluids*, 21.
- Champeney, D. C. 1973. *Fourier transforms and their physical applications* London, Academic Press.
- Chandra, R. 2001. *Parallel programming in OpenMP*, Morgan Kaufmann Publishers, Morgan Kaufmann Publishers.
- Crawford, D. R., Saffman, P. G. & Yuen, H. C. 1980. Evolution of a random inhomogeneous field of nonlinear deep-water gravity waves. *Wave Motion*, 2, 1-16.
- Davey, A. & Stewartson, K. 1974. On Three-dimensional Packets of Surface Waves. *Proc. R. Soc. Lond.*, A. 338, 101-110.
- Dean, R. G. Freak waves: a possible explanation. Proc. NATO advanced research workshop on water wave kinematics, series E: applied sciences, 1990 Molde, Norway. Dordrecht, The Netherlands, Kluwer Academic Publishers, 609-612.

- Didenkulova, I. I., Slunyaev, A. V., Pelinovsky, E. N. & Kharif, C. 2006. Freak waves in 2005. *Natural Hazards and Earth System Science*, 6, 1007-1015.
- Dysthe, K., Krogstad, H. E. & Muller, P. 2008. Oceanic rogue waves. *Annual Review of Fluid Mechanics*.
- Dysthe, K. B. 1979. Note on a Modification to the Nonlinear Schrodinger Equation for Application to Deep Water Waves. *Proceedings of the Royal Society of London. A. Mathematical and Physical Sciences*, 369, 105-114.
- Dysthe, K. B., Trulsen, K., Krogstad, H. E. & Socquet-Juglard, H. 2003. Evolution of a narrow-band spectrum of random surface gravity waves. *Journal of Fluid Mechanics*, 478, 1-10.
- Eliasson, B. & Shukla, P. K. 2010. Numerical investigation of the instability and nonlinear evolution of narrow-band directional ocean waves. *Physical Review Letters*, 105, 014501(1) -014501(4).
- Faulkner, D. 2002. Shipping Safety: A Matter of Concern. *Ingenia*
- Fedele, F. The occurrence of extreme crests and the nonlinear wave-wave interaction in deep-water random seas. *In: CHUNG, J. S., IZUMIYAMA, K., SAYED, M. & HONG, S. W.*, eds., 2004 Toulon. 55-62.
- Fermi, E., Pasta, J. & Ulam, S. 1965. Collected papers of Enrico Fermi. *In: SEGRE, E. (ed.)*. Chicago: University of Chicago.
- Forristall, G. Z. 2000. Wave crest distributions: Observations and second-order theory. *Journal of Physical Oceanography*, 30, 1931-1943.
- Galchenko, A., Babanin, A. V., Chalikov, D., Young, I. R. & Haus, B. K. 2012. Influence of wind forcing on modulation and breaking of one-dimensional deep-water wave groups. *Journal of Physical Oceanography*, 42, 928-939.
- Gramstad, O. & Trulsen, K. 2007. Influence of crest and group length on the occurrence of freak waves. *Journal of Fluid Mechanics*, 582, 463-472.
- Gramstad, O. & Trulsen, K. 2010. Can swell increase the number of freak waves in a wind sea? *Journal of Fluid Mechanics*, 650, 57-79.
- Hasimoto, H. & Ono, H. 1972. Nonlinear Modulation of Gravity Waves. *J. Phys. Soc. Jpn*, 33, 805-811
- Hasselmann, K. 1962. On the Non-linear Energy Transfer in a Gravity-wave Spectrum, Part 1. General Theory. *Journal of Fluid Mechanics*, 12, 481-500.
- Hasselmann, K., Barnett, T. P., Bouws, E., Carlson, H., Cartwright, D. E., Eake, K., Euring, J. A., Gicnapp, A., Hasselmann, D. E., Kruseman, P., Meerburg, A., Mullen, P., Olbers, D. J., Richren, K., Sell, W. & Walden, H. 1973. Measurements of wind-wave growth and swell decay during the joint North Sea wave project (JONSWAP).
- Hjelmervik, K. B. & Trulsen, K. 2009. Freak wave statistics on collinear currents. *Journal of Fluid Mechanics*, 637, 267-284.
- Holthuijsen, L. H. 2007. *Waves in oceanic and coastal waters*, Leiden, Cambridge University Press
- Infeld, E. 1981. Quantitative Theory of the Fermi-Pasta-Ulam Recurrence in the Nonlinear Schrödinger Equation. *Physical Review Letters*, 47, 717-718.
- Janssen, P. & Alpers, W. Why SAR wave mode data of ERS and Envisat are inadequate for giving the probability of occurrence of freak waves. 2006 Frascati.
- Janssen, P. & Bidlot, J. 2009. *On the Extension of the Freak Wave Warning System and Its Verification*, Shinfield Park, European Centre for Medium-Range Weather Forecasts, Technical Memorandum.
- Janssen, P. a. E. M. 1981. Modulational instability and the Fermi-Pasta-Ulam recurrence. *Physics of fluids*, 24, 23-26.
- Janssen, P. a. E. M. 1983. Long-time behaviour of a random inhomogeneous field of weakly nonlinear surface gravity waves. *J. Fluid Mech.*, 133, 113-132.
- Janssen, P. a. E. M. 1985. Stability of a random inhomogeneous field of weakly nonlinear surface gravity waves with application to the JONSWAP study. *In: MITSUYASU, Y. T. A. H. (ed.) The Ocean Surface*. Reidel, Dordrecht, The Netherlands.

- Janssen, P. a. E. M. 2003. Nonlinear four-wave interactions and freak waves. *Journal of Physical Oceanography*, 33, 863-884.
- Janssen, P. a. E. M. 2009. On some consequences of the canonical transformation in the Hamiltonian theory of water waves. *Journal of Fluid Mechanics*, 637, 1-44.
- Kharif, C., Kraenkel, R. A., Manna, M. A. & Thomas, R. 2010. The modulational instability in deep water under the action of wind and dissipation. *Journal of Fluid Mechanics*, 664, 138-149.
- Kharif, C. & Pelinovsky, E. 2003. Physical mechanisms of the rogue wave phenomenon. *European Journal of Mechanics, B/Fluids*, 22, 603-634.
- Kinsman, B. 1965. *Wind waves, their generation and propagation on the ocean surface*, Prentice-Hall.
- Komen, G. J., Cavaleri, L., Donelan, M., Hasselmann, K., Hasselmann, S. & Janssen, P. a. E. M. 1994. *Dynamics and modelling of ocean waves*, Cambridge ; New York, NY, USA, Cambridge University Press.
- Lake, B. M., Yuen, H. C., Rungaldier, H. & Ferguson, W. E. 1977. Nonlinear deep-water waves: theory and experiment. Part 2. Evolution of a continuous wave train. *Journal of Fluid Mechanics*, 83, 49-74.
- Landsberg, H. E. 1955. *Advances in Geophysics*, Burlington, Elsevier.
- Lawton, G. 2001. Monsters of the deep. *New Scientist*, 170, 28-32.
- Lighthill, M. J. 1965. Contributions to the theory of waves in non-linear dispersive systems. *IMA Journal of Applied Mathematics (Institute of Mathematics and Its Applications)*, 1, 269-306.
- Longuet-Higgins, M. S. 1952. On the Statistical Distribution of the Heights of Sea Waves. *Journal of Marine Research*, 11, 245-266.
- Longuet-Higgins, M. S. 1963. The effect of non-linearities on statistical distributions in the theory of sea waves. *Journal of Fluid Mechanics*, 17, 459-480.
- Longuet-Higgins, M. S. 1976. On the Nonlinear Transfer of Energy in the Peak of a Gravity-Wave Spectrum: A Simplified Model. *Proceedings of the Royal Society of London. Series A, Mathematical and Physical Sciences*, 347, 311-328
- Longuet-Higgins, M. S. 1978a. The Instabilities of Gravity Waves of Finite Amplitude in Deep Water II. Subharmonics. *Proceedings of the Royal Society of London. A. Mathematical and Physical Sciences*, 360, 489-505.
- Longuet-Higgins, M. S. 1978b. The Instabilities of Gravity Waves of Finite Amplitude in Deep Water. I. Superharmonics. *Proceedings of the Royal Society of London. A. Mathematical and Physical Sciences*, 360, 471-488.
- Martin, D. U. & Yuen, H. C. 1980a. Quasi-recurring energy leakage in the two-space-dimensional nonlinear Schrödinger equation. *Physics of fluids*, 23, 881-883.
- Martin, D. U. & Yuen, H. C. 1980b. Spreading of energy in solutions of the nonlinear Schrödinger equation. *Physics of Fluids*, 23, 1269-1271.
- Mclean, J. W., Ma, Y. C., Martin, D. U., Saffman, P. G. & Yuen, H. C. 1981. Three-dimensional instability of finite-amplitude water waves. *Physical Review Letters*, 46, 817-820.
- Mei, C. C., Stiassnie, M. & Yue, D. 2005. *Broad-Banded Nonlinear Surface Waves in the Open Sea. Theory and Applications of Ocean Surface Waves*. Singapore: World Scientific.
- Mori, N., Onorato, M. & Janssen, P. a. E. M. 2011. On the estimation of the kurtosis in directional sea states for freak wave forecasting. *Journal of Physical Oceanography*, 41, 1484-1497.
- Mori, N., Onorato, M., Janssen, P. a. E. M., Osborne, A. R. & Serio, M. 2007. On the extreme statistics of long-crested deep water waves: Theory and experiments. *Journal of Geophysical Research C: Oceans*, 112.
- Nikolkina, I. & Didenkulova, I. 2011. Rogue waves in 2006-2010. *Natural Hazards and Earth System Sciences*, 11, 2913-2924.
- Nikolkina, I. & Didenkulova, I. 2012. Catalogue of rogue waves reported in media in 2006-2010. *Natural Hazards*, 61, 989-1006.

- Ochi, M. K. 2005. *Ocean waves the stochastic approach*, Cambridge, Cambridge University Press.
- Onorato, M., Cavaleri, L., Fouques, S., Gramstad, O., Janssen, P. a. E. M., Monbaliu, J., Osborne, A. R., Pakozdi, C., Serio, M., Stansberg, C. T., Toffoli, A. & Trulsen, K. 2009a. Statistical properties of mechanically generated surface gravity waves: A laboratory experiment in a three-dimensional wave basin. *Journal of Fluid Mechanics*, 627, 235-257.
- Onorato, M., Osborne, A., Fedele, R. & Serio, M. 2003. Landau damping and coherent structures in narrow-banded 1 + 1 deep water gravity waves. *Physical Review E - Statistical, Nonlinear, and Soft Matter Physics*, 67, 463051-463056.
- Onorato, M., Osborne, A. R. & Serio, M. 2002. Extreme wave events in directional, random oceanic sea states. *Physics of fluids*, 14, 25-28.
- Onorato, M., Osborne, A. R., Serio, M. & Bertone, S. 2001. Freak Waves in Random Oceanic Sea States. *Physical Review Letters*, 86, 5831-5834.
- Onorato, M., Osborne, A. R., Serio, M. & Cavaleri, L. 2005. Modulational instability and non-Gaussian statistics in experimental random water-wave trains. *Physics of fluids*, 17, 1-4.
- Onorato, M., Osborne, A. R., Serio, M., Cavaleri, L., Brandini, C. & Stansberg, C. T. 2004. Observation of strongly non-Gaussian statistics for random sea surface gravity waves in wave flume experiments. *Physical Review E - Statistical, Nonlinear, and Soft Matter Physics*, 70, 067302/1-067302/4.
- Onorato, M., Osborne, A. R., Serio, M., Cavaleri, L., Brandini, C. & Stansberg, C. T. 2006. Extreme waves, modulational instability and second order theory: wave flume experiments on irregular waves. *European Journal of Mechanics, B/Fluids*, 25, 586-601.
- Onorato, M. & Proment, D. 2012. Approximate rogue wave solutions of the forced and damped nonlinear Schrödinger equation for water waves. *Physics Letters A*, <http://dx.doi.org/10.1016/j.physleta.2012.05.063>.
- Onorato, M., Proment, D. & Toffoli, A. 2011. Triggering rogue waves in opposing currents. *Physical Review Letters*, 107.
- Onorato, M., Waseda, T., Toffoli, A., Cavaleri, L., Gramstad, O., Janssen, P. a. E. M., Kinoshita, T., Monbaliu, J., Mori, N., Osborne, A. R., Serio, M., Stansberg, C. T., Tamura, H. & Trulsen, K. 2009b. Statistical properties of directional ocean waves: The role of the modulational instability in the formation of extreme events. *Physical Review Letters*, 102.
- Osborne, A. R. & Petti, M. 1994. Laboratory-generated, shallow-water surface waves: Analysis using the periodic, inverse scattering transform. *Physics of Fluids*, 6, 1727-1744.
- Pelinovsky, E., Talipova, T. & Kharif, C. 2000. Nonlinear-dispersive mechanism of the freak wave formation in shallow water. *Physica D: Nonlinear Phenomena*, 147, 83-94.
- Petrova, P., Cherneva, Z. & Soares, C. G. 2006. Distribution of crest heights in sea states with abnormal waves. *Applied Ocean Research*, 28, 235-245.
- Pierson, W. J. 1955. Wind generated gravity waves. *Advances in Geophysics*, 2, 93-178.
- Pierson, W. J. & Moskowitz, L. 1964. A Proposed Spectral Form for Fully Developed Wind Seas Based on the Similarity Theory of S. A. Kitaigorodskii. *Journal of Geophysical Research*, 69, 5181-5190.
- Prevosto, M. 1998. Effect of Directional Spreading and Spectral Bandwidth on the Nonlinearity of the Irregular Waves. *the Eighth International Offshore and Polar Engineering Conference*. Montréal, Canada: International Society of Offshore and Polar Engineers.
- Prevosto, M., Krogstad, H. E. & Robin, A. 2000. Probability distributions for maximum wave and crest heights. *Coastal Engineering*, 40, 329-360.
- Regev, A., Agnon, Y., Stiassnie, M. & Gramstad, O. 2008. Sea-swell interaction as a mechanism for the generation of freak waves. *Physics of fluids*, 20, 112102-112102-8.
- Rice, S. O. 1944. Mathematical analysis of random noise. *Bell System Technical Journal*, 23 and 24.
- Rowlands, G. 1980. Time recurrent behaviour in the nonlinear Schrodinger equation. *Journal of Physics A: Mathematical and General*, 13, 2395-2399.

- Ruffles, P. 2001. Gas turbine technology: powering the future. *Ingenia*
- Segur, H., Henderson, D., Carter, J., Hammack, J., Li, C. M., Pheiff, D. & Socha, K. 2005. Stabilizing the Benjamin-Feir instability. *Journal of Fluid Mechanics*, 539, 229-271.
- Sharma, J. N. & Dean, R. G. 1981. Second-Order Directional Seas and Associated Wave Forces. *Society of Petroleum Engineers journal*, 21, 129-140.
- Socquet-Juglard, H., Dysthe, K., Trulsen, K., Krogstad, H. E. & Liu, J. 2005. Probability distributions of surface gravity waves during spectral changes. *Journal of Fluid Mechanics*, 542, 195-216.
- Stewart, R. H. 2008. *Introduction to Physical Oceanography*.
- Stiassnie, M. & Kroszynski, U. I. 1982. Long-time evolution of an unstable water-wave train. *Journal of Fluid Mechanics*, 116, 207-225.
- Stiassnie, M., Regev, A. & Agnon, Y. 2008. Recurrent solutions of Alber's equation for random water-wave fields. *J. Fluid Mech.*, 598, 245-266.
- Stokes, G. G. 1847. On the Theory of Oscillatory Waves. *Transactions of the Cambridge Philosophical Society*, 8, 441-455.
- Strikwerda, J. C. 1989. *Finite Difference Scheme and Partial Differential Equations*, California, Wadsworth Inc.
- Tayfun, M. A. 1980. Narrow-Band Nonlinear Sea Waves. *J. Geophys. Res.*, 85, 1548-1552.
- Toffoli, A., Babanin, A., Onorato, M. & Waseda, T. 2010a. Maximum steepness of oceanic waves: Field and laboratory. *Geophysical Research Letters*, 37.
- Toffoli, A., Benoit, M., Onorato, M. & Bitner-Gregersen, E. M. 2009. The effect of third-order nonlinearity on statistical properties of random directional waves in finite depth. *Nonlinear Processes in Geophysics*, 16, 131-139.
- Toffoli, A., Cavaleri, L., Babanin, A. V., Benoit, M., Bitner-Gregersen, E. M., Monbaliu, J., Onorato, M., Osborne, A. R. & Stansberg, C. T. 2011. Occurrence of extreme waves in three-dimensional mechanically generated wave fields propagating over an oblique current. *Nat. Hazards Earth Syst. Sci.*, 11, 895-903.
- Toffoli, A., Gramstad, O., Trulsen, K., Monbaliu, J., Bitner-Gregersen, E. & Onorato, M. 2010b. Evolution of weakly nonlinear random directional waves: Laboratory experiments and numerical simulations. *Journal of Fluid Mechanics*, 664, 313-336.
- Toffoli, A., Lefèvre, J. M., Bitner-Gregersen, E. & Monbaliu, J. 2005. Towards the identification of warning criteria: Analysis of a ship accident database. *Applied Ocean Research*, 27, 281-291.
- Toffoli, A., Lefevre, J. M., Monbaliu, J., Savina, H. & Bitner-Gregersen, E. Freak Waves: Clues for Prediction in Ship Accidents? , 2003 Honolulu, HI. 1368-1374.
- Toffoli, A., Onorato, M., Babanin, A. V., Bitner-Gregersen, E., Osborne, A. R. & Monbaliu, J. 2007. Second-order theory and setup in surface gravity waves: A comparison with experimental data. *Journal of Physical Oceanography*, 37, 2726-2739.
- Toffoli, A., Onorato, M., Bitner-Gregersen, E., Osborne, A. R. & Babanin, A. V. 2008. Surface gravity waves from direct numerical simulations of the Euler equations: A comparison with second-order theory. *Ocean Engineering*, 35, 367-379.
- Toffoli, A., Onorato, M. & Monbaliu, J. 2006. Wave statistics in unimodal and bimodal seas from a second-order model. *European Journal of Mechanics B-Fluids*, 25, 649-661.
- Tracy, E. R. & Chen, H. H. 1988. Nonlinear self-modulation: An exactly solvable model. *Physical Review A*, 37, 815-839.
- Trulsen, K. & Dysthe, K. 1992. Action of windstress and breaking on the evolution of a wavetrain. In: BANNER, M. & GRIMSHAW, R. (eds.) *Breaking Waves*. Springer-Verlag.
- Trulsen, K. & Dysthe, K. Freak waves—A three-dimensional wave simulation. Proceedings of the 21st Symposium on Naval Hydrodynamics 1997 Trondheim. 550.
- Trulsen, K. & Dysthe, K. B. 1996. A modified nonlinear Schrödinger equation for broader bandwidth gravity waves on deep water. *Wave Motion*, 24, 281-289.
- Tulin, M. P. & Waseda, T. 1999. Laboratory observations of wave group evolution, including breaking effects. *Journal of Fluid Mechanics*, 378, 197-232.

- Waseda, T., Kinoshita, T. & Tamura, H. 2009. Evolution of a random directional wave and freak wave occurrence. *Journal of Physical Oceanography*, 39, 621-639.
- Weigner, E. 1932. On the Quantum Correction for Thermodynamics Equilibrium. *Physical Review*, 40, 749-759.
- White, B. S. & Fornberg, B. 1998. On the chance of freak waves at sea. *Journal of Fluid Mechanics*, 355, 113-138.
- Whitham, G. B. 1965. A general approach to linear and non-linear dispersive waves using a Lagrangian. *Journal of Fluid Mechanics*, 22, 273-283.
- Wiegel, R. L. 1964. *Oceanographical engineering*, California, Prentice-Hall.
- Wu, G., Liu, Y. & Yue, D. K. P. 2006. A note on stabilizing the Benjamin–Feir instability. *Journal of Fluid Mechanics*, 556, 45-54.
- Young, I. R. 1999. *Wind Generated Ocean Waves*, Burlington, Elsevier Science.
- Yuen, H. C. & Ferguson Jr, W. E. 1978a. Fermi-Pasta-Ulam recurrence in the two-space dimensional nonlinear Schrödinger equation. *Physics of fluids*, 21, 2116-2118.
- Yuen, H. C. & Ferguson Jr, W. E. 1978b. Relationship between Benjamin-Feir instability and recurrence in the nonlinear Schrödinger equation. *Physics of fluids*, 21, 1275-1278.
- Yuen, H. C. & Lake, B. M. 1980. Instabilities of waves on deep water. In: *Annual Review of Fluid Mechanics*, M. Van Dyke; J.V. Wehausen; J.L. Lumley (eds.), 12, 303-334.
- Yuen, H. C. & Lake, B. M. 1982. Nonlinear Dynamics of Deep Water Gravity Waves. *Advanced in Applied Mechanics*, 22, 67-229.
- Zakharov, V. E. 1966. The Instability of Waves in Nonlinear Dispersive Media. *JETP (USSR)*, 51, 1107 - 1114.
- Zakharov, V. E. 1968. Stability of periodic waves of finite amplitude on the surface of a deep fluid. *J. Appl. Mech. Tech. Phys.*, 9, 190-194.
- Zakharov, V. E., Dyachenko, A. I. & Shamin, R. V. 2010. How probability for freak wave formation can be found. *European Physical Journal: Special Topics*, 185, 113-124.
- Zakharov, V. E. & Shabat, A. B. 1972. Exact theory of two-dimensional self-focusing and one-dimensional self-modulation of waves in nonlinear media. *Sov. Phys, JETP*, 34, 62-69.
- Zakharov, V. E. & Shamin, R. V. 2010. Probability of the occurrence of freak waves. *JETP Letters*, 91, 62-65.
- Zuevsky, A. 2008. Random Half-order Differential Correlation Functions. *Report on Mathematical Physics*, 61, 189-198.

Appendix A: Derivation of the Invariants

The invariants in the Chapter 4 were derived as follows:

1. First invariant

Evaluating equation (3.1) at $\mathbf{r} = \mathbf{0}$ gives

$$i \left(\frac{\partial \rho}{\partial t} + \frac{1}{2} \sqrt{\frac{g}{k_o}} \frac{\partial \rho}{\partial x_1} \right) - \frac{1}{4} \sqrt{\frac{g}{k_o^3}} \left(\frac{\partial^2 \rho}{\partial x_1 \partial r_1} - 2 \frac{\partial^2 \rho}{\partial x_2 \partial r_2} \right) = 0. \quad (\text{A.1})$$

Integrating (A.1) over the two-dimensional domain $x_1 \in [0, 2\pi / p]$, $x_2 \in [0, 2\pi / q]$ and applying the periodicity yields,

$$I_1 = \int \rho(\mathbf{x}, \mathbf{r}, t) \Big|_{\mathbf{r}=\mathbf{0}} d\mathbf{x} \quad (\text{A.2})$$

which is related to the wave action.

2. Second invariant

The second invariant consists of two components. The first component of this invariant is defined by taking the first order partial derivative of the equation (3.1) with respect to r_1 , that is $\partial / \partial r_1$, and evaluating at $\mathbf{r} = \mathbf{0}$, which gives

$$i \left(\frac{\partial^2 \rho}{\partial r_1 \partial t} + \frac{1}{2} \sqrt{\frac{g}{k_o}} \frac{\partial^2 \rho}{\partial r_1 \partial x_1} \right) - \frac{1}{4} \sqrt{\frac{g}{k_o^3}} \left(\frac{\partial^3 \rho}{\partial x_1 \partial r_1^2} - 2 \frac{\partial^3 \rho}{\partial r_1 \partial x_2 \partial r_2} \right) = \frac{\sqrt{gk_o^5}}{2} \frac{\partial}{\partial x} (\rho^2(\mathbf{x}, \mathbf{0}, t)). \quad (\text{A.3})$$

Again, integrating (A.3) over the two-dimensional domain $x_1 \in [0, 2\pi / p]$, $x_2 \in [0, 2\pi / q]$ and applying the periodicity yields,

$$I_{21} = \int \frac{\partial \rho(\mathbf{x}, \mathbf{r}, t)}{\partial r_1} \Big|_{\mathbf{r}=\mathbf{0}} d\mathbf{x} \quad (\text{A.4})$$

which is related to the wave momentum along r_1 .

Similarly, taking the first order partial derivative of equation (3.1) with respect to r_2 , that is $\partial/\partial r_2$, evaluating at $\mathbf{r}=\mathbf{0}$ and then integrating over the two-dimensional domain $x_1 \in [0, 2\pi/p]$, $x_2 \in [0, 2\pi/q]$ gives

$$I_{22} = \int \left. \frac{\partial \rho(\mathbf{x}, \mathbf{r}, t)}{\partial r_2} \right|_{\mathbf{r}=\mathbf{0}} d\mathbf{x} \quad (\text{A.5})$$

which is related to the wave momentum along r_2 .

3. Third Invariant

To obtain the explicit formula for this invariant, firstly, taking the second order partial derivative of the equation (3.1) with respect to r_1 , that is $\partial^2/\partial r_1^2$, evaluating at $\mathbf{r}=\mathbf{0}$ and integrating over the two-dimensional domain $x_1 \in [0, 2\pi/p]$, $x_2 \in [0, 2\pi/q]$ as well as applying the periodicity yields,

$$i \frac{\partial \rho}{\partial t} \left(\int \frac{\partial^2 \rho}{\partial r_1^2} d\mathbf{x} \right) = 2\sqrt{gk_o^5} \int \frac{\partial \rho}{\partial r_1} \frac{\partial \rho}{\partial x_1} d\mathbf{x}. \quad (\text{A.6})$$

Applying a similar procedure to r_2 gives

$$i \frac{\partial \rho}{\partial t} \left(\int \frac{\partial^2 \rho}{\partial r_2^2} d\mathbf{x} \right) = 2\sqrt{gk_o^5} \int \frac{\partial \rho}{\partial r_2} \frac{\partial \rho}{\partial x_2} d\mathbf{x}. \quad (\text{A.7})$$

Evaluating equation (3.1) at $\mathbf{r}=\mathbf{0}$, then multiplying by ρ and integrating over \mathbf{x} yields,

$$i \int \left(\rho \frac{\partial \rho}{\partial t} + \frac{1}{2} \sqrt{\frac{g}{k_o}} \rho \frac{\partial \rho}{\partial x_1} \right) d\mathbf{x} = \frac{1}{4} \sqrt{\frac{g}{k_o^3}} \int \left(\rho \frac{\partial^2 \rho}{\partial x_1 \partial r_1} - 2\rho \frac{\partial^2 \rho}{\partial x_2 \partial r_2} \right) d\mathbf{x}.$$

Integrating the right hand side of this equation by parts over \mathbf{x} , and applying the periodicity yields,

$$\frac{i}{2} \int \frac{\partial \rho^2}{\partial t} dx + \frac{1}{4} \sqrt{\frac{g}{k_o^3}} \int \left(\frac{\partial \rho}{\partial r_1} \frac{\partial \rho}{\partial x_1} \right) dx - \frac{1}{2} \sqrt{\frac{g}{k_o^3}} \int \left(\frac{\partial \rho}{\partial r_2} \frac{\partial \rho}{\partial x_2} \right) dx = 0. \quad (\text{A.8})$$

Substituting (A.6) and (A.7) into (A.8) gives the third invariant as follows:

$$I_3 = \int \rho^2(\mathbf{x}, \mathbf{r}, t) \Big|_{r=0} dx + \frac{1}{4k_0^4} \int \frac{\partial^2 \rho(\mathbf{x}, \mathbf{r}, t)}{\partial r_1^2} \Big|_{r=0} dx - \frac{1}{2k_0^4} \int \frac{\partial^2 \rho(\mathbf{x}, \mathbf{r}, t)}{\partial r_2^2} \Big|_{r=0} dx \quad (\text{A.9})$$

which is related to the energy of the system.

Publications

Journal Paper

Ribal, A., Babanin, A. V., Young, I., Toffoli, A. & Stiassnie, M. 2013. Recurrent solutions of the Alber equation initialized by Joint North Sea Wave Project spectra. *Journal of Fluid Mechanics*, 719, 314-344.

The following conference papers have been presented/published in support of and during this work:

1. Ribal, A., Babanin, A., Young, I., Toffoli, A. & Stiassnie, M. 2012. Recurrent solutions of Alber equation initialized by JONSWAP spectra. *WISE Meeting*. Barcelona, Spain, 16 - 20 April 2012.
2. Ribal, A., Stiassnie, M., Babanin, A. & Young, I. 2012. On the instability of wave-fields with JONSWAP spectra to inhomogeneous disturbances, and the consequent long-time evolution. *Geophysical Research Abstracts*. Vienna, Austria: EGU General Assembly 2012, Vol. 14, pp. EGU2012-3279.